JYU DISSERTATIONS 360

Heini Ijäs

Functional DNA Nanostructures for Molecular Transportation and Biosensing

UNIVERSITY OF JYVÄSKYLÄ
FACULTY OF MATHEMATICS
AND SCIENCE

JYU DISSERTATIONS 360

Heini Ijäs

Functional DNA Nanostructures for Molecular Transportation and Biosensing

Esitetään Jyväskylän yliopiston matemaattis-luonnontieteellisen tiedekunnan suostumuksella
julkisesti tarkastettavaksi maaliskuun 12. päivänä 2021 kello 12.

Academic dissertation to be publicly discussed, by permission of
the Faculty of Mathematics and Science of the University of Jyväskylä,
on March 12, 2021 at 12 o'clock.

JYVÄSKYLÄN YLIOPISTO
UNIVERSITY OF JYVÄSKYLÄ

JYVÄSKYLÄ 2021

Editors
Varpu Marjomäki
Department of Biological and Environmental Sciences, University of Jyväskylä
Päivi Vuorio
Open Science Centre, University of Jyväskylä

Permanent link to this publication: http://urn.fi/URN:ISBN:978-951-39-8556-1

ISBN 978-951-39-8556-1 (PDF)
URN:ISBN:978-951-39-8556-1
ISSN 2489-9003

ABSTRACT

Ijäs, Heini
Functional DNA nanostructures for molecular transportation and biosensing
Jyväskylä: University of Jyväskylä, 2021, 85 p.
(JYU Dissertations
ISSN 2489-9003; 360)
ISBN 978-951-39-8556-1 (PDF)
Yhteenveto: Toiminnalliset DNA-nanorakenteet molekyylikuljettimina ja biosensoreina
Diss.

In this thesis, DNA nanostructures were constructed with the DNA origami method and their ability to function as stimuli-responsive nanoscale devices and molecular transport vehicles was studied. DNA origami structures can be utilized *e.g.* in the development of biosensing techniques and biomedical applications. For this, their functionality, suitability for the transportation and encapsulation of cargo, and structural stability in physiological conditions need to be thoroughly characterized. In the first experimental part of the work, two pH-responsive DNA origami devices were designed and their functionality was studied: DNA nanocapsules for molecular transportation and zipper-like DNA origami structures for biosensor development. Spectroscopic and electrochemical methods were applied to confirm that the conformational state of the devices could be controlled accurately and repeatedly with the solution pH by functionalizing the devices site-specifically with DNA triplexes. For studying molecular transportation, the nanocapsules were loaded with gold nanoparticles and enzymes, and an encapsulation and display of the loaded cargo could be induced by changing the solution pH. In addition, the binding of the anticancer drug doxorubicin to DNA origami structures was characterized, yielding improved understanding on how DNA origami structures can be harnessed for transportation of DNA intercalators. Finally, the structural stability of the developed DNA origami nanocarriers under destabilizing physiological factors was studied. The nanocapsule was shown to remain functional in physiologically relevant salt conditions. The nuclease digestion rates of doxorubicin-loaded DNA origami structures depended both on the DNA origami superstructure and the doxorubicin loading density, yielding doxorubicin release at customizable rates. The detailed biophysical and biochemical characterization of functional DNA origami nanostructures presented in this thesis will help building a solid ground for the development of DNA nanostructure –based applications.

Keywords: DNA origami; DNA triplexes; doxorubicin; drug delivery; enzymes; fluorescence; nanoparticles.

Heini Ijäs, University of Jyväskylä, Department of Biological and Environmental Science, P.O. Box 35, FI-40014 University of Jyväskylä, Finland

TIIVISTELMÄ

Ijäs, Heini
Toiminnalliset DNA-nanorakenteet molekyylikuljettimina ja biosensoreina
Jyväskylä: Jyväskylän yliopisto, 2021, 85 s.
(JYU Dissertations
ISSN 2489-9003; 360)
ISBN 978-951-39-8556-1 (PDF)
Yhteenveto: Toiminnalliset DNA-nanorakenteet molekyylikuljettimina ja biosensoreina
Diss.

Tässä väitöskirjatyössä valmistettiin DNA-origamitekniikan avulla DNA-nanorakenteita ja tutkittiin niiden toimintaa ympäristön ärsykkeisiin reagoivina laitteina ja molekyylikuljettimina. DNA-origamirakenteita voidaan käyttää esimerkiksi biosensoritekniikoiden ja biolääketieteen menetelmien kehittämiseen. Näitä sovelluskohteita varten niiden toiminnalisuus, soveltuvuus (lääkaine)molekyylien kuljetukseen ja kapselointiin sekä rakenteellinen kestävyys fysiologisissa olosuhteissa täytyy määrittää läpikotaisesti. Työn ensimmäisessä kokeellisessa osassa suunniteltiin kaksi pH-responsiivista DNA-origamilaitetta ja tutkittiin niiden rakennemuutoksia pH:n muuttuessa. Työssä valmistettiin DNA-nanokapseli molekyylien kuljetukseen ja vetoketjumainen DNA-origamirakenne biosensoreiden kehitykseen. Spektroskooppisten ja sähkökemiallisten mittausten avulla määritettiin, että paikkaspesifisesti DNA-kolmoisjuosteilla funktionalisoitujen laitteiden rakenteellista tilaa voitiin hallita tarkasti ja toistettavasti pH:n avulla. Molekyylikuljetusta tutkittiin lataamalla DNA-nanokapselit kultananopartikkeleilla ja entsyymeillä, jotka voitiin sulkea kapseleiden sisälle ja paljastaa ympäristölle pH:ta muuttamalla. Lisäksi karakterisoitiin syöpälääke doksorubisiinin sitoutumista DNA-origameihin ja saatiin tarkempaa tietoa siitä, miten DNA-nanorakenteita voidaan hyödyntää DNA-interkalaattorien kuljetuksessa. Lopuksi tutkittiin valmistettujen DNA-nanokuljettimien kestävyyttä fysiologisissa olosuhteissa. Nanokapselit pysyivät toiminnallisina fysiologisissa suolapitoisuuksissa. Doksorubisiinilla ladattujen DNA-origamien muoto ja niihin sitoutuneen doksorubisiinin määrä vaikuttivat siihen, miten nopeasti rakenteet hajosivat nukleaasien vaikutuksesta. Tämän seurauksena doksorubisiini vapautui ympäristöön kustomoitavilla nopeuksilla. Työssä esitetty yksityiskohtainen biofysikaalinen ja –kemiallinen karakterisointi luo kokonaisvaltaista pohjaa DNA nanorakenteiden sovelluskehitykselle.

Avainsanat: DNA-origamit; DNA-kolmoisjuosteet; doksorubisiini; entsyymit; fluoresenssi; lääkeainekuljetus; nanopartikkelit.

Heini Ijäs, Jyväskylän yliopisto, Bio- ja ympäristötieteiden laitos, PL 35, 40014 Jyväskylän yliopisto

Author's address Heini Ijäs
Department of Biological and Environmental Science
P.O. Box 35
FI-40014 University of Jyväskylä
Finland
heini.e.ijas@jyu.fi

Supervisors Prof. Janne Ihalainen
Department of Biological and Environmental Science
P.O. Box 35
FI-40014 University of Jyväskylä
Finland

Dr. Veikko Linko
Department of Bioproducts and Biosystems
Aalto University School of Chemical Engineering
P.O. Box 16100
FI-00076 Aalto
Finland

Reviewers Prof. Barbara Saccà
Zentrum für Medizinische Biotechnologie
Fakultät für Biologie
Universität Duisburg-Essen
Universitätstraße 2, 45117 Essen
Germany

Dr. Katherine E. Dunn
School of Engineering
Institute for Bioengineering
University of Edinburgh
The King's Buildings, Edinburgh EH9 3FB
Scotland, UK

Opponent Prof. Kurt V. Gothelf
Interdisciplinary Nanoscience Center
Department of Chemistry
Aarhus University
Gustav Wieds Vej 14, 8000 Aarhus C
Denmark

CONTENTS

LIST OF ORIGINAL PUBLICATIONS

The thesis is based on the following original publications, which will be referred to in the text by their Roman numerals I–IV.

I Ijäs H.*, Nummelin S.*, Shen B.*, Kostiainen M.A. & Linko V. 2018. Dynamic DNA origami devices: from strand-displacement reactions to external stimuli-responsive systems. *International Journal of Molecular Sciences* 19: 2114.

II Ijäs H., Hakaste I., Shen B., Kostiainen M.A. & Linko V. 2019. Reconfigurable DNA origami nanocapsule for pH-controlled encapsulation and display of cargo. *ACS Nano* 13: 5959–5967.

III Williamson P.*, Ijäs H.*, Shen B., Corrigan D.K. & Linko V. 2021. Probing the conformational states of a pH-sensitive DNA origami zipper via label-free electrochemical methods. *Submitted manuscript*.

IV Ijäs H., Shen B., Heuer-Jungemann A., Keller A., Kostiainen M.A., Liedl T., Ihalainen J.A. & Linko V. 2021. Unraveling the interaction between doxorubicin and DNA origami nanostructures for customizable chemotherapeutic drug release. *Nucleic Acids Research (accepted manuscript).*

* *Equal contribution*.

In publication I, the author reviewed the literature and wrote the manuscript together with all authors.

In publication II, the author designed and characterized the pH-responsive DNA origami nanocapsule, designed the experiments, performed the FRET experiments together with I.H., performed the HRP–DNA conjugation and enzyme activity assays, analyzed the data, wrote the manuscript together with V.L., and prepared most of the figures.

In publication III, the author designed the pH-responsive DNA origami zipper, designed a part of the experiments, and carried out AGE and AFM analysis of the structural features and the pH-functionality of the DNA zippers (the AFM analysis together with B.S.). The author performed the image analysis of the AFM results, wrote parts of the manuscript, and prepared a part of the figures.

In publication IV, the author designed and performed all the experiments except for the TEM and AFM imaging (performed by B.S.) and a part of the DOX aggregation experiments (performed by A.H.–J.), analyzed and modeled the data, prepared a vast majority of the figures (except for the Fig. 1), and wrote a majority of the manuscript.

ABBREVIATIONS

24HB	24-helix bundle
A	absorbance
A	acceptor (in energy transfer)
ABTS	2,2'-azino-bis(3-ethylbenzothiazoline-6-sulfonic acid)
AFM	atomic force microscopy
AGE	agarose gel electrophoresis
Agp1	*Agrobacterium tumefaciens* phytochrome 1
AuNP	gold nanoparticle
bp	base pair
D	donor (in energy transfer)
DNase I	deoxyribonuclease I
DOX	doxorubicin
DPV	differential pulse voltammetry
dsDNA	double-stranded DNA
ε	molar extinction coefficient
E_{FRET}	Förster resonance energy transfer efficiency
E_{rel}	relative Förster resonance energy transfer efficiency
EDTA	ethylenediaminetetraacetic acid
EIS	electrochemical impedance spectroscopy
Φ	fluorescence quantum yield
FRET	Förster resonance energy transfer
HRP	horseradish peroxidase
k_{cat}	turnover number
K_m	Michaelis constant
λ	wavelength
NHS	N-hydroxysuccinimide
nt	nucleotide
PEG	polyethylene glycol
pK_a	acid dissociation constant
R_0	Förster distance
RT	room temperature
SDS	sodium dodecyl sulfate
shRNA	small hairpin RNA
siRNA	small interfering RNA
ssDNA	single-stranded DNA
sulfo-SMCC	sulfosuccinimidyl 4-(N-maleimidomethyl)cyclohexane-1-carboxylate
TAE	Tris-acetate-EDTA
TEM	transmission electron microscopy
UV–Vis	ultraviolet-visible
V_{max}	maximum reaction rate

1 INTRODUCTION

The main function of DNA in nature is the storage of genetic information. The Watson-Crick base pairing between the four nucleobases of DNA gives rise to simple and predictable structural features, which are applied in DNA nanotechnology for using DNA as a building material for the self-assembly of complex nanostructures. A particularly robust and versatile approach for designing and producing DNA nanostructures is the DNA origami method: the art of folding single-stranded DNA scaffolds with synthetic DNA oligonucleotides (Rothemund 2006). DNA origami nanostructures can be designed with user-defined two- or three-dimensional geometries, and manufactured with a simple one-pot self-assembly reaction. Functional groups such as chemical modifications, specific DNA motifs, proteins, or nanoparticles can be positioned into the DNA origami framework at a sub-nanometer precision.

With its high structural resolution, versatility, and site-specific functionalization, the DNA origami technique provides a diverse toolbox for bottom-up nanofabrication. DNA origami technique has been adopted in a variety of nanoscience research fields for the development of functional and innovative nanostructures, materials, and research tools. Static DNA origami nanoassemblies have been utilized for example as nanophotonic devices, enzyme reactors, and as templates for nanolithography (Linko *et al.* 2015a, Gopinath *et al.* 2016, Shen *et al.* 2018). DNA origami nanostructures can also have dynamic functions and carry out pre-programmed tasks that are controlled with external cues such as light, temperature, or the concentration of chemical components in the solution (I, Zhang and Seelig 2011, Daljit Singh *et al.* 2018). Such DNA origami nanodevices have been used for example as precision tools for studying molecular interactions, as information relay systems, and as biosensors (Funke *et al.* 2016, Song *et al.* 2017b, Funck *et al.* 2018). Both static and dynamic DNA origami structures are also attractive platforms for drug delivery systems owing to their biocompatibility, biodegradability, high monodispersity, and precise functionalization (Balakrishnan *et al.* 2019, Keller and Linko 2020).

This thesis presents development of both static and dynamic DNA origami nanostructures for applications in biological sciences. The first part of the work focuses on the design and characterization of dynamic DNA origami devices (I, II, III). The DNA origami structures developed in this work can be controlled with solution pH and they were utilized as biosensor components and molecular transportation tools. The second and third parts of the work focus more specifically on molecular transportation and development of DNA-based drug delivery tools. In order to harness DNA origami in drug delivery, the mechanisms for the loading, shielding, and display or release of therapeutic molecules need to be thoroughly characterized. Proteins or nanoparticles can be site-specifically conjugated to DNA origami carriers in defined copy numbers. On the other hand, when mixed with small DNA-binding drug molecules, DNA origami structures can be efficiently loaded with high numbers of drugs. These two cargo transportation mechanisms are discussed in the second section of the work and in Publications II and IV. In the third and final part of the work, the structural stability and functionality of the developed DNA origami are studied in conditions that mimic the environment encountered in the bloodstream. This is used to assess the feasibility of the developed molecular transportation vehicles for further drug delivery applications, and to demonstrate customizable drug release upon nuclease digestion (II, IV).

2 REVIEW OF THE LITERATURE

2.1 DNA nanotechnology and the DNA origami method

The most common form of DNA in nature as the carrier of genetic information is the B-form double helix. The information storage in DNA is based on the four-letter code of the nucleotide bases adenine (A), thymine (T), guanine (G), and cytosine (C) connected to a sugar-phosphate backbone. In the double-stranded DNA (dsDNA) molecule, two antiparallel single-stranded DNA (ssDNA) molecules hybridize through Watson-Crick base pairing with strict base pair specificity: an A–T base pair forms through two and a G–C base pair through three hydrogen bonds. The resulting B-form dsDNA structure twists around itself into a right-handed helix with 10.4–10.5 base pairs per a full helical turn (360°), 0.34 nm rise per base pair, and a diameter of ~2 nm (Drew *et al.* 1981) (Fig. 1a). The structure is further stabilized by base stacking interactions between the nucleobases and by the hydrophobic effect arising from the arrangement of the non-polar nucleobases in the centre of the helix (Feng *et al.* 2019).

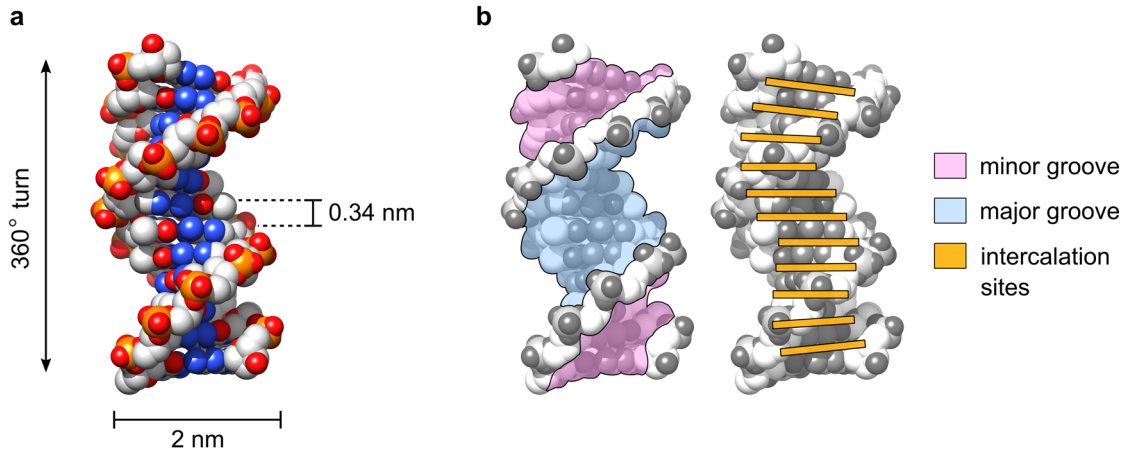

FIGURE 1 Structural features of B-form DNA. a) The three-dimensional structure and the dimensions of the DNA double-helix (Drew *et al.* 1981; PDB ID 1BNA). b) The main interaction sites in dsDNA.

The double-helical structure of B-form dsDNA provides multiple binding and interaction sites for other molecules, as illustrated in Fig. 1b. Groove-binding interactions with DNA-binding proteins, nucleic acids, or small molecules may take place either at the major groove or the minor groove of DNA (Strekowski and Wilson 2007, Rohs *et al.* 2010). Intercalation refers to a process where a small, planar molecule (or a planar residue of a larger molecule) inserts itself between two DNA base pairs. In addition, the negative charges of the phosphate groups in the DNA backbone mediate electrostatic interactions with charged particles. Attractive interactions between the anionic DNA and cationic molecules typically accompany and stabilize both intercalative and groove-binding interactions (Strekowski and Wilson 2007). Furthermore, cationic counterions (*e.g.* Na^+ and Mg^{2+}) in the solution condense at the DNA phosphates, screening their electrostatic repulsion and stabilizing the dsDNA structure (Manning 1978). When cationic molecules bind to DNA, the release of counterions generates an entropic contribution that favors the binding (Manning 1978, Strekowski and Wilson 2007).

Owing to the structural simplicity of DNA and the specificity of the Watson-Crick base pairing, predicting the interactions between two or more ssDNA molecules is extremely straightforward. DNA oligonucleotides with tailored sequences can be easily produced with modern synthesis methods to form ssDNA molecules that interact with each other in pre-defined manner. In addition to storing information, such molecules can function as building blocks for new types of materials and nanostructures formed through DNA hybridization. Indeed, the foundation of the field of structural DNA nanotechnology lies in the idea of Nadrian Seeman to take DNA from its natural context and arrange it into junctions and ordered lattices through rational design of synthetic oligonucleotide sequences (Seeman 1982).

The work of Seeman and co-workers led to the development of the double-crossover motif: a programmable building block for DNA nanostructures (Li *et al.* 1996, Jones *et al.* 2015). The motif is based on artificial DNA crossovers, which are structural analogues to the Holliday junction that forms in nature *e.g.* in the process of genetic recombination during meiosis (Fig. 2a). Natural Holliday junctions are typically connection points between symmetrical DNA sequences, which enables them to migrate along the interconnected DNA strands as an important part of their biological role. The artificial double-crossover motifs on the contrary are designed with asymmetric sequences, which lock the branched structure at an immobile configuration (Kallenbach *et al.* 1983). A double-crossover junction is formed of two immobile four-arm crossovers (Fig. 2b); this aligns the dsDNA molecules in a planar arrangement and provides the rigidity and stability required for the construction of large and complex DNA nanostructures (Fu and Seeman 1993, Seeman 2010).

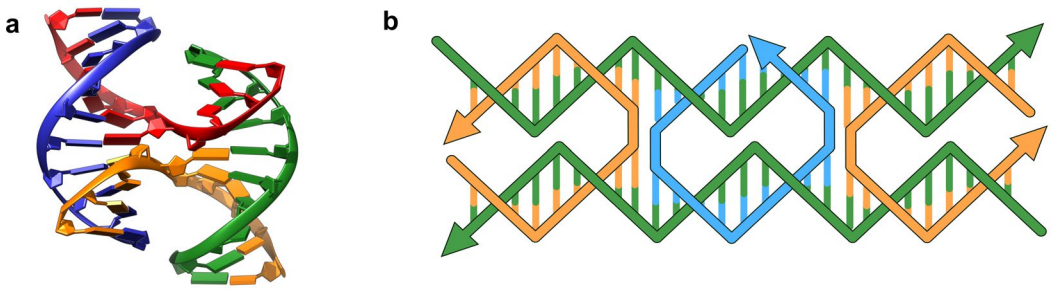

FIGURE 2 Branched DNA motifs. a) A crystal structure of a Holliday junction; a single cross-over between DNA helices (Ortiz-Lombardia *et al.* 1999; PDB ID 467D). b) An anti-parallel double-crossover motif comprising 5 ssDNA molecules. DNA directionality is indicated in the figure as arrows in the 5′–3′ direction. Adapted from Seeman (2010).

In 2006, Paul Rothemund initiated another leap in the development of DNA nanotechnology by introducing the robust and versatile DNA origami technique (Rothemund 2006). DNA origami nanostructures are assembled through hybridization of a long circular ssDNA scaffold strand and a set of short oligonucleotides termed the staple strands. The hybridization events pull different regions of the scaffold strand together into the designed geometry, as illustrated in Fig. 3a. In the final product, the scaffold is fully hybridized with the staple strands into a rigid structure that is held together by repeating DNA crossovers. The majority of DNA origami structures are folded from the 7,249 nucleotides (nt) long ssDNA genome of the bacteriophage M13mp18 (or its slight variants) through thermal annealing, *i.e.* a slow cooling from a denaturing temperature to room temperature (RT) (Castro *et al.* 2011). Typically, the assembly requires a mixture of ~200 unique synthetic staple strands, whose sequences can be generated with specialized design software (Douglas *et al.* 2009b). 5–20 mM Mg^{2+} is commonly applied in the folding reaction to screen the negative charges of the phosphate backbones and to enable the formation of a stable, densely packed DNA assembly (Douglas *et al.* 2009a). Monovalent cations, such as Na^{+}, provide much less electrostatic screening (Roodhuizen *et al.* 2019). For instance, Martin and Dietz (2012) studied the folding of DNA origami in the presence of Na^{+}, and found that a 2.4 M NaCl concentration was required for achieving a comparable folding outcome to 20 mM $MgCl_2$.

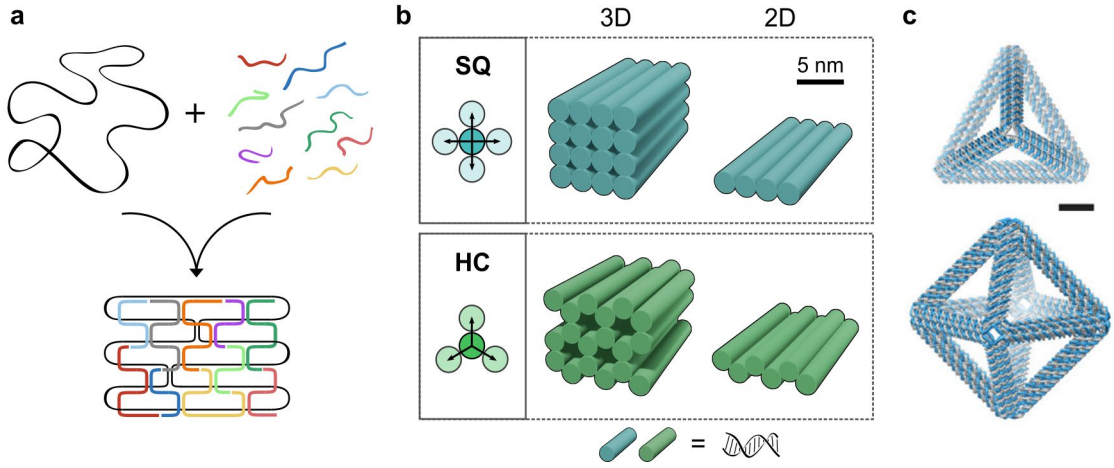

FIGURE 3 The assembly and design of scaffolded DNA origami nanostructures. a) The self-assembly of DNA origami nanostructures. The circular scaffold strand (black) is mixed with a set of staple strands (various colors). The folded DNA origami structure forms upon the hybridization of the scaffold strand and the staples, typically during a thermal annealing. b) Lattice-based two-dimensional (2D) and three-dimensional (3D) DNA origami structures. The most common lattice types are a square (SQ) and a honeycomb (HC) lattice, where each dsDNA helix (represented as cylinders) is connected to either four or three neighbouring helices, respectively. c) Examples of polyhedral 3D wireframe DNA origami structures. The length of the scale bar is 5 nm. Figure c is reprinted with permission from (Jun *et al.* 2019). Copyright 2019 American Chemical Society.

Lattice-based DNA origami can be designed in both two-dimensional (2D) and three-dimensional (3D) shapes (Fig. 3b). 2D origami are structures where dsDNA helices are linked together to form a flat sheet (Rothemund 2006). Compact 3D structures can be realized by arranging the dsDNA helices into lattices with a honeycomb, square, or hexagonal geometry (Douglas *et al.* 2009a, Ke *et al.* 2012b). Twisting, bending, and curvature can be introduced by adjusting the number of nucleotides between crossovers (Dietz *et al.* 2009, Han *et al.* 2011). In general, a single DNA origami structure containing 7,000–8,000 DNA base pairs has dimensions in the sub-100 nm range and a molecular weight of several MDa. Larger DNA origami constructions of even GDa scale can be constructed by assembling individual DNA origami into higher-order structures (Hong *et al.* 2017, Wagenbauer *et al.* 2017). Scaling up the currently expensive production of DNA origami structures up to an industrial level could become possible with biotechnological mass production (Praetorius *et al.* 2017).

In contrast to the lattice-based assemblies, wireframe origami are meshed structures where the edges of the structures are constructed of DNA beams of a chosen number of DNA helices (Fig. 3c). Wireframe origami can be fabricated in various 2D or 3D shapes, from regular polyhedral shapes to more complex and irregular architectures. The design procedures, physical properties, and potential applications of wireframe DNA origami are distinct of those of the lattice-based origami. However, as the work in this thesis is based purely on lattice-based 2D and 3D origami, these aspects of wireframe origami are not discussed further, but instead the works by *e.g.* Orponen (2018) and Piskunen *et al.* (2020) are

recommended for extensive recent reviews on the topic. DNA nanostructures and lattices can also be constructed from short synthetic oligonucleotides without a scaffold strand with tile- or brick-based assembly methods (Ke *et al.* 2012a, Hong *et al.* 2018). These methods are likewise excluded from the scope of this work.

2.2 Functionalization of DNA origami nanostructures

In addition to being produced in precisely controlled sizes and shapes, DNA origami structures can be applied as molecular scaffolds for positioning specific functional units and other molecules. For this use, DNA origami provide sub-nanometer structural resolution: along the length of the DNA helix, the position of the nucleotides or any further functional groups can be pre-defined with an accuracy that equals the separation between two base pairs; *i.e.* 0.34 nm (Fig. 1a). The diversity of modifications and functionalities has quickly grown as various fields of study have adopted DNA origami structures into their research and developed new ways to apply them for answering diverse research questions (Linko and Dietz 2013).

Different functional groups can be used to produce a variety of functional DNA origami structures – in other words, DNA nanostructures that are able to interact with their surroundings or execute pre-defined chemical or physical actions. The functional groups can be specific DNA motifs, such as blunt-ended dsDNA helices, ssDNA overhangs, multistranded DNA motifs, or DNA aptamers that recognize specific target molecules (Zhang and Seelig 2011, Douglas *et al.* 2012, Idili *et al.* 2014, Gerling *et al.* 2015). Chemical modifications can be incorporated into staple oligonucleotides during or after their synthesis, and using the modified staples in the folding reaction anchors the chemical modifications at defined sites in the structures (Madsen and Gothelf 2019). DNA origami can also be conjugated to other biomolecules and nanoparticles (Johnson *et al.* 2019a, Stephanopoulos 2020).

2.2.1 Basic mechanisms of dynamic DNA origami devices

DNA origami devices can be described as a class of functionalized DNA origami structures that are able to carry out a pre-programmed structural change in response to a defined external trigger (I, Nummelin *et al.* 2020). The development of DNA origami devices starts from the design of the origami structure. Conformational changes need to be enabled by the origami design, *e.g.* by including flexible joints formed of ssDNA residues or interlocked sliders, which provide the structures with various degrees of freedom (Marras *et al.* 2015). In order to turn random motions into well-defined and pre-programmed actions, the conformational states are typically controlled with site-specifically positioned functional groups whose interactions can be regulated with external stimuli (Daljit Singh *et al.* 2018). When the surrounding conditions favour the interaction,

the structure is locked in a "closed" state. The structure is released into an "open" or state when a trigger or a change in the conditions dismantles the interactions (Fig. 4). It is common that only the closed configuration has a defined conformational state, whereas the open configuration is flexible and mostly unconstrained. There are also some devices that can be switched between two or more well-defined conformational states, such as the plasmonic metamolecules developed by Kuzyk *et al.* (2014).

Functionalized and switchable DNA origami structures have various uses in biological sciences. They have been applied *e.g.* as measurement tools for characterizing biomolecules and their interactions, and in biomedicine for diagnostics and theraputics (Castro *et al.* 2017, Keller and Linko 2020). They can also be used as biological components in biosensors. In biosensing applications, the presence of an analyte or a change of solution conditions needs to trigger a selective and robust conformational change in the DNA origami sensor. Ideally, the sensor amplifies the recognition event into a strong output signal that can be reliably detected (Chandrasekaran 2017, Wang *et al.* 2020c). Several optical read-out strategies have been developed for switchable DNA origami sensors, including plasmonic detection (Funck *et al.* 2018) and various fluorescence and surface-enhanced Raman scattering – based detection methods (Loretan *et al.* 2020).

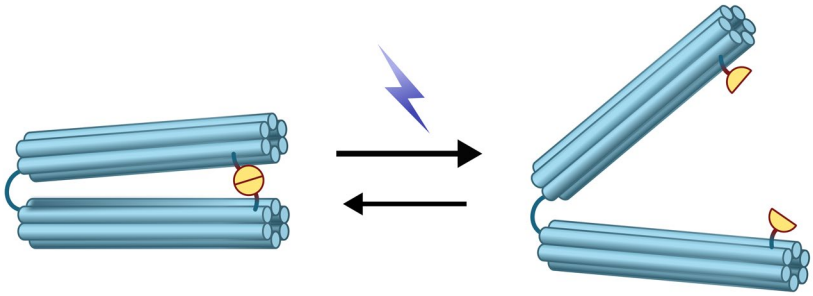

FIGURE 4 Schematic illustration of a common principle for switchable DNA origami devices. A DNA origami device is held in a "closed" state (on the left) through interactions between two or more functional units (half-circles). A physical or chemical trigger causes dissociation of the interactions, and the device switches into an "open" state. Reconfigurable devices can return back to the closed state. Adapted from Daljit Singh *et al.* (2018).

A simple approach for triggering on/off type conformational changes in DNA nanodevices is to utilize the Watson-Crick base pairing, base stacking interactions, or electrostatic repulsion between ssDNA and dsDNA residues in the DNA origami structures. Although nanomechanically designed DNA origami structures are in a random Brownian motion between different conformational states, the conformations that minimize the internal electrostatic repulsion between the negatively charged phosphate backbones are typically energetically favored. In a solution with a high ionic strength, cationic counterions associate with the DNA phosphates, screen their negative charges, and reduce the free energy of more compact conformational states (Pfeiffer *et al.* 2014, Roodhuizen *et al.* 2019). A simple and efficient method for controlling the

conformation of the structures is to adjust the strength of the electrostatic repulsion in respect to the core attractive forces between DNA molecules. The ionic strength of the solution has been used to drive conformational switching through adjusting the electrostatic repulsion in respect to hybridization of short ssDNA strands (Marras *et al.* 2018, Shi and Arya 2020), or in respect to base stacking interactions within the structures (Gerling *et al.* 2015). The interactions of hybridizing ssDNA strands and blunt-ended helices are also destabilized by elevated temperatures (Gerling *et al.* 2015, Johnson *et al.* 2019b), while compact conformational states can be favoured in the presence of molecular crowding agents (Hudoba *et al.* 2017).

External DNA oligonucleotides can also be used for actuating DNA origami devices through controlled DNA hybridization. In particular, strand displacement (or toehold-mediated strand displacement) refers to a process where a ssDNA strand added to the sample hybridizes with a complementary target strand in the DNA origami, and therefore displaces another strand initially hybridized to the target strand (Zhang and Seelig 2011). In DNA nanotechnology, this creates a simple mechanical/chemical switch that can be harnessed as a powerful method for generating controlled and kinetically well-defined actions in *e.g.* DNA walkers, logic circuits, and switchable DNA nanodevices (Zhang and Seelig 2011). Strand displacement was also utilized in the first switchable DNA origami device; the DNA box with an openable lid developed by Andersen *et al.* (2009).

Actuation with salt and DNA hybridization can thus be effectively realized with simple design choices of the DNA origami. Both the selection of stimuli for controlling DNA origami conformations and the added functionalities can be extended by introducing different stimuli-responsive groups, chemical modifications, and other molecules as a part of the DNA origami structure.

2.2.2 pH-sensitive DNA motifs

In addition to Watson-Crick base pairing, the DNA nucleotides can interact with each other and form secondary and tertiary structures through other types of hydrogen bonding interactions. In contrast to the remarkable thermodynamic stability of the B-DNA, the formation of other structural motifs of DNA is often less energetically favourable and requires a suitable environment in addition to a correct nucleotide sequence. These types of structural motifs include several multi-strand DNA motifs, of which parallel Hoogsteen-type triplexes and the C-rich intercalation motif (i-motif) (Fig. 5) are pH-sensitive (Guéron and Leroy 2000, Chandrasekaran and Rusling 2018). Their selectivity towards solution conditions gives them the potential to function as stimuli-responsive conformational switches in DNA origami structures.

A parallel Hoogsteen triplex forms when an ssDNA strand containing pyrimidine nucleotides (T and C) binds in the major groove of a dsDNA molecule that consists of polypurine- and polypyrimidine strands (Fig. 5a) (Asensio *et al.* 1999). The parallel orientation refers to the directionality of the triplex-forming strand in relation to the polypurine strand of the dsDNA molecule. The binding

takes place *via* sequence-specific hydrogen bonds termed as Hoogsteen bonds. A thymine in the ssDNA molecule can only interact with a T–A base pair in the dsDNA molecule, forming a T–A·T triplet. A cytosine in a ssDNA molecule can bind to a C–G base pair, but only in its protonated state (C^+), forming a C–G·C^+ triplet. As the average acid dissociation constant (pK_a) of protonated cytosines in triplex DNA is ~6.5, C–G·C^+ triplets are stable only at acidic conditions (Idili *et al.* 2014, Chandrasekaran and Rusling 2018). The T–A·T triplets are destabilized only at above pH 10.5 when the T nucleotides are deprotonated and lose their hydrogen bonding ability (Idili *et al.* 2014).

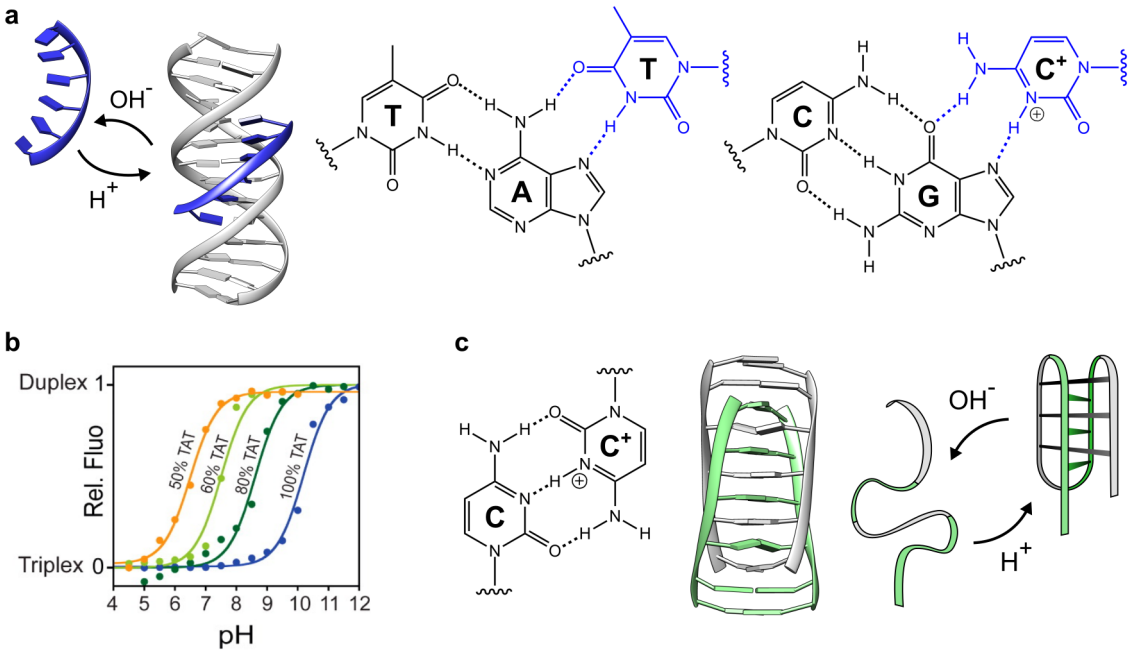

FIGURE 5 pH-sensitive and reconfigurable DNA motifs for the functionalization of DNA nanostructures. a) A parallel Hoogsteen-type triplex forms at an acidic pH (high H^+ concentration) from one dsDNA molecule (gray) and one ssDNA molecule (blue) (Asensio *et al.* 1999; PDB ID: 1BWG). Binding takes place in the major groove of the dsDNA helix *via* Hoogsteen bonds. T–A·T and C–G·C^+ triplets are connected through Watson-Crick hydrogen bonds (black dashed lines) and Hoogsteen hydrogen bonds (blue dashed lines) as illustrated. b) Programmability of the triplex pK_a. The graph presents the fraction of triplex and duplex structures of triplexes comprising 10 triplets and varying T–A·T/C–G·C^+ composition. Reprinted with permission from (Idili *et al.* 2014). Copyright 2014 American Chemical Society. c) An i-motif consists of four C-rich ssDNA strands. Two duplexes formed through hydrogen bonding of semiprotonated C-C+ pairs (left) form an intercalated structure (middle) (Esmaili and Leroy 2005; PDB ID: 1YBR). The quadruplex forms at an acidic pH (right).

The pK_a:s of the C–G·C^+ and T–A·T triplets define also the pK_a of the entire triplex – the pH value where a half of the strand population is in a triplex state. In DNA nanotechnology applications, this gives the opportunity to tune the pK_a of triplexes formed between synthetic oligonucleotides with sequence design (Idili *et al.* 2014) (Fig. 5b). More specifically, the pK_a of the triplex increases with an increasing fraction of T–A·T triplets. Both Idili *et al.* (2014) and Kuzyk *et al.* (2017)

have shown that the pK_a can be tuned from 6.5 (50% T–A·T) to 10.5 (100% T–A·T). Decreasing the T–A·T fraction below 50% did not lead to a further decrease of the pK_a, and above pH 10.5, all triplexes became unstable due to the aforementioned deprotonation of T nucleotides (Idili *et al.* 2014). pH-sensitive Hoogsteen triplexes have been incorporated into DNA origami structures for pH-controlled plasmonics (Kuzyk *et al.* 2017, Ryssy *et al.* 2020) as well as for oligomerization and isomerization (Wu and Willner 2016).

A second pH-sensitive DNA motif that has found its way into the DNA nanotechnology toolbox is the i-motif (Gehring *et al.* 1993) (Fig. 5c). As in the Hoogsteen-type C–G·C$^+$ triplets, the formation of i-motifs requires C$^+$ protonation. An i-motif consists of four C-rich ssDNA segments: two duplexes formed by base-pairing of parallel, semiprotonated cytosine strands (C–C$^+$) that intercalate between each other in an antiparallel orientation. Intermolecular i-motifs can link together multiple (2–4) ssDNA strands (middle panel of Fig. 5c) (Esmaili and Leroy 2005), or they can consist of a single ssDNA strand (right panel of Fig. 5c), such as in intramolecular i-motifs occurring naturally in telomeric sequences (Guéron and Leroy 2000). Due to the requirement of the protonation of half of the C$^+$ nucleotides, i-motifs form at an acidic pH. In DNA origami structures, i-motifs have been used *e.g.* as pH-controlled "seams" for adjusting the spacing between origami tiles (Majikes *et al.* 2017), and for opening and closing DNA origami containers with solution pH (Burns *et al.* 2018). Nesterova and Nesterov (2014) were able to adjust the pK_a of i-motifs between pH 6.4–7.2 by changing the number of cytidines, the sequences of DNA loops between the intercalative stretches, and with external DNA hairpins. However, because of their more easily predictable pK_a and a wider pH range, Hoogsteen-type triplexes still appear as the more versatile pH-sensitive motifs for DNA nanotechnology applications.

Finally, it should be noted that Hoogsteen triplexes can also form in an antiparallel fashion through C–G·G, T–A·A, and T–A·T triplets (reverse Hoogsteen triplets), but the resulting triplex is not pH-sensitive (Aviñó *et al.* 2003). In addition, a distinct multistrand DNA motif that forms through Hoogsteen bonding in G-rich DNA residues is the G-quadruplex. As guanosines do not contain chemical moieties that could undergo protonation/deprotonation events over a practicable pH area, G-quadruplexes are likewise not pH-sensitive. Instead, they have been applied as K$^+$ sensitive switches and hemin-binding functional units in DNA origami structures (Sannohe *et al.* 2010, Kuzuya *et al.* 2011, Atsumi and Belcher 2018).

2.2.3 Chemical modifications

Various chemical modifications can be included into synthetic DNA oligonucleotides either during or after the synthesis process. Modified oligonucleotides can be used to site-specifically position functional or reactive chemical groups into DNA origami structures (Madsen and Gothelf 2019). For example, the hybridization of azobenzene-modified DNA strands can be directed with UV and visible light (Asanuma *et al.* 2007), and they have been used to drive

reversible conformational switching in DNA origami devices (Kuzyk *et al.* 2016, Willner *et al.* 2017). Staple strands can also be modified with fluorescent dyes. Site-specifically positioned pairs of dye molecules can yield information about the conformational changes and integrity of DNA origami structures through Förster resonance energy transfer (FRET) (Stein *et al.* 2011). Fluorescence labelling also enables studying the localization of DNA origami structures in cell cultures with fluorescence and confocal microscopy (Lacroix *et al.* 2019), and enables the development of DNA origami –based superresolution imaging techniques (Graugnard *et al.* 2017, Scheckenbach *et al.* 2020). Chemical modifications can also provide reactive handles for the conjugation of DNA origami with other molecules, such as proteins or nanoparticles (Madsen and Gothelf 2019).

2.2.4 Gold nanoparticle- and protein conjugates

The precise positioning or compartmentalization of molecules on DNA origami nanostructures may produce new types of properties that are not encountered in a mixture of the same molecules freely diffusing in solution. The most commonly employed nano-objects in connection with DNA origami structures, devices, and higher-order assemblies are gold nanoparticles (AuNPs) (Johnson *et al.* 2019a). Arranging spherical or rod-like AuNPs on DNA origami in precise geometries can lead to various plasmonic or electronic effects (Pal *et al.* 2011, Kuzyk *et al.* 2012, Vogele *et al.* 2016). AuNPs connected to DNA origami can also produce dynamic properties, such as sliding or thermal actuation (Urban *et al.* 2018, Johnson *et al.* 2019b). AuNPs are also useful probes in transmission electron microscopy (TEM) imaging of DNA nanostructures, where they provide strong contrast.

Protein-DNA origami hybrid structures combine the well-defined structural scaffold of the DNA origami with the variety of structural, chemical, and catalytic functions of proteins. The resulting structures can be used for example as measurement tools for probing *e.g.* distance-dependent interactions and binding between proteins, such as antibodies and antigens (Shaw *et al.* 2019, Zhang *et al.* 2020), or the magnitude of forces playing a part in biomolecular interactions (Castro *et al.* 2017). Proteins can also be applied as dynamic components in DNA origami. For instance, Kosuri *et al.* (2019) were able to track the helicase activity of RecBCD with DNA origami rotors, and Valero *et al.* (2018) have constructed a DNA nanoengine powered by the T7 RNA polymerase moving along a DNA origami tube. Both protein- and nanoparticle-conjugated DNA origami can also be used in therapeutics and theranostics, as discussed later in Section 2.3.1.

Immobilized or precisely positioned enzymes can exhibit different activity levels than their free counterparts. Creating high local concentrations of enzymes through organization on DNA origami can increase the efficiency of multi-step catalytic processes in enzyme cascades (Fu *et al.* 2012, Klein *et al.* 2019, Stephanopoulos 2020). Several studies have specifically focused on studying how DNA origami may affect the functionality of protein molecules conjugated to their surface. In the case of enzymes, it has been widely acknowledged that the

proximity of the DNA origami often leads to significant changes in the enzymatic activity (Jaekel *et al.* 2019). If the substrate of the enzyme is large, encapsulation can lead to a reduced enzymatic activity through a restricted diffusion of the substrate to the enzyme (Grossi *et al.* 2017). Interestingly, the activity of many enzymes increases in the vicinity of DNA nanostructures (Lin and Wheeldon 2013, Ora *et al.* 2016, Zhang *et al.* 2016, Zhao *et al.* 2016, Klein *et al.* 2019). Proposed explanations include DNA-substrate interactions (Lin and Wheeldon 2013), a low local pH in the vicinity of the DNA backbone (Zhang *et al.* 2016), or even the effects of a highly ordered hydration layer at the origami surface (Zhao *et al.* 2016), but a consensus is still lacking (Jaekel *et al.* 2019). Understanding of the roles of the DNA origami design, the applied protein, and the experimental setup, would likely be important milestones in the development of protein-conjugated DNA origami devices harnessing customizable control over the enzymatic functions.

2.3 DNA origami in molecular transportation and drug delivery

Encapsulation of drug molecules within nanosized carriers can provide a powerful method for improving the bioavailability and bioactivity of drugs (Bertrand and Leroux 2012, Sun *et al.* 2014). Nanoparticle-based carriers can be used to transport poorly soluble drugs and to prevent degradation of the drugs in the circulation. Importantly, they can also target the delivery of drugs to specific tissues or cell types, which in turn leads to a tailored drug dosage at the target cells and fewer side effects at healthy off-target tissues – thus improving the efficiency and safety of the medication and leading to faster recovery. Nanoparticle-based delivery holds particular promise in the delivery of cytotoxic agents for the treatment of cancer. Several formulations based on *e.g.* liposomes, polymers, and inorganic nanoparticles are currently clinically approved or in clinical trials (Sun *et al.* 2014).

DNA origami nanostructure –based drug delivery provides several intrinsic advantages. DNA is a biocompatible, biodegradable, and chemically inert building material and DNA nanostructures can be easily designed with programmable molecular interactions (Linko *et al.* 2015b, Surana *et al.* 2015). They are also highly monodisperse, which is crucial for nanoparticle-based delivery. The size and shape of nanoparticles affect multiple processes in the circulation, such as the adhesion of plasma proteins on the particle surface, processing and clearance by the liver, kidneys and the spleen, and the final cell uptake (Lundqvist *et al.* 2008, Bertrand and Leroux 2012, Bastings *et al.* 2018). The structural precision of DNA origami manufacturing thus provides a key advantage in the development of drug delivery systems with well-defined retention times, clearance pathways, and target tissues (Bastings *et al.* 2018, Balakrishnan *et al.* 2019).

In some cases, plain DNA nanostructures can function as therapeutic agents by themselves. For instance, a study from 2018 found that unmodified DNA

origami nanostructures can exhibit preferential accumulation to kidneys and can alleviate acute kidney injury by scavenging reactive oxygen species and reducing oxidative stress (Jiang *et al.* 2018). Nevertheless, therapeutic DNA origami structures mainly function as carriers for other molecules (Jiang *et al.* 2020, Keller and Linko 2020). The emerged strategies for cargo loading and delivery can be roughly divided into two classes. First, biomolecules or nanoparticles with therapeutic properties can be site-specifically conjugated or encapsulated into DNA origami frameworks. Second, the strong DNA binding affinity of several small drug molecules can be used to load them into DNA origami structures for delivery. These two types of DNA origami -based molecular transportation mechanisms are reviewed separately in the next two sections.

2.3.1 Transportation of macromolecules and nanoparticles

DNA origami structures have the potential to carry and encapsulate various DNA-conjugated cargo molecules. One interesting type of cargo are proteins: functional proteins can provide a treatment to a variety of conditions, ranging from chronic diseases and protein deficiencies to acute illnesses such as cancer (Fu *et al.* 2014). However, free proteins are highly susceptible towards degradation in the circulation, they are poorly internalized into cells, and they commonly directed into endosomal degradation instead of reaching their target site at the cytoplasm. Conjugation of proteins to DNA origami can provide cell targeting and enhanced cellular uptake (Balakrishnan *et al.* 2019), as well as efficient protection towards degradation by proteases (Zhao *et al.* 2016, Wang *et al.* 2020a).

DNA origami can be used also for a delivery of nucleic acids and inorganic nanoparticles. Therapeutic nucleic acids can be easily attached to DNA origami structures through hybridization. Several studies have explored their uses in cancer treatment. For instance, DNA origami have been loaded with cytosine-phosphate-guanine (CpG) oligonucleotides and double-stranded RNA (dsRNA) for inducing a toll-like receptor –mediated immunostimulation (Schüller *et al.* 2011, Liu *et al.* 2020). Co-delivery of immunostimulatory oligonucleotides with suitable cancer cell –specific antigens can provide a route for cancer immunotherapy (Chi *et al.* 2020, Liu *et al.* 2020). The delivery of small interfering RNA (siRNA) and small hairpin RNA (shRNA) have also been shown to suppress cancer cell growth through gene silencing (Rahman *et al.* 2017, Liu *et al.* 2018b). Metal nanoparticles have uses both in therapeutics and theranostics. In particular, gold nanorods have been delivered to tumour sites for photothermal therapy, where their light absorption in the near-infrared light region leads to release of heat at the target site (Jiang *et al.* 2015, Du *et al.* 2016).

Some of the developed delivery systems have been static assemblies of DNA origami and cargo molecules (Fig. 6a). For instance, Ora *et al.* (2016) used a DNA tube for delivering luciferase enzymes into human embryonic kidney cells. Zhao *et al.* (2019), for one, applied DNA origami plates for delivering RNase A into human breast adenocarcinoma cells, resulting in cytotoxic degradation of intracellular RNA. DNA origami delivery vehicles can also be dynamic and

functionalized to perform predefined tasks such as cell targeting and cargo display or release after a specific trigger (Balakrishnan *et al.* 2019). Activation signals for drug delivery vehicles can be classified as either internal – that is, the device autonomously responds to a specific chemical trigger in the body – or external, meaning that the drug release is controlled from outside after administration. Examples of internal signals are pH, ion concentration, or the presence of target molecules, such as proteins associated with the target cell type. External signals include physical stimuli such as light, heat, ultrasound, or electric and magnetic fields (Sun *et al.* 2014).

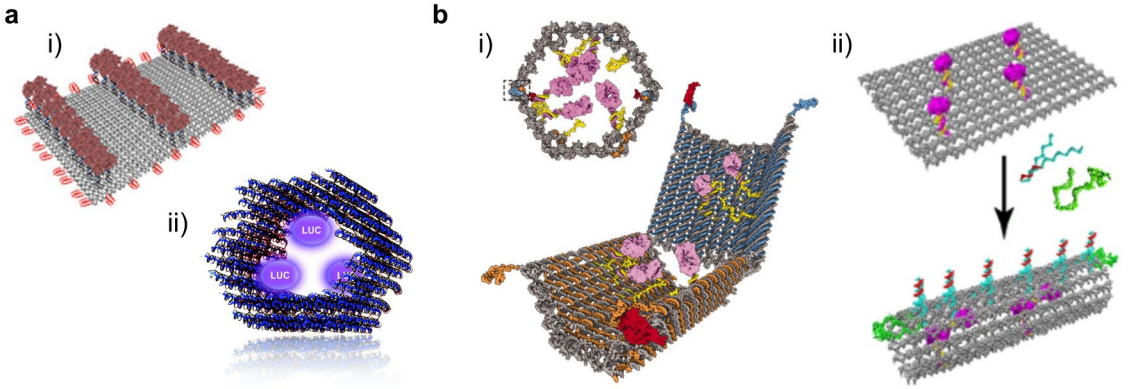

FIGURE 6 Examples of DNA origami for the transportation of proteins. a) Static DNA origami – protein structures. i) DNA origami plate for RNase A delivery. Reprinted with permission from (Zhao *et al.* 2019). Copyright 2019 American Chemical Society. ii) Encapsulation of luciferase enzymes for cellular delivery. Reprinted with permission from (Ora *et al.* 2016) - Published by The Royal Society of Chemistry. b) Dynamic, protein-loaded DNA origami. i) An aptamer-functionalized, logic-gated nanorobot exposes the encapsulated antibody fragments when recognizing the target cell. Reproduced with permission from (Douglas *et al.* 2012). Copyright 2012 AAAS. ii) A DNA origami plate is loaded with thrombin and fastened into a tube with cell targeting strands. Recognition of nucleolin opens the robot and exposes the thrombin. Reprinted with permission from (Li *et al.* 2018). Copyright 2018 Springer Nature.

Stimuli-responsive delivery of proteins was first demonstrated by Douglas *et al.* (2012) with barrel-like DNA origami "robots" (Fig. 6b, left panel). The robots were loaded with antibody fragments and functionalized with DNA aptamers; short DNA sequences that fold into secondary and tertiary shapes that bind specific molecular targets, such as proteins or a small molecules (Ni *et al.* 2011). Aptamers specific to three different cancer-cell specific proteins were included in the nanorobots in order to open the robot selectively at cancer cell surface and display the enclosed antigens. The functionality and selectivity were demonstrated with six different cancer cell lines. Albeit not directly related the drug delivery, Amir *et al.* (2014) could further show that the logic-gated nanorobots of Douglas *et al.* (2012) a could carry out computing functions in *B. discoidalis* (discoid cockroaches). Aptamer functionalization was also applied by Li *et al.* (2018), whose complex DNA nanorobot with aptamer locks would open when encountering cell surface nucleolin and expose the loaded thrombin (Fig.

6b, right panel). The devices were shown to suppress human breast cancer, human ovarian cancer, and murine melanoma tumours in mice. In addition, they were termed safe when administered to healthy Bama miniature pigs.

pH is an interesting internal trigger for DNA origami nanocarriers. While the pH of blood is maintained at ~7.4 by the bicarbonate buffering system, many tissues and cell organelles maintain distinct pH values (Casey *et al.* 2010). For instance, after DNA nanostructures are internalized into cells by *e.g.* receptor-mediated endocytosis, they enter the endocytic pathway (Wang *et al.* 2018). This subjects them to an acidification from pH 6.7 to pH 4.7 as early endosomes mature into late endosomes and eventually fuse into lysosomes. Functionalization by both i-motifs and Hoogsteen-type triplexes have been used to prepare DNA origami carriers that open in the endosomes during acidification to release or display the enclosed cargo (Burns *et al.* 2018, Liu *et al.* 2020). On the other hand, cancer cells are known to acidify their surroundings (pH 6.8–7.0) while maintaining an alkaline intracellular pH (pH 7.3–7.6) (White *et al.* 2017). The dysregulated pH is both a distinct chemical fingerprint of cancer cells, and a necessity for various cancer-cell –specific properties, such as inhibition of apoptotic signalling pathways and increased cell migration and proliferation – thus also a potential vulnerability for cancer treatment (Persi *et al.* 2018). In addition to pH, triggers such as light (Tohgasaki *et al.* 2019) or temperature (Juul *et al.* 2013) could have interesting uses in DNA origami -based drug delivery.

2.3.2 DNA-binding drugs

Several molecules used in therapeutics or diagnostics have strong affinity towards DNA. Mixing DNA-binding drugs with DNA origami provides a direct route of producing drug-loaded DNA nanostructures *via* self-assembly, and thus a convenient method for preparing customizable carriers for drug delivery.

Non-covalent DNA-binding interactions can take place through different types of weak interactions depending on the structure of the binding molecule. As shown in Fig. 1b and described in Section 2.1, these interactions can take place at various sites in dsDNA: between base pairs through intercalation or through hydrogen bonding interactions at the minor or the major grooves. In addition, DNA-binding molecules invariably carry a positive charge at a physiological pH, which mediates attractive electrostatic interactions with the phosphate backbone of DNA (Strekowski and Wilson 2007). In many cases, molecules can associate with DNA through multiple binding modes depending on factors such as the DNA base sequence or the ionic strength of the solution (Wilson *et al.* 1989, Silva *et al.* 2017). Fig. 7 shows examples of DNA-binding modes of drug molecules: intercalation (Fig. 7a) and minor groove binding (Fig. 7b).

An intercalating drug molecule that has become a particularly popular therapeutic agent in DNA nanostructure-based drug delivery is the anticancer drug doxorubicin (DOX). Other therapeutic molecules that have been loaded on DNA origami by applying their DNA binding affinity include intercalating photosensitizers (Zhuang *et al.* 2016), methylene blue (Kollmann *et al.* 2018), and the anticancer drug daunorubicin (Halley *et al.* 2016). The intercalative complex

between DOX and DNA forms when the planar tetracyclic ring moiety of DOX inserts itself between DNA base pairs, as illustrated in Fig. 7a. In addition, DOX contains a daunosamine sugar region with a NH_3^+ group that is in a cationic form at a physiological pH ($pK_a \approx 8.2$) (Fülöp *et al.* 2013). The amino sugar of intercalated DOX lies in the minor groove of DNA and stabilizes the complex through hydrogen bonding interactions (Frederick *et al.* 1990). In addition, DOX may associate with DNA through (pre-intercalative) minor-groove binding and through stacking of DOX molecules into external aggregates at high drug:DNA ratios (Pérez-Arnaiz *et al.* 2014). The insertion of DNA intercalating drugs between the DNA bases causes unwinding of the double helix and changes the mechanical properties of DNA (Biebricher *et al.* 2015). In DNA origami structures, this is known to result in a global twist and structural distortion (Zhao *et al.* 2012, Chen *et al.* 2016).

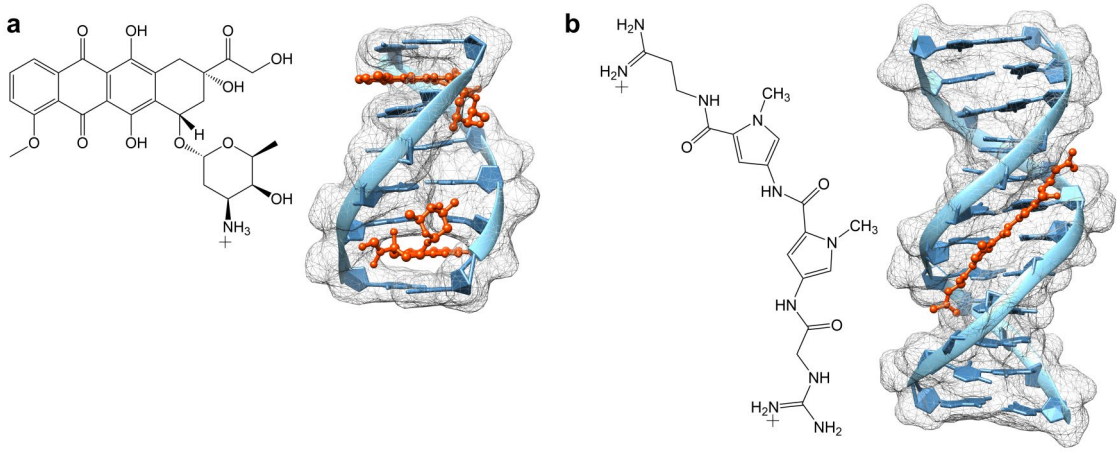

FIGURE 7 Examples of small molecules binding non-covalently to DNA. Each type of interaction is exemplified with a resolved crystal structure of the drug-DNA complex. a) Intercalation of the anticancer drug doxorubicin (DOX). Two DOX molecules (orange-red) are intercalated between G–C base pairs of a short dsDNA fragment d(CGATCG) (Frederick *et al.* 1990; PDB ID: 1D12). b) Minor-groove binding by the antiviral and antibacterial molecule netropsin (Tabernero *et al.* 1993; PDB ID: 121D).

DOX is a chemotherapeutic agent used in the treatment of a wide range of cancer types. It is thought to cause cell death by two main molecular mechanisms: first, DNA-bound DOX causes topoisomerase II poisoning that blocks DNA repair, and second, the metabolism of DOX generates reactive oxygen species that causes damage at various cell organelles (Nitiss 2009, Pommier *et al.* 2010, Thorn *et al.* 2011). DOX is typically administered as an intravenous injection of the free drug. This introduces a burst of a high DOX concentration in the bloodstream, which can cause dose-dependent side-effects, most severe being cardiotoxicity, bone marrow suppression, and a development of multidrug resistance (Margaritis and Manocha 2010, Thorn *et al.* 2011). The currently commercially available liposomal and polyethylene glycosylated (PEG) liposomal formulations of DOX can decrease the off-target side effects and deliver more drug to the tumor, but offer limited drug release (Sun *et al.* 2014). The development of

nanoparticle delivery systems with controllable and effective drug loading, retention, and release properties thus still remains a challenge.

Using DNA origami for DOX delivery offers an intrinsic advantage of high drug loading efficiency: intercalating molecules have generally been observed to bind DNA according to a nearest-neighbour exclusion model (McGhee and von Hippel 1974, Strekowski and Wilson 2007). This means that the maximum density of intercalating molecules is reached when every second intercalation site is occupied. Binding of further intercalators is highly unfavourable, but can be induced by *e.g.* stretching of the DNA molecule (Hayashi and Harada 2007). As a single DNA origami structure contains ~7,000 DNA base pairs, the association of DOX with the whole DNA origami structure can result in a high number of bound drug molecules – although some of the base pairs might be inaccessible due to superstructure-related effects and steric hindrance (Kollmann *et al.* 2018, Miller *et al.* 2020).

The first studies on DOX delivery with DNA origami were presented by Zhao *et al.* (2012) and Jiang *et al.* (2012); both studies demonstrating the efficiency of DNA origami –DOX delivery systems against human breast cancer cells *in vitro*. After this, Zhang *et al.* (2014) reported DOX –loaded DNA origami accumulating at tumour sites *in vivo* through the enhanced permeability and retention effect when administered intravenously. The uptake could be further enhanced with cancer cell -specific aptamers for active targeting (Liu *et al.* 2018a). It has been proposed that release of DOX from DNA nanostructures takes place after endosomal uptake as the endosomal acidification destabilizes the DOX-DNA complex (Jiang *et al.* 2012, Zhang *et al.* 2014). DOX can also be loaded into DNA origami that carry other types of cargo molecules. Such combination therapies for cancer treatment have been extensively studied by Baoquan Ding and co-workers, who have employed DOX in combination with *e.g.* gold nanorods (Song *et al.* 2017a), shRNA (Liu *et al.* 2018b), siRNA (Wang *et al.* 2020b), and tumour suppression genes (Liu *et al.* 2018a).

2.3.3 Stability and biocompatibility

For effective drug delivery, DNA origami structures need to retain their structural stability in the biological environment long enough to reach their target site and execute the intended therapeutic function. Nanoparticles in the blood always carry a risk of being recognized as a foreign material that is either actively removed from the body or treated as a potential pathogen (Bertrand and Leroux 2012, Surana *et al.* 2015). By default, DNA is highly immunogenic: after internalization into cells, recognition of DNA from foreign origin (non-self DNA) can lead to an onset of the antiviral response of the innate immunity and an onset of inflammation (Wu and Chen 2014). Albeit some studies have termed DNA origami structures immunologically inert *in vivo* (Zhang *et al.* 2014, Li *et al.* 2018), they are also known to *e.g.* induce an adverse immune response in splenocytes (Schüller *et al.* 2011, Auvinen *et al.* 2017). Partially disassembled DNA origami nanostructures might also cause higher immune stimulation than intact structures (Surana *et al.* 2015). Characterizing the structural stability of DNA

nanostructures in physiological media is thus a crucial aspect in the development of safe and efficient drug delivery systems (Ramakrishnan *et al.* 2018, Bila *et al.* 2019, Keller and Linko 2020).

The stability of DNA origami has been studied *in vitro* either in cell cultures or in solutions containing or mimicking physiological fluids, *in vivo*, and *in silico* (Ramakrishnan *et al.* 2018, Roodhuizen *et al.* 2019). *in vivo* studies are inarguably the only way to fully address the complexity of biological systems and the roles of various degradation and clearance pathways DNA nanoparticles experience in the body. Simplified experimental setups *in vitro* on the other hand allow identification and in-depth characterization of the various destabilizing factors and processes. Based on the existing studies, the physiological salt concentration and nuclease activity have been identified as the two main destabilizing factors of the physiological environment (Hahn *et al.* 2014).

Lattice-based DNA origami structures are typically folded in the presence of 5–20 mM Mg^{2+} (Douglas *et al.* 2009a). In blood plasma, the total Mg^{2+} concentration is roughly one order of magnitude lower, 0.65–1.05 mM, of which only 55–70 % is in a free ionized form (Jahnen-Dechent and Ketteler 2012). Introducing DNA origami into a low-Mg^{2+} environment can lead to a heavy structural deformation or disassembly when the dissociation of cations from the phosphate backbone leads to increased internal electrostatic repulsion (Hahn *et al.* 2014, Kielar *et al.* 2018). Flexible DNA origami structures with loosely packed DNA helices appear to withstand the destabilizing effects better and remain structurally intact in a lower Mg^{2+} concentration. In addition, it was shown that Mg^{2+} depleted structures can remain stable in water or in Tris-HCl buffer when a gentle buffer exchange method is used, but disturbing the DNA-Mg^{2+} interactions with Mg^{2+}-sequestering compounds such as ethylenediaminetetraacetic acid (EDTA) or phosphate ions can lead to a rapid disassembly (Kielar *et al.* 2018). The suggested explanation for the observed behavior was that Mg^{2+} ions are partially retained in the DNA structures even after buffer exchange. The design choices of the DNA origami, the applied Mg^{2+} depletion protocol, and other components of the solution thus appear to form the cornerstones of DNA origami stability in low-Mg^{2+} environments, but the existing literature still appears insufficient for fully understanding and predicting their effects.

Enzymatic degradation is the second central factor compromising the stability of DNA origami structures in the body. It is important to maintain a low concentration of DNA in the bloodstream: accumulation of DNA released from dead cells (self-DNA) can lead to a development of autoimmune diseases, while non-self DNA is normally indicative of the presence of pathogens (Wu and Chen 2014). For maintaining the homeostasis of the body, DNA in the bloodstream of organisms is digested by nucleases. Most abundant nuclease in the bloodstream is the deoxyribonuclease I (DNase I). DNase I is a minor-groove binding enzyme that catalyses the hydrolysis of the P-O3′-bond of the DNA sugar-phosphate backbone, and cleaves both ssDNA and dsDNA non-sequence-specifically into short fragments (Weston *et al.* 1992, Suck 1994). The enzymatic activity of DNase I is defined through the Kunitz unit (KU); the digestion of salmon sperm DNA

by one KU of DNase I will produce a ΔA_{260} of 0.001 min^{-1} mL^{-1} in 0.1 M sodium acetate buffer, pH 5.0 at 25 °C.

The stability of DNA origami in the presence of DNase I has been studied both with isolated DNase I and in fetal bovine serum (Ramakrishnan *et al.* 2019b). DNA origami objects have been shown to be digested considerably slower than regular dsDNA plasmids, and the relative digestion rates of DNA origami structures are superstructure-dependent (Castro *et al.* 2011, Hahn *et al.* 2014, Ramakrishnan *et al.* 2019b, IV). While individual reports on the DNase I stability of DNA origami structures can be difficult to compare and combine into a comprehensive picture for instance because of different experimental conditions, certain trends for predicting the effects of nuclease digestion have been identified. While flexible structures with fewer DNA crossovers are more resistant towards Mg^{2+} depletion, they are digested faster than the denser, closely packed DNA origami structures. DNA crossovers affect the helical parameters of dsDNA and might thus provide nuclease stability by disrupting the minor-groove attachment of DNase I (Chandrasekaran *et al.* 2020). In addition, choices made regarding the scaffold strand routing and the staple strand sequences can affect the nuclease stability (Ramakrishnan *et al.* 2019a).

For improving the stability of DNA origami structures towards both low cation concentrations or enzymatic digestion, they can be stabilized by covalent cross-linking with UV light or through enzymatic ligation (Gerling *et al.* 2018, Ramakrishnan *et al.* 2019a). Dendrimeric DNA oligonucleotides positioned on the origami surface were also shown to increase the DNase I resistance (Kim and Yin 2020). Non-covalent coating or encapsulation with other molecules, such as lipids (Perrault and Shih 2014), serum proteins (Auvinen *et al.* 2017), or various polymers (Anastassacos *et al.* 2020) has also been shown to provide resistance against nucleases, decreased immune activation, and protection from low-Mg^{2+} -induced denaturation.

3 AIMS OF THE STUDY

The aim of this thesis was to develop and study functional DNA origami structures and devices that can be applied in molecular transportation and biosensing. To achieve this goal and to build a comprehensive picture of a development and characterization of functional DNA origami structures, three main topics of study were defined: the dynamic functions of DNA origami, their ability to accommodate cargo molecules for transportation, and their structural stability under application-specific conditions. The specific aims for each publication were as follows.

I) Review the existing literature of dynamic DNA origami devices.

II) Develop a pH-responsive DNA origami nanocapsule for molecular transportation. Characterize the pH response with spectroscopic methods, study the loading and encapsulation of nanoparticles and proteins, and characterize the functionality of the nanocapsules in physiologically relevant conditions.

III) Design a DNA origami device for studying and detecting biomolecular binding interactions, such as Hoogsteen-type DNA triplex formation at low pH. Detect the conformational state of the device with electrochemical methods.

IV) Study the doxorubicin loading properties of distinct DNA origami structures. Determine the nuclease digestion rates and resulting doxorubicin release profiles for the development of customized drug release.

4 METHODS

Table 1 presents an overview of the methods used in the publications II–IV. The main methods applied or developed in this thesis by the author are marked with an asterisk, and are presented under the following subsections. These subsections aim to provide an overview of the main methods, a brief description of their theoretical basis, and a reasoning for the selection of the methods. Further experimental details of the presented methods and other methods applied in the publications can be found in the experimental sections of the corresponding publications, as listed in Table 1.

Microscopy imaging (TEM, AFM) and the AuNP–DNA conjugation presented in this thesis were performed by Dr. B. Shen at Aalto University. Electrochemical measurements were carried out at the University of Strathclyde, Glasgow, UK, by P. Williamson.

TABLE 1 Summary of the main methods used in the presented work.

Method	Publication
Sample preparation methods	
DNA origami design *	II, III
DNA origami assembly and purification *	II, III, IV
Protein–DNA conjugation *	II
AuNP–DNA conjugation *	II
Electrophoresis	
Agarose gel electrophoresis (AGE)	II, III, IV
Spectroscopic methods	
UV–Vis spectroscopy *	II, III, IV
Fluorescence spectroscopy	II, IV
Colorimetric HRP activity assays *	II
Förster resonance energy transfer (FRET) *	II
UV–Vis and fluorescence titrations for doxorubicin *	IV
UV–Vis and fluorescence assays of DNase I digestion and doxorubicin release *	IV
Electrochemical measurements	III
Imaging	
Transmission electron microscopy (TEM)	II, IV
Atomic force microscopy (AFM)	III, IV

* Details presented in the subsections.

4.1 Design and assembly of DNA origami

The DNA origami nanostructures developed in this study (the capsule and the zipper) were designed in a honeycomb lattice with the caDNAno software version 2.2.0 (Douglas *et al.* 2009b). The CanDo online software (Castro *et al.* 2011, Kim *et al.* 2012) was used to predict the flexibility and solution structures of the designs prior experimental work. The structures were functionalized with Hoogsteen triplexes by including staple strand extensions at defined locations.

The formation of a Hoogsteen triplex takes place between dsDNA and ssDNA molecules: here, a dsDNA hairpin and an ssDNA overhang. The sequences of the DNA triplexes were designed according to the reported dependency of the pK_a(calc) on the %T–A·T (Idili *et al.* 2014, Kuzyk *et al.* 2017). The correct secondary structure and thermal stability of the dsDNA hairpins were simulated with the NUPACK online simulation tool (Zadeh *et al.* 2011). The details of the Hoogsteen triplexes for the nanocapsule and the zipper are listed in Table 2. The nanocapsule was designed with 8 triplexes of the same %T–A·T

but different sequences for preventing non-specific interactions. In the zipper, the sequences of all 9 triplexes are identical; this was chosen to minimize possible slight variation in the triplex pK_a values and to produce a sharp pH response.

TABLE 2 The DNA triplexes in the capsule and zipper designs.

Design	Length nt	n(T–A·T)	n(C–G·C$^+$)	%(T–A·T)	pK_a(calc)
Capsule	20	12	8	60.0	7.2
Zipper	18	12	6	66.7	7.6

The pH-responsive DNA origami in both studies were compared to control samples whose conformation is not affected by the solution pH. Permanently open nanocapsules were prepared without pH-responsive triplex residues. Permanently closed nanocapsules were prepared by substituting the triplex residues with complementary ssDNA overhangs, whose hybridization locks the nanocapsules in a closed conformation regardless of the solution pH. An open control for the pH-responsive zipper was constructed by replacing the triplex-forming ssDNA residues with ssDNA strands with a scrambled sequence.

The DNA origami were assembled using thermal annealing. The folding process for the nanocapsule and the zipper were optimized separately for each design by comparing the folding outcome in different buffer conditions with an agarose gel electrophoresis (AGE) analysis. Based on the optimization, the nanocapsules were folded in a reaction mixture containg 20 nM of an 8064-nt scaffold and a 7.5× molar excess of 264 staples in 1× Tris-acetate-EDTA (TAE) buffer supplemented with 15 mM of $MgCl_2$ and 5 mM NaCl. The mixture was first heated to 65 °C and then cooled to 59 °C with a rate of 1 °C/15 min and finally to 12 °C with rate 0.25 °C/45 min. The zippers were folded using 20 nM of a 7560-nt scaffold and a 9.2× molar excess of 216 staples in a buffer containing 1× TAE and 15 mM $MgCl_2$. For annealing, the mixture was heated to 90 °C, cooled from 90 °C to 70 °C at 0.2 °C/8 sec, then from 70 °C to 60 °C at 0.1 °C/8 sec, and finally from 60 °C to 27 °C at a rate of 0.1 °C/2 min. The triangle, bowtie, and double-L structures used in this study were annealed according to the protocols described in the original publications (Rothemund 2006, Shen *et al.* 2018). The 24-helix bundle (24HB) design and the optimized folding protocol were provided by S. Julin (Aalto University).

PEG precipitation was used for purification of excess staple oligonucleotides from the reaction mixtures after folding (Stahl *et al.* 2014) (II, III, IV). AGE was used for basic characterization of the purification quality, and as a supporting method for spectroscopic experiments (II, III, IV). Agarose gels were prepared at a 2% (w/v) agarose concentration and pre-stained with ethidium bromide for visualizing the DNA origami structures under UV light. Microscopy

imaging with AFM (III, IV) or TEM (II, IV) was used for further structural characterization. Conformational changes of DNA origami, their interactions with other molecules, and their stability in different media were investigated with various spectroscopic methods described in the following sections.

4.2 Methods for studying structural changes of DNA origami

4.2.1 UV absorbance of nucleotides

UV absorbance of nucleotides was used to study both DNA origami sample concentration (II, III, IV) and integrity (IV). DNA origami concentrations were determined from DNA absorbance at 260 nm using the Beer-Lambert law ($A = \varepsilon \times c \times l$). The molar extinction coefficients of DNA origami at 260 nm (ε_{260}) were calculated as

$$\varepsilon_{260} = (6{,}700 \times N_{\mathrm{ds}} + 10{,}000 \times N_{\mathrm{ss}})\ \mathrm{M^{-1}cm^{-1}} \quad (1)$$

where N_{ds} is the number of nucleotides in dsDNA residues and N_{ss} is the number of nucleotides in ssDNA residues in the particular DNA origami design (Hung *et al.* 2010). Equation 1 thus takes into account the different spectroscopic properties of ssDNA and dsDNA as well as their relative amounts in the sample. The ε_{260} of short ssDNA oligonucleotides is affected by both the base composition (different extinction coefficients of the nucleosides) and sequence-dependent interactions, such as base stacking between nucleosides (Cavaluzzi and Borer 2004). In DNA origami structures, these effects are averaged out due to the large number of nucleotides and different sequences, and the ε_{260} of ssDNA nucleotides can be approximated as 10,000 $M^{-1}cm^{-1}$. The ε_{260} of dsDNA nucleotides is 6,700 $M^{-1}cm^{-1}$. The decrease of absorbance relative to ssDNA, hypochromicity, is caused by the π-stacking interactions of nucleotides in the double helix (Danilov 1974). According to an AFM-based analysis of DNA origami concentrations performed by Hung *et al.* (2010), these values for linear dsDNA also hold for DNA origami nanostructures.

N_{ds} and N_{ss} for Equation 1 were determined separately for each origami design. N_{ds} comprises both the dsDNA residues formed through base pairing of the scaffold and the staple oligonucleotides and the dsDNA residues formed as secondary structures in self-complementary regions of unpaired scaffold or staple strand residues. The base pairs between the scaffold and the staples form the majority of the dsDNA nucleotides, and their amount was calculated from the origami design. The number of base pairs in secondary structures of the scaffold strand in the applied temperature and ionic strength were simulated with the NUPACK web application (Zadeh *et al.* 2011).

In addition to routine characterization of sample concentration, the UV absorbance of nucleotides was used for assessing the dsDNA/ssDNA composition of DNA origami samples during DNase I digestion (IV). During

DNase I digestion, the nucleases catalyse the cleavage of the DNA backbone, which gradually transforms the dsDNA structures into short ssDNA fragments. Increase of N_{ss} relative to N_{ds} in the sample leads to an increase of ε_{260} and the measured A_{260}. The DNase I digestion profiles of DNA origami structures (triangle, bowtie, double-L, capsule, and 24HB) after addition of DNase I were characterized spectroscopically by following the A_{260} of the samples over time. The percentage of intact DNA origami at each time point of the kinetic measurement [%intact(t)] was calculated as

$$\%\ \text{intact}\ (t) = \frac{A_{260}(t) - A_{260}(\text{intact})}{A_{260}(\text{digested}) - A_{260}(\text{intact})} \times 100\%\,. \qquad (2)$$

$A_{260}(t)$ is the measured A_{260} at the time point t; A_{260}(intact) is the A_{260} of the sample before digestion, and A_{260} (digested) is the A_{260} of the sample after the digestion has been completed, *i.e.* the A_{260} signal has stabilized.

4.2.2 Förster resonance energy transfer

The conformational changes and the structural stability of the pH-responsive DNA origami nanocapsules were studied with Förster resonance energy transfer (FRET) experiments (II). FRET is a process of non-radiative excitation energy transfer, where a donor (D) molecule in an electronic excited state transfers its excitation energy to a ground-state acceptor (A) molecule (Lakowicz 2006). The process takes place *via* dipole-dipole interactions, and its efficiency (FRET efficiency, E_{FRET}) is strongly distance-dependent ($E_{FRET} \sim r^{-6}$, where r denotes the distance between the D and the A). This makes FRET a powerful tool for distance measurements of biomolecules and nanostructures in the 1–10 nm distance range (Sahoo 2011). For FRET experiments with DNA origami nanostructures, D–A pairs can be site-specifically positioned into the structures by utilizing fluorophore-conjugated staple oligonucleotides.

For FRET studies, the DNA nanocapsules were site-specifically labelled with Alexa Fluor 488 and Alexa Fluor 594 fluorophores. The fluorophores form a FRET pair in which Alexa Fluor 488 (D) can transfer its excitation energy to the Alexa Fluor 594 (A). The Förster distance for this D-A pair is $R_0 \approx 6.0$ nm (Fig. 8) according to the manufacturer (Thermo Fisher Scientific). R_0 (in Å) is given by $R_0 = 2.111\ [\kappa^2\, n^{-4}\, Q_D\, J(\lambda)]^{1/6}$ and thus depends on the relative orientation of the transition dipoles of the D and the A (κ^2), the refractive index of the medium (n), the quantum yield of the D (Q_D), and the overlap integral $J(\lambda)$ of D emission and A absorption (Lakowicz 2006). κ^2 can have values between 0–4 and is typically – including here – assumed to be equal to 2/3. The assumption holds if D and A undergo free rotational diffusion, which is typically a safe assumption, albeit difficult to confirm experimentally. The possible resulting inaccuracy of R_0 should still be acknowledged when evaluating values of r obtained from FRET data.

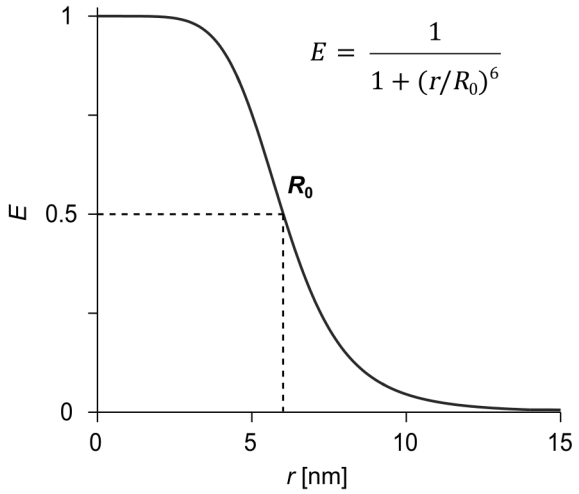

FIGURE 8 The expected dependency of FRET efficiency E on the D-A separation (r) for the Alexa Fluor 488 (D) – Alexa Fluor 594 (A) FRET pair. The Förster distance R_0 denotes the r at which E = 0.5. Here, $R_0 \approx 6.0$ nm ($\kappa^2 = 2/3$).

The E_{FRET} can be calculated from the measured intensities of D and A through various approaches: from the decrease of D intensity, the decrease of D fluorescence lifetime, or the increase of A intensity in the presence of energy transfer. Here, the fluorescence emission spectra of D-A labelled samples were collected after D excitation at 460 nm and after A excitation at 560 nm. E_{FRET} was determined from the increase of A intensity at 617 nm as

$$E_{\mathrm{FRET}} = \frac{I_{\mathrm{AD}}\varepsilon_{\mathrm{AA}} - I_{\mathrm{AA}}\varepsilon_{\mathrm{AD}}}{I_{\mathrm{AA}}\varepsilon_{\mathrm{DD}}}\,, \tag{3}$$

where $\varepsilon_{\mathrm{AA}}$ is the molar extinction coefficient of A at the A excitation wavelength (560 nm), and $\varepsilon_{\mathrm{AD}}$ and $\varepsilon_{\mathrm{DD}}$ are the molar extinction coefficients of A and D at the D excitation wavelength (460 nm), respectively. I_{AD} is the A emission intensity following excitation at 460 nm and I_{AA} is the A emission intensity after excitation at 560 nm. When the experiment is based on the comparison of FRET efficiencies of different samples or time points, a simplified quantity, the relative E_{FRET} (E_{rel}), can be used instead:

$$E_{\mathrm{rel}} = \frac{I_{\mathrm{AD}}}{I_{\mathrm{AD}} + I_{\mathrm{DD}}}\,. \tag{4}$$

E_{rel} was used when the conformational changes of the nanocapsule were studied with kinetic experiments. All FRET experiments were performed using either a Biotek Cytation 3 or a Synergy plate reader, and the FRET signal from the pH-functionalized nanocapsule was compared to the permanently open and closed control samples.

4.3 Cargo loading and release

4.3.1 DNA conjugation and loading of proteins and nanoparticles

The encapsulation of cargo inside the DNA origami nanocapsule was carried out by conjugating the cargo particles with ssDNA oligonucleotides and attaching the conjugates to the origami through hybridization with a complementary ssDNA overhang in the nanocapsule inner cavity (II). Horseradish peroxidase (HRP) was selected as a model enzyme for demonstrating the encapsulation of proteins because it is readily commercially available, has a typical globular tertiary structure, and its peroxidase activity can be easily monitored with several substrate molecules using colorimetric or fluorometric assays. This will yield information on the functionality of the cargo after loading and encapsulation (Section 4.3.2). AuNPs were applied as cargo nanoparticles for their high contrast in TEM imaging.

A wide selection of methods has been developed for both covalent and non-covalent conjugation of proteins and DNA (Trads *et al.* 2017, Jaekel *et al.* 2019). The chemical reactivity of primary amine (NH_2) or thiol (SH) groups at the protein surface provides a convenient route for covalent conjugation. NH_2 groups are present in lysine side chains and at the protein N-terminus, and SH groups in cysteine side chains. The conjugation of HRP with DNA was performed with a two-step approach using thiol-modified ssDNA oligonucleotides and a sulfosuccinimidyl 4-(N-maleimidomethyl)cyclohexane-1-carboxylate (sulfo-SMCC) crosslinker (Fig. 9a). The crosslinker contains both a N-hydroxysuccinimide (NHS) ester and a maleimide group. In the first step of the conjugation, HRP was mixed with the sulfo-SMCC cross-linker, leading to a covalent linkage of the amine groups of the protein and the NHS ester groups. The step is also called maleimide activation, as it introduces maleimide groups at the protein surface for further conjugation reactions. After this, excess free cross-linkers in the solution were removed by buffer exchange with 10 kDa spin-filtration. In the second conjugation step, the maleimide groups of the crosslinker were reacted with thiol-modified oligonucleotides. Thioether bond formation between the maleimide and the thiol groups links the proteins and the ssDNA molecules together.

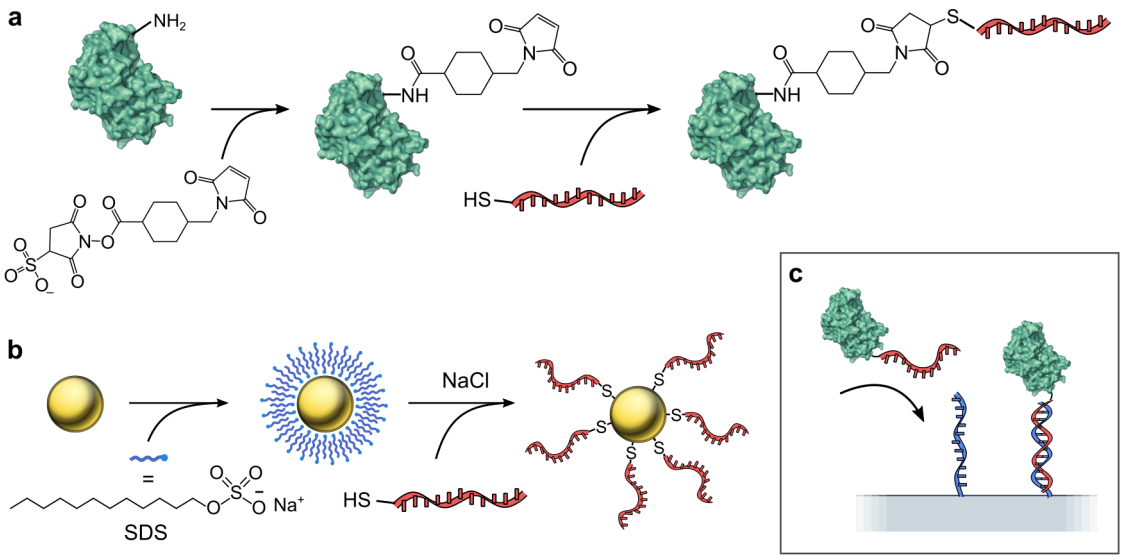

FIGURE 9 DNA conjugation of HRP and AuNPs and the attachment of cargo in the DNA origami nanocapsule. a) Two-step conjugation of HRP and thiol-modified ssDNA through a sulfo-SMCC crosslinker. b) Covalent conjugation of AuNPs and thiol-modified ssDNA strands in the presence of SDS. Adapted from Liu and Liu (2017). c) Attachment of cargo on DNA origami: the conjugate strand (red) hybridizes with the cargo anchoring strand (blue) on the origami. The figures are not in scale.

HRP has been estimated to carry three solvent-accessible surface lysines (O'Brien *et al.* 2001). Because of the multiple amine residues on the protein surface, the conjugation is likely to yield a heterogeneous mixture of HRP–DNA conjugates with 1 to 3 conjugated oligonucleotides per protein. On the other hand, HRP contains no surface cysteines that could have unwanted reactivity with the maleimide group of the crosslinker.

The thiol-modified oligonucleotides were also used for producing AuNP-DNA conjugates (*i.e.* DNA-modified AuNPs) through gold-thiol bond formation. Surface functionalization of AuNPs (5 nm diameter) was carried out through a salting process in the presence of sodium dodecyl sulfate (SDS) (Fig. 9b). SDS is an anionic surfactant that forms a stabilizing layer on the gold nanoparticles before DNA is added. DNA adsorption on gold is then achieved by gradually increasing the NaCl concentration in the solution (Hurst *et al.* 2006, Liu and Liu 2017).

The DNA-conjugated cargo molecules were attached to DNA origami through hybridization (Fig. 9c). One of the staple strands in the nanocapsule cavity was designed with an ssDNA overhang with a complementary sequence to the conjugated strand. Attachment of the cargo to the capsules was achieved by subjecting the mixture of cargo particles and DNA origami to a brief heating-annealing process (from +40 °C to +20 °C at –0.1 °C min^{-1} for AuNPs and at the rate of −0.1 °C/40 s for HRP).

4.3.2 HRP activity assays

The site-specific attachment of HRP on DNA origami and the effect of the attachment on its enzymatic activity were studied with a 2,2'-azino-bis(3-ethylbenzothiazoline-6-sulfonic acid) (ABTS) assay. HRP was loaded into DNA capsules (both pH-responsive capsules and open controls) as described in Section 4.3.1, after which unbound enzymes were removed by PEG precipitation (Stahl *et al.* 2014). The enzymatic activity of HRP in the purified, enzyme-loaded nanocapsules was measured both at pH 6.4 and 7.8, and compared to the enzymatic activity of free HRP in the same conditions.

In the presence of H_2O_2, the oxidation of ABTS by HRP produces the radical $ABTS^{\bullet+}$ (Fig. 10a) (Childs and Bardsley 1975). The catalytic activity of HRP in each of the studied conditions was determined by measuring the product formation rate (increase of $ABTS^{\bullet+}$ concentration) from $ABTS^{\bullet+}$ absorption at 420 nm, and analysing the data with a Michaelis-Menten model. The Michaelis-Menten equation defines the initial rate of product formation (v_0) as

$$v_0 = \frac{\mathrm{d[P]}}{\mathrm{d}t} = \frac{V_{\max} \times [\mathrm{S}]}{K_{\mathrm{m}} + [\mathrm{S}]} \tag{5}$$

where [P] and [S] refer to the concentrations of the product and the substrate, respectively; $V_{\max}$ is the maximum rate of reaction at the applied enzyme concentration, and K_{m} is the Michaelis constant (Nelson and Cox 2008). When the enzyme is mixed with its substrate, the system undergoes first a brief pre-steady state period where the concentration of the enzyme-substrate complex builds up. The process is usually too fast to observe in the measurement. After the enzyme-substrate complex reaches a constant concentration, the system follows steady-state kinetics, which are probed in the experiment. Here, product formation takes place first at a constant initial reaction rate v_0, and slows down as the substrate is being consumed. $V_{\max}$ and K_{m} were determined by measuring v_0 at different [ABTS] (Fig. 10b) and fitting the Michaelis-Menten equation to the obtained v_0 *vs.* [ABTS] data (Fig. 10c). Michaelis-Menten kinetics apply when the concentration of the enzyme is small compared to the concentration of the substrate; *i.e.* [E] << [S]. Here, this was ensured by using ABTS at a concentration of 0.125–4 mM, H_2O_2 at a 4 mM concentration, and HRP at a concentration of ≤ 2 nM.

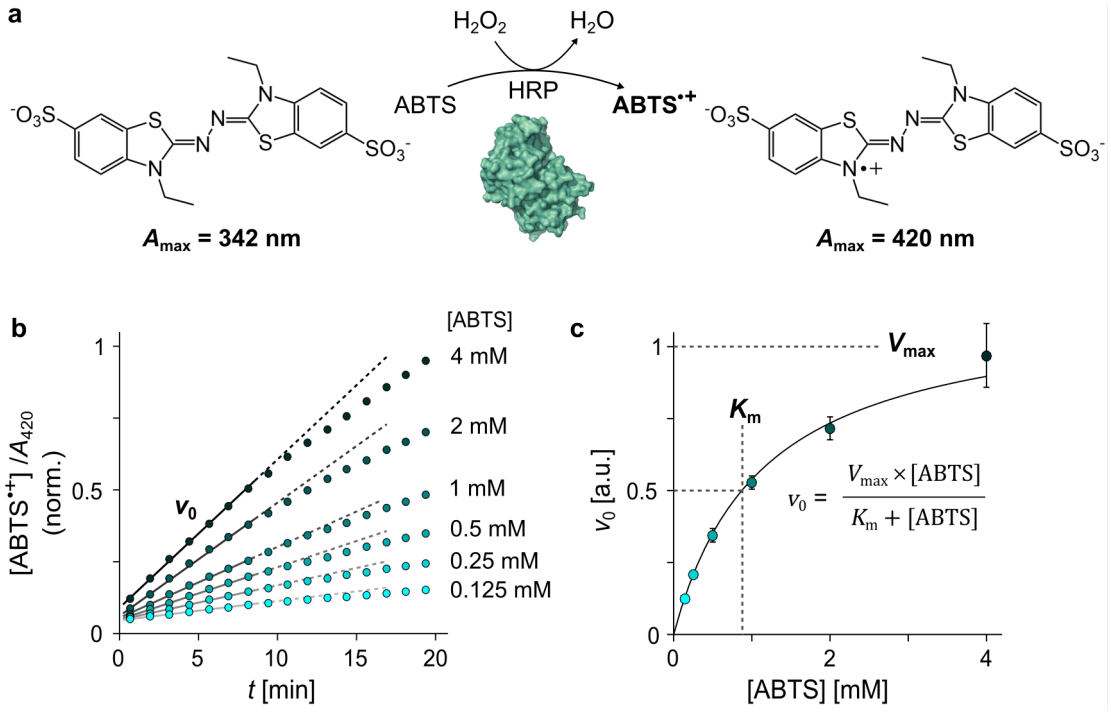

FIGURE 10 ABTS assay for determining the enzymatic activity of HRP. a) HRP catalyses the oxidation of the substrate ABTS in the presence of H_2O_2, producing the ABTS$^{\bullet+}$ radical. b) ABTS$^{\bullet+}$ formation at different ABTS concentrations [ABTS] is followed with A_{420}. The v_0 for each [ABTS] is determined at the initial linear phase of the ABTS$^{\bullet+}$ formation. c) V_{max} and K_m are obtained by fitting the collected v_0 *vs.* [ABTS] data with the Michaelis-Menten equation.

4.3.3 Doxorubicin loading and release – UV–Vis and fluorescence titrations

When DNA origami nanostructures are mixed with DOX, the DNA-binding affinity of DOX leads to a spontaneous, reversible assembly of non-covalently bound DOX-loaded DNA nanostructures. This assembly of drug-loaded DNA origami structures – the loading process – ends in a state of a thermodynamic equilibrium (Fig. 11).

In the loading process, DOX and DNA are mixed together at total DOX and base pair concentrations of $c(\mathrm{DOX})_0$ and $c(\mathrm{bp})_0$. The loading takes place during an equilibration time t; during this time, the amount of DOX bound to DNA increases until the system reaches a thermodynamic equilibrium where the concentrations of DNA-bound DOX molecules [$c(\mathrm{DOX})_b$] and free DOX molecules [$c(\mathrm{DOX})_{ub}$] have stabilized (Fig. 11, right panel). DNA base pairs are either bound to DOX [$c(\mathrm{bp})_b$] or unbound [$c(\mathrm{bp})_{ub}$].

In this work, the formed equilibrium was described and analysed with a 1:2 supramolecular binding model (Thordarson 2011). Here, the 1:2 model was chosen in order to describe the two binding modes that intercalating molecules, including DOX, can have in solutions of relatively low ionic strength: intercalation and external binding to the helix driven by electrostatic interactions

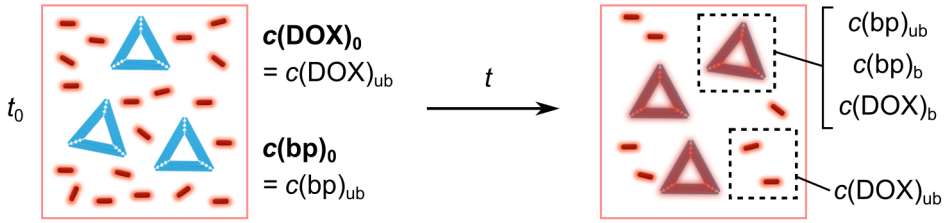

Figure 11 Schematic illustration of the DOX loading process. Loading takes place over the equilibration time t after DOX and DNA origami are initially mixed together at t_0.

(Gandecha *et al.* 1985, Pérez-Arnaiz *et al.* 2014). The model was seen to fit the observed experimental trends better than a 1:1 model. However, it should be noted that the DOX–DNA association could also be modeled with other approaches, such as by applying the neighbour exclusion model formulated by McGhee and von Hippel (McGhee and von Hippel 1974, Rocha 2010, Zadegan *et al.* 2017).

The chosen 2-component binding model describes the fraction of bound DOX molecules in the equilibrium state as

$$f_b := \frac{c(\mathrm{DOX})_\mathrm{b}}{c(\mathrm{DOX})_0} = 1 - \frac{1}{1 + K_{11}c(\mathrm{bp})_\mathrm{ub} + K_{11}K_{12}c(\mathrm{bp})_\mathrm{ub}^2}\,, \tag{6}$$

where K_{11} and K_{12} are the association constants of 1:1 and 1:2 DOX:bp complexes, respectively. Equation 6 is thus a combination of the Hill equations that describe the formation of the two types of complexes (DOX + bp ⇋ DOX:bp, and DOX–bp + bp ⇋ DOX:bp$_2$) (Goutelle *et al.* 2008). $c(\mathrm{bp})_\mathrm{ub}$ depends on K_{11}, K_{12}, $c(\mathrm{DOX})_0$, and $c(\mathrm{bp})_0$ and can be solved from the cubic equation

$$Ac(\mathrm{bp})_\mathrm{ub}^3 + Bc(\mathrm{bp})_\mathrm{ub}^2 + Cc(\mathrm{bp})_\mathrm{ub} - c(\mathrm{bp})_0 = 0\,, \tag{7}$$

where

$$\begin{cases} A = K_{11}K_{12} \\ B = K_{11}[2K_{12}c(\mathrm{DOX})_0 - K_{12}c(\mathrm{bp})_0 + 1]\,. \\ C = K_{11}[c(\mathrm{DOX})_0 - c(\mathrm{bp})_0] + 1 \end{cases} \tag{8}$$

Equation 7 has three solutions, of which the smallest positive real solution gives $c(\mathrm{bp})_\mathrm{ub}$.

For finding K_{11} and K_{12}, a 3 µM solution of DOX was titrated with DNA origami structures. In order to maintain a constant DOX concentration in the sample, the titrant containing the DNA origami was also supplemented with 3 µM DOX. DOX molecules are conjugated systems whose planar aromatic residues generate light absorption and fluorescence at visible wavelengths. The intercalation of DOX between DNA base pairs leads to static quenching of its fluorescence and an absorption spectrum shift upon formation of a ground-state

complex (Lakowicz 2006, Airoldi *et al.* 2014). When the fraction of DNA-bound DOX in the sample increases during the titration, changes are thus observed in both the absorption and fluorescence properties of the sample. A Horiba Aqualog spectrofluorometer was used to collect the absorption spectra and the excitation-emission matrices of the samples with 240–700 nm excitation after each addition of DNA. Based on the obtained results, excitation wavelengths 450 nm, 460 nm, 470 nm, 480 nm, and 494 nm were chosen for further analysis.

The observed quenching of DOX fluorescence (decrease of the fluorescence quantum yield Φ *vs.* $c(\mathrm{bp})_0$ at the selected excitation wavelengths) was fitted to Equation 9 with the BindFit online fitting tool (http://supramolecular.org/):

$$\Delta\Phi_{\mathrm{obs}} = \frac{\Phi_{\Delta 11} K_{11} c(\mathrm{bp})_{\mathrm{ub}} + \Phi_{\Delta 12} K_{11} K_{12} c(\mathrm{bp})_{\mathrm{ub}}^2}{1 + K_{11} c(\mathrm{bp})_{\mathrm{ub}} + K_{11} K_{12} c(\mathrm{bp})_{\mathrm{ub}}^2} \,. \tag{9}$$

Here, $\Delta\Phi_{\mathrm{obs}}$ is the observed quantum yield decrease relative to free DOX and $\Phi_{\Delta 11}$ and $\Phi_{\Delta 12}$ are the relative quantum yields of the 1:1 and 1:2 complexes, respectively. $c(\mathrm{bp})_{\mathrm{ub}}$ is the free nucleotide concentration obtained from Equation 6.

In addition to providing information about the DOX-DNA association, the binding model and equations 6–9 were applied for calculating the concentrations of free and bound DOX in the reverse situation where DNA origami structures are digested by DNase I [$c(\mathrm{bp})_0$ decreases] and DOX is subsequently released. The release experiment was performed for DNA origami structures both with and without DOX. DNA origami samples without DOX contained 2 nM origami. DOX-loaded DNA origami were prepared by incubating 2 nM DNA origami with either 3 µM or 6 µM of DOX. DNase I was added at 34 KU mL^{-1} final concentration, and the absorbance and fluorescence spectra of the samples were recorded at specified time intervals to collect data of the changes in the system over time. The absorbance spectra were used to determine the dsDNA/ssDNA composition of the samples as described in Section 4.2.1. The DOX fluorescence quantum yield after 494 nm excitation was used to calculate the amount of released DOX. For calculating the amount of released DOX from the quantum yield recovery (measured $\Delta\Phi_{\mathrm{obs}}$), Equation 9 was re-arranged as a quadratic equation for solving $c(\mathrm{bp})_{\mathrm{ub}}$ at each time point:

$$\begin{aligned}&(K_{11}K_{12}\Delta\Phi_{\mathrm{obs}} - K_{11}K_{12}\Phi_{\Delta 12})c(\mathrm{bp})_{\mathrm{ub}}^2 \\ &+(K_{11}\Delta\Phi_{\mathrm{obs}} - K_{11}\Phi_{\Delta 11})c(\mathrm{bp})_{\mathrm{ub}} + \Delta\Phi_{\mathrm{obs}} = 0\end{aligned} \tag{10}$$

The fractions of bound DOX (f_{b}) for each time point and $c(\mathrm{bp})_{\mathrm{ub}}$ were then obtained from Equation 5.

5 RESULTS AND DISCUSSION

5.1 pH-controlled DNA origami devices

For studying the actuation of dynamic DNA origami devices with external stimuli, two pH-controlled DNA origami structures were designed in this work: a DNA nanocapsule and a DNA zipper (Fig. 12). The structures share a similar operating principle: they are functionalized with Hoogsteen-type DNA triplexes, which lock the structures into a closed conformation at a pH below the adjustable pK_a of the triplexes. When the pH increases, the disassembly of the triplexes into dsDNA and ssDNA counterparts releases the devices into an unconstrained open state. The other structural features of the devices were designed to fit the intended applications: the nanocapsule was designed for the transportation of molecular cargo, and the zipper was designed to function as a modular research tool for studying various on/off type binding interactions between an adjustable number of interacting biomolecules.

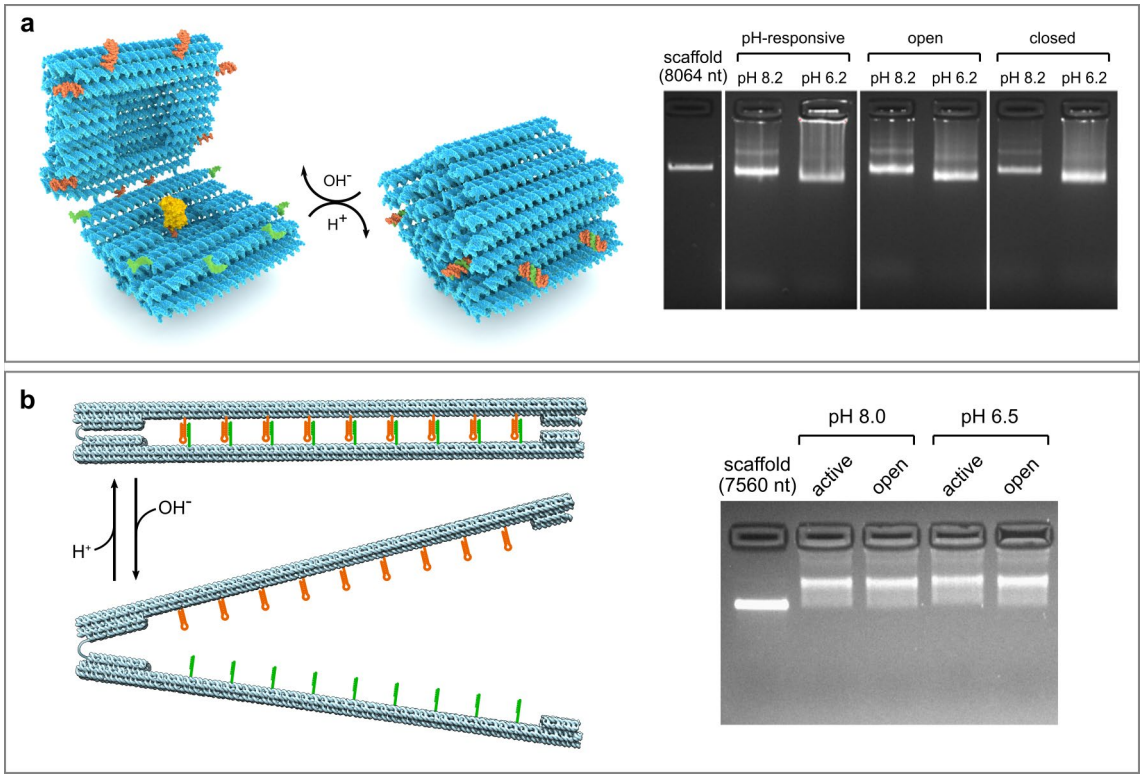

FIGURE 12 Illustrations (left panel) and AGE characterization (right panel) of the pH-responsive DNA origami structures and control structures. a) The DNA nanocapsule. In the illustration, the dsDNA hairpins and ssDNA strands of the Hoogsteen triplexes are shown in orange and green, respectively. The capsule is portrayed with a loaded HRP enzyme (yellow). The AGE analysis shows the electrophoretic mobility of pH-responsive, permanently open, and permanently closed capsules after PEG purification of excess staples and resuspension in either pH 6.2 or 8.2 folding buffer. Reproduced with permission from Publication II (https://pubs.acs.org/doi/10.1021/acsnano.9b01857). Copyright 2019 American Chemical Society. b) The DNA zipper. The dsDNA and ssDNA residues of the triplexes are shown in orange and green color. The AGE analysis shows PEG-purified pH-responsive (active) zippers and open controls after incubating the samples at either pH 8.0 or 6.5.

The nanocapsule is a hollow structure with two halves linked together with flexible ssDNA residues and functionalized with 8 pairs of triplex-forming oligonucleotides (Fig. 12a). In the closed state, the structure is roughly spherical with outer dimensions of 31 nm × 28 nm × 33 nm (w × h × l), and it contains an 11 nm × 12 nm × 13 nm inner cavity for accommodating cargo particles – such as a single HRP enzyme, presented in yellow in the illustration in Fig. 12a.

The DNA origami zipper design is presented in Fig. 12b. The zipper consists of two long arms connected at one end with a flexible ssDNA scaffold region. Each arm is a bundle of six dsDNA helices, with an approximate diameter of 6.2 nm and a length of 180 nm. Studied molecules or functional groups can be attached to the arms at desired locations and copy number (maximum 9 per arm). The association or dissociation of interacting components is amplified into a conformational change of the whole origami structure for detection. In this study, the zipper was functionalized with 9 copies of Hoogsteen triplexes.

The electrophoretic mobility of the folded capsules was slightly higher than that of the single-stranded 8,064-nt scaffold in 2% agarose (Fig. 12a, right panel). Furthermore, for all sample types - pH-responsive capsules, open controls, and closed controls – the electrophoretic mobility of samples that were incubated at pH 6.2 before the analysis was higher than of those incubated at pH 8.2. The electrophoretic mobility thus could not be used for analyzing the conformational state of the capsules in different pH media. The yield of correctly folded, monomeric structures was estimated as (79 ± 2)% based on the intensity of the leading band on the gel. The folded zipper origami structures migrated as a smeared band with a lower mobility than the 7,560-nt scaffold (Fig. 12b, right panel). The migration of both open controls and active (pH-responsive) zippers was similar at both pH 6.5 and 8.0, which shows that all samples are structurally intact. Akin to the nanocapsules, the AGE analysis did not reliably reveal pH-dependent conformation changes of the zippers. To obtain this information, the conformational changes of the nanocapsules were probed with FRET and TEM, and the zippers were studied with AFM imaging and electrochemical measurements.

5.1.1 Reconfigurable conformational changes of the DNA nanocapsules

The conformational state of the nanocapsules in solution under different pH conditions was studied with FRET experiments (Section 4.2.2) and TEM imaging. Measuring the FRET signal from the bulk sample is an effective way to gain information about the average conformational state of nanocapsules in solution, as the observed signal is averaged both over the integration time in the fluorescence detection and over the high number of individual particles in the sample. TEM imaging was performed to support the spectroscopic results, and the analysis of individual structures can reveal how much structural variation is included in the sample average obtained from FRET measurements.

The E_{FRET} of fluorescently labelled capsules was measured over a pH range of 6.0–8.0 (Fig. 13a). The high E_{FRET} observed between pH 6.4–6.8 indicates a closed state of the capsules, which could be confirmed with TEM imaging (Fig. 13b, top panel). Between pH 7.6–8.0, the system was determined to be in an open state with $E_{\mathrm{FRET}} \approx 0$. According to the dependency of E_{FRET} on r presented in Fig. 8, the measured E_{FRET} values correspond to approximate D–A distances of ~5 nm in the closed state and > 10 nm in the open state, given that R_0 = 6 nm. TEM imaging showed that the open capsules are in a flexible state that can adopt a variety of open conformations (Fig. 13b, bottom panel). Below pH 6.4, an additional increase of E_{FRET} was observed. This could indicate possible sample aggregation or an influence of the low pH on the photophysical properties of the fluorophores or on the energy transfer process. The applicable pH range for the system was thus determined as 6.4–8.0. In this pH range, the pH response of the capsules could be described with a Hill equation,

$$E_{\mathrm{FRET}} = \frac{E_{\mathrm{FRET}}(\mathrm{closed}) \times (10^{-\mathrm{pH}})^n}{(10^{-\mathrm{p}K_{\mathrm{a}}})^n + (10^{-\mathrm{pH}})^n} \,. \tag{11}$$

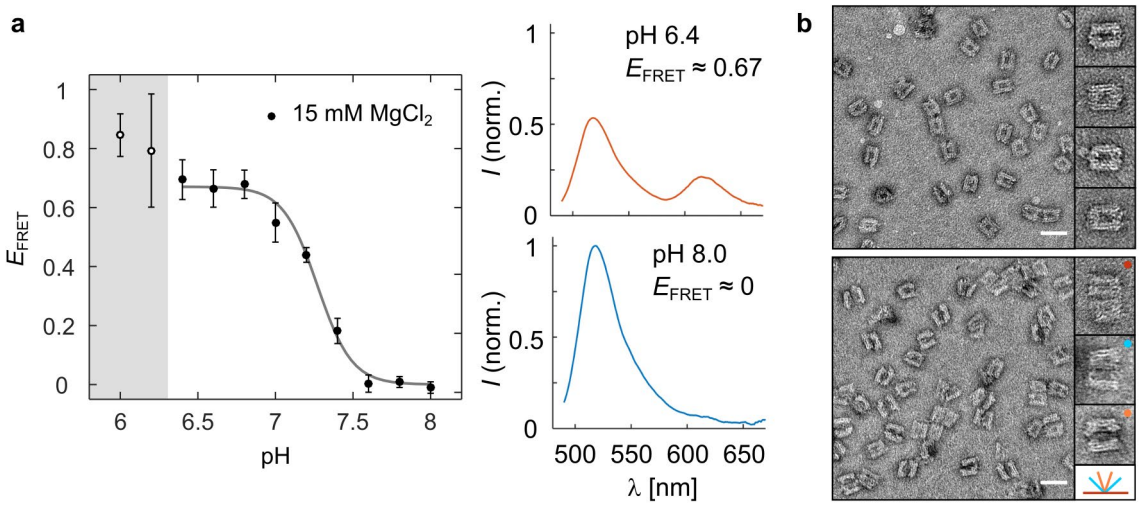

FIGURE 13 Characterization of the pH response of the DNA origami nanocapsule with FRET and TEM. a) The detected E_{FRET} *vs.* solution pH (left panel) and fluorescence spectra for pH 6.4 (closed) and pH 8.0 (open) samples after donor excitation (right panel). Between pH 6.4–8.0, the E_{FRET} of the system can be fitted with a Hill equation (solid line; Equation 11). The system – or the measurement – is not applicable below pH 6.4 (grayed out in the figure). The error bars represent the standard error of the mean of 3 replicates. b) TEM images of the capsules in the closed state (top) and open state (bottom). Scale bars in the figure are 50 nm. The width of each inset is 60 nm. Reproduced with permission from Publication II (https://pubs.acs.org/doi/10.1021/acsnano.9b01857). Copyright 2019 American Chemical Society.

The Hill equation can be applied for describing various types of physicochemical equilibria, such as here, the binding and dissociation of protons (Hill 1910, Goutelle *et al.* 2008). $pK_a = 7.27 \pm 0.02$ and a Hill coefficient $n = 3.9 \pm 0.5$ produced the best fit to the obtained data. The experimentally obtained pK_a value was thus well in line with the predicted value (pH 7.2). The high value of the Hill coefficient arises from the sharp transition observed between the two states of the system (open and closed), and suggests a cooperative behavior of the system. The fit result is presented in Fig. 13a. The pH-controlled conformational changes were shown to be reconfigurable when the pH of the sample was repeatedly adjusted between pH 6.3–6.4 and pH 7.7 and the E_{rel} was monitored with kinetic fluorescence measurements (Fig. 14). A comparison of the E_{rel} (Equation 4) of the pH-responsive nanocapsules and the permanently open and closed controls is also shown in Fig. 14.

The experiment also revealed the kinetics of the opening and closing. The opening is a rapid process: when the Hoogsteen hydrogen bonding interactions within the pH latches were destabilized by adjusting the pH above the pK_a with sodium hydroxide, the capsules opened faster than the time resolution of the measurement (30 seconds). On the other hand, the closing is an orders of magnitude slower process and a full stabilization of the capsules into a closed conformation required an incubation of several hours in acidic conditions. It has been shown that both the formation and disassembly of DNA triplexes can take place within milliseconds (Idili *et al.* 2014). It appears that the bulky DNA origami

does not considerably affect the kinetics of the triplex disassembly. The time scale of the closing process is comparable to the kinetics observed for similar DNA origami designs when the closing is induced through strand-displacement reactions (Grossi *et al.* 2017), even though strand displacement reactions are slower than the diffusion of ions and the formation of DNA triplexes.

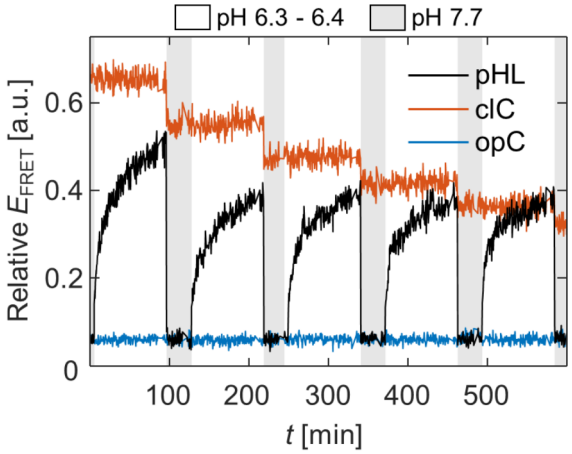

FIGURE 14 Reconfigurable conformational changes of the DNA origami nanocapsule and the kinetics of the opening and closing processes. Abbreviations: pHL = pH-responsive nanocapsule; clC = closed control; opC = open control. Reproduced with permission from Publication II (https://pubs.acs.org/doi/10.1021/acsnano.9b01857). Copyright 2019 American Chemical Society.

An important aspect for potential drug delivery applications is that the pH response of the Hoogsteen triplexes can be adjusted to a specific pH environment. The pK_a of the nanocapsule was shown to hold good agreement to previous studies, as the triplet composition of 60% T–A·T yielded the expected pK_a (7.27 vs. predicted 7.2). It is thus reasonable to assume that the pK_a can be adjusted with the base composition as shown in previous reports (Idili *et al.* 2014, Kuzyk *et al.* 2017). Although the capsules require a long time for closing when the samples are initially prepared, the opening can be induced in a fast and sensitive manner in an alkaline target environment. Such environment could be found, for instance, in cancer cell cytoplasm. As another requirement for drug delivery, the structure should also remain functional in physiological conditions. The presented FRET and TEM-based characterization of the pH functionality were carried out in TAE buffers. The effects of physiological salt concentrations (low Mg^{2+} and high Na^{+}) and blood plasma were tested separately (Section 5.3.1).

Although the pH-responsive nanocapsule was designed primarily for molecular transportation and for drug delivery, such capsule-like structures can also have potential other applications. For instance, a closely related DNA origami nanocapsule design without pH-latch functionalization was used as a surface-immobilized aptamer-embedded sensor for detecting hemoglobin and glycated hemoglobin in surface plasmon resonance experiments (Duanghathaipornsuk *et al.* 2020).

5.1.2 Electrochemical characterization of the DNA zippers

The pH functionality of the DNA zippers was first confirmed with AFM imaging (Fig. 15a). DNA zippers were incubated overnight either in an acidic (pH 6.5) or an alkaline (pH 8.0) TAE buffer supplemented with 15 mM $MgCl_2$ and 5 mM NaCl. The structures were deposited on mica and imaged using a Bruker Dimension Icon instrument in ScanAsyst air mode and Scanasyst-air probes. At pH 6.5, ~74% of pH-sensitive zippers identified as individual structures were found in a tightly closed conformation in image analysis. The image analysis was performed manually by measuring the vertex angles of 141 imaged structures with the angle measurement tool of ImageJ2 version 1.51g (Rueden *et al.* 2017). At pH 8.0, a distribution of different open conformations was observed. Only ~2% of the structures (n = 220) were in a closed configuration at pH 8.0, which shows that the closed configuration is highly unfavourable unless stabilized by the Hoogsteen triplexes. Open control zippers were in an open configuration at both pH 6.5 and 8.0. For further data on the AFM characterization, see Fig. 2 and Fig. S3–S4 (III). The imaging result thus confirmed that the buffer pH induces a significant conformational change in the active zippers specifically due to triplex formation.

The DNA zippers were then immobilized on polycrystalline gold electrodes *via* gold-thiol bond formation at three thiol-modified oligonucleotides in the structure. The immobilization was confirmed with differential pulse voltammetry (DPV) and electrochemical impedance spectroscopy (EIS) using potassium ferri/ferrocyanide ($Fe(CN)_6^{(-3/-4)}$) as a redox couple. To observe the conformational switching, the zippers were immobilized on the electrode at pH 6.5, and the DPV peak current was monitored when the pH of the buffer was increased to pH 8.0. A decreased peak current was observed for both the active and the control zippers at pH 8.0. Part of the signal change was attributed to the change of the buffer system rather than changes happening in the sample. Fig. 15b shows the signal change for both types of samples after the effect of the buffer was subtracted. The level of significance observed for the reduction of current for the active zippers was higher than for the control zippers (p = 0.0004 and p = 0.0487, respectively). This is thus the main indication that there are factors specific to the active samples that lead to an additional decrease of the current when the pH is changed. The results demonstrate that the pH-triggered changes in the DNA origami layer can be probed with label-free electrochemical methods. However, in addition to the pH-triggered opening, possible contributions of *e.g.* the agglomeration of the pH-responsive zippers at low pH (Fig. S3, III), or other unidentified experimental variables should be acknowledged.

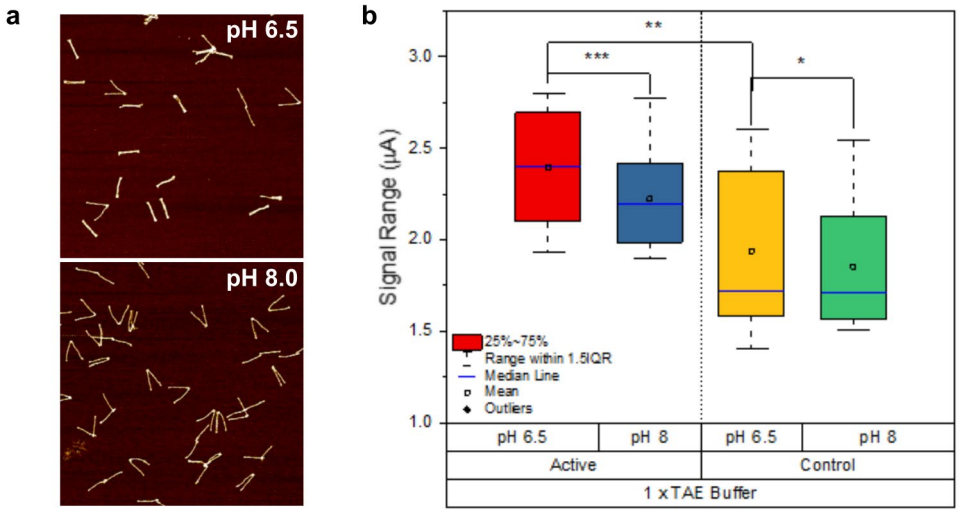

FIGURE 15 The pH response of the DNA zippers. a) AFM images of the pH-responsive zippers in the closed state (pH 6.5) and the open state (pH 8.0). The size of the AFM images is 2 × 2 µm². b) DPV peak current data of active and control zippers after correcting for the signal change associated with the pH difference of the buffers. Levels of significance given at, *ns* $p > 0.05$, * $p \leqslant 0.05$, ** $p \leqslant 0.01$, *** $p \leqslant 0.001$., **** $p \leqslant 0.0001$). The electrochemical measurements for figure b were conducted by P. Williamson (University of Strathclyde).

While nucleic acids and DNA nanostructures such as framework nucleic acids are widely applied in biosensor development, the use of DNA origami –based electrochemical biosensors are still relatively unexplored (Chandrasekaran 2017, Kogikoski *et al.* 2019). Recently, electrochemical detection of the binding of microRNA to DNA origami as well as the binding of DNA origami to DNA origami by using methylene blue as a redox indicator were demonstrated (Han *et al.* 2019, Arroyo-Currás *et al.* 2020). Ge *et al.* (2019) in turn immobilized glucose oxidase – HRP enzyme pairs on DNA origami plates and detected their enzymatic activity with electrochemical methods. In these previous studies, the DNA origami was used as a static platform for a precise arrangement of functional groups. To our knowledge, the study presented here shows for the first time the detection of conformational changes of an unlabeled, switchable DNA origami device with electrochemical means.

The developed DNA zipper structure can also be modified for studying different types of biomolecular interactions or detection of analytes. For instance in Fig. 16, the zipper structure has been functionalized with recombinant *Agrobacterium tumefaciens* phytochrome 1 (Agp1) proteins. A dibenzocyclooctyne (DBCO)-maleimide crosslinker was used for a covalent conjugation of engineered surface cysteines of the phytochromes (E379C) with azide-modified oligonucleotides according to a method developed by Mukhortava and Schlierf (2016) (Kettunen 2020). The Hoogsteen triplexes of the DNA zipper were replaced with ssDNA strands, which function as anchors for the protein-ssDNA conjugates. Successful attachment of proteins to the zipper arms was confirmed with AFM imaging. Following the development of sensitive detection methods for the zipper conformation, the protein-functionalized device could yield information on *e.g.* the red-light induced dimerization of Agp1 (Noack *et al.* 2007).

Furthermore, light-activated tertiary or quaternary structural changes could have interesting uses for instance as a novel method to actuate dynamic DNA nanodevices with red and far-red light.

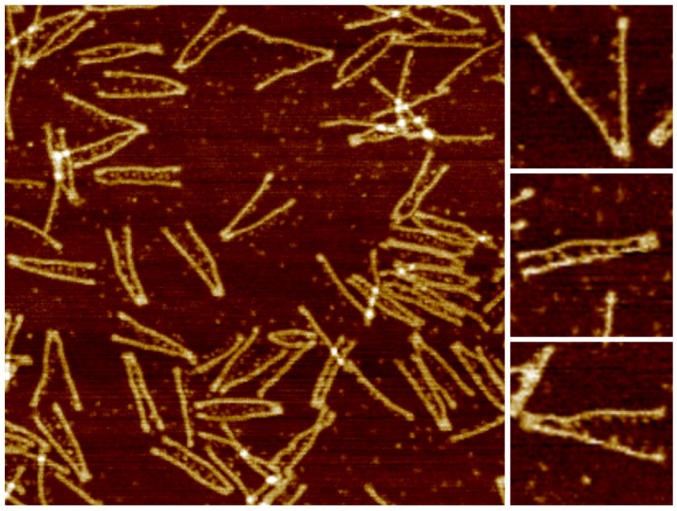

FIGURE 16 AFM images of Agp1-functionalized DNA zippers. Each zipper contains 9 attachment sites for protein-ssDNA conjugates on each arm. Despite some free protein background, the correct attachment of globular proteins on the zipper arms can be visually confirmed. The size of the main AFM image is 1 × 1 μm^2, and the magnified inset figures on the right are 200 × 200 nm^2 each.

5.2 Molecular transportation with DNA origami

In this work, DNA origami structures were used for the transportation of proteins, nanoparticles, and the DNA-binding drug DOX. Proteins (HRP enzymes) and AuNPs were loaded and encapsulated into the pH-sensitive DNA nanocapsules for pH-triggered display. The loading and encapsulation efficiency as well as their effects on the cargo were studied. DOX was loaded into 5 DNA origami structures for studying the formation of the DOX–DNA complexes and the effects of experimental conditions and DNA origami superstructure on the DOX loading yield.

5.2.1 Loading and encapsulation of nanoparticles and enzymes

The loading of the DNA nanocapsule with molecular cargo was studied with HRP enzymes and AuNPs. Both types of cargo molecules were conjugated to DNA prior to loading and anchored in the nanocapsule through hybridization with a complementary ssDNA overhang positioned in the inner cavity (Section 4.3.1). Here, loading thus refers to the attachment of cargo molecules inside the cavity at high pH, and encapsulation refers to the process of closing the capsules by lowering the pH of the solution after loading.

First, the loading efficiency, loading specificity, and encapsulation yield were studied. For studying the loading of HRP, nanocapsules were prepared both with or without a cargo anchoring strand in the cavity, incubated with HRP-DNA conjugates to allow DNA hybridization, and the excess (unbound) enzymes were removed with PEG precipitation. The catalytic activity of HRP after purification at pH 8.2 was monitored with an ABTS assay (Section 4.3.2). After purification, clear HRP activity was detected from nanocapsules assembled with the cargo anchoring strand (Fig. 17a). No activity was detected if the capsules were assembled without a cargo anchoring strand, showing that practically all enzymes were removed in the purification and that the loading takes place specifically by hybridization of the conjugate strand and the cargo anchoring strand. The successful encapsulation of HRP was confirmed by measuring the E_{FRET} of the system after closing the capsules after loading. Identical E_{FRET} was obtained for both empty and HRP-loaded pH-responsive nanocapsules at pH 6.4, showing that the enzyme loading did not hinder the closing process (data presented in the Fig. S7, II).

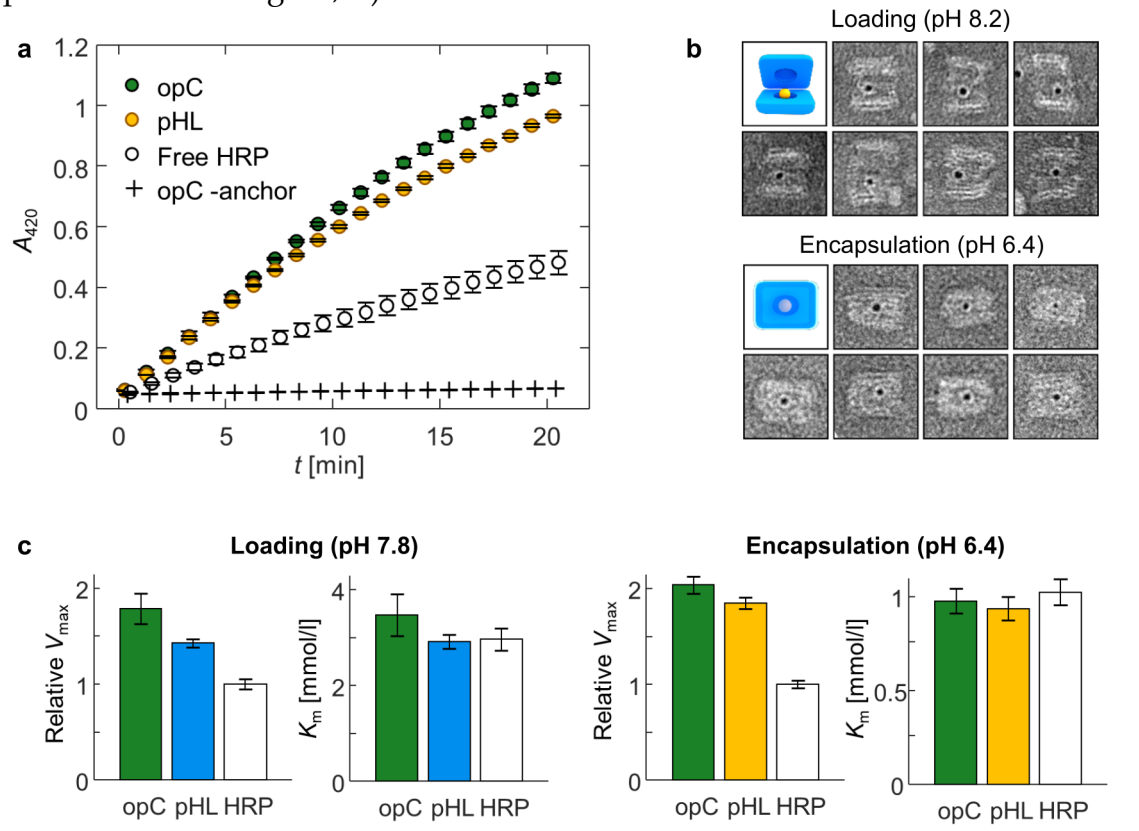

FIGURE 17 Loading and encapsulation of HRP and AuNPs. a) ABTS oxidation by HRP and different types of capsule samples at pH 8.2 after HRP loading and purification of unbound HRP. pHL and opC = pH-responsive and open control capsules with a cargo anchoring strand; opC –anchor = open controls without a cargo anchoring strand. Enzyme concentration in the HRP sample was 2 nM. DNA origami concentration in pHL, opC, and opC –anchor samples was 2 nM. b) TEM micrographs of AuNP-loaded, pH-responsive capsules after loading (pH 8.2, top panel) and encapsulation (pH 6.4, bottom panel). Each subfigure is 50 × 50 nm in size. c) The enzymatic activity of HRP in terms of V_{max} and K_m. All figures have been reproduced with permission from Publication II (https://pubs.acs.org/doi/10.1021/acsnano.9b01857). Copyright 2019 American Chemical Society.

The loading and encapsulation of AuNPs was studied with TEM imaging after negative staining with uranyl formate (Fig. 17b). AuNP-loaded capsule samples were imaged with TEM after cargo loading, and the number of successfully loaded *vs.* empty nanocapsules was counted. The results showed that AuNPs were localized inside the capsules after loading; the loading efficiency with our loading approach was estimated as 40–55% (obtained by dividing the number of nanocapsules with an AuNP at the correct location by the total number of observed structures, n = 110). When the capsules were closed by decreasing the solution pH, AuNP-loaded capsules in a closed conformation were observed.

Finally, as the capsules are designed for shielding their molecular cargo during transportation, it is crucial to characterize their ability to isolate their contents from the surrounding molecular environment. This was tested with two experiments. In the first experiment, empty nanocapsules were mixed in the closed state with AuNPs and the localization of nanoparticles was studied with TEM. AuNPs were not observed inside the capsules, which shows that large molecular weight particles, such as the DNA-functionalized AuNPs, are effectively blocked from entering the capsules in the closed state. In the second experiment, the enzymatic activity of loaded and encapsulated HRP was studied to see whether the diffusion of the small molecular weight ABTS is restricted by the DNA barrier. Enzymatic activity was determined from samples of HRP-loaded pH-responsive nanocapsules, HRP-loaded open control nanocapsules, and free HRP at both pH 6.4 and pH 7.8. The analysis was based on the comparison of the V_{max} and K_m values obtained by fitting the data with the Michaelis-Menten model (Fig. 17c).

The results revealed a clear increase of the enzymatic activity of HRP caused by the loading and the encapsulation, as seen in Fig. 17c as an enhanced V_{max} for both types of capsule samples compared to free HRP at both pH 7.8 and pH 6.4. The V_{max} enhancement of HRP is in line with previous reports on the catalytic enhancement of HRP caused by the proximity of DNA nanostructures (Lin and Wheeldon 2013, Zhang *et al.* 2016, Zhao *et al.* 2016). This originates to an increased k_{cat} (number of substrate molecules converted to product by one HRP enzyme per unit of time) in the proximity of the DNA origami through an unknown molecular mechanism (Jaekel *et al.* 2019). As a limitation of the analysis, the magnitude of k_{cat} enhancement could not be determined based on the existing data, as this would require an accurate quantification of the HRP concentration in each sample. HRP concentration in the capsule samples was unknown, and only an upper limit of ≤ 2 nM (the DNA origami concentration in the sample) could be stated.

Interestingly, no clear indication of a reduced enzymatic activity (V_{max}, k_{cat}) was observed when the nanocapsules were closed (pH-sensitive capsules at pH 6.4), even though this could be expected to restrict the diffusion of the substrate to the enzyme. The K_m values of all sample types were also similar, which can indicate that the affinity of the enzyme to the substrate – or its accessibility to the substrate – is similar for all sample types. This is admittedly a simplified interpretation of K_m, which depends on the rate constants of the association of the enzyme-substrate complex (k_1), the dissociation of the enzyme-substrate

complex (k_{-1}), and the dissociation of the enzyme-product complex (k_2) by $K_m = (k_{-1} + k_2)/k_1$ (Nelson and Cox 2008). It can nevertheless provide a basis to assume that the enzyme-substrate interactions are not considerably altered by the loading and encapsulation.

Put together, the obtained V_{max} and K_m values showed that the enzymatic activity of HRP was retained in the loading and encapsulation and that the nanocapsule could be applied for molecular transportation of active HRP. The observed increase of enzymatic activity was in line with other studies. The results also indicate that the DNA origami structure is porous enough to enable free diffusion of the substrate to the enzyme, as well as the diffusion of the product from the enzyme. It is also worthwhile to note that the presented measurements only probe the steady-state kinetics of HRP – that is, the product formation rate after the enzyme–substrate complex concentration has stabilized and the product formation takes place at a constant velocity of v_0. It is possible that a restricted diffusion could be observed in the initial pre-steady state kinetics as a delayed saturation of the enzyme with the substrate. An analysis of this depth was not carried out in this work, but could present a potential continuation for studies of controlling enzyme kinetics with DNA origami nanostructures.

5.2.2 The loading process of doxorubicin

The DOX loading properties of DNA origami structures were characterized with a set of experiments based on detecting changes in the spectroscopic properties of DOX and DNA origami (IV). The main methods for studying the formation of DOX–DNA origami complexes were UV–Vis and fluorescence titrations (Section 4.3.3). The experiments were performed with 3 μM DOX in 40 mM Tris-HCl buffer supplemented with 10 mM $MgCl_2$ at pH 7.4. In these conditions, DOX has distinct fluorescence before addition of DNA, shown in the excitation-emission matrix in Fig. 18a. DOX was then titrated with DNA origami solutions to study its interaction with 5 distinctly shaped DNA origami structures (Fig. 18b). The selected DNA origami structures included 3 structures with a 2D geometry: triangle, bowtie, and double-L, and 2 structures with a 3D geometry: a permanently closed nanocapsule applied as a control in Publication II and a 24-helix bundle (24HB).

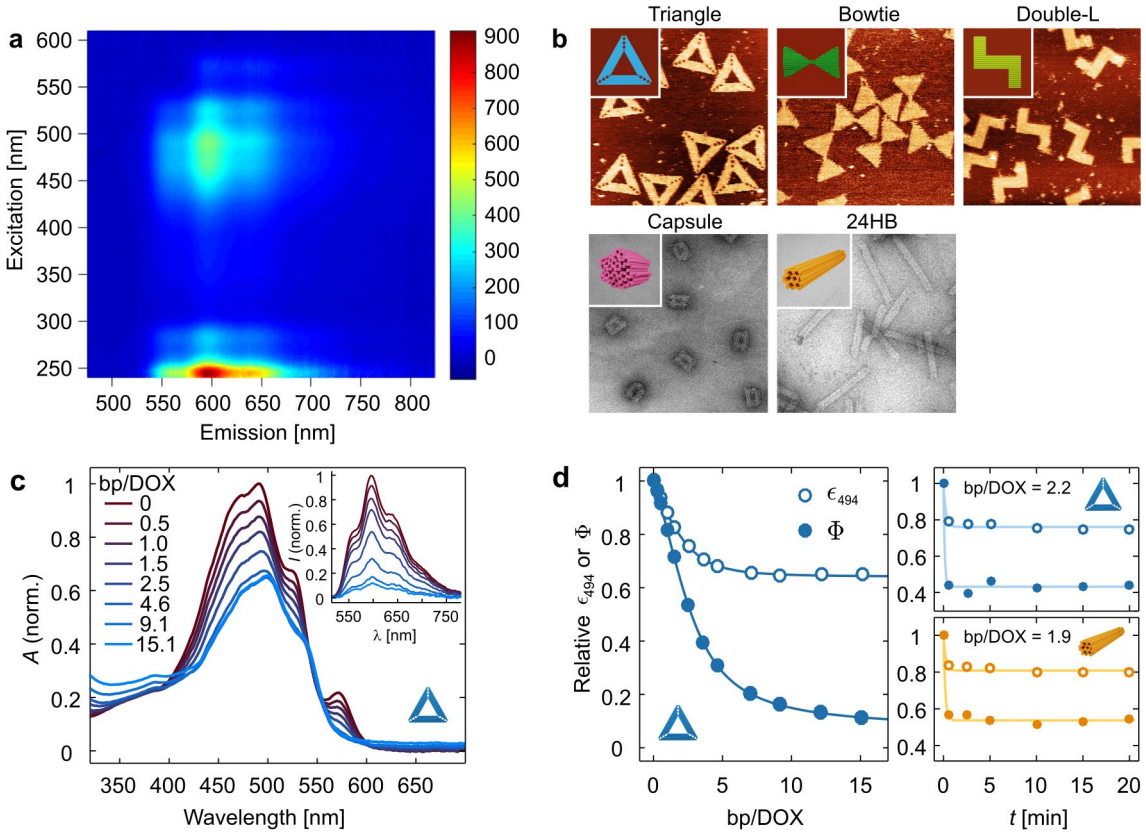

FIGURE 18 Titration of DOX with DNA origami. a) The excitation-emission matrix of 3 µM DOX before addition of DNA. b) Microscopy images and illustrations of the DNA origami structures used in the study. AFM images are shown for the 2D structures (triangle, bowtie, and double-L) in the top panel. The 3D structures (capsule and 24HB) are accompanied by TEM images in the bottom panel. The AFM images are 500 × 500 nm^2 in size, and the TEM images are 300 × 300 nm^2. c) Representative changes in the absorption and fluorescence emission (494 nm excitation, inset figure) of DOX upon titration with the triangle origami. d) The extinction coefficient of DOX at 494 nm (ε_{494}, empty circles) and the fluorescence quantum yield from 494 nm excitation (Φ_{494}, filled circles) when the amount of base pairs in the sample is increased (left panel) and when incubated in the presence of a constant base pair concentration (right panel). The solid line in the left panel presents a fit of the 1:2 binding model to the data. In the right panel, the data points have been fitted with an exponential decay model for illustrating the time dependency of the binding. Subfigures b, c, and d have been reproduced from Publication IV.

The titration experiments were used for estimating the binding affinity of DOX to DNA origami, the optimal loading (equilibration) time, and the maximum DOX loading content for the studied DNA origami – and possible differences between the DNA origami designs. During titration, similar spectral changes were detected for all origami shapes. The result for the triangle origami is shown in Fig. 18c. In Figures 18c–d, the DNA concentration in the sample is expressed as the ratio between the total DNA base pair concentration and DOX concentration in the sample (DOX/bp). Fitting the observed decrease of the fluorescence quantum yield with the 1:2 binding model described in Section 4.3.3 (Equation 9) yielded average association constants of K_{11} = (2.0 ± 0.3) × 10^5 M^{-1} and K_{12} = (2.6 ± 0.2) × 10^5 M^{-1}. The values have been averaged for all the DNA

origami shapes. The left panel of Fig. 18d shows the fit result for the triangle origami for the fluorescence quantum yield for 494 nm excitation and the extinction coefficient of DOX at 494 nm. The binding model further suggests that at the applied experimental conditions, DOX–DNA binding may not be completely intercalative (quenched fluorescence), but also include a component of externally bound, gently fluorescent DOX.

The incubation time needed for reaching a binding equilibrium between DOX and DNA origami was studied for the triangle and the 24HB. Less than a 30 second incubation after addition of DNA (bp/DOX ≈ 2) was termed sufficient for reaching a stabilized spectroscopic signal (Fig. 18d, right panel). This indicates that the amount of DOX bound to the DNA origami structures has stabilized. Furthermore, a loading time of seconds appears sufficient for preparing DOX-loaded DNA origami for drug-delivery applications, independent on the DNA origami design. The fast association kinetics are in line with results published for linear dsDNA (Pérez-Arnaiz *et al.* 2014), but have not been previously confirmed for DNA origami structures. In fact, the results are contradictory to some earlier studies where the DOX loading concentration in DNA origami has been claimed to increase even after 48 h incubation (Jiang *et al.* 2012, Liu *et al.* 2018a). Loading times of several hours to tens of hours are also generally common in literature (Zhang *et al.* 2014, Song *et al.* 2017a, Zeng *et al.* 2018, Liu *et al.* 2018b, Pan *et al.* 2020).

Here, the DOX loading content of DNA origami was expressed as the number of bound DOX molecules per DNA base pair (DOX_b/bp). The loading yield is an important aspect to characterize because it greatly determines both the cost-efficiency and the general efficiency of the treatment (Coleridge and Dunn 2020). However, some previous studies have reported controversially high DOX loading contents in DNA origami; up to 113 bound DOX molecules per DNA base pair (DOX_b/bp) (Jiang *et al.* 2012). The achieved maximum average loading density in the titration experiment was 0.36 ± 0.10 DOX_b/bp. In a supporting experiment, the DOX concentration in DOX-triangle samples was measured after purification of unbound DOX by spin-filtration or PEG precipitation, and the maximum loading yield was estimated as 0.45 ± 0.04 DOX_b/bp. Some variation within the tested DNA origami was observed; the highest loading density in the titration was determined for the bowtie at 0.45 DOX_b/bp, and the lowest for the 24HB at 0.19 DOX_b/bp (Fig. 19). The 24HB also appears to be an outlier when comparing the plots of the fraction of bound DOX molecules of all DOX molecules (f_b) and DOX_b/bp in the titration. Based on this analysis alone, it is not possible to confirm whether the observations reflect real differences between the origami designs or just an inaccuracy of the measurement. However, a lower loading yield in the densely packed 24HB design would be in line with Miller *et al.* (2020), who showed that part of the intercalation sites in DNA origami can be blocked due to the steric hindrance of the closely packed helices. Overall, DOX_b/bp < 1 is a reasonable loading density, as it is in line with the neighbour exclusion model and with previous binding densities determined for calf thymus dsDNA (Barcelo *et al.* 1988, Strekowski and Wilson 2007, Pérez-Arnaiz *et al.* 2014).

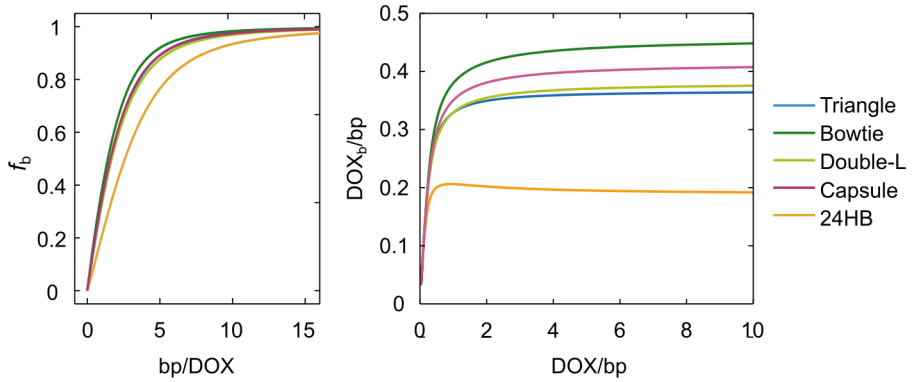

FIGURE 19 The association of DOX with DNA origami during the titration expressed as either the fraction of bound DOX molecules (f_b) (left panel) or the number of bound DOX molecules per DNA base pair (DOX_b/bp) (right panel). Note that the *x* axis of the subfigure in the right panel has been inverted for emphasizing the maximum DOX loading yield reached at low bp/DOX ratios. Reproduced from Publication IV.

In Table 3, our results are compared to the sample preparation methods and loading outcomes in other studies. The discrepancy between our results and the previously reported loading times and loading densities led us to suspect that especially the reported continuous loading processes (Jiang *et al.* 2012, Liu *et al.* 2018a) could reflect other phenomena than the DOX-DNA association. Additional spectroscopic characterization was thus performed both for DOX in the absence of DNA origami and for DOX-loaded DNA origami.

As a summary of the characterization, 3 potential pitfalls in the sample preparation and characterization process were identified. 1) The high pH (8.0–8.3) and Mg^{2+} ions of DNA origami folding buffers promote DOX aggregation. The extent of aggregation increases with DOX concentration and the incubation time; in particular, neutral DOX molecules above the pK_a of the NH_3^+ group are poorly soluble (0.55 mM) (Fülöp *et al.* 2013). 2) The aforementioned self-aggregation of DOX can take place during the loading process, and may partly explain why some studies have reported DOX loading concentrations of DOX_b/bp >> 1. The selection of the purification method for removing free DOX from the sample after loading seems to be crucial: the highest DOX loading yields have been reported in studies where free DOX is purified by sedimentation of the DOX-loaded DNA origami by centrifugation (Jiang *et al.* 2012, Zhang *et al.* 2014, Zeng *et al.* 2018, Pan *et al.* 2020). We showed that this method leads not only to the sedimentation of DOX-loaded origami, but also to the sedimentation of DOX aggregates (Fig. 3, IV). According to our experiments, spin-filtration (Song *et al.* 2017a, Liu *et al.* 2018a, b, Wang *et al.* 2020b) may be better suited for purification, provided that the tendency of DOX to bind to the filter membrane is acknowledged (Fig. S11–S12, IV). Moreover, the purification leads to a rapid release of a fraction of the bound DOX to reach a new binding equlibrium (Fig. S13, IV). Finally, 3) the spectroscopic properties of DOX depend on the pH and the Mg^{2+} concentration of the buffer. When quantifying DOX concentration in DNA origami–DOX samples, the changes in both the molar extinction coefficient

and the fluorescence quantum yield of DOX need to be taken into account for ensuring valid interpretation of the spectroscopic variables.

TABLE 3 A comparison the DOX loading conditions and the DOX loading densities (DOX_b/bp) in previous studies for different DNA origami structures. The DOX_b/bp values have been calculated based on the reported DOX and DNA origami concentrations in the final sample after purification of free DOX.

Study	Origami [1]	Loading conditions *c*(DOX)	*t*, *T*	DOX_b/bp
Jiang et al. (2012)	Triangle (7,200 bp) 6-helix bundle (7,056 bp)	2 mM	24 h, RT	111 113
Zhang *et al.* (2014)	Triangle (7,200 bp)	2 mM	24 h, RT	56
Song *et al.* (2017)	Triangle (7,200 bp)	0.1 mM	12 h, RT	0.28
Liu *et al.* (2018a)	Triangle (7,200 bp)	2.5 mM	12 h, RT	8.7
Liu *et al.* (2018b)	Triangle (7,200 bp)	2 mM	12 h, RT	6.9
Zeng *et al.* (2018)	Triangle (7,200 bp) Rectangle (a) (6,880 bp) Cross (6,762 bp)	1 mM	24 h, 37 °C	24 25 25
Pan *et al.* (2020)	Rectangle (b) (6,408 bp)	2 mM	6 h, 25 °C	5.3
Wang *et al.* (2020b)	Tube (6,347 bp)	n/a [2]	12 h, RT	0.32
IV	Triangle (7,200 bp) Bowtie (6,934 bp) Double-L (7,064 bp) Capsule (7,716 bp) 24HB (7,560 bp)	3–20 μM	< 1 h, RT	0.19–0.45

[1] The number of base pairs per one DNA origami structure is indicated in parentheses. The values have been calculated based on the information provided in the original publications for the triangle (Rothemund 2006), 6-helix bundle (Stearns et al. 2009), rectangle (a) (Wang et al. 2012), cross (Liu et al. 2011), rectangle (b) (Pan et al. 2020), tube (Wang et al. 2020b), bowtie and double-L (Shen et al. 2018), and capsule (II). The values are reported without possible secondary structures in unpaired scaffold residues.
[2] Either 0.3 mM or 10 mM depending on how the description of the experiment is interpreted.

The study thus highlights several contradictory aspects in existing literature of DNA origami–DOX delivery systems, and aims to explain in particular the poorly defined or overestimated DOX loading yields of DNA origami structures. The study provides guidelines for sample preparation and spectroscopic characterization of DOX–DNA origami complexes. The results suggest that the

previously reported high DOX loading yields might result partially from DOX aggregation during prolonged incubation or from poorly executed spectroscopic quantification of the amount of bound DOX. It should be noted that Halley *et al.* (2016) have likewise reported drug overloading and formation of aggregates at high drug concentrations for the chemically similar compound daunorubicin, but the potential implications for DOX- and daunorubicin-loaded DNA origami structures have not been further discussed. For instance, it is possible that DOX molecules bound externally to DNA in addition to the intercalated DOX molecules can increase the density of bound DOX. We have shown that DOX release takes place rapidly in a low-DOX environment in our experimental conditions, but the release rate could be strongly dependent on the type of binding interaction. Further detailed studies on the binding mechanism, composition, and stability of DOX-loaded DNA origami structures would thus benefit the development of safe and functionally well-defined DNA origami-based DOX delivery systems.

5.3 The structural stability of DNA origami

Characterizing the stability and drug release profiles of nanocarriers is important from the clinical perspective of developing safe and functionally well-defined delivery systems. The structural stability of DNA origami under various destabilizing physiological factors was studied in this work *in vitro*. Structural characterization of the DNA nanocapsules was performed in different salt conditions and in the presence of blood plasma using FRET. DOX-loaded DNA origami structures were subjected to DNase I digestion and their stability and DOX release properties were characterized with a combined UV–Vis/fluorescence assay.

5.3.1 Functionality of the DNA nanocapsules in physiological salt conditions and in blood plasma

The structural integrity and pH functionality of the DNA nanocapsules were studied with FRET experiments in buffers with different concentrations of NaCl and $MgCl_2$, and in buffers supplemented with blood plasma. Changing the salt concentration of the buffer can cause an increased internal electrostatic repulsion. If the repulsive forces exceed the adhesive hydrogen bonding interactions in the DNA triplexes, this can lead to opening of the capsules. The E_{rel} recorded during one closing–opening cycle showed that the closing phase is sensitive to the $MgCl_2$ concentration in the buffer (Fig. 20a), and that a 15 mM $MgCl_2$ concentration was required for reaching a high population of closed capsules in the sample. The effect of Mg^{2+} removal after closing was studied in a separate experiment (Fig. 20b). Decreasing the Mg^{2+} concentration down to 0.6 mM by buffer exchange with spin-filtration did not affect the shape of the emission spectrum with 460 nm excitation. This shows that although a reduced Mg^{2+} concentration slowed down

the closing process, after closing the conformational state was not affected by a low-Mg^{2+} environment.

In Fig. 20a, the effect of a physiological Na^+ concentration was tested by increasing the NaCl concentration of the buffer from 5 mM to 150 mM after closing the capsules. The increased Na^+ concentration did not affect the closed conformation, and the capsules could be opened by increasing the pH to 7.7. As this only tells about the effect of physiological Na^+ concentration for DNA origami structures in an optimal Mg^{2+} environment, the combined effect of Mg^{2+} depletion and Na^+ addition on closed, pH-responsive nanocapsules was studied in the experiment presented in Fig. 20b. Here it was noted that Mg^{2+}-depleted structures were slightly sensitive to an addition of Na^+ ions, observed as a slight decrease of the E_{FRET} (increase of D emission and decrease of A emission) after addition of 150 mM NaCl into samples containing 0.6 mM $MgCl_2$.

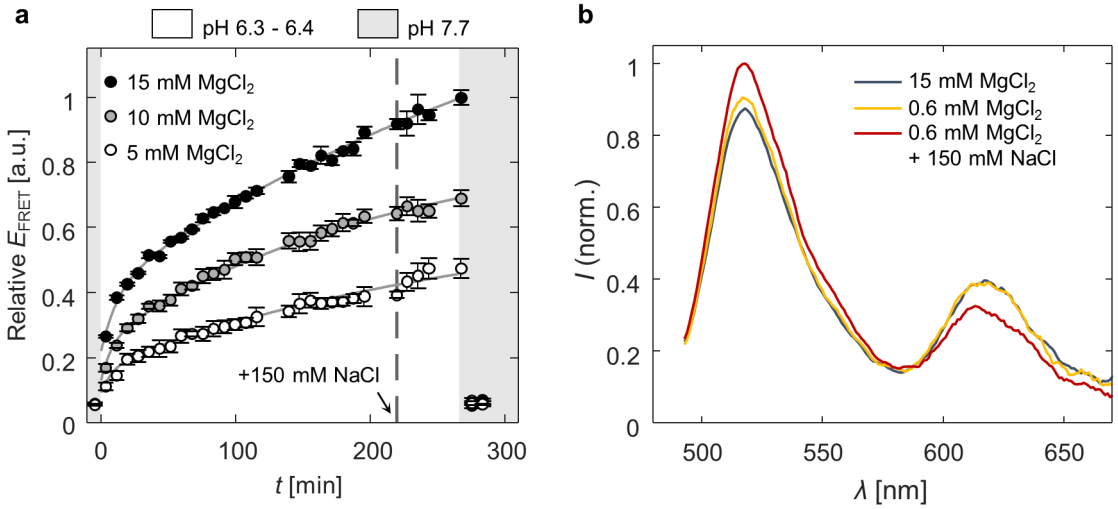

FIGURE 20 The functionality of pH-responsive DNA capsules in different salt conditions, probed by FRET experiments. a) The effect of buffer $MgCl_2$ concentration on the closing process and the effect of NaCl on the closed nanocapsules. The dashed line indicates the time point of the NaCl addition. b) The fluorescence spectra from 460 nm excitation for pH-responsive nanocapsules in different salt conditions at pH 6.4. Reprinted with permission from Publication II (https://pubs.acs.org/doi/10.1021/acsnano.9b01857). Copyright 2019 American Chemical Society.

Supplementing the buffer with blood plasma can provide a more comprehensive picture of the stability and functionality of the nanodevices in physiological conditions. Plasma is a complex mixture of organic and inorganic constituents (*e.g.* proteins and cations) (Krebs 1950), and the functionality of DNA origami devices in blood could be compromised by *e.g.* nuclease degradation, the salt concentration, or the adhesion of plasma proteins on the structures (Lundqvist *et al.* 2008, Bertrand and Leroux 2012). For studying how blood plasma affects the closed capsules, the emission spectra of FRET-labeled capsules in pH 6.4 FOB (15 mM $MgCl_2$) was collected both before and after adding plasma at either 1% or 10% concentration (v/v). As shown in Fig. 21, addition of 1% plasma did not affect the E_{FRET}, and the capsules can be assumed to remain in a closed

conformation. However, addition of plasma to the acidic nanocapsule sample also increases the pH of the sample. It is thus expected that addition of large volumes of plasma (pH 7.4) will lead to opening of the nanocapsules (pK_a of 7.27). This effect may be visible in the spectrum collected in the presence of 10% plasma as an increased donor emission and decreased acceptor emission, but the analysis of the fluorescence spectrum in 10% plasma is also technically challenging. The technical challenges arise from the optical properties of blood plasma: because of the high concentration of different components, plasma scatters and absorbs light and has an intrinsic fluorescence (Wolfbeis and Leiner 1985, Madhuri *et al.* 2003). The background fluorescence of plasma was not characterized separately in this study. All the effects scale with plasma concentration and will obstruct the FRET signal from the fluorophores, as seen as the elevated baseline in the 10% plasma results.

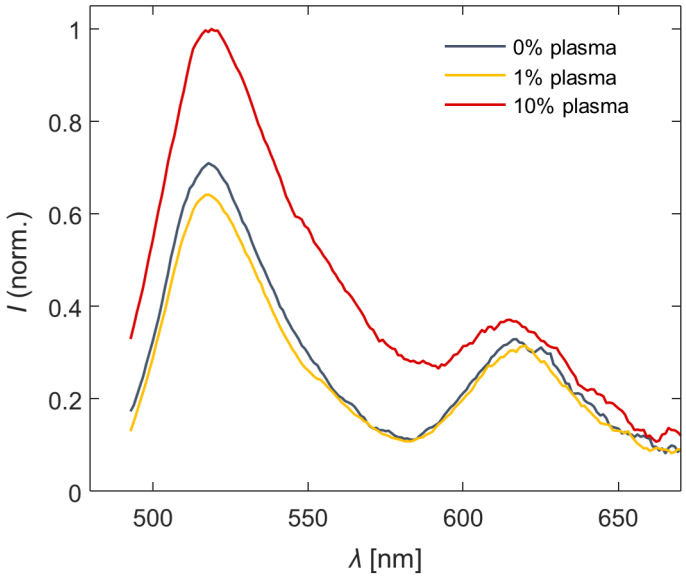

FIGURE 21 Fluorescence emission of FRET-labelled pH-responsive nanocapsules after addition of blood plasma. Before addition of plasma, the samples were incubated at pH 6.4 in the presence of 15 mM $MgCl_2$ to reach the closed configuration. The spectra have been obtained with 460 nm excitation. Reprinted with permission from Publication II (https://pubs.acs.org/doi/10.1021/acsnano.9b01857). Copyright 2019 American Chemical Society.

The stability studies presented here thus provide a starting point for estimating the applicability of pH-responsive nanodevices in drug delivery applications. In particular, Mg^{2+} -depleted nanocapsules retaining their closed configuration is in particular an encouraging result for potential *in vivo* studies. The pK_a of the system is defined by the T–A·T content of the Hoogsteen triplexes, and could be adjusted to a higher value that would be better compatible with the pH in bloodstream. The results give also some indication of the combined effects of different chemical factors in the solution; the Mg^{2+} -depleted structures were shown to be more susceptible to destabilizing conditions, such as a high NaCl concentration, in line with previous observations (Kielar *et al.* 2018). The

limitations of the applied analysis methods were also apparent. As shown by the disturbance of the FRET signal by 10% plasma, different types of assays would be required to obtain reliable data on the structural stability of the capsules in biological fluids. Further studies could thus reveal whether the DNA nanocapsules could be applied as drug delivery vehicles without further modifications, or if additional stabilization methods, such as ligation, covalent cross-linking, or protective coating should be applied for enhancing their *in vivo* stability.

5.3.2 DNase I digestion of doxorubicin-loaded DNA origami

The structural stability of DNA origami structures and DOX-loaded DNA origami structures under nuclease digestion was studied with UV–Vis and fluorescence spectroscopy. The nuclease digestion of the DNA origami and DOX release upon the digestion were monitored simultaneously from the increase of the UV absorbance of nucleotides (Section 4.2.1) and DOX fluorescence recovery (Section 4.3.3). The DNA origami design (the superstructure) is known to be a major determinant in the DNase I resistance of DNA origami (Castro *et al.* 2011, Hahn *et al.* 2014, Ramakrishnan *et al.* 2019b). Here, the DNase I digestion rates were determined for the triangle, bowtie, double-L, capsule, and 24HB origami (IV). To study the effect of the DOX loading density on the digestion rate, the origami were loaded with DOX at two different loading concentrations: 3 μM DOX loading concentration leading to a loading density of 0.14–0.20 DOX_b/bp, and 6 μM DOX loading concentration leading to 0.20–0.31 DOX_b/bp for the tested structures.

The analysis of the UV absorbance of the nucleotides showed that the DNA origami structures were digested at superstructure- and DOX loading concentration -dependent rates (Fig. 22). The largest effect on the digestion rate was caused by the DNA origami superstructure; the difference in the digestion rate determined for the 24HB (the most resistant structure) and the triangle (the least resistant structure) was roughly two orders of magnitude. In general, the 2D structures were digested faster than the 3D structures. When DOX was added into the samples, the digestion slowed down with an increasing DOX loading concentration in a similar manner for all the structures. On average, 3 μM DOX slowed down the digestion by (71 ± 10)% compared to the origami samples prepared without DOX. Increasing the DOX loading to 6 μM caused a further (66 ± 18)% decrease of the digestion rate compared to the 3 μM concentration. Inhibition of the enzymatic activity of DNA-cleaving (as well as DNA-processing) enzymes has been observed previously for DOX and other intercalators, which indicates that the observed reduction in the digestion rate likely originates from an inhibitory effect of the bound DOX molecules (Facchinetti *et al.* 1978, Jollès *et al.* 1996, Biebricher *et al.* 2015).

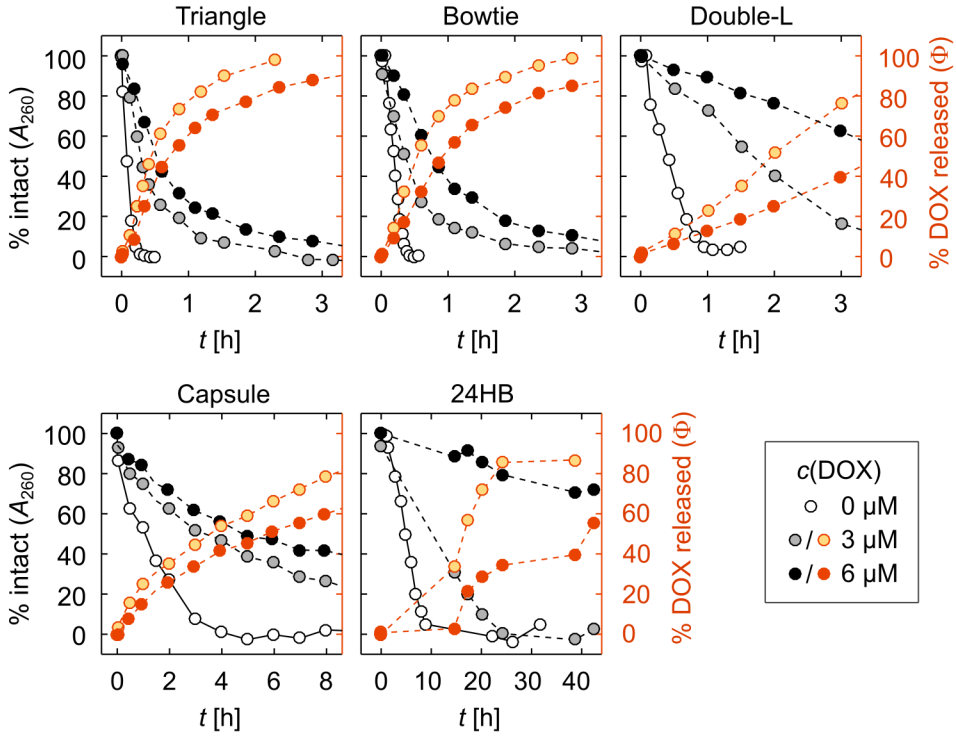

FIGURE 22 DNase I digestion (white, gray, and black circles) and DOX release profiles (orange circles) of plain DNA origami structures and DOX-loaded DNA origami structures. Reproduced from Publication IV.

The digestion of the dsDNA structure of the DNA origami also causes dissociation of the bound (intercalated and/or externally bound) DOX molecules. In Fig. 22, the DOX release is shown as the percentage of DOX molecules released from the structures. The percentage of released DOX correlated closely with the percentage of intact DNA origami (dsDNA) residues in the sample. Thus, 6 μM DOX loading concentration resulted in a slower release of DOX than the 3 μM loading concentration.

Here, the DNase I digestion and DOX release rates of DNA origami were studied in detail *in vitro* to show the relative differences between DNA origami structures and the effect of loaded DOX on the enzymatic activity of nucleases. It is important to note that the digestion timescales presented here are not directly comparable to the stability of the structures in the body. The applied DNase I concentration (34 U mL^{-1}) is approximately 100 times higher than the DNase I concentration in blood (Cherepanova *et al.* 2007) and the enzymatic activity is affected by the cation concentration and temperature (here, the measurements were carried out in the presence of 10 mM of $MgCl_2$ at RT). As described in Section 2.3.3, DNase I digestion is also only one of the factors compromising the stability of drug-loaded DNA origami in a physiological environment. As observed in the Mg^{2+} and Na^+ stability studies performed for the nanocapsule (Section 5.3.1), the structural resistance towards DNase I digestion could likewise be altered in a low-Mg^{2+} environment. Further studies could thus aim to combine the information obtained here for DNase I stability with the effects of further physiological factors.

6 CONCLUSIONS

The DNA origami method provides a versatile structural foundation for the development of functional nanostructures and nanomaterials. In this thesis, DNA origami nanostructures were used both as biosensor components and as transportation vehicles for nanoparticles, proteins, and DNA-binding drugs. As main methods in the work, a variety of UV–Vis and fluorescence spectroscopy assays were applied and developed for probing the structural changes of DNA origami and their interactions with other molecules. In addition to the spectroscopic results, structural information was obtained with electrophoretic mobility assays, imaging techniques (TEM and AFM), and electrochemical measurements.

The pH-controlled devices – DNA nanocapsules and DNA zippers – were constructed by functionalizing DNA origami with pH-sensitive Hoogsteen triplexes. Hoogsteen triplexes are versatile functional units whose pK_a value can be adjusted through sequence design to customize the pH response of the whole device. The devices developed in this work were designed to switch between closed and open configurations; the closed state prevailing at pH < pK_a (7.2 for the nanocapsules and 7.6 for the zippers) when the DNA triplexes form, and the open state at pH > pK_a. The conformational changes of the nanocapsules were used for encapsulating and displaying gold nanoparticles and enzymes that were site-specifically attached into the inner cavity. This could present a mechanism for a pH-selective shielding and display of cargo in drug delivery. In biosensing, DNA origami nanostructures can provide improved sensitivity, specificity, and a signal-to-noise ratio compared to conventional DNA biosensors. The presented electrochemical detection of the DNA zipper provides perspectives into the development of unlabeled electrochemical detection of either the presented pH-sensitive DNA devices, or similar devices functionalized for the detection of different analytes or solution conditions.

Structurally complex, pre-programmed nanodevices such as the DNA nanocapsule make a full use of the addressability and structural complexity of the DNA origami technique. In biomedicine, such devices could eventually lead to a development of advanced drug delivery systems and DNA nanorobots. On

the other hand, effective DNA origami –based drug delivery systems can also be constructed of static DNA origami assemblies. DNA origami structures consist of a high number of DNA base pairs, and they can be loaded with large quantities of DNA-binding drugs. This type of cargo loading approach differs greatly from the site-specific attachment of single cargo particles into the DNA origami nanocapsules, and could be easier to realize in a cost-efficient manner. However, understanding the thermodynamic properties of the drug-DNA origami complexes for predicting their composition and stability can be considerably more challenging.

The challenges of the loading process were recognized in the presented study on DOX-loaded DNA origami structures. The delivery of DOX with DNA origami structures has gathered increasing interest after the first *in vitro* cell studies in 2012, and the complexity of the delivery systems and the combination therapies has since vastly increased. On a first glance, it appears that the field has by now progressed far beyond the need for fundamental characterization of the DOX-DNA origami loading process and the formed complexes. However, an inspection of the existing literature revealed that a majority of studies this far have reported DOX loading densities that would be impossible to achieve with the presumed intercalative binding mode. According to the presented characterization, the former results may further hint to either poorly defined sample preparation processes or invalid spectroscopic analysis of the composition of the produced complexes.

The presented study thus led to pinpointing several experimental factors that need to be taken into account in the sample preparation process and in the spectroscopic analysis of the DOX-DNA origami complexes. While these observations may appear as technical details, they have also more profound implications. For instance, we suggest that depending on the applied sample preparation methods, DOX-DNA origami complexes can form purely through intercalation, they may contain a varying contribution of externally bound DOX, or even contain high amounts of DOX either stacked as aggregates on the origami surface or in self-aggregates. It is not yet possible to say which complexation method would provide the optimal properties for drug delivery. However, the different types of complexes will have distinct physico-chemical properties, and it is thus important to establish sample preparation methods that lead to a well-defined product. The presented results together with the critical evaluation of the previous literature will hopefully inspire further discussion and studies investigating the formation, composition, and stability of DOX-DNA origami carriers. This will enable ensuring the validity of conclusions made about the therapeutic efficiency of DNA origami–based DOX delivery systems, and help developing safe and well-specified drug carriers.

The first two parts of the work focused on characterizing the properties of the developed DNA origami devices and the cargo-loaded DNA origami structures. The aim of the third part of the work, the stability studies, was to evaluate the applicability of the developed structures in drug delivery. The results include encouraging results for instance on the low-Mg^{2+} stability of the nanocapsules, and they describe a potential approach for sustained and

customizable DOX release from DNA origami structures under DNase I digestion through design of the DNA origami superstructure. However, it is also apparent that still more physiological factors and their combined effects need to be taken into account to fully characterize the stability and biocompatibility of the developed systems. Further stability studies, as well as the development of methods for improving the stability of DNA origami in the physiological environment, still provide multiple interesting topics for future studies.

In research aiming for the eventual development of real-world applications, it is also necessary to assess the applicability of the developed nanosystems in a broader perspective. The DNA origami technique is an advanced nanofabrication method that has opened doors to the development of nanostructures and –devices of unprecedented structural complexity and customizability. On the downside, the high cost of DNA origami nanostructures currently still limits their real-life applicability. In real-world applications, DNA origami nanostructures will be competing against other available technologies in terms of robustness and cost-efficiency and it is thus important to demonstrate the benefit gained by using such an advanced fabrication technique. It is possible that the advanced functions performed by DNA nanomachines could become the strength of the technique for instance in biomedical applications or sensing technologies. On the other hand, simply the ease of constructing nanostructures with fully customized shapes can provide valuable customizable properties, such as presented here for the DOX release. Development of techniques for high-yield and low-cost manufacturing, such as the recently demonstrated biological mass-production, may still bring the manufacturing costs to a level where for example DNA origami drug delivery systems will be able to compete with conventional drugs and with other types of nanoformulations.

The work presented in this thesis thus provides several viewpoints to the development of functional DNA origami structures: studies on their dynamic functions, cargo loading methods, and structural stability. The results emphasize the diversity of the functionalities that can be realized in the nanoscale by harnessing the manufacturing precision and modularity of DNA origami nanostructures. The provided outlooks will aid further development of both the presented functional nanostructures and devices, as well as novel DNA origami –based applications in biological sciences.

Acknowledgements

The research presented in this thesis was carried out in the years 2017–2021. Funding for the work during this period was provided by the Jane and Aatos Erkko Foundation, the Emil Aaltonen Foundation, and the University of Jyväskylä Graduate School for Doctoral Studies. I am grateful for these funding sources for enabling me to carry out the PhD work. I thank the pre-examiners Prof. Barbara Saccà and Dr. Katherine Dunn for the careful evaluation of the thesis and insightful comments, and Prof. Kurt Gothelf for agreeing to act as my opponent in the upcoming public examination of the work.

During my PhD time, I have had the greatest opportunity to be a member of two research groups: both as a doctoral student in the group of Prof. Janne Ihalainen at the University of Jyväskylä, and since May 2017, as a visiting doctoral student in the Biohybrid Materials group at Aalto University. This has made the past four years a grand journey for me – both in a literal and in a symbolic sense. In both universities, I have had the joy to meet and work with great people who have helped me onwards as colleagues and co-authors. The exceptional situation and the social distancing of the past year has truly emphasized the importance of these communities in making the daily work with science enjoyable and inspiring.

Of all these people, I would like to first and foremost express my most sincere gratitude to my supervisors, Prof. Janne Ihalainen and Dr. Veikko Linko. Janne, thank you for the invaluable guidance, support, and encouragement. I can happily say that this refers not only to the last four years, but also to a whole decade of academic journey that has brought me to this point – starting from the first HOPS discussion in 2010, and including the possibility to start this project in early 2017. Veikko, you have been the person most closely involved in all the research I have carried out. Thank you for all the effort you have put into planning, carrying out, and finalizing the research projects with me. Our countless discussions, as well as the moments we have spent sitting down sharing ideas, planning experiments, or solving the toughest problems have always yielded inspiration and motivation to keep pushing forward.

I conducted the majority of my research work in Aalto University in the Biohybrid Materials group. Big thanks to everyone in the group for the company, new ideas, and direct and indirect support during the years. I wish to thank Prof. Mauri Kostiainen for providing the opportunity to be a part of the group. I am grateful for all your valuable ideas and insights to the projects, and I have learned a lot from your approaches to science and exemplary dedication. I wish to acknowledge Dr. Boxuan Shen for the particularly close collaboration and numerous fun and helpful discussions over the years, and Iiris Hakaste for the enjoyable and fruitful lab work we did together. I also thank my office mates and fellow PhD students Dr. Salla Välimäki, Dr. Antti Korpi, and Sofia Julin for the invaluable peer support and for the good atmosphere in the office that I have missed a lot in the home office.

I also want to express my gratitude for the whole group at the University of Jyväskylä – the current and former group members. Everyone in the group has had a part in creating a friendly and inclusive atmosphere that has always made me feel at home during my short visits. Moreover, I would like to thank Alli Liukkonen and Dr. Heikki Häkkänen for the help and guidance in the laboratory, and Iida Kettunen for the committed work for the Master's thesis project, which was a joy to supervise as a part of my research work.

I also wish to thank all the collaborators in other universities who have helped me accomplish my research goals and broaden my perspectives to the research topics. In particular, I thank Prof. Tim Liedl for helpful discussions and ideas, and Paul Williamson and Dr. Damion Corrigan for the tight collaboration in the final meters of my PhD work that enabled me to finish the thesis on schedule.

Finally, I would like to thank my family for the love and support that has made it possible to get onto the academic path and continue all the way to the PhD degree. The moments we have spent together during the doctoral studies have been immensely important to me and provided a safe haven in turbulent times. Special thanks to Dr. Anita Pätynen for all the like-minded discussions along the way that have helped to pull the little sister through the PhD studies, as well as to the whole family Pätynen on whose couch I have spent so many nights during my visits to Jyväskylä. Most of all, I want to thank my beloved husband Tommi Ijäs: thank you for supporting my decision to carry out the PhD work and for standing by my side every day.

YHTEENVETO (RÉSUMÉ IN FINNISH)

Toiminnalliset DNA-nanorakenteet molekyylikuljettimina ja biosensoreina

DNA-nanoteknologia on monitieteinen tutkimusala, jossa käytetään DNA-molekyylejä nanomittakaavan (< 100 nm) kappaleiden ja materiaalien rakennusaineena. DNA-nanorakenteita voidaan valmistaa useilla eri menetelmillä. Yksi erityisen käyttökelpoiseksi ja monipuoliseksi osoittautunut menetelmä on DNA:n laskostaminen niin kutsutuiksi DNA-origameiksi. DNA-origamit muodostetaan pitkästä geneettisestä DNA-juosteesta ja useista lyhyistä synteettisistä DNA-juosteista. Etukäteen suunniteltu nanorakenne muodostuu itsejärjestymisen kautta, kun juosteet sitoutuvat toisiinsa DNA:n emäsparisäännön (A–T, G–C) mukaisesti. Näin voidaan rakentaa monimutkaisia nanorakenteita jopa alle nanometrin rakenteellisella tarkkuudella. DNA-origameja voidaan lisäksi helposti funktionalisoida, eli liittää niihin tarkasti määriteltyihin kohtiin muita molekyylejä tai nanopartikkeleita, jotka antavat rakenteille uusia fysikaalisia tai kemiallisia ominaisuuksia.

Siinä missä DNA:n rooli luonnossa on pääosin geneettisen informaation säilyttäminen, DNA-origameille kehitetään jatkuvasti uusia ja monipuolisia käyttökohteita. Funktionalisoiduista DNA-origameista voidaan rakentaa esimerkiksi nanolaitteita, jotka muuttavat rakennettaan ennalta määrätyllä tavalla tietyn ulkoisen ärsykkeen vaikutuksesta (I). Tässä työssä oltiin erityisen kiinnostuneita siitä, miten DNA-origameja voidaan hyödyntää uusien biosensoritekniikoiden ja biolääketieteen menetelmien kehittämisessä.

Työn ensimmäisessä kokeellisessa osassa suunniteltiin ja valmistettiin kaksi erilaista ympäristön pH-arvoon reagoivaa DNA-origami –nanolaitetta: molekyylikuljetukseen soveltuva kapselimainen DNA-origami (II) ja biomolekyylien välisten vuorovaikutusten tutkimiseen suunniteltu vetoketjumainen DNA-origami (III). Laitteiden pH-vaste saatiin aikaan kiinnittämällä niihin DNA-juosteita, jotka muodostavat happamassa ympäristössä (matala pH) DNA-kolmoisjuosteen. Laitteet suunniteltiin niin, että ne lukittuivat kiinni, kun kolmoisjuosteet muodostuivat. Emäksisessä ympäristössä (korkea pH) kolmoisjuosteet purkautuivat ja DNA-laitteet avautuivat.

Laitteiden toiminnallisuus varmistettiin tutkimalla niiden rakennemuutoksia liuoksessa, jonka pH:ta muutettiin. DNA-nanokapselin avautumista ja sulkeutumista tutkittiin fluoresenssin resonanssienergiansiirtoon (FRET) perustuvalla menetelmällä, jolla voidaan määrittää kahden fluoresoivan merkkiaineiden välinen etäisyys. Kapselin puolikkaisiin kiinnitettiin merkkiaineet, joiden etäisyys toisistaan mitattiin eri pH-arvoissa fluoresenssimittauksen avulla ja näin määritettiin kapselin puolikkaiden välinen etäisyys. Lisäksi apuna käytettiin elektronimikroskopiakuvantamista. Mittaustuloksista nähtiin, että kapselin avautuminen ja sulkeutuminen tapahtuivat pH-arvon 7.27 ympäristössä. Tämä vastasi hyvin sitä pH-arvoa, jossa DNA-kolmoisjuosteiden odotettiin aiempien tutkimuksien perusteella muodostuvan. Lisäksi havaittiin, että kapseleiden sulkemiseksi tarvittiin useiden tuntien inkubointi happamassa liuoksessa (pH 6.4–

6.8), mutta avautuminen tapahtui välittömästi sen jälkeen, kun liuoksen pH muutettiin emäksiseksi (pH 7.6–8.0).

DNA-vetoketjurakenteen sulkeutuminen happamassa liuoksessa todistettiin ensin tutkimalla rakenteita atomivoimamikroskoopilla (III). Tämän jälkeen rakenteet suljettiin, kiinnitettiin kullasta valmistetulle elektrodille ja niiden avautumista havainnoitiin sähkökemiallisilla mittauksilla. Kun liuoksen pH:ta nostettiin, mittauksessa havaittu sähkövirta pieneni. Tämän voitiin olettaa johtuvan ainakin osittain DNA:ssa tapahtuvista rakennemuutoksista. Tällainen mittausasetelma on lisäksi esimerkki DNA-origamien hyödyntämisestä biosensoreina: biologinen komponentti reagoi muutoksen liuosympäristössä tai sitoutuu kohdemolekyyliin ja tuottaa havaittavan signaalin. Biosensoreilla on lukuisia käyttökohteita esimerkiksi diagnostiikassa. Työssä kehitettyä menetelmää havaita DNA-origamilaitteen rakennemuutos sähkökemiallisen mittauksen avulla voitaisiin kehittää edelleen paitsi pH:n muutosten, myös muunlaisten ärsykkeiden havaitsemiseen.

Biolääketieteen yksi kiinnostava tutkimuskohde on se, miten lääkeaineita voidaan kuljettaa kohdekudoksiin nanopartikkeleiden avulla ja täten lisätä lääkehoidon tehokkuutta ja turvallisuutta. Työn toisena pääaihepiirinä tutkittiin molekyylikuljetusta eli kehitettiin menetelmiä, joiden avulla DNA-origameja voidaan käyttää proteiinien, nanopartikkeleiden ja DNA:han sitoutuvien lääkeainemolekyylien kuljetukseen. pH:lla kontrolloitavien nanokapseleiden sisälle voitiin lastata yksittäisiä kultananopartikkeleita ja piparjuuren peroksidaasientsyymejä, ja sulkea kapselit tämän jälkeen pH:ta laskemalla (II). Kapseleihin lastattujen entsyymien toimintaa tutkittiin kolorimetrisella mittauksella. Työssä osoitettiin, että nanokapseleihin lastatut entsyymit säilyivät toimintakykyisinä ja niiden katalyyttinen toiminta tehostui vapaisiin entsyymeihin verrattuna. DNA-nanokapselit voisivat siis soveltua esimerkiksi terapeuttisten proteiinien kuljetukseen. pH:n aiheuttamaa avautumista voitaisiin puolestaan hyödyntää mekanismina, jolla kapselit avautuvat tarkasti ja nopeasti sen jälkeen, kun ne ovat päätyneet kohdekudoksen tai kohdesolujen sisälle.

Tämän jälkeen DNA:han sitoutuvan syöpälääkemolekyylin, doksorubisiinin, lastaamista eri muotoisiin DNA-nanorakenteisiin tutkittiin absorptio- ja fluoresenssispektroskopian avulla (IV). Tulokset osoittivat, että doksorubisiinin sitoutuminen DNA-rakenteisiin tapahtuu erittäin nopeasti (sekunneissa) ja että doksorubisiinimolekyylejä voi sitoutua DNA-origameihin n. 2-3 emäsparin välein (0.36 ± 0.10 doksorubisiinimolekyyliä yhtä emäsparia kohden). Lisäksi havaittiin, että DNA-origamien kyky sitoa doksorubisiinia on yliarvioitu useissa aiemmissa tutkimuksissa. Mittaustulosten perusteella tämä voi selittyä sillä, että doksorubisiini sakkautuu helposti näytteenvalmistuksen aikana. Lisäksi sitä irtoaa oletettua nopeammin DNA-rakenteista näytteenvalmistuksen jälkeen ja sen optisten ominaisuuksien muuttuminen erilaisissa liuoksissa voi johtaa yliarvioituun doksorubisiinin määrään näytteessä. Doksorubisiinilla lastattujen DNA-nanorakenteiden tehokkuus syöpäsolujen ja –kasvainten hoidossa on osoitettu monissa tutkimuksissa, mutta saatujen tulosten valossa on mahdollista, että osa havaituista vaikutuksista on voinut johtua näytteiden sisältämistä sakkautuneista

tai vapaista lääkeainemolekyyleistä. On tärkeää, että tällaiset tekijät otetaan jatkossa huomioon kehitettäessä DNA-nanorakenteisiin pohjautuvia syöpähoitoja.

Työn kolmantena aihepiirinä tutkittiin sitä, kuinka hyvin DNA-origamirakenteet säilyvät ehjinä fysiologisissa olosuhteissa. Tämä on tärkeä nanolääketieteen tutkimuskohde, sillä lääkeainekuljetuksessa käytettävien nanorakenteiden täytyy säilyä ehjinä verenkierrossa kohdekudokseen saakka. DNA-nanorakenteet voivat hajota verenkierrossa veren matalan magnesiumpitoisuuden ja korkean natriumpitoisuuden vuoksi. Veri sisältää myös runsaasti DNA:ta hajottavia entsyymejä. Tutkimuksessa kehitetyt DNA-nanokapselit pysyivät toiminnallisina fysiologisissa magnesium- ja natriumpitoisuuksissa sekä liuoksessa, johon oli lisätty veriplasmaa (II). Doksorubisiinilla ladattujen DNA-origamirakenteiden kestävyyttä tutkittiin liuoksessa, joka sisälsi veren deoksiribonukleaasi I (DNaasi I) –entsyymiä (IV). DNaasi I hajotti muodoiltaan erilaisia DNA-origamirakenteita eri nopeuksilla. Joustavat ja levymäiset DNA-origamirakenteet hajosivat nopeammin kuin rakenteet, joissa DNA-juosteet oli järjestetty tiiviiksi, kolmiulotteisiksi rakenteiksi. Hajoamisnopeuteen vaikutti myös se, kuinka paljon rakenteisiin oli lastattu doksorubisiinia; korkeampi tiheys doksorubisiinia teki rakenteista kestävämpiä entsymaattista hajotusta vastaan. Koska doksorubisiini vapautuu ympäristöön rakenteiden hajotessa, työn tärkeä havainto oli se, että entsymaattisen hajotuksen aiheuttama lääkkeen vapautuminen DNA-origamirakenteista on mahdollista säätää halutuksi DNA-origamien muodon avulla.

DNA-origamitekniikka on ainutlaatuisen monipuolinen ja tarkka menetelmä nanokokoisten rakenteiden valmistamiseksi. Tämä tutkimus havainnollistaa sitä, miten DNA-origamirakenteiden avulla voidaan toteuttaa nanomittakaavassa vaivattomasti erilaisia tarkoin suunniteltuja toimintoja. Esimerkiksi lääkeainekuljetustekniikoiden kehityksessä DNA-origamitutkimuksella on todennäköisesti edessään vielä pitkä tie ennen ensimmäisiä kaupallisia sovelluksia. Tämä työ edesauttaa tehokkaiden, turvallisten ja toiminnaltaan tarkasti määriteltyjen sovellusten kehitystä tutkimalla yksityiskohtaisella tasolla DNA-origamirakenteiden toimintaa biosensoreina ja molekyylikuljettimina sekä niiden kestävyyttä fysiologisissa olosuhteissa.

REFERENCES

Airoldi M., Barone G., Gennaro G., Giuliani A.M. & Giustini M. 2014. Interaction of doxorubicin with polynucleotides. a spectroscopic study. *Biochemistry* 53: 2197–2207.

Amir Y., Ben-Ishay E., Levner D., Ittah S., Abu-Horowitz A. & Bachelet I. 2014. Universal computing by DNA origami robots in a living animal. *Nature Nanotechnology* 9: 353–357.

Anastassacos F.M., Zhao Z., Zeng Y. & Shih W.M. 2020. Glutaraldehyde Cross-Linking of Oligolysines Coating DNA Origami Greatly Reduces Susceptibility to Nuclease Degradation. *Journal of the American Chemical Society* 142: 3311–3315.

Andersen E.S., Dong M., Nielsen M.M., Jahn K., Subramani R., Mamdouh W., Golas M.M., Sander B., Stark H., Oliveira C.L.P., Pedersen J.S., Birkedal V., Besenbacher F., Gothelf K. V. & Kjems J. 2009. Self-assembly of a nanoscale DNA box with a controllable lid. *Nature* 459: 73–76.

Arroyo-Currás N., Sadeia M., Ng A.K., Fyodorova Y., Williams N., Afif T., Huang C.M., Ogden N., Andresen Eguiluz R.C., Su H.J., Castro C.E., Plaxco K.W. & Lukeman P.S. 2020. An electrochemical biosensor exploiting binding-induced changes in electron transfer of electrode-attached DNA origami to detect hundred nanometer-scale targets. *Nanoscale* 12: 13907–13911.

Asanuma H., Liang X., Nishioka H., Matsunaga D., Liu M. & Komiyama M. 2007. Synthesis of azobenzene-tethered DNA for reversible photo-regulation of DNA functions: hybridization and transcription. *Nature protocols* 2: 203–212.

Asensio J.L., Brown T. & Lane A.N. 1999. Solution conformation of a parallel DNA triple helix with 5′ and 3′ triplex-duplex junctions. *Structure* 7: 1–11.

Atsumi H. & Belcher A.M. 2018. DNA Origami and G-quadruplex hybrid complexes induce size control of single-walled carbon nanotubes via biological activation. *ACS Nano* 12: 7986–7995.

Auvinen H., Zhang H., Nonappa, Kopilow A., Niemelä E.H., Nummelin S., Correia A., Santos H.A., Linko V. & Kostiainen M.A. 2017. Protein Coating of DNA Nanostructures for Enhanced Stability and Immunocompatibility. *Advanced Healthcare Materials* 6: 1700692.

Aviñó A., Cubero E., González C., Eritja R. & Orozco M. 2003. Antiparallel Triple Helices. Structural Characteristics and Stabilization by 8-Amino Derivatives. *Journal of the American Chemical Society* 125: 16127–16138.

Balakrishnan D., Wilkens G.D. & Heddle J.G. 2019. Delivering DNA origami to cells. *Nanomedicine* 14: 911–925.

Barcelo F., Martorell J., Gavilanes F. & Gonzalez-Ros J.M. 1988. Equilibrium binding of daunomycin and adriamycin to calf thymus DNA. Temperature and ionic strength dependence of thermodynamic parameters. *Biochemical Pharmacology* 37: 2133–2138.

Bastings M.M.C., Anastassacos F.M., Ponnuswamy N., Leifer F.G., Cuneo G., Lin C., Ingber D.E., Ryu J.H. & Shih W.M. 2018. Modulation of the Cellular

Uptake of DNA Origami through Control over Mass and Shape. *Nano Letters* 18: 3557–3564.

Bertrand N. & Leroux J.C. 2012. The journey of a drug-carrier in the body: An anatomo-physiological perspective. *Journal of Controlled Release* 161: 152–163.

Biebricher A.S., Heller I., Roijmans R.F.H., Hoekstra T.P., Peterman E.J.G. & Wuite G.J.L. 2015. The impact of DNA intercalators on DNA and DNA-processing enzymes elucidated through force-dependent binding kinetics. *Nature Communications* 6: 7304.

Bila H., Kurisinkal E.E. & Bastings M.M.C. 2019. Engineering a stable future for DNA-origami as a biomaterial. *Biomaterials Science* 7: 532–541.

Burns J.R., Lamarre B., Pyne A.L.B., Noble J.E. & Ryadnov M.G. 2018. DNA Origami Inside-Out Viruses. *ACS Synthetic Biology* 7: 767–773.

Casey J.R., Grinstein S. & Orlowski J. 2010. Sensors and regulators of intracellular pH. *Nature Reviews Molecular Cell Biology* 11: 50–61.

Castro C.E., Dietz H. & Högberg B. 2017. DNA origami devices for molecular-scale precision measurements. *MRS Bulletin* 42: 925–929.

Castro C.E., Kilchherr F., Kim D.N., Shiao E.L., Wauer T., Wortmann P., Bathe M. & Dietz H. 2011. A primer to scaffolded DNA origami. *Nature Methods* 8: 221–229.

Cavaluzzi M.J. & Borer P.N. 2004. Revised UV extinction coefficients for nucleoside-5′-monophosphates and unpaired DNA and RNA. *Nucleic acids research* 32: e13.

Chandrasekaran A.R. 2017. DNA Nanobiosensors: An Outlook on Signal Readout Strategies. *Journal of Nanomaterials* 2017: 2820619.

Chandrasekaran A.R. & Rusling D.A. 2018. Survey and summary: Triplex-forming oligonucleotides: A third strand for DNA nanotechnology. *Nucleic Acids Research* 46: 1021–1037.

Chandrasekaran A.R., Vilcapoma J., Dey P., Wong-Deyrup S.W., Dey B.K. & Halvorsen K. 2020. Exceptional Nuclease Resistance of Paranemic Crossover (PX) DNA and Crossover-Dependent Biostability of DNA Motifs. *Journal of the American Chemical Society* 142: 6814–6821.

Chen H., Zhang H., Pan J., Cha T.G., Li S., Andréasson J. & Choi J.H. 2016. Dynamic and Progressive Control of DNA Origami Conformation by Modulating DNA Helicity with Chemical Adducts. *ACS Nano* 10: 4989–4996.

Cherepanova A., Tamkovich S., Pyshnyi D., Kharkova M., Vlassov V. & Laktionov P. 2007. Immunochemical assay for deoxyribonuclease activity in body fluids. *Journal of Immunological Methods* 325: 96–103.

Chi Q., Yang Z., Xu K., Wang C. & Liang H. 2020. DNA nanostructure as an efficient drug delivery platform for immunotherapy. *Frontiers in Pharmacology* 10: 1585.

Childs R.E. & Bardsley W.G. 1975. The steady state kinetics of peroxidase with 2,2′-azino-di-(3-ethylbenzthiazoline-6-sulphonic acid) as chromogen. *Biochemical Journal* 145: 93–103.

Coleridge E.L. & Dunn K.E. 2020. Assessing the cost-effectiveness of DNA origami nanostructures for targeted delivery of anti-cancer drugs to tumours. *Biomedical Physics & Engineering Express* 6: 065030.

Daljit Singh J.K., Luu M.T., Abbas A. & Wickham S.F.J. 2018. Switchable DNA-origami nanostructures that respond to their environment and their applications. *Biophysical Reviews* 10: 1283–1293.

Danilov V.I. 1974. On the origin of the hypochromic effect in double-stranded polynucleotides. *FEBS Letters* 47: 155–157.

Dietz H., Douglas S.M. & Shih W.M. 2009. Folding DNA into twisted and curved nanoscale shapes. *Science* 325: 725–730.

Douglas S.M., Bachelet I. & Church G.M. 2012. A logic-gated nanorobot for targeted transport of molecular payloads. *Science* 335: 831–834.

Douglas S.M., Dietz H., Liedl T., Högberg B., Graf F. & Shih W.M. 2009a. Self-assembly of DNA into nanoscale three-dimensional shapes. *Nature* 459: 414–418.

Douglas S.M., Marblestone A.H., Teerapittayanon S., Vazquez A., Church G.M. & Shih W.M. 2009b. Rapid prototyping of 3D DNA-origami shapes with caDNAno. *Nucleic Acids Research* 37: 5001–5006.

Drew H.R., Wing R.M., Takano T., Broka C., Tanaka S., Itakura K. & Dickerson R.E. 1981. Structure of a B-DNA dodecamer: conformation and dynamics. *Proceedings of the National Academy of Sciences of the United States of America* 78: 2179–2183.

Du Y., Jiang Q., Beziere N., Song L., Zhang Q., Peng D., Chi C., Yang X., Guo H., Diot G., Ntziachristos V., Ding B. & Tian J. 2016. DNA-Nanostructure–Gold-Nanorod Hybrids for Enhanced In Vivo Optoacoustic Imaging and Photothermal Therapy. *Advanced Materials* 28: 10000–10007.

Duanghathaipornsuk S., Shen B., Cameron B.D., Ijäs H., Linko V., Kostiainen M.A. & Kim D.S. 2020. Aptamer-embedded DNA origami cage for detecting (glycated) hemoglobin with a surface plasmon resonance sensor. *Materials Letters* 275: 128141.

Esmaili N. & Leroy J.L. 2005. i-motif solution structure and dynamics of the d(AACCCC) and d(CCCCAA) tetrahymena telomeric repeats. *Nucleic Acids Research* 33: 213–224.

Facchinetti T., Mantovani A., Cantoni L., Cantoni R. & Salmona M. 1978. Intercalation with DNA is a prerequisite for Daunomycin, Adriamycin and its congeners in inhibiting DNAase I. *Chemico-Biological Interactions* 20: 97–102.

Feng B., Sosa R.P., Mårtensson A.K.F., Jiang K., Tong A., Dorfman K.D., Takahashi M., Lincoln P., Bustamante C.J., Westerlund F. & Nordén B. 2019. Hydrophobic catalysis and a potential biological role of DNA unstacking induced by environment effects. *Proceedings of the National Academy of Sciences of the United States of America* 116: 17169–17174.

Frederick C.A., Williams L.D., Ughetto G., Marel G.A. van der, Boom H.J. van, Rich A. & Wang A.H.J. 1990. Structural Comparison of Anticancer Drug-DNA Complexes: Adriamycin and Daunomycin. *Biochemistry* 29: 2538–2549.

Fu J., Liu M., Liu Y., Woodbury N.W. & Yan H. 2012. Interenzyme substrate diffusion for an enzyme cascade organized on spatially addressable DNA nanostructures. *Journal of the American Chemical Society* 134: 5516–5519.

Fu T.-J. & Seeman N.C. 1993. DNA Double-Crossover Molecules. *Biochemistry* 32:

3211–3220.
Fu A., Tang R., Hardie J., Farkas M.E. & Rotello V.M. 2014. Promises and Pitfalls of Intracellular Delivery of Proteins. *Bioconjugate Chemistry* 25: 1602–1608.
Fülöp Z., Gref R. & Loftsson T. 2013. A permeation method for detection of self-aggregation of doxorubicin in aqueous environment. *International Journal of Pharmaceutics* 454: 559–561.
Funck T., Nicoli F., Kuzyk A. & Liedl T. 2018. Sensing Picomolar Concentrations of RNA Using Switchable Plasmonic Chirality. *Angewandte Chemie - International Edition* 57: 13495–13498.
Funke J.J., Ketterer P., Lieleg C., Schunter S., Korber P. & Dietz H. 2016. Uncovering the forces between nucleosomes using DNA origami. *Science Advances* 2: e1600974.
Gandecha B.M., Brown J.R. & Crampton M.R. 1985. Dissociation kinetics of DNA-anthracycline and DNA-anthraquinone complexes determined by stopped-flow spectrophotometry. *Biochemical Pharmacology* 34: 733–736.
Ge Z., Fu J., Liu M., Jiang S., Andreoni A., Zuo X., Liu Y., Yan H. & Fan C. 2019. Constructing Submonolayer DNA Origami Scaffold on Gold Electrode for Wiring of Redox Enzymatic Cascade Pathways. *ACS Applied Materials and Interfaces* 11: 13881–13887.
Gehring K., Leroy J.L. & Guéron M. 1993. A tetrameric DNA structure with protonated cytosine-cytosine base pairs. *Nature* 363: 561–565.
Gerling T., Kube M., Kick B. & Dietz H. 2018. Sequence-programmable covalent bonding of designed DNA assemblies. *Science Advances* 4: eaau1157.
Gerling T., Wagenbauer K.F., Neuner A.M. & Dietz H. 2015. Dynamic DNA devices and assemblies formed by shape-complementary, non-base pairing 3D components. *Science* 347: 1446–1452.
Gopinath A., Miyazono E., Faraon A. & Rothemund P.W.K. 2016. Engineering and mapping nanocavity emission via precision placement of DNA origami. *Nature* 535: 401–405.
Goutelle S., Maurin M., Rougier F., Barbaut X., Bourguignon L., Ducher M. & Maire P. 2008. The Hill equation: A review of its capabilities in pharmacological modelling. *Fundamental and Clinical Pharmacology* 22: 633–648.
Graugnard E., Hughes W.L., Jungmann R., Kostiainen M.A. & Linko V. 2017. Nanometrology and super-resolution imaging with DNA. *MRS Bulletin* 42: 951–958.
Grossi G., Dalgaard Ebbesen Jepsen M., Kjems J. & Andersen E.S. 2017. Control of enzyme reactions by a reconfigurable DNA nanovault. *Nature Communications* 8: 992.
Guéron M. & Leroy J.L. 2000. The i-motif in nucleic acids. *Current Opinion in Structural Biology* 10: 326–331.
Hahn J., Wickham S.F.J., Shih W.M. & Perrault S.D. 2014. Addressing the instability of DNA nanostructures in tissue culture. *ACS Nano* 8: 8765–8775.
Halley P.D., Lucas C.R., McWilliams E.M., Webber M.J., Patton R.A., Kural C., Lucas D.M., Byrd J.C. & Castro C.E. 2016. Daunorubicin-Loaded DNA Origami Nanostructures Circumvent Drug-Resistance Mechanisms in a

Leukemia Model. *Small* 12: 308–320.
Han S., Liu W., Yang S. & Wang R. 2019. Facile and Label-Free Electrochemical Biosensors for MicroRNA Detection Based on DNA Origami Nanostructures. *ACS Omega* 4: 11025–11031.
Han D., Pal S., Nangreave J., Deng Z., Liu Y. & Yan H. 2011. DNA origami with complex curvatures in three-dimensional space. *Science* 332: 342–346.
Hayashi M. & Harada Y. 2007. Direct observation of the reversible unwinding of a single DNA molecule caused by the intercalation of ethidium bromide. *Nucleic Acids Research* 35: e125.
Hill A.V. 1910. The possible effects of the aggregation of the molecules of haemoglobin on its dissociation curves. *J Physiol (Lond)* 40: iv–vii.
Hong F., Jiang S., Lan X., Narayanan R.P., Šulc P., Zhang F., Liu Y. & Yan H. 2018. Layered-Crossover Tiles with Precisely Tunable Angles for 2D and 3D DNA Crystal Engineering. *Journal of the American Chemical Society* 140: 14670–14676.
Hong F., Zhang F., Liu Y. & Yan H. 2017. DNA Origami: Scaffolds for Creating Higher Order Structures. *Chemical Reviews* 117: 12584–12640.
Hudoba M.W., Luo Y., Zacharias A., Poirier M.G. & Castro C.E. 2017. Dynamic DNA Origami Device for Measuring Compressive Depletion Forces. *ACS Nano* 11: 6566–6573.
Hung A.M., Micheel C.M., Bozano L.D., Osterbur L.W., Wallraff G.M. & Cha J.N. 2010. Large-area spatially ordered arrays of gold nanoparticles directed by lithographically confined DNA origami. *Nature Nanotechnology* 5: 121–126.
Hurst S.J., Lytton-Jean A.K.R. & Mirkin C.A. 2006. Maximizing DNA loading on a range of gold nanoparticle sizes. *Analytical Chemistry* 78: 8313–8318.
Idili A., Vallée-Bélisle A. & Ricci F. 2014. Programmable pH-triggered DNA nanoswitches. *Journal of the American Chemical Society* 136: 5836–5839.
Jaekel A., Stegemann P. & Saccà B. 2019. Manipulating enzymes properties with DNA nanostructures. *Molecules* 24: 3694.
Jahnen-Dechent W. & Ketteler M. 2012. Magnesium basics. *Clinical Kidney Journal* 5: i3–i14.
Jiang D., Ge Z., Im H.J., England C.G., Ni D., Hou J., Zhang L., Kutyreff C.J., Yan Y., Liu Y., Cho S.Y., Engle J.W., Shi J., Huang P., Fan C., Yan H. & Cai W. 2018. DNA origami nanostructures can exhibit preferential renal uptake and alleviate acute kidney injury. *Nature Biomedical Engineering* 2: 865–877.
Jiang S., Ge Z., Mou S., Yan H. & Fan C. 2020. Designer DNA nanostructures for therapeutics. *Chem*.
Jiang Q., Shi Y., Zhang Q., Li N., Zhan P., Song L., Dai L., Tian J., Du Y., Cheng Z. & Ding B. 2015. A Self-Assembled DNA Origami-Gold Nanorod Complex for Cancer Theranostics. *Small* 11: 5134–5141.
Jiang Q., Song C., Nangreave J., Liu X., Lin L., Qiu D., Wang Z.G., Zou G., Liang X., Yan H. & Ding B. 2012. DNA origami as a carrier for circumvention of drug resistance. *Journal of the American Chemical Society* 134: 13396–13403.
Johnson J.A., Dehankar A., Robbins A., Kabtiyal P., Jergens E., Ho Lee K., Johnston-Halperin E., Poirier M., Castro C.E. & Winter J.O. 2019a. The path towards functional nanoparticle-DNA origami composites. *Materials Science*

and Engineering R: Reports 138: 153–209.

Johnson J.A., Dehankar A., Winter J.O. & Castro C.E. 2019b. Reciprocal Control of Hierarchical DNA Origami-Nanoparticle Assemblies. *Nano Letters* 19: 8469–8475.

Jollès B., Laigle A., Priebe W. & Garnier-Suillerot A. 1996. Comparison of DNA sequence selectivity of anthracycline antibiotics and their 3′-hydroxylated analogs. *Chemico-Biological Interactions* 100: 165–176.

Jones M.R., Seeman N.C. & Mirkin C.A. 2015. Programmable materials and the nature of the DNA bond. *Science* 347: 1260901.

Jun H., Shepherd T.R., Zhang K., Bricker W.P., Li S., Chiu W. & Bathe M. 2019. Automated sequence design of 3D polyhedral wireframe DNA origami with honeycomb edges. *ACS Nano* 13: 2083–2093.

Juul S., Iacovelli F., Falconi M., Kragh S.L., Christensen B., Frøhlich R., Franch O., Kristoffersen E.L., Stougaard M., Leong K.W., Ho Y.P., Sørensen E.S., Birkedal V., Desideri A. & Knudsen B.R. 2013. Temperature-controlled encapsulation and release of an active enzyme in the cavity of a self-assembled DNA nanocage. *ACS Nano* 7: 9724–9734.

Kallenbach N.R., Ma R.I. & Seeman N.C. 1983. An immobile nucleic acid junction constructed from oligonucleotides. *Nature* 305: 829–831.

Ke Y., Ong L.L., Shih W.M. & Yin P. 2012a. Three-dimensional structures self-assembled from DNA bricks. *Science* 338: 1177–1183.

Ke Y., Voigt N. V., Gothelf K. V. & Shih W.M. 2012b. Multilayer DNA origami packed on hexagonal and hybrid lattices. *Journal of the American Chemical Society* 134: 1770–1774.

Keller A. & Linko V. 2020. Challenges and Perspectives of DNA Nanostructures in Biomedicine. *Angewandte Chemie - International Edition* 59: 15818–15833.

Kettunen I. 2020. Red light-sensing phytochrome-DNA conjugates for nanotechnology applications. *Master's thesis, University of Jyväskylä.*

Kielar C., Xin Y., Shen B., Kostiainen M.A., Grundmeier G., Linko V. & Keller A. 2018. On the Stability of DNA Origami Nanostructures in Low-Magnesium Buffers. *Angewandte Chemie - International Edition* 57: 9470–9474.

Kim D.N., Kilchherr F., Dietz H. & Bathe M. 2012. Quantitative prediction of 3D solution shape and flexibility of nucleic acid nanostructures. *Nucleic Acids Research* 40: 2862–2868.

Kim Y. & Yin P. 2020. Enhancing Biocompatible Stability of DNA Nanostructures Using Dendritic Oligonucleotides and Brick Motifs. *Angewandte Chemie - International Edition* 59: 700–703.

Klein W.P., Thomsen R.P., Turner K.B., Walper S.A., Vranish J., Kjems J., Ancona M.G. & Medintz I.L. 2019. Enhanced Catalysis from Multienzyme Cascades Assembled on a DNA Origami Triangle. *ACS Nano* 13: 13677–13689.

Kogikoski S., Paschoalino W.J., Cantelli L., Silva W. & Kubota L.T. 2019. Electrochemical sensing based on DNA nanotechnology. *TrAC Trends in Analytical Chemistry* 118: 597–605.

Kollmann F., Ramakrishnan S., Shen B., Grundmeier G., Kostiainen M.A., Linko V. & Keller A. 2018. Superstructure-Dependent Loading of DNA Origami Nanostructures with a Groove-Binding Drug. *ACS Omega* 3: 9441–9448.

Kosuri P., Altheimer B.D., Dai M., Yin P. & Zhuang X. 2019. Rotation tracking of genome-processing enzymes using DNA origami rotors. *Nature* 572: 136–140.

Krebs H.A. 1950. Chemical composition of blood plasma and serum. *Annual review of biochemistry* 19: 409–430.

Kuzuya A., Sakai Y., Yamazaki T., Xu Y. & Komiyama M. 2011. Nanomechanical DNA origami 'single-molecule beacons' directly imaged by atomic force microscopy. *Nature Communications* 2: 449.

Kuzyk A., Schreiber R., Fan Z., Pardatscher G., Roller E.M., Högele A., Simmel F.C., Govorov A.O. & Liedl T. 2012. DNA-based self-assembly of chiral plasmonic nanostructures with tailored optical response. *Nature* 483: 311–314.

Kuzyk A., Schreiber R., Zhang H., Govorov A.O., Liedl T. & Liu N. 2014. Reconfigurable 3D plasmonic metamolecules. *Nature Materials* 13: 862.

Kuzyk A., Urban M.J., Idili A., Ricci F. & Liu N. 2017. Selective control of reconfigurable chiral plasmonic metamolecules. *Science Advances* 3: e1602803.

Kuzyk A., Yang Y., Duan X., Stoll S., Govorov A.O., Sugiyama H., Endo M. & Liu N. 2016. A light-driven three-dimensional plasmonic nanosystem that translates molecular motion into reversible chiroptical function. *Nature Communications* 7: 10591.

Lacroix A., Vengut-Climent E., Rochambeau D. De & Sleiman H.F. 2019. Uptake and Fate of Fluorescently Labeled DNA Nanostructures in Cellular Environments: A Cautionary Tale. *ACS Central Science* 5: 882–891.

Lakowicz J.R. 2006. *Principles of fluorescence spectroscopy (3rd edition)*. Springer Science+Business Media, LLC.

Li S., Jiang Q., Liu S., Zhang Y., Tian Y., Song C., Wang J., Zou Y., Anderson G.J., Han J.Y., Chang Y., Liu Y., Zhang C., Chen L., Zhou G., Nie G., Yan H., Ding B. & Zhao Y. 2018. A DNA nanorobot functions as a cancer therapeutic in response to a molecular trigger in vivo. *Nature Biotechnology* 36: 258–264.

Li X., Yang X., Qi J. & Seeman N.C. 1996. Antiparallel DNA double crossover molecules as components for nanoconstruction. *Journal of the American Chemical Society* 118: 6131–6140.

Lin J.-L. & Wheeldon I. 2013. Kinetic Enhancements in DNA–Enzyme Nanostructures Mimic the Sabatier Principle. *ACS Catalysis* 3: 560–564.

Linko V. & Dietz H. 2013. The enabled state of DNA nanotechnology. *Current Opinion in Biotechnology* 24: 555–561.

Linko V., Eerikäinen M. & Kostiainen M.A. 2015a. A modular DNA origami-based enzyme cascade nanoreactor. *Chemical Communications* 51: 5351–5354.

Linko V., Ora A. & Kostiainen M.A. 2015b. DNA Nanostructures as Smart Drug-Delivery Vehicles and Molecular Devices. *Trends in Biotechnology* 33: 586–594.

Liu S., Jiang Q., Zhao X., Zhao R., Wang Y., Wang Y., Liu J., Shang Y., Zhao S., Wu T., Zhang Y., Nie G. & Ding B. 2020. A DNA nanodevice-based vaccine for cancer immunotherapy. *Nature Materials*.

Liu B. & Liu J. 2017. Methods for preparing DNA-functionalized gold

nanoparticles, a key reagent of bioanalytical chemistry. *Analytical Methods* 9: 2633–2643.

Liu J., Song L., Liu S., Jiang Q., Liu Q., Li N., Wang Z.G. & Ding B. 2018a. A DNA-Based Nanocarrier for Efficient Gene Delivery and Combined Cancer Therapy. *Nano Letters* 18: 3328–3334.

Liu J., Song L., Liu S., Zhao S., Jiang Q. & Ding B. 2018b. A Tailored DNA Nanoplatform for Synergistic RNAi-/Chemotherapy of Multidrug-Resistant Tumors. *Angewandte Chemie - International Edition* 57: 15486–15490.

Liu W., Zhong H., Wang R. & Seeman N.C. 2011. Crystalline two-dimensional DNA-origami arrays. *Angewandte Chemie - International Edition* 50: 264–267.

Loretan M., Domljanovic I., Lakatos M., Rüegg C. & Acuna G.P. 2020. DNA origami as emerging technology for the engineering of fluorescent and plasmonic-based biosensors. *Materials* 13: 2185.

Lundqvist M., Stigler J., Elia G., Lynch I., Cedervall T. & Dawson K.A. 2008. Nanoparticle size and surface properties determine the protein corona with possible implications for biological impacts. *Proceedings of the National Academy of Sciences of the United States of America* 105: 14265–14270.

Madhuri S., Vengadesan N., Aruna P., Koteeswaran D., Venkatesan P. & Ganesan S. 2003. Native Fluorescence Spectroscopy of Blood Plasma in the Characterization of Oral Malignancy. *Photochemistry and Photobiology* 78: 197.

Madsen M. & Gothelf K. V. 2019. Chemistries for DNA Nanotechnology. *Chemical Reviews* 119: 6384–6458.

Majikes J.M., Ferraz L.C.C. & LaBean T.H. 2017. PH-Driven Actuation of DNA Origami via Parallel I-Motif Sequences in Solution and on Surfaces. *Bioconjugate Chemistry* 28: 1821–1825.

Manning G.S. 1978. The molecular theory of polyelectrolyte solutions with applications to the electrostatic properties of polynucleotides. *Quarterly Reviews of Biophysics* 11: 179–246.

Margaritis A. & Manocha B. 2010. Controlled release of doxorubicin from doxorubicin/γ-polyglutamic acid ionic complex. *Journal of Nanomaterials* 2010: 780171.

Marras A.E., Shi Z., Lindell M.G., Patton R.A., Huang C.-M., Zhou L., Su H.-J., Arya G. & Castro C.E. 2018. Cation-Activated Avidity for Rapid Reconfiguration of DNA Nanodevices. *ACS Nano* 12: 9484–9494.

Marras A.E., Zhou L., Su H.J. & Castro C.E. 2015. Programmable motion of DNA origami mechanisms. *Proceedings of the National Academy of Sciences of the United States of America* 112: 713–718.

Martin T.G. & Dietz H. 2012. Magnesium-free self-assembly of multi-layer DNA objects. *Nature Communications* 3: 1103.

McGhee J.D. & Hippel P.H. von. 1974. Theoretical aspects of DNA-protein interactions: Co-operative and non-co-operative binding of large ligands to a one-dimensional homogeneous lattice. *Journal of Molecular Biology* 86: 469–489.

Miller H.L., Contera S., Wollman A.J.M., Hirst A., Dunn K.E., Schröter S., O'Connell D. & Leake M.C. 2020. Biophysical characterisation of DNA origami nanostructures reveals inaccessibility to intercalation binding sites.

Nanotechnology 31: 235605.
Mukhortava A. & Schlierf M. 2016. Efficient Formation of Site-Specific Protein-DNA Hybrids Using Copper-Free Click Chemistry. *Bioconjugate Chemistry* 27: 1559–1563.
Nelson D.L. & Cox M.M. 2008. *Lehninger Principles of Biochemistry (5th edition)*. W. H. Freeman and Company (New York).
Nesterova I. V. & Nesterov E.E. 2014. Rational design of highly responsive pH sensors based on DNA i-Motif. *Journal of the American Chemical Society* 136: 8843–8846.
Ni X., Castanares M., Mukherjee A. & Lupold S.E. 2011. Nucleic Acid Aptamers: Clinical Applications and Promising New Horizons. *Current Medicinal Chemistry* 18: 4206–4214.
Nitiss J.L. 2009. Targeting DNA topoisomerase II in cancer chemotherapy. *Nature Reviews Cancer* 9: 338–350.
Noack S., Michael N., Rosen R. & Lamparter T. 2007. Protein conformational changes of Agrobacterium phytochrome Agp1 during chromophore assembly and photoconversion. *Biochemistry* 46: 4164–4176.
Nummelin S., Shen B., Piskunen P., Liu Q., Kostiainen M.A. & Linko V. 2020. Robotic DNA Nanostructures. *ACS Synthetic Biology* 9: 1923–1940.
O'Brien A.M., Ó'Fágáin C., Nielsen P.F. & Welinder K.G. 2001. Location of crosslinks in chemically stabilized horseradish peroxidase: Implications for design of crosslinks. *Biotechnology and Bioengineering* 76: 277–284.
Ora A., Järvihaavisto E., Zhang H., Auvinen H., Santos H.A., Kostiainen M.A. & Linko V. 2016. Cellular delivery of enzyme-loaded DNA origami. *Chemical Communications* 52: 14161–14164.
Orponen P. 2018. Design methods for 3D wireframe DNA nanostructures. *Natural Computing* 17: 147–160.
Ortiz-Lombardia M., Gonzalez A., Eritja R., Aymami J., Azorin F. & Coll M. 1999. Crystal structure of a DNA Holliday junction. *Nature Structural Biology* 6: 913–917.
Pal S., Deng Z., Wang H., Zou S., Liu Y. & Yan H. 2011. DNA directed self-assembly of anisotropic plasmonic nanostructures. *Journal of the American Chemical Society* 133: 17606–17609.
Pan Q., Nie C., Hu Y., Yi J., Liu C., Zhang J., He M., He M., Chen T. & Chu X. 2020. Aptamer-Functionalized DNA Origami for Targeted Codelivery of Antisense Oligonucleotides and Doxorubicin to Enhance Therapy in Drug-Resistant Cancer Cells. *ACS Applied Materials and Interfaces* 12: 400–409.
Pérez-Arnaiz C., Busto N., Leal J.M. & García B. 2014. New insights into the mechanism of the DNA/doxorubicin interaction. *Journal of Physical Chemistry B* 118: 1288–1295.
Perrault S.D. & Shih W.M. 2014. Virus-inspired membrane encapsulation of DNA nanostructures to achieve in vivo stability. *ACS Nano* 8: 5132–5140.
Persi E., Duran-Frigola M., Damaghi M., Roush W.R., Aloy P., Cleveland J.L., Gillies R.J. & Ruppin E. 2018. Systems analysis of intracellular pH vulnerabilities for cancer therapy. *Nature Communications* 9: 2997.
Pfeiffer C., Rehbock C., Hühn D., Carrillo-Carrion C., Aberasturi D.J. De, Merk

V., Barcikowski S. & Parak W.J. 2014. Interaction of colloidal nanoparticles with their local environment: The (ionic) nanoenvironment around nanoparticles is different from bulk and determines the physico-chemical properties of the nanoparticles. *Journal of the Royal Society Interface* 11: 20130931.

Piskunen P., Nummelin S., Shen B., Kostiainen M.A. & Linko V. 2020. Increasing complexity in wireframe DNA nanostructures. *Molecules* 25: 1823.

Pommier Y., Leo E., Zhang H. & Marchand C. 2010. DNA topoisomerases and their poisoning by anticancer and antibacterial drugs. *Chemistry and Biology* 17: 421–433.

Praetorius F., Kick B., Behler K.L., Honemann M.N., Weuster-Botz D. & Dietz H. 2017. Biotechnological mass production of DNA origami. *Nature* 552: 84–87.

Rahman M.A., Wang P., Zhao Z., Wang D., Nannapaneni S., Zhang C., Chen Z., Griffith C.C., Hurwitz S.J., Chen Z.G., Ke Y. & Shin D.M. 2017. Systemic Delivery of Bc12-Targeting siRNA by DNA Nanoparticles Suppresses Cancer Cell Growth. *Angewandte Chemie - International Edition* 56: 16023–16027.

Ramakrishnan S., Ijäs H., Linko V. & Keller A. 2018. Structural stability of DNA origami nanostructures under application-specific conditions. *Computational and Structural Biotechnology Journal* 16: 342–349.

Ramakrishnan S., Schärfen L., Hunold K., Fricke S., Grundmeier G., Schlierf M., Keller A. & Krainer G. 2019a. Enhancing the stability of DNA origami nanostructures: Staple strand redesign: Versus enzymatic ligation. *Nanoscale* 11: 16270–16276.

Ramakrishnan S., Shen B., Kostiainen M.A., Grundmeier G., Keller A. & Linko V. 2019b. Real-Time Observation of Superstructure-Dependent DNA Origami Digestion by DNase I Using High-Speed Atomic Force Microscopy. *ChemBioChem* 20: 2818–2823.

Rocha M.S. 2010. Revisiting the neighbor exclusion model and its applications. *Biopolymers* 93: 1–7.

Rohs R., Jin X., West S.M., Joshi R., Honig B. & Mann R.S. 2010. Origins of specificity in protein-DNA recognition. *Annual Review of Biochemistry* 79: 233–269.

Roodhuizen J.A.L., Hendrikx P.J.T.M., Hilbers P.A.J., Greef T.F.A. De & Markvoort A.J. 2019. Counterion-Dependent Mechanisms of DNA Origami Nanostructure Stabilization Revealed by Atomistic Molecular Simulation. *ACS Nano* 13: 10798–10809.

Rothemund P.W.K. 2006. Folding DNA to create nanoscale shapes and patterns. *Nature* 440: 297–302.

Rueden C.T., Schindelin J., Hiner M.C., DeZonia B.E., Walter A.E., Arena E.T. & Eliceiri K.W. 2017. ImageJ2: ImageJ for the next generation of scientific image data. *BMC Bioinformatics* 18: 529.

Ryssy J., Natarajan A.K., Wang J., Lehtonen A.J., Nguyen M.-K., Klajn R. & Kuzyk A. 2020. Light-Responsive Dynamic DNA-Origami-Based Plasmonic Assemblies. *Angewandte Chemie International Edition*.

Sahoo H. 2011. Förster resonance energy transfer - A spectroscopic nanoruler:

Principle and applications. *Journal of Photochemistry and Photobiology C: Photochemistry Reviews* 12: 20–30.

Sannohe Y., Endo M., Katsuda Y., Hidaka K. & Sugiyama H. 2010. Visualization of dynamic conformational switching of the G-quadruplex in a DNA nanostructure. *Journal of the American Chemical Society* 132: 16311–16313.

Scheckenbach M., Bauer J., Zähringer J., Selbach F. & Tinnefeld P. 2020. DNA origami nanorulers and emerging reference structures. *APL Materials* 8: 110902.

Schüller V.J., Heidegger S., Sandholzer N., Nickels P.C., Suhartha N.A., Endres S., Bourquin C. & Liedl T. 2011. Cellular immunostimulation by CpG-sequence-coated DNA origami structures. *ACS Nano* 5: 9696–9702.

Seeman N.C. 1982. Nucleic acid junctions and lattices. *Journal of Theoretical Biology* 99: 237–247.

Seeman N.C. 2010. Nanomaterials based on DNA. *Annual Review of Biochemistry* 79: 65–87.

Shaw A., Hoffecker I.T., Smyrlaki I., Rosa J., Grevys A., Bratlie D., Sandlie I., Michaelsen T.E., Andersen J.T. & Högberg B. 2019. Binding to nanopatterned antigens is dominated by the spatial tolerance of antibodies. *Nature Nanotechnology* 14: 184–190.

Shen B., Linko V., Tapio K., Pikker S., Lemma T., Gopinath A., Gothelf K. V., Kostiainen M.A. & Toppari J.J. 2018. Plasmonic nanostructures through DNA-assisted lithography. *Science Advances* 4: eaap8978.

Shi Z. & Arya G. 2020. Free energy landscape of salt-Actuated reconfigurable DNA nanodevices. *Nucleic Acids Research* 48: 548–560.

Silva E.F., Bazoni R.F., Ramos E.B. & Rocha M.S. 2017. DNA-doxorubicin interaction: New insights and peculiarities. *Biopolymers* 107: e22998.

Song L., Jiang Q., Liu J., Li N., Liu Q., Dai L., Gao Y., Liu W., Liu D. & Ding B. 2017a. DNA origami/gold nanorod hybrid nanostructures for the circumvention of drug resistance. *Nanoscale* 9: 7750–7754.

Song J., Li Z., Wang P., Meyer T., Mao C. & Ke Y. 2017b. Reconfiguration of DNA molecular arrays driven by information relay. *Science* 357: eaan3377.

Stahl E., Martin T.G., Praetorius F. & Dietz H. 2014. Facile and scalable preparation of pure and dense DNA origami solutions. *Angewandte Chemie - International Edition* 53: 12735–12740.

Stearns L.A., Chhabra R., Sharma J., Liu Y., Petuskey W.T., Yan H. & Chaput J.C. 2009. Template-directed nucleation and growth of inorganic nanoparticles on DNA scaffolds. *Angewandte Chemie - International Edition* 48: 8494–8496.

Stein I.H., Schüller V., Böhm P., Tinnefeld P. & Liedl T. 2011. Single-molecule FRET ruler based on rigid DNA origami blocks. *ChemPhysChem* 12: 689–695.

Stephanopoulos N. 2020. Hybrid Nanostructures from the Self-Assembly of Proteins and DNA. *Chem* 6: 364–405.

Strekowski L. & Wilson B. 2007. Noncovalent interactions with DNA: An overview. *Mutation Research - Fundamental and Molecular Mechanisms of Mutagenesis* 623: 3–13.

Suck D. 1994. DNA recognition by DNase I. *Journal of Molecular Recognition* 7: 65–70.

Sun T., Zhang Y.S., Pang B., Hyun D.C., Yang M. & Xia Y. 2014. Engineered nanoparticles for drug delivery in cancer therapy. *Angewandte Chemie - International Edition* 53: 12320–12364.

Surana S., Shenoy A.R. & Krishnan Y. 2015. Designing DNA nanodevices for compatibility with the immune system of higher organisms. *Nature Nanotechnology* 10: 741–747.

Tabernero L., Verdaguer N., Coll M., Fita I., Marel G.A. van der, Boom J.H. van, Rich A. & Aymamí J. 1993. Molecular Structure of the A-Tract DNA Dodecamer d(CGCAAATTTGCG) Complexed with the Minor Groove Binding Drug Netropsin. *Biochemistry* 32: 8403–8410.

Thordarson P. 2011. Determining association constants from titration experiments in supramolecular chemistry. *Chemical Society Reviews* 40: 1305–1323.

Thorn C.F., Oshiro C., Marsh S., Hernandez-Boussard T., McLeod H., Klein T.E. & Altman R.B. 2011. Doxorubicin pathways: Pharmacodynamics and adverse effects. *Pharmacogenetics and Genomics* 21: 440–446.

Tohgasaki T., Shitomi Y., Feng Y., Honna S., Emura T., Hidaka K., Sugiyama H. & Endo M. 2019. A Photocaged DNA Nanocapsule for Controlled Unlocking and Opening inside the Cell. *Bioconjugate Chemistry* 30: 1860–1863.

Trads J.B., Tørring T. & Gothelf K. V. 2017. Site-Selective Conjugation of Native Proteins with DNA. *Accounts of Chemical Research* 50: 1367–1374.

Urban M.J., Both S., Zhou C., Kuzyk A., Lindfors K., Weiss T. & Liu N. 2018. Gold nanocrystal-mediated sliding of doublet DNA origami filaments. *Nature Communications* 9: 1454.

Valero J., Pal N., Dhakal S., Walter N.G. & Famulok M. 2018. A bio-hybrid DNA rotor-stator nanoengine that moves along predefined tracks. *Nature Nanotechnology* 13: 496–503.

Vogele K., List J., Pardatscher G., Holland N.B., Simmel F.C. & Pirzer T. 2016. Self-Assembled Active Plasmonic Waveguide with a Peptide-Based Thermomechanical Switch. *ACS Nano* 10: 11377–11384.

Wagenbauer K.F., Sigl C. & Dietz H. 2017. Gigadalton-scale shape-programmable DNA assemblies. *Nature* 552: 78–83.

Wang S.T., Gray M.A., Xuan S., Lin Y., Byrnes J., Nguyen A.I., Todorova N., Stevens M.M., Bertozzi C.R., Zuckermann R.N. & Gang O. 2020a. DNA origami protection and molecular interfacing through engineered sequence-defined peptoids. *Proceedings of the National Academy of Sciences of the United States of America* 117: 6339–6348.

Wang R., Nuckolls C. & Wind S.J. 2012. Assembly of heterogeneous functional nanomaterials on DNA origami scaffolds. *Angewandte Chemie - International Edition* 51: 11325–11327.

Wang P., Rahman M.A., Zhao Z., Weiss K., Zhang C., Chen Z., Hurwitz S.J., Chen Z.G., Shin D.M. & Ke Y. 2018. Visualization of the Cellular Uptake and Trafficking of DNA Origami Nanostructures in Cancer Cells. *Journal of the American Chemical Society* 140: 2478–2484.

Wang Z., Song L., Liu Q., Tian R., Shang Y., Liu F., Liu S., Zhao S., Han Z., Sun J., Jiang Q. & Ding B. 2020b. A Tubular DNA Nanodevice as a siRNA/Chemo-

Drug Co-delivery Vehicle for Combined Cancer Therapy. *Angewandte Chemie - International Edition*.

Wang S., Zhou Z., Ma N., Yang S., Li K., Teng C., Ke Y. & Tian Y. 2020c. DNA Origami-Enabled Biosensors. *Sensors (Basel, Switzerland)* 20: 6899.

Weston S.A., Lahm A. & Suck D. 1992. X-ray structure of the DNase I-d(GGTATACC)2 complex at 2·3 Å resolution. *Journal of Molecular Biology* 226: 1237–1256.

White K.A., Grillo-Hill B.K. & Barber D.L. 2017. Cancer cell behaviors mediated by dysregulated pH dynamics at a glance. *Journal of Cell Science* 130: 663–669.

Willner E.M., Kamada Y., Suzuki Y., Emura T., Hidaka K., Dietz H., Sugiyama H. & Endo M. 2017. Single-Molecule Observation of the Photoregulated Conformational Dynamics of DNA Origami Nanoscissors. *Angewandte Chemie - International Edition* 56: 15324–15328.

Wilson W.D., Tanious F.A., Barton H.J., Strekowski L., Boykin D.W. & Jones R.L. 1989. Binding of 4′, 6-Diamidino-2-phenylindole (DAPI) to GC and Mixed Sequences in DNA: Intercalation of a Classical Groove-Binding Molecule. *Journal of the American Chemical Society* 111: 5008–5010.

Wolfbeis O.S. & Leiner M. 1985. Mapping of the total fluorescence of human blood serum as a new method for its characterization. *Analytica Chimica Acta* 167: 203–215.

Wu J. & Chen Z.J. 2014. Innate Immune Sensing and Signaling of Cytosolic Nucleic Acids. *Annual Review of Immunology* 32: 461–488.

Wu N. & Willner I. 2016. PH-Stimulated Reconfiguration and Structural Isomerization of Origami Dimer and Trimer Systems. *Nano Letters* 16: 6650–6655.

Zadegan R.M., Lindau E.G., Klein W.P., Green C., Graugnard E., Yurke B., Kuang W. & Hughes W.L. 2017. Twisting of DNA Origami from Intercalators. *Scientific Reports* 7: 7382.

Zadeh J.N., Steenberg C.D., Bois J.S., Wolfe B.R., Pierce M.B., Khan A.R., Dirks R.M. & Pierce N.A. 2011. NUPACK: Analysis and design of nucleic acid systems. *Journal of Computational Chemistry* 32: 170–173.

Zeng Y., Liu J., Yang S., Liu W., Xu L. & Wang R. 2018. Time-lapse live cell imaging to monitor doxorubicin release from DNA origami nanostructures. *Journal of Materials Chemistry B* 6: 1605–1612.

Zhang Q., Jiang Q., Li N., Dai L., Liu Q., Song L., Wang J., Li Y., Tian J., Ding B. & Du Y. 2014. DNA origami as an in vivo drug delivery vehicle for cancer therapy. *ACS Nano* 8: 6633–6643.

Zhang P., Liu X., Liu P., Wang F., Ariyama H., Ando T., Lin J., Wang L., Hu J., Li B. & Fan C. 2020. Capturing transient antibody conformations with DNA origami epitopes. *Nature Communications* 11: 1–9.

Zhang D.Y. & Seelig G. 2011. Dynamic DNA nanotechnology using strand-displacement reactions. *Nature Chemistry* 3: 103–113.

Zhang Y., Tsitkov S. & Hess H. 2016. Proximity does not contribute to activity enhancement in the glucose oxidase-horseradish peroxidase cascade. *Nature Communications* 7: 13982.

Zhao S., Duan F., Liu S., Wu T., Shang Y., Tian R., Liu J., Wang Z.G., Jiang Q. &

Ding B. 2019. Efficient Intracellular Delivery of RNase A Using DNA Origami Carriers. *ACS Applied Materials and Interfaces* 11: 11112–11118.

Zhao Z., Fu J., Dhakal S., Johnson-Buck A., Liu M., Zhang T., Woodbury N.W., Liu Y., Walter N.G. & Yan H. 2016. Nanocaged enzymes with enhanced catalytic activity and increased stability against protease digestion. *Nature Communications* 7: 10619.

Zhao Y.X., Shaw A., Zeng X., Benson E., Nyström A.M. & Högberg B. 2012. DNA origami delivery system for cancer therapy with tunable release properties. *ACS Nano* 6: 8684–8691.

Zhuang X., Ma X., Xue X., Jiang Q., Song L., Dai L., Zhang C., Jin S., Yang K., Ding B., Wang P.C. & Liang X.J. 2016. A Photosensitizer-Loaded DNA Origami Nanosystem for Photodynamic Therapy. *ACS Nano* 10: 3486–3495.

ORIGINAL PAPERS

I

DYNAMIC DNA ORIGAMI DEVICES: FROM STRAND-DISPLACEMENT REACTIONS TO EXTERNAL STIMULI-RESPONSIVE SYSTEMS

by

Ijäs H., Nummelin S., Shen B., Kostiainen M.A. & Linko V. 2018

International Journal of Molecular Sciences 19: 2114.

DOI:10.3390/ijms19072114

International Journal of
Molecular Sciences

MDPI

Review

Dynamic DNA Origami Devices: from Strand-Displacement Reactions to External-Stimuli Responsive Systems

Heini Ijäs [1,2], Sami Nummelin [1], Boxuan Shen [1], Mauri A. Kostiainen [1,3] and Veikko Linko [1,*]

1 Biohybrid Materials, Department of Bioproducts and Biosystems, Aalto University, P.O. Box 16100, 00076 Aalto, Finland; heini.ijas@aalto.fi (H.I.); sami.nummelin@aalto.fi (S.N.); boxuan.shen@aalto.fi (B.S.); mauri.kostiainen@aalto.fi (M.A.K.)
2 Department of Biological and Environmental Science, University of Jyväskylä, P.O. Box 35, 40014 Jyväskylä, Finland
3 HYBER Center of Excellence, Department of Applied Physics, Aalto University, 00076 Aalto, Finland
* Correspondence: veikko.linko@aalto.fi; Tel.: +358-45-673-9997

Received: 30 June 2018; Accepted: 18 July 2018; Published: 20 July 2018

Abstract: DNA nanotechnology provides an excellent foundation for diverse nanoscale structures that can be used in various bioapplications and materials research. Among all existing DNA assembly techniques, DNA origami proves to be the most robust one for creating custom nanoshapes. Since its invention in 2006, building from the bottom up using DNA advanced drastically, and therefore, more and more complex DNA-based systems became accessible. So far, the vast majority of the demonstrated DNA origami frameworks are static by nature; however, there also exist dynamic DNA origami devices that are increasingly coming into view. In this review, we discuss DNA origami nanostructures that exhibit controlled translational or rotational movement when triggered by predefined DNA sequences, various molecular interactions, and/or external stimuli such as light, pH, temperature, and electromagnetic fields. The rapid evolution of such dynamic DNA origami tools will undoubtedly have a significant impact on molecular-scale precision measurements, targeted drug delivery and diagnostics; however, they can also play a role in the development of optical/plasmonic sensors, nanophotonic devices, and nanorobotics for numerous different tasks.

Keywords: DNA nanotechnology; DNA origami; self-assembly; molecular devices; mechanical movement; robotics

1. Introduction

In his idiosyncratic talk "There's plenty of room at the bottom" in 1959, Richard Feynman envisioned that it should be possible to build nanoscale machines that could carry out chemical synthesis through mechanical movement [1]. He also presented Albert R. Hibbs's idea of miniature surgical robots that could perform predefined tasks in the human body [1]. Now, almost 60 years later, thanks to modern biology, we know that the human body is actually a large-scale biofactory that is comprised of a great number of tiny and accurate nanomachines, such as motor proteins and enzymes, as a result of billions of years of evolutionary processes on Earth. However, we are not merely products of those natural nanomachines or simply hosts to them, but we are also able to look at them with our state-of-the-art microscopes, and even more interestingly, to create artificial and completely new nanodevices. In other words, we are putting Feynman's idea into practice.

At the time of Feynman's talk, the structure of double-stranded DNA (dsDNA) was resolved just six years before [2]. However, it was known that DNA carries genetic information and how

DNA strands hybridize to each other following Watson–Crick base-pairing rules [2]. Nevertheless, it took almost 30 years before the potential of DNA molecules as programmable construction materials [3]—and not merely as the storage of genetic information—was proposed by Nadrian Seeman [4]. Since then, the field of structural DNA nanotechnology constantly grew and it started to truly flourish during the last decade [5,6]. Today, researchers routinely use DNA to build not only static two- and three-dimensional (2D and 3D) nanostructures via self-assembly [4–11], but also dynamic and precise nanodevices and robots [12,13] that Feynman could hardly imagine. As a matter of fact, Feynman's statement "Biology is not simply writing information; it is doing something about it" [1] is literally realized in the case of DNA molecules and DNA nanotechnology.

Although structural DNA nanotechnology constantly evolved during the last 35 years, starting from Seeman's vision of using DNA junctions and lattices to build DNA crystals [6,7], the recently witnessed big boom in the field started from the invention of 2D DNA origami in 2006, a technique developed by Paul Rothemund [14]. DNA origami is based on a long single-stranded DNA (ssDNA) scaffold that is folded into a desired nanoscale shape with the help of dozens of short oligonucleotides [14]. Since 2006, the method was extended to 3D shapes [15,16], designs with curvatures and twists [17,18], wireframe-based and automatically designed structures [19–21], and assemblies that can reach micrometer or gigadalton scales [22,23]. Inspired by DNA origami, scaffoldless methods that are based on brick-like assemblies were also developed [24,25].

The benefits of using the DNA origami technique are not only the virtues of custom nanoscale shapes, but also extremely accurate molecular-scale positioning and patterning. These features can be used in controlling chemical reactions [26–28], creating tunable plasmonic systems [29,30], and building carriers for drug delivery [12,31–35]. Precise and addressable DNA origami can also be used as rulers and in optical super-resolution imaging [36], forming crystals and nanoparticle superlattices [37,38], and creating inorganic nanostructures [39]. Recently, it was also observed that DNA origami structures are more resilient than previously understood [40], and that the mass production of DNA origami is affordable [41]. Therefore, highly versatile and modular DNA origami is about to become a standard molecular-scale tool in numerous laboratories.

In this review, we discuss DNA origami nanostructures that can be used as dynamic and controllable nanodevices, such as walking robots [42], logic-gated nanopills [12], and rotors [43] (see Scheme 1). The development of such molecular machines is based on tailoring the DNA sequences in such a way that the structures firstly self-assemble into desired shapes, and are thereby able to perform predefined tasks via translational or rotational movement. In this respect, dynamic DNA origami devices can be considered analogous to protein shapes and functions that are encoded in the sequences of the polypeptide and nucleic-acid molecules [8]. Importantly, DNA origami provides a straightforward route from sequence design to actual shapes, unlike protein synthesis. However, it is noteworthy that de novo protein design allows the synthesis of completely new proteins with tailored functions [44]. A combination of these two techniques would have potential to revolutionize biomedicine and molecular nanotechnology.

In many dynamic systems, the ability to simulate molecular motion and fluctuations becomes increasingly important. There are ways to predict DNA origami dynamics based on rigid-beam models (CanDo) [45,46], atomistic molecular-dynamics simulation [47], and coarse-grained models (oxDNA) [48,49]. Additionally, mass-weighted chemical elastic network models (MWCENM) and symmetry-constrained elastic network models (SCENM) [50] can be used to estimate the structural fluctuations.

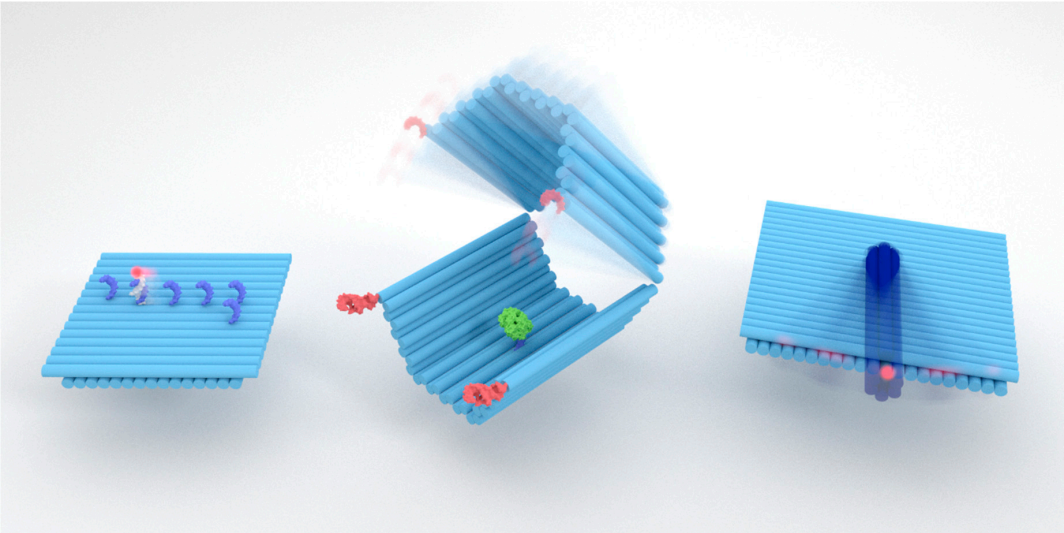

Scheme 1. Artistic rendering of selected examples of dynamic DNA origami devices: (**Left**) a cargo-sorting robot walking on a DNA origami-templated track [42]; (**Middle**) a logic-gated DNA origami "nanopill" that selectively displays the loaded cargo [12]; (**Right**) a DNA origami robotic arm that performs rotational movement under an electric field [43].

Although the focus of this review is on the DNA origami-based devices, it is noteworthy to mention that diverse DNA-based molecular machines were already introduced years before DNA origami. Famous examples include a machine that performs movement based on a DNA conformation change (DNA switches between B- and Z-forms) [51], and DNA tweezers that can be fueled by additional DNA strands to switch the configuration between open and closed states [52]. By taking advantage of simple DNA nanostructures, it is possible to form nanomechanical devices with different rotational or translational states [53,54], and to control their movement using, e.g., RNA strands instead of DNA [55]. Later on, DNA nanostructure-based tweezers [56,57], whose arms can be further equipped with enzymes to facilitate control over chemical reactions were proposed. There are also numerous DNA-based walkers that utilize strand-displacement reactions and employ so-called toehold exchanges. Toeholds are short ssDNA overhangs at the end of dsDNA molecules that firstly bind to reactant ssDNA, i.e., they serve as "docking sites" that initiate the strand-displacement reactions. Such devices were extensively reviewed in References [58,59].

Here, we review dynamic DNA origami devices by dividing the discussion into sections using the criteria of interaction type. In Section 2, we firstly discuss DNA origami assemblies with DNA–DNA interactions, i.e., the mechanical design of DNA origami and the systems that take advantage of strand-displacement reactions, base-stacking interactions, or transient DNA binding. Section 3 is devoted to dynamic DNA origami devices that move due to some other molecular interaction. In other words, the molecular interaction produces a desired movement, or alternatively, the interaction can be characterized using the device as a measurement tool. Section 4 reviews the DNA origami movement due to external stimuli such as light, temperature, pH, and electromagnetic fields, and the devices that can be utilized to probe multiple interactions. Section 5 concludes the discussion and gives future perspectives in this immensely growing field.

2. DNA–DNA Interactions: Strand Displacement, Base Stacking and Transient Binding

Here, dynamic DNA origami systems based on DNA–DNA interactions are introduced. This section covers devices whose movements rely on base-pairing (strand-displacement) systems that exhibit dynamic behavior based on DNA base-stacking interactions and tight-fitting DNA components.

As early as 2009, Andersen et al. [15] fabricated a hollow DNA origami "cuboid" from six 2D origami sheets. The 3D box contained a controllable lid functionalized with a "lock–key system" comprised of dsDNAs with sticky-end extensions. Fluorescent dyes, Cy3 and Cy5, embedded in the opposite faces of the box, facilitated the detection of irreversible lid-opening through a strand-displacement reaction using Förster resonance energy transfer (FRET). Three years later, Zadegan et al. [60] demonstrated reversible opening and closing of a lid in a hollow 3D DNA origami box as a response to supplied opening and closing ssDNA keys. In 2017, Grossi et al. [61] constructed a DNA nanovault with a similar reversible opening/closing mechanism (Figure 1a). They were able to encapsulate a single enzyme inside the vault and demonstrate that closing the nanovault resulted in a notable reduction in enzyme activity. Another type of a dynamic DNA origami device was introduced by Tomaru et al. [62], who created a DNA origami comprised of a "rotor" and a "base" component, connected with a short scaffold segment. They demonstrated a step-wise rotation of a rotor on top of the base through sequential strand-displacement reactions.

Recently, Selnihhin et al. [63] applied a toehold-mediated strand-displacement-based lock–key system in a dynamic DNA origami beacon designed for high-sensitivity biosensing. By functionalizing the device with high numbers of fluorophores interacting via FRET in a closed-state device, they could demonstrate that opening the devices with target DNA keys caused a detectable decrease in FRET efficiency, even at DNA concentrations as low as 100 pM.

To build dynamic devices, it is essential to understand the mechanical behavior of DNA origami and their responses under external physical forces. Numerous studies exploited these aspects of DNA nanostructures [64]; for example, Zhou et al. [65] designed and characterized a tunable DNA origami structure with a compliant part able to bend into different angles under the tension caused by ssDNAs with various lengths. Later, they also studied a four-bar bistable mechanical system with a designed energy landscape, and showed that the conformational dynamics of the device could be controlled via strand displacement [66]. In 2015, Marras et al. [67] demonstrated mechanical designs of DNA origami inspired by macroscopic devices, including a hinge (rotational motion), a slider joint (translational motion), and a complex crank–slider mechanism integrated from the former two (see Figure 1b). In addition, a Bennett linkage which could be actuated via strand displacement was also characterized.

As another class of DNA–DNA interaction, a number of non-autonomous, autonomous, and directed DNA walkers were introduced and analyzed both experimentally and theoretically [58,59,68]. By taking advantage of the DNA origami addressability and programmability, the environment where the walker or robot is moving can be defined and precisely tuned. One example of such a system was presented by Lund et al. [69], where "molecular spiders" made of a streptavidin body equipped with three catalytic deoxyribozyme legs were set to autonomously move along the predefined path on top of a DNA origami template. A very recent and sophisticated example of DNA-assembled robotics on a DNA origami platform was created by Thubagere et al. [42]. They developed an algorithm for sorting two types of cargo and their destinations on a DNA origami platform (Figure 1c). The DNA robot constructed from three functional domains was able to pick up the cargo and release it at the desired location. The movement of the robot was solely based on random walk, and thus, it did not require any additional energy to operate. The robot performed on average 300 steps during the cargo sorting, which is a huge improvement (one to two magnitudes) on previously reported DNA walkers that performed tasks while walking.

In 2016, Ke et al. [70] presented a nanoactuator design consisting of four DNA origami beams linked into a rhombus shape via flexible ssDNA joints (Figure 1d). The opening angle of the device was controlled through ssDNA lock strands of different lengths. Attaching two halves of enhanced GFP (eGFP) to the device and closing the device with short locking strands was shown to bring the halves together and restore fluorescence of the protein. A similar working principle was amplified into a large-scale reconfiguration of a 2D origami lattice by Choi et al. [71]. They built a DNA accordion rack from long DNA beams connected via multiple flexible joints. The aspect ratio of the whole lattice could be controlled by adding DNA lock strands at selected positions in the structure. By applying

toehold-mediated strand-displacement processes, multiple rounds of conformational switching could be demonstrated. In addition to using strand displacement, the needed DNA trigger can also be grown using DNA polymerase, as described by Agarwal et al. [72]. They demonstrated the straightening and rigidifying of a deformed wireframe DNA origami having ssDNA gaps by growing a complementary gap-filling strand on site by DNA polymerase.

Base stacking of blunt-ended dsDNA segments can form strong attractive interactions between different DNA nanostructures, or within a single device [73,74]. Gerling et al. [74] showed that transitions between different conformational states in various DNA origami designs could be controlled by adjusting the strength of base-stacking interactions between shape-complementary parts with cation concentration or temperature. A tweezer-type structure based on the design from Reference [74], and its rapid dynamics triggered by cation concentration change were recently characterized using high-speed atomic force microscopy (AFM) [75] and small-angle X-ray scattering (SAXS) [76]. Base-stacking interactions were also used as a driving force in conveying information in large 2D DNA origami arrays [77]. The system constructed by Song et al. [77] consisted of multiple interconnected trapezoidal "antijunction units". Selected units were firstly locked into a defined conformation through the addition of trigger strands complementary to ssDNA regions at the edges of the units. Neighboring units would then switch into the same conformation, since new base-stacking interactions formed in the process would lower the energy of the system. This was seen to generate a cascade of conformational switching, so that all the units in the system would eventually be found in the same conformational state.

DNA–DNA interactions, including base stacking, can also be used to assemble complex nanomachines from multiple DNA origami elements, as demonstrated by Ketterer et al. [78]. They manufactured a miniature rotary apparatus analogous to F1F0-adenosine triphosphate (ATP) synthase (Figure 1e). The device was constructed from multiple tight-fitting DNA origami components by guiding the self-assembly with specific base-stacking interactions or DNA hybridization events. Based on single-particle fluorescence microscopy recordings, the devices were shown to exhibit random Brownian rotary motion. Controlling the movement of such devices with external triggers could lead to the realization of intricate DNA-based nanomachines.

Recently, dynamic DNA devices were combined with plasmonic systems, whose optical responses are extremely sensitive to the relative positions and orientations of the components. Kuzyk et al. [79] assembled a metamolecule from two gold nanorods (AuNRs) and two interconnected DNA origami beams. The origami beams were connected via a single Holliday junction in the middle, and ssDNA at the ends of the beams were used in strand displacement to switch the structure between a closed state and an open state. By switching the origami, the relative angle between the two AuNRs was altered, which resulted in a change in the circular dichroism (CD) signal (see Section 4 for similar systems with other stimuli). In addition to the dynamic DNA origami device, oligonucleotide-functionalized AuNR could also walk on a static origami via strand displacement [80].

Although not being an actual device, it is worth mentioning that the dynamic interaction between short oligonucleotides has promising applications in super-resolution imaging. The so-called transient binding describes a temporary binding of complementary DNA strands at a temperature close to the melting point of oligonucleotides with specific sequences and lengths. DNA origami with docking strands, which allow the transient binding of dye-labeled oligonucleotides, were used in DNA point accumulation for imaging in nanoscale topography (DNA-PAINT) in super-resolution microscopy [36,81,82] (see Figure 1f). Furthermore, super-resolution imaging of whole cells was recently realized by combining DNA-PAINT with spinning-disc confocal microscopy [83].

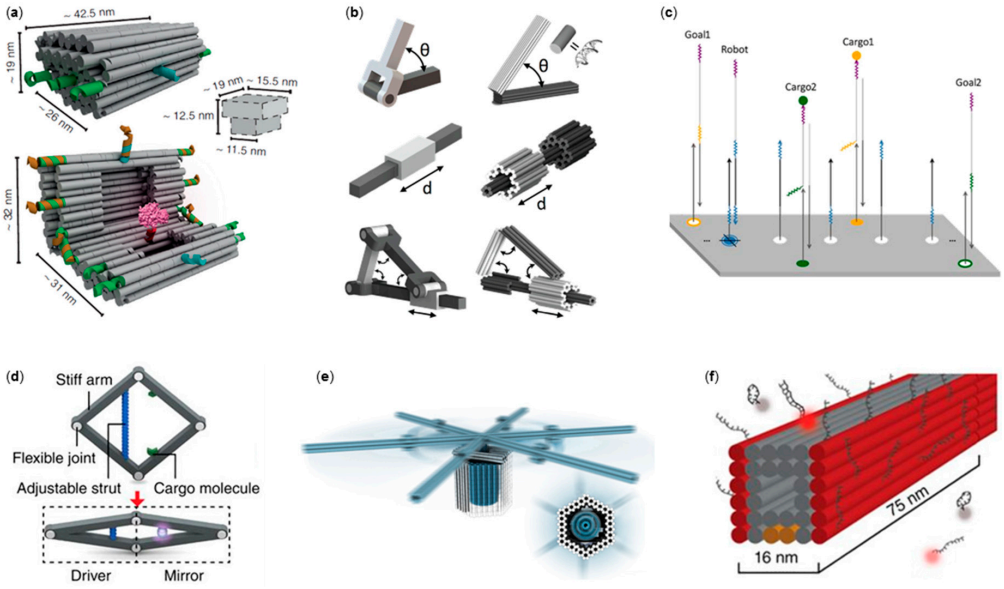

Figure 1. DNA origami mechanics via DNA–DNA interaction. (**a**) A DNA nanovault that displays cargo when opened via strand displacement [61]; (**b**) DNA origami nanomechanics [67]; (**c**) A robot that picks up cargo and delivers it to a goal on top of a DNA origami [42]; (**d**) A DNA origami actuator; movement on the left (driver) side is mirrored to the right side [70] (**e**) A DNA origami rotary apparatus constructed from tight-fitting components [78]; (**f**) Super-resolution imaging with DNA origami by taking advantage of transient DNA binding [81] (**a**) is reproduced with permission from the authors of [61], published by Nature Publishing Group, 2017; (**b**) is reproduced with permission from the authors of [67], copyright National Academy of Sciences 2015; (**c**) is reproduced with permission from the authors of [42], copyright The American Association for the Advancement of Science, 2017; (**d**) is reproduced with permission from the authors of [70], published by Nature Publishing Group, 2016; (**e**) is reproduced with permission from the authors of [78], published by The American Association for the Advancement of Science, 2016; (**f**) is reproduced with permission from the authors of [81], copyright Nature Publishing Group, 2014.

3. DNA Origami Devices with Molecular Interactions

In this section, DNA devices with dynamic properties mediated by molecular interactions (other than DNA–DNA) between the device and other molecules in the solution are discussed. The scale of the dynamic devices ranges from tools designed for measuring or detecting a specific molecular interaction to aptamer-functionalized objects for nanorobotics, computing, and drug delivery.

An early example of dynamic DNA origami devices used in molecular detection is the single-molecule beacons presented by Kuzuya et al. in 2011 [84] (Figure 2a). These "DNA origami pliers" or "DNA origami forceps" consist of two rigid beams connected via a flexible DNA crossover region, which allows the arms to rotate relative to each other. When a target such as protein, metal ion, or human microRNA (miRNA) binds to both arms of the device, the arms are locked into a parallel orientation. Thus, single-molecule binding events are amplified into a major conformational change that can be detected using transmission electron microscopy (TEM) or AFM.

Other neat examples showing the potential of DNA origami-based measurement tools are the various studies carried out with DNA origami devices and nucleosomes [85–87]. Funke et al. [85] and Le et al. [86] both introduced measurement devices with similar hinge-like designs, where two DNA origami arms were joined together at one end via a flexible ssDNA hinge (Figure 2b). The system presented by Funke et al. was initially introduced as a static tool for placing molecules at set distances with extreme precision [88]. In the nucleosome studies, the molecular interaction under interest changed the opening angle of the device, which could then be used as a measure of the interaction

strength. The device was used to study both nucleosome unwrapping at different ionic strengths [86] and the strength of attractive interactions between two nucleosomes [85]. Le et al. [87] used their device for probing various properties of nucleosome–DNA interaction, such as nucleosomal end-to-end distance, nucleosome conformation, and nucleosome stability.

The previous examples of molecular measurement devices all share a relatively similar working principle: molecular binding or interaction under interest converts the device into a discrete, relatively immobile orientation, which is then characterized. In contrast to this, Hudoba et al. [89] measured compressive depletion forces in a solution with a dynamic device that constantly fluctuated between an open (uncompressed) and a closed (compressed) state. Increased depletion forces caused by molecular crowding agents, particularly by poly(ethylene-glycol) (PEG), were observed to shift the dynamics of the device more toward the closed state.

DNA origami devices with specific interactions with other biomolecules of interest can be constructed with the help of aptamers. Aptamers are oligonucleotides which bind a specific target molecule with high affinity. One type of dynamic aptamer-functionalized system is a container that is held closed by the aptamer regions hybridized to complementary DNA strands [12,90]. The container is released into an open state when the aptamers come in contact and bind to their target molecule, which creates an intriguing potential to use these types of DNA devices as specifically targeted drug-delivery vehicles.

A famous example of an aptamer-functionalized DNA origami container is a logic-gated nanorobot introduced by Douglas et al. [12] (Figure 2c). The robots were equipped with different combinations of aptamers. The robot held in a closed state would open and release its cargo only when two different triggers were simultaneously encountered, thus creating a logical AND-gate. In a later study, Amir et al. [91] developed the idea of recreating logical functions and performing molecular computing using DNA nanorobots even further. When aptamer-functionalized robots were mixed in defined molar ratios with robots that could either activate or deactivate the original robots via DNA–DNA interactions, the robot mixtures could emulate a variety of logical functions and perform rudimentary computing inside living cockroaches. Recently, it was demonstrated that a mixture of three interacting robots (similar to those in Reference [91]) could behave according to Isaac Asimov's three laws of robotics [92,93]. With these logic-gated DNA nanorobots and a microRNA molecule (a human miR-16 analog) as a damage signal of the system, the authors were able to recreate Isaac Asimov's famous "Runaround" scenario (dynamics between robot populations), using approximately 100 billion robots [92].

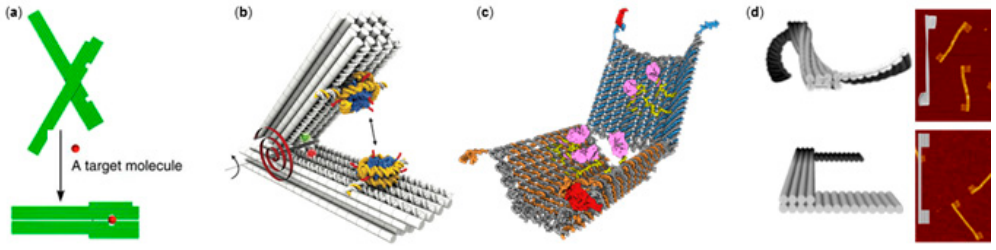

Figure 2. DNA origami devices with molecular interactions. (**a**) DNA origami pliers or forceps that exhibit conformational change upon a target molecule binding [84]; (**b**) A DNA origami measurement device equipped by nucleosomes to probe nucleosome–nucleosome interaction [85]; (**c**) A logic-gated nanorobot that displays cargo when specific antigens bind to aptamer-encoded DNA locks [12]; (**d**) DNA origami twisting and rotation through the application of DNA intercalating molecules [94]; (**a**) is reproduced with permission from the authors of [84], published by Nature Publishing Group, 2011; (**b**) is reproduced with permission from the authors of [85], published by The American Association for the Advancement of Science, 2017; (**c**) is reproduced with permission from the authors of [12], copyright The American Association for the Advancement of Science, 2012; (**d**) is reproduced with permission from the authors of [94], copyright American Chemical Society, 2016.

Recently, the in vivo therapeutic potential of aptamer-functionalized DNA origami nanorobots was shown by Li et al. [90], who designed a tubular DNA origami device by rolling up 2D origami sheet with the help of nucleolin-binding aptamers. The devices were shown to unroll and expose active thrombin in the vicinity of targeted endothelial tumor cells, leading to the inhibition of tumor growth.

Dynamic DNA origami devices are often constructed by linking rigid dsDNA elements with flexible hinges or pivot points formed of ssDNA. Chen et al. [94] studied the possibility of inducing controllable dynamic behavior in structures consisting solely of dsDNA. They utilized DNA-binding adducts, such as ethidium bromide (EtBr), which intercalate between DNA base pairs and cause torsional deformation of dsDNA by unwinding the duplex. By increasing the intercalator concentration in the solution, they demonstrated a significant twist along the length of the whole DNA origami (Figure 2d). The change was shown to be fine-tunable via intercalator concentration, and partially reversible when intercalators were removed via the addition of competing DNA strands.

In addition to moving DNA origami devices, DNA origami itself can act as a template in a highly dynamic assembly. As an intriguing example of such a system, a programmable DNA origami rod was used as a cargo mimic for motor proteins [95]. By controlling the number and types of proteins linked to the cargo mimic, a molecular-scale tug-of-war can be assembled for probing the collective motility of the selected motor proteins. Similarly, dynamic DNA origami diffusion can be assisted by lipid bilayers [96–98]. This type of lipid-assisted diffusion is not fully controllable and does not exactly fall into the category of DNA origami devices; however, interestingly, by employing lipid bilayers, DNA origami can be dynamically arranged into well-defined lattices and other higher-order assemblies. The DNA origami diffusion on top of a lipid layer can be tuned using cholesterol modifications in DNA origami, taking advantage of lipid membrane phases (liquid-disordered or solid-ordered) or by adjusting cation concentration. Therefore, it is likely, that a combination of DNA origami with proteins and lipids may find uses in developing dynamic nanomachines.

4. DNA Origami Devices Triggered by External Stimuli or Multiple Interactions

This section deals with DNA origami nanosystems in which plasmonic effects, or dynamic and controllable movement, e.g., switching or rotation, are induced using a wide spectrum of external stimuli ranging from photoregulation to pH and thermally directed assembly to electromagnetic fields.

Yang et al. [99] were among the first to show UV-controllable DNA origami structures. They demonstrated the assembly and disassembly of predesigned multi-orientational patterns constructed from rigid DNA hexagons with photoresponsive azobenzene-modified oligonucleotides inserted either into one, two, or three edges. Later on, Kohman and Han [100] demonstrated light-triggered reconfiguration of a hollow spherical DNA nanostructure. The sphere was obtained from two hemispheres linked together via a DNA scaffold, and the sphere was sealed from the equator using nine crossover strands modified with photolabile *o*-nitrobenzyl moieties. Irradiation at the specific wavelength of 302 nm resulted in almost quantitative and irreversible cleavage of nitrobenzyl groups, showing tethered hemispheres in TEM images (Figure 3a). A similar light-controlled container was presented by Takenaka et al. with capture and release properties of gold nanoparticles [101].

Kuzyk et al. [102] designed an elegant, light-driven 3D plasmonic DNA origami nanostructure, which was based on reversible cis–trans photoisomerization of azobenzene units. They used a similar design to that described in Section 2; however, the design now contained azobenzene units that were assembled to form a chiral template with an adjustable angle. Optical control between locked (ca. 50° angle) and relaxed (ca. 90° angle) conformational states was obtained using ultraviolet (UV) and visible (Vis) light illumination. The insertion of two AuNRs into the bundles resulted in a tunable plasmonic chiroptical response with large amplitude modulation upon light stimuli. Elaborating on the previous design [102], Kuzyk et al. [103] demonstrated that the plasmonic metamolecules could also be reconfigured via pH changes, which triggered the selective control over the chiral locked or relaxed state (Figure 3b). The DNA "lock" was based on a DNA triplex formation through pH-sensitive and sequence-specific parallel Hoogsteen interactions occurring between an ssDNA and a duplex DNA.

Tuning of the relative contents of TAT/CGC triplets enabled the programmability and discrimination of chiral quasi-enantiomers over a wide pH range. The programmable pH response was also successfully used in the reconfiguration of hexagonal DNA origami dimer and trimer systems using i-motif and Hoogsteen-type interactions [104].

Jiang et al. [105] introduced chiral plasmonic nanostructures by assembling AuNRs into an L-type configuration using two DNA origami triangles as templates. These two templates were specifically connected using a programmable seam that was able to respond to different stimuli. A clear dynamic and reversible plasmonic effect was detected from circular-dichroism spectra when the system was triggered by light (azobenzene-induced G-quadruplex stretching of the seam) or pH changes (folding/unfolding of cytosine-rich i-motifs). The irreversible cleavage of disulfide bonds of the seam via the reduction of glutathione tripeptide and the cleavage of restriction-enzyme-sensitive DNA sequences was also demonstrated.

Turek and co-workers [106] created thermoresponsive DNA origami tweezers in which the actuation was based on reversible temperature-induced coil-to-globule transition of the thermoresponsive polymer poly(*N*-isopropylacrylamide) (PNIPAM). Above the lower critical solution temperature (LCST) of 32 °C, PNIPAM became hydrophobic, causing the folding of both rigid arms (Figure 3c), which was detected as an increased fluorescence of the gold nanoparticle (AuNP) and Cy5 located at the tip of the tweezer in equivalent positions.

Nickels et al. [107] demonstrated that a folded bracket-shape DNA origami functioned as a nanoscopic force clamp for probing multiple different interactions. In this nanodevice, the system of interest (red rectangle, Figure 3d) was linked between two immobile attachment points via entropic ssDNA springs that exert a constant force on a piconewton (pN) scale over time. The force can be tuned by controlling ssDNA strand length, i.e., the entropic force can be increased with reducing nucleotide amount. This leaves ssDNA reservoirs on both sides of the clamp (as seen in Figure 3d). Conformational transitions of the system of interest can be monitored via single-molecule FRET. With this device, switching between two different states of a FRET-pair-equipped four-way Holliday junction was resolved. The authors also demonstrated the sensitivity of the system by characterizing protein-induced DNA bending. Very recently, related to abovementioned force spectroscopy, Dutta and co-workers [108] reported a DNA origami tension probe (DOTP) capable of depicting the traction forces generated by living cells. Various DOTP combinations were employed to map the forces applied by human blood platelets during initial adhesion and activation. Traction forces with piconewton (pN) resolution were measured utilizing tension-to-fluorescence transduction upon unfolding the DNA hairpin that was incorporated into the system.

In addition to the examples above, external electromagnetic fields can be used to manipulate DNA origami movement. Recently, Kopperger and co-workers [43] displayed a truly dynamic DNA origami platform for a nanoscale (up to 400 nm) robotic arm controlled by electric fields. The system was composed of a rigid DNA origami plate equipped with a 25-nm-long six-helix-bundle (6HB) arm attached via ssDNA scaffold crossovers (see the close up in Figure 3e). The flexible joint allowed stochasting switching of the arm due to transient binding, which was detected from FRET signals generated by the donor fluorophore on the tip of the arm and two acceptor dyes mounted on the rectangular base plate. Electrically controlled movement of the robot arm (angular movement up to 25 Hz) was measured when the system was mounted at the center of a cross-shaped electrophoretic chamber with two perpendicular fluid channels. The electric field was applied by two pairs of electrodes inserted in the reservoirs at the ends of the channels. Furthermore, the ability to move inorganic nanoparticles, e.g., AuNRs, using the robotic arm was demonstrated. DNA origami polarizability can also be used to direct and trap DNA origami via dielectrophoresis in a non-uniform electric field, as shown by Kuzyk et al. [109] and Shen et al. [110].

Lauback et al. [111] introduced yet another way of controlling DNA origami movement by employing external magnetic fields. Three quasi-analogous nanostructures, i.e., lever, rotor, and hinge systems (Figure 3f), having diverse angular movement paths, were demonstrated. All constructs were

assembled from three components: a base platform, a stiff 56-helix-bundle rotor arm equipped with a micromagnetic bead on the free rotating end, and a ductile pivot anchoring the rotor to the base platform via biotin–streptavidin affinity. The concept allowed sustained rotational motion (up to 2 Hz), the capability of operating up to 80 pNnm of torque, and a definite control ($\pm 8^{\circ}$ resolution) over the angular conformation.

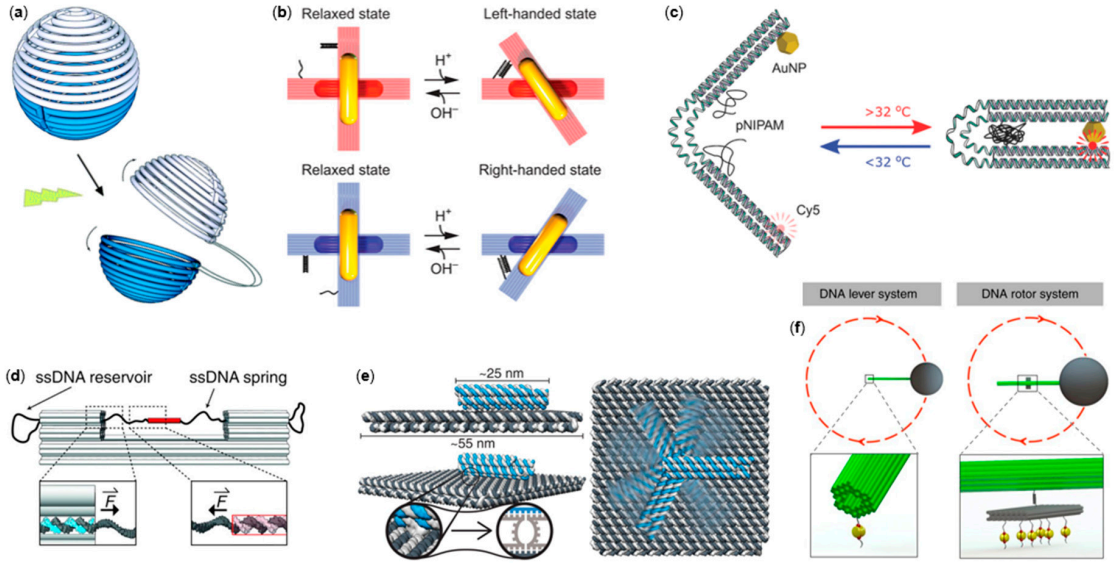

Figure 3. DNA origami movement using stimuli. (**a**) A spherical DNA origami container that can be opened by light [100]; (**b**) Reconfigurable chiral plasmonic metamolecules [103]; (**c**) A thermoresponsive actuator [106]; (**d**) An autonomous nanoscopic force clamp [107]. (**e**) An electric-field-directed robotic arm [43]. (**f**) Magnetic actuators; a lever system and a rotor [111]. (**a**) is reproduced with permission from the authors of [100], copyright The Royal Society of Chemistry, 2015; (**b**) is reproduced with permission from the authors of [103], published by The American Association for the Advancement of Science, 2017; (**c**) is reproduced with permission from the authors of [106], copyright John Wiley and Sons, 2018; (**d**) is reproduced with permission from the authors of [107], copyright The American Association for the Advancement of Science, 2016; (**e**) is reproduced with permission from the authors of [43], copyright The American Association for the Advancement of Science, 2018; (**f**) is reproduced with permission from the authors of [111], published by Nature Publishing Group, 2018.

5. Conclusions and Perspectives

"What are the possibilities of small but movable machines? They may or may not be useful, but they surely would be fun to make," pondered Feynman in his talk [1]. Here, we reviewed DNA origami-based nanomachines that exhibit translational and rotational motion when triggered by various types of stimuli. We also addressed Feynman's question by discussing the usefulness of these nanomachines. The summary of stimuli/interactions, implementations, and possible applications reviewed in this article are listed in Table 1.

Table 1. Summary of the reviewed types of DNA origami motion.

Interaction/Stimulus	Implementation	Application
DNA oligonucleotides	Lock–key systems based on toehold-mediated strand displacement Transient binding	Containers [15,60,61] Biosensing [63] Reconfigurable plasmonics [79] Reconfigurable actuators and lattices [70,71] DNA point accumulation for imaging in nanoscale topography (DNA-PAINT) [81–83] Robotic walkers [42] Rotary devices [62]
Entropic elasticity and steric effects	ssDNA as an entropic spring	Nanomechanical devices [65–67] Force spectrometers [107]
DNA base stacking	Shape-complementary, blunt-ended dsDNA regions	Large-scale assembly [22,73,74]; reconfigurable devices [74]; information relay [77] Rotary devices [78]
Site-specific binding of target molecules	Incorporation of residues with specific chemical reactivity Modified oligonucleotide aptamers	Measurement devices [70,85–89,107] Drug delivery and nanorobotics [12,90–92]
Non-site-specific interactions with other molecules	Mixing DNA origami with crowding agents (e.g., poly(ethylene-glycol)), intercalators, or lipid bilayers	Measurement of molecular crowding [89] Fine-tunable twisting motion [94] Lipid-assisted diffusion [96–98]
Light (UV/Vis)	Incorporation of photoresponsive molecules, e.g., azobenzenes	Photo-controllable assembly and disassembly of nanostructures [104] Photo-cleavable and -controlled containers [100,101] Reconfigurable plasmonics [102]
pH changes, Hoogsteen interactions	pH-sensitive DNA regions, e.g., i-motifs, G-quadruplexes, or triplex-forming sequences	Reconfigurable plasmonics [103,105] Assembly and disassembly of nanostructures [104]
Temperature changes	Thermoresponsive polymers	Thermoresponsive actuation [106]
Electric or magnetic fields	Polarizability of DNA in electric fields Magnetic beads linked to origami	Rotary devices, hinges, and levers [43,111]

Although the future of artificial DNA-based nanodevices seems bright, there are several challenges and problems that should be resolved. One obvious issue in Feynman's surgical nanorobot vision is that the DNA structures might degrade in many biologically relevant conditions [40]. Therefore, plenty of strategies for coating and protecting DNA origami were recently introduced [31,112–116]. However, the challenge is to ensure the functionality of the dynamic devices with such protection systems. Even in the simple static systems, functionality may be suppressed due to the protective coating. For example, an enzyme-loaded DNA origami container [117] coated with synthetic polymers [113] showed significant decrease in enzyme activity compared to a non-coated container. Nevertheless, the field of DNA nanotechnology is already at the state where DNA origami-based dynamic drug-delivery systems are increasingly coming into view [32,33,61,90]. Feynman's postulate regarding mechanical machines is already proved, since we can build accurate DNA origami devices that allow, for instance, molecular-scale precision measurements that are either challenging or not even achievable using other techniques [13]. These devices facilitate the characterization of DNA stacking forces [118], nucleosome–nucleosome and nucleosome–DNA interactions [85–88], and, for example, the probing of protein–DNA interactions [107]. Moreover, employing external stimuli such as electric [43] or magnetic fields [111], it is possible to bridge microscale manipulation to nanoscale devices, and thereby control the movement of these nanomachines with short response times. Further engineering of these programmable and dynamic DNA origami nanomachines will lead this research field from proof-of-principle examples to actual utility.

Author Contributions: The article was written with contributions of all authors. H.I., S.N., and B.S. contributed equally to this work.

Funding: This research was funded by the Academy of Finland (grant numbers 286845 and 308578), Jane and Aatos Erkko Foundation, Sigrid Jusélius Foundation, Magnus Ehrnrooth Foundation, and Emil Aaltonen Foundation.

Acknowledgments: This work was supported through the funding agencies above and it was carried out under the Academy of Finland Centers of Excellence Programme (2014–2019).

Conflicts of Interest: The authors declare no conflict of interest.

References

1. Feynman, R.P. There's plenty of room at the bottom. *Eng. Sci.* **1960**, *23*, 22–36.
2. Watson, J.D.; Crick, F.H.C. Molecular structure of nucleic acids. *Nature* **1953**, *171*, 737–738. [CrossRef] [PubMed]
3. Jones, M.R.; Seeman, N.C.; Mirkin, C.A. Programmable materials and the nature of the DNA bond. *Science* **2015**, *347*, 1260901. [CrossRef] [PubMed]
4. Seeman, N.C. Nucleic acid junctions and lattices. *J. Theor. Struct. Biol.* **1982**, *99*, 237–247. [CrossRef]
5. Wang, P.; Meyer, T.A.; Pan, V.; Dutta, P.K.; Ke, Y. The beauty and utility of DNA origami. *Chem* **2017**, *2*, 359–382. [CrossRef]
6. Nummelin, S.; Kommeri, J.; Kostiainen, M.A.; Linko, V. Evolution of structural DNA nanotechnology. *Adv. Mater.* **2018**, *30*, 1703721. [CrossRef] [PubMed]
7. Seeman, N.C. DNA in a material world. *Nature* **2003**, *421*, 427–431. [CrossRef] [PubMed]
8. Linko, V.; Dietz, H. The enabled state of DNA nanotechnology. *Curr. Opin. Biotechnol.* **2013**, *24*, 555–561. [CrossRef] [PubMed]
9. Hong, F.; Zhang, F.; Liu, Y.; Yan, H. DNA origami: Scaffolds for creating higher order structures. *Chem. Rev.* **2017**, *117*, 12584–12640. [CrossRef] [PubMed]
10. Bathe, M.; Rothemund, P.W.K. DNA nanotechnology: A foundation for programmable nanoscale materials. *MRS Bull.* **2017**, *42*, 882–888. [CrossRef]
11. Seeman, N.C.; Sleiman, H.F. DNA nanotechnology. *Nat. Rev. Mater.* **2017**, *3*, 17068. [CrossRef]
12. Douglas, S.M.; Bachelet, I.; Church, G.M. A logic-gated nanorobot for targeted transport of molecular payloads. *Science* **2012**, *335*, 831–834. [CrossRef] [PubMed]
13. Castro, C.E.; Dietz, H.; Högberg, B. DNA origami devices for molecular-scale precision measurements. *MRS Bull.* **2017**, *42*, 925–929. [CrossRef]

14. Rothemund, P.W.K. Folding DNA to create nanoscale shapes and patterns. *Nature* **2006**, *440*, 297–302. [CrossRef] [PubMed]
15. Andersen, E.S.; Dong, M.; Nielsen, M.M.; Jahn, K.; Subramani, R.; Mamdouh, W.; Golas, M.M.; Sander, B.; Stark, H.; Oliveira, C.L.P.; et al. Self-assembly of a nanoscale DNA box with a controllable lid. *Nature* **2009**, *459*, 73–76. [CrossRef] [PubMed]
16. Douglas, S.M.; Dietz, H.; Liedl, T.; Högberg, B.; Graf, F.; Shih, W.M. Self-assembly of DNA into nanoscale three-dimensional shapes. *Nature* **2009**, *459*, 414–418. [CrossRef] [PubMed]
17. Dietz, H.; Douglas, S.M.; Shih, W.M. Folding DNA into twisted and curved nanoscale shapes. *Science* **2009**, *325*, 725–730. [CrossRef] [PubMed]
18. Han, D.; Pal, S.; Nangreave, J.; Deng, Z.; Liu, Y.; Yan, H. DNA origami with complex curvatures in three-dimensional space. *Science* **2011**, *332*, 342–346. [CrossRef] [PubMed]
19. Benson, E.; Mohammed, A.; Gardell, J.; Masich, S.; Czeizler, E.; Orponen, P.; Högberg, B. DNA rendering of polyhedral meshes at the nanoscale. *Nature* **2015**, *523*, 441–444. [CrossRef] [PubMed]
20. Veneziano, R.; Ratanalert, S.; Zhang, K.; Zhang, F.; Yan, H.; Chiu, W.; Bathe, M. Designer nanoscale DNA assemblies programmed from the top down. *Science* **2016**, *352*, 1534. [CrossRef] [PubMed]
21. Linko, V.; Kostiainen, M.A. Automated design of DNA origami. *Nat. Biotechnol.* **2016**, *34*, 826–827. [CrossRef] [PubMed]
22. Wagenbauer, K.F.; Sigl, C.; Dietz, H. Gigadalton-scale shape-programmable DNA assemblies. *Nature* **2017**, *552*, 78–83. [CrossRef] [PubMed]
23. Tikhomirov, G.; Petersen, P.; Qian, L. Fractal assembly of micrometer-scale DNA origami arrays with arbitrary patterns. *Nature* **2017**, *552*, 67–71. [CrossRef] [PubMed]
24. Ke, Y.; Ong, L.L.; Shih, W.M.; Yin, P. Three-dimensional structures self-assembled from DNA bricks. *Science* **2012**, *338*, 1177–1183. [CrossRef] [PubMed]
25. Ong, L.L.; Hanikel, N.; Yaghi, O.K.; Grun, C.; Strauss, M.T.; Bron, P.; Lai-Kee-Him, J.; Schueder, F.; Wang, B.; Wang, P.; et al. Programmable self-assembly of three-dimensional nanostructures from 10,000 unique components. *Nature* **2017**, *552*, 72–77. [CrossRef] [PubMed]
26. Linko, V.; Nummelin, S.; Aarnos, L.; Tapio, K.; Toppari, J.J.; Kostiainen, M.A. DNA-based enzyme reactors and systems. *Nanomaterials* **2016**, *6*, 139. [CrossRef] [PubMed]
27. Gothelf, K.V. Chemical modifications and reactions in DNA nanostructures. *MRS Bull.* **2017**, *42*, 897–903. [CrossRef]
28. Grossi, G.; Jaekel, A.; Andersen, E.S.; Saccà, B. Enzyme-functionalized DNA nanostructures as tools for organizing and controlling enzymatic reactions. *MRS Bull.* **2017**, *42*, 920–924. [CrossRef]
29. Kuzyk, A.; Schreiber, R.; Fan, Z.; Pardatscher, G.; Roller, E.-M.; Högele, A.; Simmel, F.C.; Govorov, A.O.; Liedl, T. DNA-based self-assembly of chiral plasmonic nanostructures with tailored optical response. *Nature* **2012**, *483*, 311–314. [CrossRef] [PubMed]
30. Shen, B.; Linko, V.; Tapio, K.; Pikker, S.; Lemma, T.; Gopinath, A.; Gothelf, K.V.; Kostiainen, M.A.; Toppari, J.J. Plasmonic nanostructures through DNA-assisted lithography. *Sci. Adv.* **2018**, *4*, eaap8978. [CrossRef] [PubMed]
31. Perrault, S.D.; Shih, W.M. Virus-inspired membrane encapsulation of DNA nanostructures to achieve in vivo stability. *ACS Nano* **2014**, *8*, 5132–5140. [CrossRef] [PubMed]
32. Linko, V.; Ora, A.; Kostiainen, M.A. DNA nanostructures as smart drug-delivery vehicles and molecular devices. *Trends Biotechnol.* **2015**, *33*, 586–594. [CrossRef] [PubMed]
33. Surana, S.; Shenoy, A.R.; Krishnan, Y. Designing DNA nanodevices for compatibility with the immune system of higher organisms. *Nat. Nanotechnol.* **2015**, *10*, 741–747. [CrossRef] [PubMed]
34. Ora, A.; Järvihaavisto, E.; Zhang, H.; Auvinen, H.; Santos, H.A.; Kostiainen, M.A.; Linko, V. Cellular delivery of enzyme-loaded DNA origami. *Chem. Commun.* **2016**, *52*, 14161–14164. [CrossRef] [PubMed]
35. Zhang, Y.; Tu, J.; Wang, D.; Zhu, H.; Maity, S.K.; Qu, X.; Bogaert, B.; Pei, H.; Zhang, H. Programmable and multifunctional DNA-based materials for biomedical applications. *Adv. Mater.* **2018**, *30*, 1703658. [CrossRef] [PubMed]
36. Graugnard, E.; Hughes, W.L.; Jungmann, R.; Kostiainen, M.A.; Linko, V. Nanometrology and super-resolution imaging with DNA. *MRS Bull.* **2017**, *42*, 951–959. [CrossRef]
37. Julin, S.; Nummelin, S.; Kostiainen, M.A.; Linko, V. DNA nanostructure-directed assembly of metal nanoparticle superlattices. *J. Nanopart. Res.* **2018**, *20*, 119. [CrossRef] [PubMed]

38. Zhang, T.; Hartl, C.; Fischer, S.; Frank, K.; Nickels, P.; Heuer-Jungemann, A.; Nickel, B.; Liedl, T. 3D DNA origami crystals. *Adv. Mater.* **2018**, *30*, 1800273. [CrossRef] [PubMed]
39. Shen, B.; Tapio, K.; Linko, V.; Kostiainen, M.A.; Toppari, J.J. Metallic nanostructures based on DNA nanoshapes. *Nanomaterials* **2016**, *6*, 146. [CrossRef] [PubMed]
40. Kielar, C.; Xin, Y.; Shen, B.; Kostiainen, M.A.; Grundmeier, G.; Linko, V.; Keller, A. On the stability of DNA origami nanostructures in low-magnesium buffers. *Angew. Chem. Int. Ed.* **2018**, *57*, 9470–9474. [CrossRef] [PubMed]
41. Praetorius, F.; Kick, B.; Behler, K.L.; Honemann, M.N.; Weuster-Botz, D.; Dietz, H. Biotechnological mass production of DNA origami. *Nature* **2017**, *552*, 84–87. [CrossRef] [PubMed]
42. Thubagere, A.J.; Li, W.; Johnson, R.F.; Chen, Z.; Doroudi, S.; Lee, Y.L.; Izatt, G.; Srinivas, N.; Woods, D.; Winfree, E.; et al. A cargo-sorting DNA robot. *Science* **2017**, *357*, eaan6558. [CrossRef] [PubMed]
43. Kopperger, E.; List, J.; Madhira, S.; Rothfischer, F.; Lamb, D.C.; Simmel, F.C. A self-assembled nanoscale robotic arm controlled by electric fields. *Science* **2018**, *359*, 296–301. [CrossRef] [PubMed]
44. Huang, P.-S.; Boyken, S.E.; Baker, D. The coming of age of de novo protein design. *Nature* **2016**, *537*, 320–327. [CrossRef] [PubMed]
45. Castro, C.E.; Kilchherr, F.; Kim, D.-N.; Shiao, E.L.; Wauer, T.; Wortmann, P.; Bathe, M.; Dietz, H. A primer to scaffolded DNA origami. *Nat. Methods* **2011**, *8*, 221–229. [CrossRef] [PubMed]
46. Kim, D.-N.; Kilchherr, F.; Dietz, H.; Bathe, M. Quantitative prediction of 3D solution shape and flexibility of nucleic acid nanostructures. *Nucleic Acids Res.* **2012**, *40*, 2862–2868. [CrossRef] [PubMed]
47. Maffeo, C.; Yoo, J.; Aksimentiev, A. De novo reconstruction of DNA origami structures through atomistic molecular dynamics simulation. *Nucleic Acids Res.* **2016**, *44*, 3013–3019. [CrossRef] [PubMed]
48. Sharma, R.; Schreck, J.S.; Romano, F.; Louis, A.A.; Doye, J.P.K. Characterizing the motion of jointed DNA nanostructures using a coarse-grained model. *ACS Nano* **2017**, *11*, 12426–12435. [CrossRef] [PubMed]
49. Shi, Z.; Castro, C.E.; Arya, G. Conformational dynamics of mechanically compliant DNA nanostructures from coarse-grained molecular dynamics simulations. *ACS Nano* **2017**, *11*, 4617–4630. [CrossRef] [PubMed]
50. Jo, S.; Kim, S.; Lee, B.H.; Tandon, A.; Kim, B.; Park, S.H.; Kim, M.K. Fabrication and characterization of finite-size DNA 2D ring and 3D buckyball structures. *Int. J. Mol. Sci.* **2018**, *19*, 1895. [CrossRef] [PubMed]
51. Mao, C.; Sun, W.; Shen, Z.; Seeman, N.C. A nanomechanical device based on the B-Z transition of DNA. *Nature* **1999**, *397*, 144–146. [CrossRef] [PubMed]
52. Yurke, B.; Turberfield, A.J.; Mills, A.P., Jr.; Simmel, F.C.; Neumann, J.L. A DNA-fuelled molecular machine made of DNA. *Nature* **2000**, *406*, 605–608. [CrossRef] [PubMed]
53. Yan, H.; Zhang, X.; Shen, Z.; Seeman, N.C. A robust DNA mechanical device controlled by hybridization topology. *Nature* **2002**, *415*, 62–65. [CrossRef] [PubMed]
54. Simmel, F.C.; Yurke, B. A DNA-based molecular device switchable between three distinct mechanical states. *Appl. Phys. Lett.* **2002**, *80*, 883–885. [CrossRef]
55. Zhong, H.; Seeman, N.C. RNA used to control a DNA rotary nanomachine. *Nano Lett.* **2006**, *6*, 2899–2903. [CrossRef] [PubMed]
56. Liu, M.; Fu, J.; Hejesen, C.; Yang, Y.; Woodbury, N.W.; Gothelf, K.V.; Liu, Y.; Yan, H. A DNA tweezer-actuated enzyme nanoreactor. *Nat. Commun.* **2013**, *4*, 2127. [CrossRef] [PubMed]
57. Xin, L.; Zhou, C.; Yang, Z.; Liu, D. Regulation of an enzyme cascade reaction by a DNA machine. *Small* **2013**, *9*, 3088–3091. [CrossRef] [PubMed]
58. Bath, J.; Turberfield, A.J. DNA nanomachines. *Nat. Nanotechnol.* **2007**, *2*, 275–284. [CrossRef] [PubMed]
59. Pan, J.; Li, F.; Cha, T.G.; Chen, H.; Choi, J.H. Recent progress on DNA based walkers. *Curr. Opin. Biotechnol.* **2015**, *34*, 56–64. [CrossRef] [PubMed]
60. Zadegan, R.M.; Jepsen, M.D.E.; Thomsen, K.E.; Okholm, A.H.; Schaffert, D.H.; Andersen, E.S.; Birkedal, V.; Kjems, J. Construction of a 4 zeptoliters switchable 3D DNA origami box. *ACS Nano* **2012**, *6*, 10050–10053. [CrossRef] [PubMed]
61. Grossi, G.; Jepsen, M.D.E.; Kjems, J.; Andersen, E.S. Control of enzyme reactions by a reconfigurable DNA nanovault. *Nat. Commun.* **2017**, *8*, 992. [CrossRef] [PubMed]
62. Tomaru, T.; Suzuki, Y.; Kawamata, I.; Nomura, S.M.; Murata, S. Stepping operation of a rotary DNA origami device. *Chem. Commun.* **2017**, *53*, 7716–7719. [CrossRef] [PubMed]
63. Selnihhin, D.; Sparvath, S.M.; Preus, S.; Birkedal, V.; Andersen, E.S. Multifluorophore DNA origami beacon as a biosensing platform. *ACS Nano* **2018**, *12*, 5699–5708. [CrossRef] [PubMed]

64. Castro, C.E.; Su, H.J.; Marras, A.E.; Zhou, L.; Johnson, J. Mechanical design of DNA nanostructures. *Nanoscale* **2015**, *7*, 5913–5921. [CrossRef] [PubMed]
65. Zhou, L.; Marras, A.E.; Su, H.-J.; Castro, C.E. DNA origami compliant nanostructures with tunable mechanical properties. *ACS Nano* **2014**, *8*, 27–34. [CrossRef] [PubMed]
66. Zhou, L.; Marras, A.E.; Su, H.-J.; Castro, C.E. Direct design of an energy landscape with bistable DNA origami mechanisms. *Nano Lett.* **2015**, *15*, 1815–1821. [CrossRef] [PubMed]
67. Marras, A.E.; Zhou, L.; Su, H.-J.; Castro, C.E. Programmable motion of DNA origami mechanics. *Proc. Natl. Acad. Sci. USA* **2015**, *112*, 713–718. [CrossRef] [PubMed]
68. Khara, D.C.; Schreck, J.S.; Tomov, T.E.; Berger, Y.; Ouldridge, T.E.; Doye, J.P.K.; Nir, E. DNA bipedal motor walking dynamics: An experimental and theoretical study of the dependency on step size. *Nucleic Acids Res.* **2017**, *46*, 1553–1561. [CrossRef] [PubMed]
69. Lund, K.; Manzo, A.J.; Dabby, N.; Michelotti, N.; Johnson-Buck, A.; Nangreave, J.; Taylor, S.; Pei, R.; Stojanovic, M.N.; Walter, N.G.; et al. Molecular robots guided by prescriptive landscapes. *Nature* **2010**, *465*, 206–210. [CrossRef] [PubMed]
70. Ke, Y.; Meyer, T.; Shih, W.M.; Bellot, G. Regulation at a distance of biomolecular interactions using a DNA origami nanoactuator. *Nat. Commun.* **2016**, *7*, 10935. [CrossRef] [PubMed]
71. Choi, Y.; Choi, H.; Lee, A.C.; Lee, H.; Kwon, S. A Reconfigurable DNA accordion rack. *Angew. Chem. Int. Ed.* **2018**, *57*, 2811–2815. [CrossRef] [PubMed]
72. Agarwal, N.P.; Matthies, M.; Joffroy, B.; Schmidt, T.L. Structural transformation of wireframe DNA origami via DNA polymerase assisted gap-filling. *ACS Nano* **2018**, *12*, 2546–2553. [CrossRef] [PubMed]
73. Woo, S.; Rothemund, P.W.K. Programmable molecular recognition based on the geometry of DNA nanostructures. *Nat. Chem.* **2011**, *3*, 620–627. [CrossRef] [PubMed]
74. Gerling, T.; Wagenbauer, K.F.; Neuner, A.M.; Dietz, H. Dynamic DNA devices and assemblies formed by shape-complementary, non-base pairing 3D components. *Science* **2015**, *347*, 1446–1452. [CrossRef] [PubMed]
75. Willner, E.M.; Kamada, Y.; Suzuki, Y.; Emura, T.; Hidaka, K.; Dietz, H.; Sugiyama, H.; Endo, M. Single-molecule observation of the photoregulated conformational dynamics of DNA origami nanoscissors. *Angew. Chem. Int. Ed.* **2017**, *56*, 15324–15328. [CrossRef] [PubMed]
76. Bruetzel, L.D.; Walker, P.U.; Gerling, T.; Dietz, H.; Lipfert, J. Time-resolved small-angle X-ray scattering reveals millisecond transitions of a DNA origami switch. *Nano Lett.* **2018**, *18*, 2672–2676. [CrossRef] [PubMed]
77. Song, J.; Li, Z.; Wang, P.; Meyer, T.; Mao, C.; Ke, Y. Reconfiguration of DNA molecular arrays driven by information relay. *Science* **2017**, *357*, eaan3377. [CrossRef] [PubMed]
78. Ketterer, P.; Willner, E.M.; Dietz, H. Nanoscale rotary apparatus formed from tight-fitting 3D DNA components. *Sci. Adv.* **2016**, *2*, e1501209. [CrossRef] [PubMed]
79. Kuzyk, A.; Schreiber, R.; Zhang, H.; Govorov, A.O.; Liedl, T.; Liu, N. Reconfigurable 3D plasmonic metamolecules. *Nat. Mater.* **2014**, *13*, 862–866. [CrossRef] [PubMed]
80. Zhou, C.; Duan, X.; Liu, N. A plasmonic nanorod that walks on DNA origami. *Nat. Commun.* **2015**, *6*, 8102. [CrossRef] [PubMed]
81. Jungmann, R.; Avendano, M.S.; Woehrstein, J.B.; Dai, M.; Shih, W.M.; Yin, P. Multiplexed 3D cellular super-resolution imaging with DNA-PAINT and Exchange-PAINT. *Nat. Methods* **2014**, *11*, 313–318. [CrossRef] [PubMed]
82. Schnitzbauer, J.; Strauss, M.T.; Schlichthaerle, T.; Schueder, F.; Jungmann, R. Super-resolution microscopy with DNA-PAINT. *Nat. Protoc.* **2017**, *12*, 1198–1228. [CrossRef] [PubMed]
83. Schueder, F.; Lara-Gutíerrez, J.; Beliveau, B.J.; Saka, S.K.; Sasaki, H.M.; Woehrstein, J.B.; Strauss, M.T.; Grabmayr, H.; Yin, P.; Jungmann, R. Multiplexed 3D super-resolution imaging of whole cells using spinning disk confocal microscopy and DNA-PAINT. *Nat. Commun.* **2017**, *8*, 2090. [CrossRef] [PubMed]
84. Kuzuya, A.; Sakai, Y.; Yamazaki, T.; Xu, Y.; Komiyama, M. Nanomechanical DNA origami "single-molecule beacons" directly imaged by atomic force microscopy. *Nat. Commun.* **2011**, *2*, 449. [CrossRef] [PubMed]
85. Funke, J.J.; Ketterer, P.; Lieleg, C.; Schunter, S.; Korber, P.; Dietz, H. Uncovering the forces between nucleosomes using DNA origami. *Sci. Adv.* **2016**, *2*, e1600974. [CrossRef] [PubMed]
86. Funke, J.J.; Ketterer, P.; Lieleg, C.; Korber, P.; Dietz, H. Exploring nucleosome unwrapping using DNA DNA origami. *Nano Lett.* **2016**, *16*, 7891–7898. [CrossRef] [PubMed]

87. Le, J.V.; Luo, Y.; Darcy, M.A.; Lucas, C.R.; Goodwin, M.F.; Poirier, M.G.; Castro, C.E. Probing nucleosome stability with a DNA origami nanocaliper. *ACS Nano* **2016**, *10*, 7073–7084. [CrossRef] [PubMed]
88. Funke, J.J.; Dietz, H. Placing molecules with Bohr radius resolution using DNA origami. *Nat. Nanotechnol.* **2016**, *11*, 47–52. [CrossRef] [PubMed]
89. Hudoba, M.W.; Luo, Y.; Zacharias, A.; Poirier, M.G.; Castro, C.E. Dynamic DNA origami device for measuring compressive depletion forces. *ACS Nano* **2017**, *11*, 6566–6573. [CrossRef] [PubMed]
90. Li, S.; Jiang, Q.; Liu, S.; Zhang, Y.; Tian, Y.; Song, C.; Wang, J.; Zou, Y.; Anderson, G.J.; Han, J.Y.; et al. A DNA nanorobot functions as a cancer therapeutic in response to a molecular trigger in vivo. *Nat. Biotechnol.* **2018**, *36*, 258–264. [CrossRef] [PubMed]
91. Amir, Y.; Ben-Ishay, E.; Levner, D.; Ittah, S.; Abu-Horowitz, A.; Bachelet, I. Universal computing by DNA origami robots in a living animal. *Nat. Nanotechnol.* **2014**, *9*, 353–357. [CrossRef] [PubMed]
92. Kaminka, G.A.; Spokoini-Stern, R.; Amir, Y.; Agmon, N.; Bachelet, I. Molecular robots obeying Asimov's three laws of robotics. *Artif. Life* **2017**, *23*, 343–350. [CrossRef] [PubMed]
93. Asimov, I. *I, Robot*; Bantam Books: New York, NY, USA, 2004; ISBN 9780553803709.
94. Chen, H.; Zhang, H.; Pan, J.; Cha, T.G.; Li, S.; Andréasson, J.; Choi, J.H. Dynamic and progressive control of DNA origami conformation by modulating DNA helicity with chemical adducts. *ACS Nano* **2016**, *10*, 4989–4996. [CrossRef] [PubMed]
95. Derr, N.D.; Goodman, B.S.; Jungmann, R.; Leschziner, A.E.; Shih, W.M.; Reck-Peterson, S.L. Tug-of-war in motor protein ensembles revealed with a programmable DNA origami scaffold. *Science* **2012**, *338*, 662–665. [CrossRef] [PubMed]
96. Sato, Y.; Endo, M.; Morita, M.; Takinoue, M.; Sugiyama, H.; Murata, S.; Nomura, S.M.; Suzuki, Y. Environment-dependent self-assembly of DNA origami lattices on phase-separated lipid membranes. *Adv. Mater. Interfaces* **2018**, *5*, 1800437. [CrossRef]
97. Suzuki, Y.; Endo, M.; Sugiyama, H. Lipid-bilayer-assisted two-dimensional self-assembly of DNA origami nanostructures. *Nat. Commun.* **2015**, *6*, 8052. [CrossRef] [PubMed]
98. Kocabey, S.; Kempter, S.; List, J.; Xing, Y.; Bae, W.; Schiffels, D.; Shih, W.M.; Simmel, F.C.; Liedl, T. Membrane-assisted growth of DNA origami nanostructure arrays. *ACS Nano* **2015**, *9*, 3530–3539. [CrossRef] [PubMed]
99. Yang, Y.; Endo, M.; Hidaka, K.; Sugiyama, H. Photo-controllable DNA origami nanostructures assembling into predesigned multiorientational patterns. *J. Am. Chem. Soc.* **2012**, *134*, 20645–20653. [CrossRef] [PubMed]
100. Kohman, R.E.; Han, X. Light sensitization of DNA nanostructures via incorporation of photo-cleavable spacers. *Chem. Commun.* **2015**, *51*, 5747–5750. [CrossRef] [PubMed]
101. Takenaka, T.; Endo, M.; Suzuki, Y.; Yang, Y.; Emura, T.; Hidaka, K.; Kato, T.; Miyata, T.; Namba, K.; Sugiyama, H. Photoresponsive DNA nanocapsule having an open/close system for capture and release of nanomaterials. *Chem. Eur. J.* **2014**, *20*, 14951–14954. [CrossRef] [PubMed]
102. Kuzyk, A.; Yang, Y.; Duan, X.; Stoll, S.; Govorov, A.O.; Sugiyama, H.; Endo, M.; Liu, N. A light-driven three-dimensional plasmonic nanosystem that translates molecular motion into reversible chiroptical function. *Nat. Commun.* **2016**, *7*, 10591. [CrossRef] [PubMed]
103. Kuzyk, A.; Urban, M.J.; Idili, A.; Ricci, F.; Liu, N. Selective control of reconfigurable chiral plasmonic metamolecules. *Sci. Adv.* **2017**, *3*, e1602803. [CrossRef] [PubMed]
104. Wu, N.; Willner, I. pH-stimulated reconfiguration and structural isomerization of origami dimer and trimer systems. *Nano Lett.* **2016**, *16*, 6650–6655. [CrossRef] [PubMed]
105. Jiang, Q.; Liu, Q.; Shi, Y.; Wang, Z.-G.; Zhan, P.; Liu, J.; Liu, C.; Wang, H.; Shi, X.; Zhang, L.; et al. Stimulus-responsive plasmonic chiral signals of gold nanorods organized on DNA origami. *Nano Lett.* **2017**, *17*, 7125–7130. [CrossRef] [PubMed]
106. Turek, V.A.; Chikkaraddy, R.; Cormier, S.; Stockham, B.; Ding, T.; Keyser, U.F.; Baumberg, J.J. Thermo-responsive actuation of a DNA origami flexor. *Adv. Funct. Mater.* **2018**, *28*, 1706410. [CrossRef]
107. Nickels, P.C.; Wünsch, B.; Holzmeister, P.; Bae, W.; Kneer, L.M.; Grohmann, D.; Tinnefeld, P.; Liedl, T. Molecular force spectroscopy with a DNA origami-based nanoscopic force clamp. *Science* **2016**, *354*, 305–307. [CrossRef] [PubMed]
108. Dutta, P.K.; Zhang, Y.; Blanchard, A.T.; Ge, C.; Rushdi, M.; Weiss, K.; Zhu, C.; Ke, Y.; Salaita, K. Programmable multivalent DNA-origami tension probes for reporting cellular traction forces. *Nano Lett.* **2018**, *18*. [CrossRef] [PubMed]

109. Kuzyk, A.; Yurke, B.; Toppari, J.J.; Linko, V.; Törmä, P. Dielectrophoretic trapping of DNA origami. *Small* **2008**, *4*, 447–450. [CrossRef] [PubMed]
110. Shen, B.; Linko, V.; Dietz, H.; Toppari, J.J. Dielectrophoretic trapping of multilayer DNA origami nanostructures and DNA origami-induced local destruction of silicon dioxide. *Electrophoresis* **2015**, *36*, 255–262. [CrossRef] [PubMed]
111. Lauback, S.; Mattioli, K.R.; Marras, A.E.; Armstrong, M.; Rudibaugh, D.P.; Sooryakumar, R.; Castro, C.E. Real-time magnetic actuation of DNA nanodevices via modular integration with stiff micro-levers. *Nat. Commun.* **2018**, *9*, 1446. [CrossRef] [PubMed]
112. Mikkilä, J.; Eskelinen, A.-P.; Niemelä, E.H.; Linko, V.; Frilander, M.J.; Törmä, P.; Kostiainen, M.A. Virus-encapsulated DNA origami nanostructures for cellular delivery. *Nano Lett.* **2014**, *14*, 2196–2200. [CrossRef] [PubMed]
113. Kiviaho, J.K.; Linko, V.; Ora, A.; Tiainen, T.; Järvihaavisto, E.; Mikkilä, J.; Tenhu, H.; Nonappa; Kostiainen, M.A. Cationic polymers for DNA origami coating—Examining their binding efficiency and tuning the enzymatic reaction rates. *Nanoscale* **2016**, *8*, 11674–11680. [CrossRef] [PubMed]
114. Agarwal, N.P.; Matthies, M.; Gür, F.N.; Osada, K.; Schmidt, T.L. Block copolymer micellization as a protection strategy for DNA origami. *Angew. Chem. Int. Ed.* **2017**, *56*, 5460–5464. [CrossRef] [PubMed]
115. Auvinen, H.; Zhang, H.; Nonappa; Kopilow, A.; Niemelä, E.H.; Nummelin, S.; Correia, A.; Santos, H.A.; Linko, V.; Kostiainen, M.A. Protein coating of DNA nanostructures for enhanced stability and immunocompatibility. *Adv. Healthcare Mater.* **2017**, *6*, 1700692. [CrossRef] [PubMed]
116. Ponnuswamy, N.; Bastings, M.M.C.; Nathwani, B.; Ryu, J.H.; Chou, L.Y.T.; Vinther, M.; Li, W.A.; Anastassacos, F.M.; Mooney, D.J.; Shih, W.M. Oligolysine-based coatings protects DNA nanostructures from low-salt denaturation and nuclease degradation. *Nat. Commun.* **2017**, *8*, 15654. [CrossRef] [PubMed]
117. Linko, V.; Eerikäinen, M.; Kostiainen, M.A. A modular DNA origami-based enzyme cascade nanoreactor. *Chem. Commun.* **2015**, *51*, 5351–5354. [CrossRef] [PubMed]
118. Kilchherr, F.; Wachauf, C.; Pelz, B.; Rief, M.; Zacharias, M.; Dietz, H. Single-molecule dissection of stacking forces in DNA. *Science* **2016**, *353*, aaf5508. [CrossRef] [PubMed]

II

RECONFIGURABLE DNA ORIGAMI NANOCAPSULE FOR PH-CONTROLLED ENCAPSULATION AND DISPLAY OF CARGO

by

Ijäs H., Hakaste I., Shen B., Kostiainen M.A. & Linko V. 2019

ACS Nano 13: 5959−5967

DOI:10.1021/acsnano.9b01857

ACS NANO

Cite This: *ACS Nano* 2019, 13, 5959−5967

www.acsnano.org

ARTICLE

Reconfigurable DNA Origami Nanocapsule for pH-Controlled Encapsulation and Display of Cargo

Heini Ijäs,[†,‡] Iiris Hakaste,[†] Boxuan Shen,[†] Mauri A. Kostiainen,[†,§] and Veikko Linko*[,†,§]

[†]Biohybrid Materials, Department of Bioproducts and Biosystems, Aalto University, 00076 Aalto, Finland

[‡]Nanoscience Center, Department of Biological and Environmental Science, University of Jyväskylä, P.O. Box 35, 40014 Jyväskylä, Finland

[§]HYBER Center of Excellence, Department of Applied Physics, Aalto University, 00076 Aalto, Finland

Supporting Information

ABSTRACT: **DNA nanotechnology provides a toolbox for creating custom and precise nanostructures with nanometer-level accuracy. These nano-objects are often static by nature and serve as versatile templates for assembling various molecular components in a user-defined way. In addition to the static structures, the intrinsic programmability of DNA nanostructures allows the design of dynamic devices that can perform predefined tasks when triggered with external stimuli, such as drug delivery vehicles whose cargo display or release can be triggered with a specified physical or chemical cue in the biological environment. Here, we present a DNA origami nanocapsule that can be loaded with cargo and reversibly opened and closed by changing the pH of the surrounding solution. Moreover, the threshold pH value for opening/closing can be rationally designed. We characterize the reversible switching and a rapid opening of "pH-latch"-equipped nanocapsules using Förster resonance energy transfer. Furthermore, we demonstrate the full cycle of capsule loading, encapsulation, and displaying the payload using metal nanoparticles and functional enzymes as cargo mimics at physiologically relevant ion concentrations.**

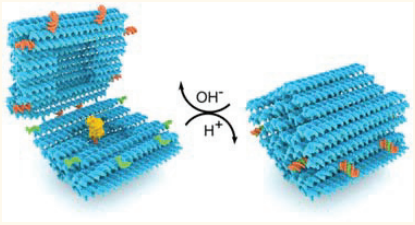

KEYWORDS: *DNA nanotechnology, DNA origami, pH control, Förster resonance energy transfer, nanoparticles, enzymes, drug delivery*

DNA nanotechnology[1−3] provides an essential foundation for programmable and innovative nanoscale structures, devices and advanced materials. DNA nanostructures have been successfully used for example in creating static nanophotonic devices,[4−7] nanoscopic rulers[8,9] and templates for material assembly.[10,11] Nevertheless, it is extremely intriguing to explore the possibilities to build dynamic devices[12−14] using DNA as a construction material, especially by applying the robust and versatile DNA origami technique.[15] Examples of such dynamic DNA origami-based devices include robotics,[16−18] molecular-scale precision measurement and diagnostic tools,[19] plasmonic/nanophotonic systems,[20] reconfigurable metamolecules,[21,22] and information relay systems.[23] Dynamic DNA nanostructures can also find interesting uses in drug delivery[24,25] since these nanoscale devices are readily modifiable for targeted delivery and loading of the specified molecular cargo.[26,27] Moreover, they can be programmed to perform user-defined tasks upon external stimuli, for example, encapsulation and subsequent display and release of cargo.[28,29]

So far, dynamics of signal-responsive prototypes of DNA drug-delivery vehicles have been realized by conformational changes due to a temperature gradient,[30] strand displacement reactions,[31] DNA−protein interactions,[24,25] or by taking advantage of photoactivated properties of the system.[29,32] Regulation of the dynamic properties may become extremely challenging in biologically relevant environments, especially with systems relying on the introduction of additional regulating molecules, such as oligonucleotides for strand displacement reactions. For this, pH change of the environment presents an intriguing trigger for the cargo release of drug-delivery vehicles functioning autonomously in biological environments. Various compartments of the cell are characterized by a distinct pH, and deviations from the normal pH can be linked to abnormal cell behavior. For instance, while healthy cells maintain a lower intracellular pH (∼7.2) compared to the extracellular pH (∼7.4), cancer cells are

Received: March 8, 2019
Accepted: April 16, 2019
Published: April 16, 2019

DOI: 10.1021/acsnano.9b01857
ACS Nano 2019, 13, 5959−5967

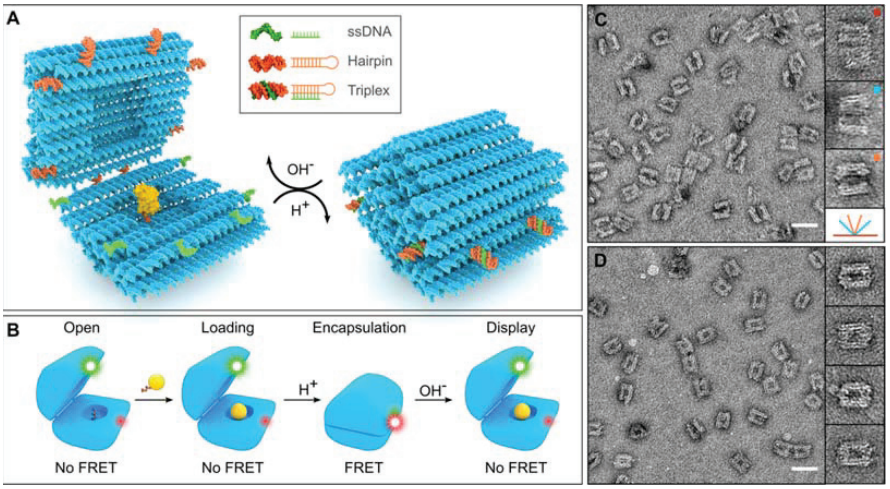

Figure 1. DNA origami nanocapsule design and function. (A) A hinged DNA origami nanocapsule with a HRP payload can be reversibly opened and closed with the help of eight programmable pH-responsive latches. At high pH, the latches are open (a hairpin (orange) and a ssDNA (green) detached) and the capsule halves can move freely, whereas at low pH, the latches form a triplex DNA thus closing the capsule. (B) A schematic figure series depicts the full cycle of capsule function. The open capsule can be loaded with a cargo (yellow sphere with an attachment strand) *via* hybridization of the anchoring and attachment strands. The loaded cargo can be encapsulated by lowering pH and further displayed by increasing pH. The dynamics of the opening and closing can be followed by FRET analysis when the capsule is equipped by a FRET pair (green and red dyes). (C) TEM images reveal open nanocapsules with a variety of opening angles from completely open to barely ajar structures. Insets show representative structures with corresponding opening angles depicted at the bottom with the same color codes. The monomer capsule yield after folding is 79 ± 2%. (D) Closed nanocapsules under TEM. Insets show zoomed-in representative structures. Scale bars in subfigures C and D are 50 nm. The width of each inset is 60 nm.

distinguished by an inverted pH gradient with low extracellular pH (~6.8−7.0) and high intracellular pH (~7.3−7.6) necessary for the multiple altered characteristics of cancer cells.[33,34] This raises an interest to demonstrate controlled cargo release upon similar slight pH increases in physiological conditions. pH-driven actuation also holds the advantage of being simple and easy to implement: DNA motifs such as cytosine-rich i-motifs and Hoogsteen-type polypurine-polypyrimidine triplexes are intrinsically pH responsive,[35−37] and incorporating them into larger DNA nanostructures can be used to control the dynamics of the structures, avoiding the need for more laborious or costly chemical modifications or conjugation of external molecules as stimuli-responsive units. Indeed, both DNA origami structures[22,38−41] and tile-based DNA polyhedra[42−44] have been successfully functionalized with pH-responsive DNA moieties for applications in various fields of research.

In this article, we have designed and assembled a reconfigurable, compact, and cargo-shielding DNA origami nanocapsule (Figure 1A) whose reversible opening/closing cycle can be controlled by a sharp pH change. In other words, the capsule is equipped with multiple rationally designed "pH-latches" that work cooperatively. Each of the latches is comprised of two parts: a double-stranded DNA (dsDNA) and a single-stranded DNA (ssDNA). Depending on the pH of the environment, these counterparts can either form a parallel triplex DNA *via* Hoogsteen bonding (closed state of the capsule, low pH) or hang freely from the capsule (open state, high pH). The open/close transition (acid dissociation constant, pK_a) of the system can be rationally designed by selecting the base contents of the latch strands,[22,45] thus adding another level of modularity to the system. We have analyzed the dynamics and functionality of the capsule in detail by Förster resonance energy transfer (FRET) measurements. Moreover, the capsule has a functionalizable cavity for anchoring molecular payloads, and by taking advantage of the reversible opening/closing cycle of the capsule, we have demonstrated successive loading, encapsulation, and display of molecular payloads. We have used gold nanoparticles (AuNPs) as cargo mimics for transmission electron microscopy (TEM)-based verification and horseradish peroxidase (HRP) enzymes for proving the functionality of the encapsulated cargo by characterizing of enzyme activity.

RESULTS AND DISCUSSION

Here, we present the design of a dynamic DNA origami nanocapsule and use FRET- and TEM-based analysis to show that the nanocapsule can be opened and closed with solution pH and harnessed for loading and display of cargo molecules. The DNA nanocapsule was folded as a single structure from the 8064-nucleotide (nt) scaffold. The design consists of two capsule halves linked together at one long edge by four ssDNA hinges (Figure 1A), each consisting of 10 nucleotides of nonhybridized scaffold DNA. The outer dimensions of the nanocapsule are *ca.* 31 nm × 28 nm × 33 nm ($w \times h \times l$), making it roughly spherical, and it contains an inner cavity with dimensions of 11 nm × 12 nm × 13 nm. The walls of the nanocapsule consist of two layers of DNA double helices to ensure the required rigidity and stability for shielding the loaded cargo. In order to avoid multimerization or aggregation of the nanocapsules through blunt-end stacking interactions, the outward pointing ends of each DNA helix were passivated with 8-nt long single-stranded poly-T overhangs.

DOI: 10.1021/acsnano.9b01857
ACS Nano 2019, 13, 5959−5967

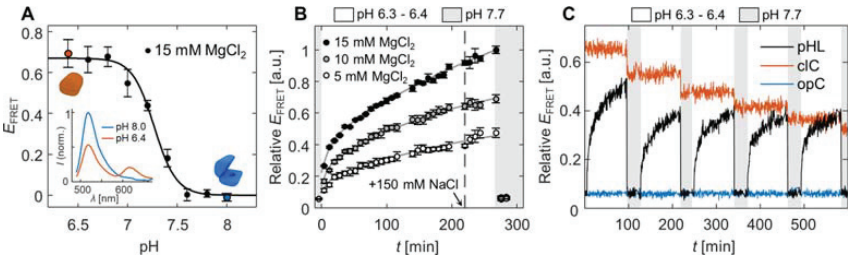

Figure 2. The pH-controlled opening and closing of nanocapsules in solution characterized by FRET. (A) Dependence of FRET efficiency on the solution pH near the pK_a = 7.27. Inset figure shows emission spectra of the sample at pH 6.4 and pH 8.0 resulting from the donor excitation at 460 nm. A Hill equation (solid line) has been fitted to the data points to determine values of pK_a and Hill coefficient *n*. FRET efficiency values have been calculated based on average donor and acceptor emission intensity values in three parallel samples. Error limits for each data point have been calculated according to the propagation of error, based on the standard deviation between the initial measurements. (B) Closing and opening kinetics of nanocapsules in the presence of 15, 10, and 5 mM $MgCl_2$. At *t* = 0, acetic acid is added to the pH 7.7 solution to rapidly decrease the pH to 6.3. At *t* = 220 min, the NaCl concentration in the samples is increased to a physiological concentration (150 mM). Sodium hydroxide addition at *t* = 266 min leads to all samples returning to fully open states. FRET efficiency values have been averaged from three parallel (and independent) samples, error bars representing the standard error of the mean. (C) Repeated opening/closing cycles of the nanocapsules equipped with pH latches (pHL). In addition to the pHL nanocapsules, the same pH cycling was performed for permanently closed (clC) and open (opC) control samples. E_{FRET} values in subfigures B and C have both been normalized to the highest efficiency value observed at a 15 mM $MgCl_2$ concentration (in subfigure B).

For introducing a closing/opening mechanism of choice, a total of eight latch sites were included in the design at the interface between the capsule halves. The staple strands at these sites can be replaced by strands containing a desired latch functionality. Here, we designed eight pairs of pH latch DNA sequences that were inserted at these sites as staple strand extensions: One part of the latch is a DNA duplex, consisting of complementary polypurine and pyrimidine regions in a single 20 bp hairpin motif. The other part of the latch in the adjacent half is a single-stranded, 20 nt polypyrimidine DNA oligonucleotide that forms a parallel DNA triplex with the duplex. Each latch is designed with a unique base sequence but identical 60% T-A·T base triplex content to ensure that all latches will open at the same pH,[22,45] but the triplex formation will only take place between the intended counterparts. The aforementioned T-A·T base content was chosen to yield pK_a ∼ 7.2 according to previously reported triplexes with similar lengths.[22] This targeted pK_a value was selected to demonstrate the capsule function in physiologically relevant conditions (blood pH ∼ 7.4, healthy cells ∼7.2, and cancer cells typically ∼7.4−7.6).[33,34,46]

In addition to the pH latch (pHL) nanocapsules, we designed and assembled two types of controls: permanently open nanocapsules with no locking mechanism (opC) and permanently closed nanocapsules (clC), in which the pH latches were replaced with complementary ssDNA overhangs. To first confirm the structural integrity and correct folding of all types of nanocapsules, the assembled structures were analyzed with TEM and agarose gel electrophoresis (AGE). The nanocapsules visualized with TEM showed well-defined shapes, negligible aggregation (monomer yield of capsules calculated from the gel electrophoresis was 79 ± 2% (s.d., *n* = 3)), and clearly distinguishable open and closed conformations (Figure 1C,D). While nanocapsules in a closed state appear structurally homogeneous under TEM, the structural flexibility of open nanocapsules is reflected in a variety of different opening angles. On agarose gels, all folded structures show a well-defined monomer band and low amount of oligomerization, but surprisingly, the open and closed states cannot be differentiated by electrophoretic mobility (Figure S2).

In order to demonstrate that the opening and closing of the pHL nanocapsules can be controlled with solution pH, we labeled the opposing halves of the capsule with an Alexa Fluor 488 (donor)−Alexa Fluor 594 (acceptor) FRET pair using oligonucleotides with fluorophore end modifications. The emission profiles upon donor excitation at 460 nm were measured from samples prepared at various pH values between 6.0 and 8.0 in 1 × TAE (40 mM Tris, ∼20 mM acetic acid, and 1 mM ethylenediaminetetraacetic acid (EDTA)) with 15 mM $MgCl_2$ and 5 mM NaCl. FRET efficiency at each pH was quantified from the acceptor emission intensity increase at 616 nm.

In acidic conditions (pH 6.4−6.8), a donor excitation results in a clearly observable acceptor emission (Figure 2A, inset) and a high FRET efficiency, E_{FRET} = 0.67 ± 0.03 (Figure 2A). This indicates that a significant amount of donor excitation energy is transferred to the acceptor in a close proximity and, subsequently, that a high portion of the capsules are in a closed state. In contrast to the high-FRET state at acidic pH, pHL samples prepared in basic conditions (pH 7.6−8.0) are in a flexible, open state characterized by $E_{FRET} \approx 0$. Emission spectra of the open and closed states of the pHL nanocapsule show a high correspondence to opC and clC control samples. Furthermore, emission spectra of opC and clC are not affected by pH (Figure S1), confirming that the observed FRET efficiency differences in pHL nanocapsules result solely from pH-driven conformational changes. Lowering the pH below 6.4 leads to an increased amount of sample aggregation or possibly other forms of loss of structural integrity, observed as a further increase in FRET efficiency unrelated to the pH-dependent conformational change of individual structures (Figure S3). The aggregation was observed to be less significant in opC and clC control samples, indicating that interactions between pH latches of separate nanocapsules may play a role in the aggregation process. At higher pH values, the level of aggregation in all samples is very low, including negligible multimerization *via* blunt-end stacking interactions due to an effective passivation of the outward-pointing DNA double-helix ends with poly-T overhangs.

DOI: 10.1021/acsnano.9b01857
ACS Nano 2019, 13, 5959−5967

At pH 7.0−7.5 (within *ca.* 0.5 pH units) with a pK_a of 7.27 ± 0.02, the pHL nanocapsules undergo a steep transition between the closed and open states. The transition is characterized by a high Hill coefficient, 3.9 ± 0.5, consistent with the idea of a two-state system working in a cooperative manner. The pK_a value depends on the relative amount of T-A·T base triads in the pH latches (here 60%) and has high agreement to the pK_a = 7.2 reported by Kuzyk *et al.* for plasmonic DNA origami devices actuated with one DNA triplex with identical length (20 base triads) and T-A·T content.[22] Due to the good agreement of the results, we propose that the pK_a of our system could be adjusted in a similar fashion demonstrated by both Idili *et al.*[45] and Kuzyk *et al.*[22] to a lower pH by decreasing or to a higher pH by increasing the percentage of T-A·T triplets in the pH latch strands, enabling fine-tuning the opening threshold for the desired biological target. Interestingly, we note that the pH sensitivity does not appear to be affected by the number of pH latches, as the shape and steepness of the pH response curves of the pHL nanocapsules and the plasmonic metamolecules presented by Kuzyk *et al.*[15] are also very similar.

In addition to static measurements, we performed series of kinetic measurements following the FRET efficiency in an individual sample after changing the solution pH by addition of small volumes of either acid or base (Figure 2B). We observed that the closed capsules in acidic conditions open extremely rapidly after the addition of sodium hydroxide: Measured FRET efficiency drops to the level of opC control even before the first measurement at 30 s. In contrast, closing the nanocapsules takes place gradually over a time course of several hours after lowering the pH of the sample from 7.7 to 6.3.

When the closing process was initiated in the presence of lowered cation concentrations (10 mM or 5 mM $MgCl_2$), we observed significantly reduced rates of closing as well as a lower amount of closed structures at the end of the incubation period (Figure 2B). Since the positive charge of the divalent cations screens the repulsive electrostatic interactions between the large, negatively charged nanocapsule halves, the result indicates a heavy role of electrostatic effects in the dynamic properties of the system. It is likely that a reduced amount of electrostatic repulsion both increases the probability of formation of the closed state by reducing the energetic penalty of bringing the two capsule halves together as well as stabilizes the formed triplexes in the closed state by decreasing the repulsion both between the large structural units as well as the interacting latch strands. Thus, we found 15 mM $MgCl_2$ to be the required concentration for successfully preparing and closing the nanocapsules. At higher $MgCl_2$ concentrations (*e.g.*, 30 mM), further weakening of the electrostatic repulsion between individual capsules starts to lead to an increased level of aggregation (Figure S3).

The response time and dynamics of stimuli-responsive nanosystems can be heavily dependent on the type of triggering stimulus. In our system, solution pH change and the associated protonation/deprotonation of cytosine N3 atoms in the pH latch oligonucleotides can be expected to take place in a millisecond time scale according to the diffusion rate of ions. For instance, Idili *et al.*[45] reported both folding (associated with intramolecular triplex formation) and unfolding of small pH-responsive triplex nanoswitches in solution taking place within milliseconds, and reconfiguration times of several hundred milliseconds have also been achieved with larger DNA origami devices actuated by ion concentrations.[47] In contrast, systems relying on the strand displacement reactions may yield slower reaction rates due to a number of limiting factors: bifurcation in the branch migration (especially for long strands), concentration of the strands in the reaction, and the low diffusion constant of large oligonucleotides. Moreover, each full strand displacement reaction cycle generates byproducts to the solution, which may limit their use in specific applications. The closing kinetics of our system are comparable to similar systems functioning with strand displacement,[48] indicating that the closing process is affected more by how the overall design of the DNA origami system promotes the formation of the compact closed state, rather than the initial trigger. The advantage gained by the pH-sensitivity is reflected in the opening phase of the nanocapsules, where the response time is extremely fast and does not rely on the addition of further triggering elements into the system.

After the capsules had been closed at low pH and in the presence of a sufficient level of $MgCl_2$, we tested how their conformational state responds to physiological salt conditions. In the experiment presented in Figure 2B, we showed that closed nanocapsules can be introduced to a physiological NaCl concentration (150 mM) without any change in the FRET efficiency. To be able to carry out the measurements in a kinetic manner, the Mg^{2+} concentration (5, 10, or 15 mM) was not changed during the measurement. To study the possible effects of a low physiological Mg^{2+} concentration (∼0.6 mM in blood),[49] we also performed a separate experiment where closed pHL capsules (with 15 mM $MgCl_2$) were first diluted to the $MgCl_2$ concentration of 0.6 mM and after that introduced to a 150 mM NaCl concentration (see Supporting Information). Emission spectra collected from these samples showed no decrease of FRET efficiency from the $MgCl_2$ depletion, but in low-Mg^{2+} conditions, the FRET efficiency was slightly decreased (*ca.* 22%) after the addition of NaCl (Figure S4A). This observation is supported by the previous observation that Mg^{2+} ions might be easily replaced by monovalent Na^+ in the DNA origami structure at low-Mg^{2+} conditions (<1 mM), thus causing slightly deformed DNA objects.[50] In addition, we also characterized the FRET efficiency of closed pHL nanocapsules in the presence of 1% and 10% blood plasma (solution pH increases through addition of plasma, but nevertheless, it stays below 7.2) (Figure S4B). These results together show that the closed state can be maintained at physiologically relevant conditions, which can be considered an essential property for potential *in vivo* drug-delivery applications.

We also showed that the opening/closing cycle presented in Figure 2B can be repeated multiple times by the addition of small volumes of acetic acid or sodium hydroxide (Figure 2C). Here, the shorter closing period (90 min vs 300 min in Figure 2B) is not enough to reach the stabilization/plateau of the FRET efficiency in the closing phase. Nevertheless, the shapes of the FRET efficiency curves in each closing phase are very similar to each other, proving the reversibility of the capsule function. This shows that the closing process is not disturbed by repeated adjustment of the solution pH. When the same pH cycling was performed for opC and clC nanocapsules, no effect was observed in the FRET efficiency of opC, but the FRET efficiency of the clC gradually decreased over each sodium hydroxide addition. TEM images of clC samples before and after five rounds of pH cycling indicate that this is linked to the

DOI: 10.1021/acsnano.9b01857
ACS Nano 2019, 13, 5959−5967

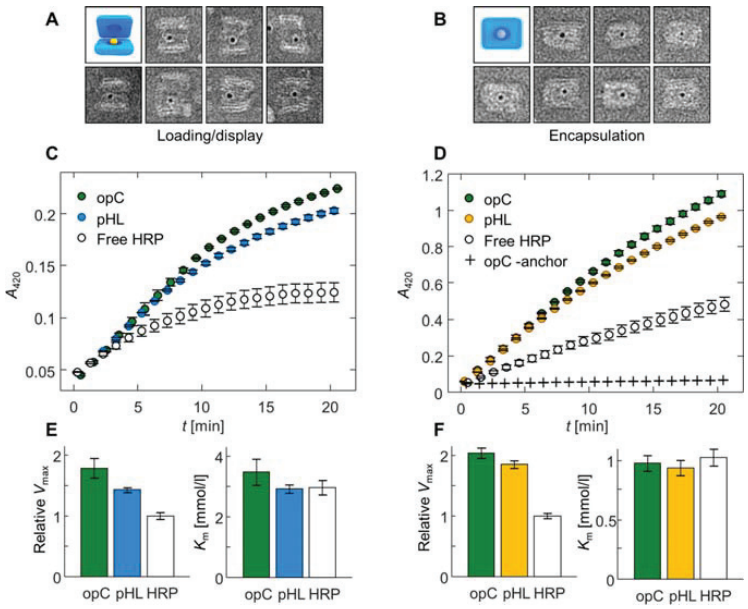

Figure 3. High-pH loading (left panel) and low-pH encapsulation (right panel) of AuNPs and HRP. (A) TEM images of nanocapsules in an open state (pH 8.2), displaying loaded AuNP cargo molecules. (B) AuNPs encapsulated within closed pHL nanocapsules at pH 6.4. The width of each frame in subfigures A and B is 50 nm. (C) Catalytic activity of HRP-loaded pHL and opC nanocapsules as well as free HRP at pH 7.8. Product formation (oxidation of ABTS to $ABTS^{\bullet+}$ by HRP) in the presence of 1 mM ABTS and 4 mM H_2O_2 is observed with an increase of $ABTS^{\bullet+}$ absorption at 420 nm. Values at each time point have been calculated as the mean of three parallel samples, and error bars represent the standard error of the mean. (D) Product formation at pH 6.4 (1 mM ABTS, 4 mM H_2O_2), including an opC control assembled without a cargo anchoring strand (opC-anchor). Product formation curves for all measured ABTS concentrations (0.125−4 mM) at both pH values are presented in Figure S8. (E) Maximum reaction velocities (V_{max}) and Michaelis constants (K_m) at pH 7.8 from the Michaelis−Menten fit to the initial product formation rates between 0 and 300 s in each sample type. V_{max} values have been normalized to the value of free HRP. Values for both V_{max} and K_m have been calculated as the weighted mean of fit results for three parallel samples, weighted by the fit error. Error bars show the error of the weighted mean. (F) V_{max} and K_m values at pH 6.4. The values and error bars were calculated as in subfigure E.

accumulation of structural damage (Figure S5). Furthermore, we tested that the effect is not related to Na^+ concentration (increasing up to 65 mM due to increasing volumes of sodium hydroxide) with a control experiment where equal concentration and volume of NaCl was added to the samples (data not shown).

After showing that the nanocapsule opening and closing can be reliably triggered by changing the solution pH, we loaded the nanocapsules in the open state with cargo molecules. We applied both AuNPs and HRP enzymes as two distinct model types of cargo. To visually examine the loading of cargos in the nanocapsule, AuNPs were used because of their high contrast in TEM images, while HRP was chosen for studying the effects of loading and encapsulation on cargo functionality. In the chosen encapsulation strategy, the cargo molecule is first conjugated to one or more DNA oligonucleotides. The conjugate is mixed with nanocapsules that present a complementary, single-stranded oligonucleotide in their inner cavity, so that hybridization of the complementary strands leads to attachment of the cargo inside the cavity (Figure 1B). The AuNP-DNA conjugates were prepared with a modified salting protocol,[51] and they were purified and mixed with a nanocapsule, followed by a thermal annealing to increase the loading yield. Analogous HRP-DNA conjugates were produced by covalently linking HRP *via* its surface lysines to thiol-modified oligonucleotides with the sulfosuccinimidyl 4-(*N*-maleimidomethyl)cyclohexane-1-carboxylate (sulfo-SMCC) cross-linker.

TEM images of AuNP-loaded nanocapsules show that the pHL nanocapsules can be successfully loaded by anchoring the particles into the nanocapsule cavity at high pH (Figure 3A). By counting the number of open nanocapsule structures that display a AuNP at the expected attachment site, we estimated that the loading yield of the particles is 40−55% (n = 110) (Figure S6). Decreasing the pH leads to cargo encapsulation, and importantly, TEM images confirm that the loaded cargo does not prevent the capsules from closing (Figure 3B). Likewise, the FRET efficiencies of HRP-loaded pHL and opC nanocapsules at pH 6.4 are identical to the corresponding capsule samples without cargo (Figure S7), so that the result obtained from individual structures under TEM is also generalizable to bulk solution.

In addition to immobilizing cargo molecules within the nanocapsules, we characterized how the functionality of the cargo responds to the loading and encapsulation process. Thus, we compared the enzymatic activity of HRP in three different sample types at both pH 6.4 and 7.8: free HRP without DNA strand(s), HRP inside pHL nanocapsules, and HRP inside opC nanocapsules. The measurements were performed by detecting the rate of ABTS oxidation by HRP in the presence of H_2O_2.

DOI: 10.1021/acsnano.9b01857
ACS Nano 2019, 13, 5959−5967

The oxidation of ABTS by HRP leads to the formation of an $ABTS^{\bullet+}$ radical, which has an absorption maximum at 420 nm, and therefore velocity of the process can be measured spectrometrically by following the increase of A_{420} after the substrate is mixed to HRP-containing samples.

We first ensured that the cargo attachment within the nanocapsules is specific to the cargo anchoring strand. Since HRP cannot be reliably detected in TEM images, the specificity was assessed with enzyme activity measurements. The opC capsules were assembled either with or without a cargo anchoring strand (additional opC-anchor control), mixed with HRP-DNA conjugates, and purified from unbound enzymes with PEG precipitation.[52] After purification, clear HRP activity was detected in the opC samples assembled with the cargo anchoring strand, while the opC-anchor controls showed virtually no activity (Figure 3D). In addition to confirming that HRP binding to the nanocapsules is specific to the anchoring strand, this shows that PEG precipitation efficiently removes unbound enzymes from the samples.

We observed that HRP remains fully functional after loading and encapsulation. Furthermore, the ABTS oxidation rates were higher in the nanocapsule-HRP samples (both pHL and opC) than in the samples containing free HRP at both measured pH values. This can be seen both directly in the product formation curves (Figure 3C,D) as well as in the maximum reaction rates (V_{max}) determined for each sample type by a Michaelis−Menten analysis of catalytic rates measured at varying ABTS concentrations (Figure 3E,F) (product formation plots and Michaelis−Menten curves for each sample are presented in Figure S8). All sample types displayed greater reaction rates at pH 6.4 than at pH 7.8, which is a predictable result based on the known fact that the catalytic activity of HRP is pH dependent, increasing with decreasing pH, and a pH optimum at pH 6.0−6.5.[53] At pH 6.4, the V_{max} of HRP inside both types of nanocapsules at 2 nM nanocapsule concentration was approximately 2 times larger than of free HRP at a 2 nM enzyme concentration (Figure 3F). At pH 7.8, the difference was similar but slightly less prominent (1.5-fold in pH lock capsule sample, and 1.8-fold in the open control) (Figure 3E). Since the quantity V_{max} depends on both enzyme concentration and its catalytic activity ($V_{max} = k_{cat}[E]_{total}$, where k_{cat} is the turnover number of the enzyme, and $[E]_{total}$ the enzyme concentration), differences in V_{max} can likewise signify either enzyme concentration or activity differences between the compared samples. While the exact HRP concentration in the HRP-loaded nanocapsules is unknown, the DNA origami concentration in the samples sets an effective 2 nM upper limit to the HRP concentration, since this would correspond to a 100% encapsulation yield. In this case, the results would indicate a 2-fold increase in the k_{cat} of HRP upon encapsulation. As with the 40−55% encapsulation yield estimated for the AuNPs, the real encapsulation yield of HRP is also likely smaller than 100%. Thus, the k_{cat} value can likewise be expected to be further enhanced. The activity increase is well in line with previous studies showing that the catalytic activity of enzymes conjugated to DNA nanostructures can differ significantly from free enzymes.[53−55] In the case of HRP, this has been observed as an activity increase; Zhao *et al.*[55] reported as high as a 10-fold enhancement of k_{cat} when HRP was confined inside DNA nanocages. While a comprehensive understanding of the mechanisms of such activity effects has not yet been reached,[56] one explanation for the higher catalytic rate of DNA origami-conjugated HRP has been suggested to be a lower local pH near the origami surface.[53] According to the activity profile reported by Zhang *et al.*,[53] HRP activity is also more sensitive to pH changes around pH 6.4 than pH 7.8, which could in part explain why we also observe a slightly larger activity enhancement at pH 6.4 than at pH 7.8.

Interestingly, at pH 6.4, the formation of $ABTS^{\bullet+}$ both in pHL and opC nanocapsules is highly similar (Figure 3D). The Michaelis constant K_m describes the ability of the substrate to interact with the enzyme, so that higher K_m values can indicate either that the enzymes are less accessible to the substrate or that their affinity toward the substrate at the specific conditions is lower. K_m values of HRP inside an open or closed nanocapsule, or of free HRP, show no significant differences between each other (Figure 3E,F) at either of the measured pHs. While it could be assumed that at pH 6.4, the closed state of the pHL nanocapsules blocks the diffusion of ABTS to the encapsulated HRP, the results on the contrary suggest that HRP is equally accessible to the substrate in all of the cases. This leads to a conclusion that the nanocapsules are porous enough for the low molecular weight (548.68 g/mol) ABTS to diffuse into the inner cavity. However, encapsulation still provides shielding from larger molecules. The pHL nanocapsules mixed at a closed, low pH state with AuNPs do not contain particles within the capsules (Figure S6), demonstrating that the DNA barrier effectively blocks these larger particles (5 nm gold core) from entering the nanocapsule cavity.

CONCLUSIONS

In this work, we have presented the design and characterization of a dynamic DNA origami nanocapsule. We have shown that the nanocapsule can be loaded with various types of molecular cargo, here AuNPs and HRP, and that the cargo can be selectively displayed after exposing the nanocapsule to the specified external cue. Our multilayer DNA origami-based carrier has been designed for high stability and protection of enclosed molecules and for functionalization with multiple stimuli-responsive units for cooperative actuation.

We have shown that when the nanocapsules were equipped with multiple DNA residues that form Hoogsteen triplexes in low pH, reconfiguration between open and closed conformational states could be induced with solution pH changes in a predictable and repeatable manner under physiologically relevant salt conditions. Application of Hoogsteen triplexes for pH-actuation gives an important aspect of programmability for the system. The pK_a can be chosen simply by selecting the base content of the latch strands, and the measured pK_a was seen to be in close agreement with the predicted value for the latch sequences.[22] As determined from FRET analysis, the conformational state of the nanocapsules is also highly sensitive to pH differences. An approximately 0.5 pH unit increase is sufficient to switch the bulk sample from a closed state to an open state with a very rapid response time.

In order to reach full functionality as a drug delivery vehicle, we envision that our system could still be further functionalized with additional stimuli-responsive or targeting groups for specific cell types. It could also be interesting to explore how various protein- or polymer-coating strategies[49,57] presented for static objects could be applied for such dynamic systems to increase the *in vivo* stability and compatibility while preserving the delicate functionality and dynamic properties of the system. All in all, the presented compatibility with physiologically

DOI: 10.1021/acsnano.9b01857
ACS Nano 2019, 13, 5959−5967

relevant medium, programmability of the pK_a value, high pH sensitivity, and fast kinetics of the opening give our system multiple intriguing properties in terms of the development of smart, targeted DNA-based drug delivery systems that are capable of responding to stimuli present in living organisms and that would function independently of additional external triggers.

METHODS

Nanocapsule Design and Assembly. The DNA nanocapsule was designed in a honeycomb lattice using caDNAno v 2.2.0,[58] and the three-dimensional structure was predicted with CanDo simulations.[59,60] Self-assembly of the structures was performed as a single batch reaction containing a 20 nM p8064 scaffold (Tilibit Nanosystems) and 7.5× excess of staple strands (Integrated DNA Technologies) in 1× capsule folding buffer (FOB) (1× capsule FOB: 1× TAE, 15 mM $MgCl_2$, 5 mM NaCl). The reactions were heated in G-storm G1 Thermal Cycler to 65 °C and annealed by cooling to 59 °C with a rate of 1 °C/15 min and then to 12 °C with rate 0.25 °C/45 min. The excess staple strands were removed from the solution using PEG precipitation in the presence of 7.5% (w/v) PEG 8000.[52] Folding yield was assessed by integration over the AGE band intensities (Figure S2A).

Fluorescence Measurements. FRET-labeled nanocapsule samples were analyzed with a Biotek Cytation 3 plate reader using black Costar flat bottom 96-well plates. The donor (Alexa Fluor 488) was excited at 460 nm and the acceptor (Alexa Fluor 546) at 560 nm. All FRET measurements were conducted at room temperature. FRET efficiency was calculated from the increase of acceptor emission in the presence of energy transfer:

$$E = \frac{I_{AD}\varepsilon_{AA} - I_{AA}\varepsilon_{AD}}{I_{AA}\varepsilon_{DD}}$$

where I_{AD} is the acceptor emission intensity following donor excitation, I_{AA} is the acceptor emission intensity (at 616 nm) after acceptor excitation, ε_{AA} is the acceptor extinction coefficient at the acceptor excitation wavelength (30,817 M^{-1} cm^{-1}), and ε_{AD} and ε_{DD} are the acceptor and donor extinction coefficients at the donor excitation wavelength (1985 $M^{-1}cm^{-1}$ and 19,848 $M^{-1}cm^{-1}$). Extinction coefficient values at the excitation wavelengths were calculated by combining the measured absorption spectra of the fluorophore-modified oligonucleotides with the fluorophore extinction coefficients at absorption maxima provided by IDT. Calculating the FRET efficiency as described enables using the value of I_{AA} as an internal reference for acceptor emission intensity (and implicitly, quantum yield) in the absence of energy transfer. In addition, the equation includes an assumption that donor and acceptor fluorophores are present in the sample in a 1:1 molar ratio, which can be reasonably assumed for a DNA origami system where both the number and location of the fluorophores are highly controlled.

For the pH titration experiment, nanocapsule samples folded in the normal FOB (pH 8.2) were resuspended to pH-adjusted buffers (pH 6.0−8.0 in 0.2 pH unit intervals) after PEG purification of excess staples. In order to determine the values for the closed state, FRET efficiency E_{FRET} (closed), pK_a, and the Hill coefficient n, FRET efficiencies measured at each pH were fitted with the Hill equation:

$$E_{FRET} = \frac{E_{FRET}(\text{closed}) \times (10^{-pH})^n}{(10^{-pK_a})^n + (10^{-pH})^n}$$

Kinetic Fluorescence Measurements. FRET efficiency measurements for the kinetic response of the FRET efficiency after solution pH changes were based on single-wavelength recordings of the sample emission intensity at 517 nm (I_{DD}) and 616 nm (I_{AD}) after donor excitation at 460 nm. Changes in capsule conformation were followed by calculating relative FRET efficiency as

$$E_{rel} = \frac{I_{AD}}{I_{AD} + I_{DD}}$$

where pH of the sample was cycled between 6.1−6.3 and 7.7−8.0 by adding small volumes (2−4 μL) of 0.5 M acetic acid or 0.5 M sodium hydroxide.

TEM Imaging. Nanocapsule samples which were purified with PEG precipitation were absorbed on plasma cleaned (20 s oxygen plasma flash) Formvar carbon-coated copper grids (FCF400-Cu, Electron Microscopy Science) for TEM imaging. A 3 μL droplet of DNA origami solution was applied onto the carbon-coated side of the TEM grid, and the excess sample solution was blotted away with filter paper after an incubation of 2 min. The samples were stained using a 2% aqueous uranyl formate solution with 25 mM NaOH. Excess stain solution was blotted away with filter paper after 40 s. After these procedures, the sample was left to dry under ambient conditions for at least 30 min before imaging. The TEM images were obtained using a FEI Tecnai 12 Bio-Twin instrument operated at an acceleration voltage of 120 kV.

AuNP-DNA Conjugate Preparation and AuNP Encapsulation. The steps of AuNP-DNA conjugation were all carried out at 40 °C with constant shaking, if not stated otherwise. First, 20 μL of AuNPs of 5 nm diameter (Sigma-Aldrich) was incubated with 0.4 μL 1% SDS water solution for 20 min. Then 2 μL of thiolated oligos (100 μM, Integrated DNA Technologies) was added and incubated for 30 min. In the salting process, first 0.2 μL of 2.5 M NaCl was added at 2 min interval for 6 times, followed by additions of 0.4 μL and 0.8 μL of NaCl for 6 times each at the same interval. After the salting, the AuNP-DNA conjugates were mixed with 30 μL of folding buffer (with 0.02% SDS) and incubated for 1 h. Finally, the conjugates were purified from the free oligos by spin-filtration through a 100 kDa MWCO Amicon filter at RT and 14000 rcf for 10 min and repeated for 4 times. In each filtration step, 480 μL of folding buffer at either pH 6 or pH 8 was added in order to match the nanocapsule sample pH. For the AuNP encapsulation, the AuNP-DNA and nanocapsule with complementary cargo strands were mixed in a 10:1 AuNP:origami ratio and thermally annealed from 40 to 20 °C (−0.1 °C/min).

HRP-DNA Conjugation and HRP Encapsulation. HRP (Thermo Scientific) was covalently conjugated to single-stranded 5′-thiol-modified DNA oligonucleotides (Integrated DNA Technologies) by using the sulfosuccinimidyl 4-(*N*-maleimidomethyl)-cyclohexane-1-carboxylate (sulfo-SMCC) cross-linker (Thermo Scientific). To form maleimide-activated HRP, HRP and sulfo-SMCC were individually dissolved in 50 mM phosphate buffer (pH 7.2), mixed in a 1:20 enzyme:cross-linker molar ratio, and incubated at RT for 2 h. The thiol groups in the oligonucleotides were deprotected by incubating the strands dissolved in water with an 100-fold molar excess of tris(2-carboxyethyl)phosphine (TCEP) (Aldrich Chemistry) for 1−2 h at RT. The unreacted cross-linker in the HRP-sulfo-SMCC mixture, as well as excess TCEP in the DNA-TCEP mixture, was removed by spin-filtration with Amicon Ultra 10 kDa cutoff filters (EMD Millipore). One mM EDTA was added in the oligo buffer during spin-filtration. Maleimide-activated HRP was then mixed with the thiol-modified oligos in a 1:2 DNA:enzyme ratio. HRP was used in excess in order to minimize the amount of free oligonucleotides in the product. HRP contains six surface lysines, out of which three have been shown to be accessible to chemical modifications,[61] so conjugation with thiol-modified oligonucleotides can be expected to yield a mixture of conjugates with different HRP:DNA ratios. Since this heterogeneity is not relevant for loading the nanocapsule, conjugate composition was not further analyzed. Thus, the conjugates were used without further purification and mixed in a 15−20-fold molar excess with cargo-strand containing nanocapsules in 1× FOB (pH 8.2). To maximize the encapsulation yield, the HRP-nanocapsule mixture was thermally annealed (from 40 to 20 °C, −0.1 °C/40 s). After annealing, the samples were incubated further for 12 h at +4 °C, after which unbound enzymes were removed by PEG precipitation. Enzyme-loaded, purified nanocapsules were resuspended in 1× FOB at either pH 6.4 or 7.8, and the enzymatic activity in the samples was measured after overnight incubation at +4 °C.

HRP Activity Measurements. Enzymatic activity of HRP was determined by measuring the rate of ABTS oxidation in the presence

DOI: 10.1021/acsnano.9b01857
ACS Nano 2019, 13, 5959−5967

of H_2O_2 at varying ABTS concentrations. Measurements were performed in 1× FOB adjusted to pH 6.4 or pH 7.8 with acetic acid, at either 2 nM HRP concentration (free HRP samples) or 2 nM DNA origami concentration (HRP-loaded nanocapsule samples) with a total 80 μL sample volume on a clear 96-well microwell plate (Thermo Scientific) at +25 °C. The samples were first diluted with a FOB containing H_2O_2, in a 4 mM final H_2O_2 concentration. Immediately after this, an ABTS solution was added to the sample in either 0.125 mM, 0.25 mM, 0.5 mM, 1 mM, 2 mM, or 4 mM final ABTS concentration. Formation of the oxidized product $ABTS^{\bullet+}$ was monitored by measuring the A_{420} of the samples in 20 s intervals over 20 min with a Cytation 3 cell imaging multimode reader (BioTek). To determine V_{max} and K_m for each sample type, the initial oxidation rates for each ABTS concentration were determined by fitting a linear equation to the data points at the first 300 s after starting the reaction, and a Michaelis–Menten equation,

$$v = \frac{V_{max} \times [ABTS]}{K_m + [ABTS]}$$

was fitted to the data points. Curve fitting was done with OriginPro version 2019 (OriginLab Corporation, Northampton, MA, USA).

ASSOCIATED CONTENT

Supporting Information

The Supporting Information is available free of charge on the ACS Publications website at DOI: 10.1021/acsnano.9b01857.

Supporting methods, a list of staple strands for pHL, opC, and clC nanocapsules, figures showing the nanocapsule design, additional FRET measurements with opC and clC samples and HRP-loaded nanocapsules, characterization of nanocapsules with AGE, aggregation caused by low pH and high Mg^{2+} concentrations, Mg^{2+} depletion and plasma experiments, supplementary TEM images of pH cycling and AuNP loading, and product formation at all ABTS concentrations and Michaelis–Menten curves for HRP activity measurements (PDF)

AUTHOR INFORMATION

Corresponding Author

*E-mail: veikko.linko@aalto.fi.

ORCID

Heini Ijäs: 0000-0001-7880-332X
Iiris Hakaste: 0000-0001-8434-9039
Boxuan Shen: 0000-0002-1107-828X
Mauri A. Kostiainen: 0000-0002-8282-2379
Veikko Linko: 0000-0003-2762-1555

Notes

The authors declare no competing financial interest.

ACKNOWLEDGMENTS

We acknowledge the provision of facilities and technical support by Aalto University at OtaNano - Nanomicroscopy Center (Aalto-NMC). The financial support through the Academy of Finland (grant numbers 286845, 308578, 303804, 267497), Jane and Aatos Erkko Foundation, and Sigrid Jusélius Foundation is gratefully acknowledged. This work was carried out under the Academy of Finland Centers of Excellence Programme (2014–2019). We would also like to thank J. Ihalainen for helpful discussions and comments on the manuscript and J. Rumfeldt for help in interpreting the pH titration data.

REFERENCES

(1) Seeman, N. C.; Sleiman, H. F. DNA Nanotechnology. *Nat. Rev. Mater.* **2017**, *3*, 17068.
(2) Bathe, M.; Rothemund, P. W. K. DNA Nanotechnology: A Foundation for Programmable Nanoscale Materials. *MRS Bull.* **2017**, *42*, 882–888.
(3) Nummelin, S.; Kommeri, J.; Kostiainen, M. A.; Linko, V. Evolution of Structural DNA Nanotechnology. *Adv. Mater.* **2018**, *30*, 1703721.
(4) Roller, E.-M.; Argyropoulos, C.; Högele, A.; Liedl, T.; Pilo-Pais, M. Plasmon–Exciton Coupling Using DNA Templates. *Nano Lett.* **2016**, *16*, 5962–5966.
(5) Gopinath, A.; Miyazono, E.; Faraon, A.; Rothemund, P. W. K. Engineering and Mapping of Nanocavity Emission *via* Precision Placement of DNA Origami. *Nature* **2016**, *535*, 401–405.
(6) Kuzyk, A.; Jungmann, R.; Acuna, G. P.; Liu, N. DNA Origami Route for Nanophotonics. *ACS Photonics* **2018**, *5*, 1151–1163.
(7) Shen, B.; Kostiainen, M. A.; Linko, V. DNA Origami Nanophotonics and Plasmonics at Interfaces. *Langmuir* **2018**, *34*, 14911–14920.
(8) Steinhauer, C.; Jungmann, R.; Sobey, T. L.; Simmel, F. C.; Tinnefeld, P. DNA Origami as a Nanoscopic Ruler for Super-Resolution Microscopy. *Angew. Chem., Int. Ed.* **2009**, *48*, 8870–8873.
(9) Graugnard, E.; Hughes, W. L.; Jungmann, R.; Kostiainen, M. A.; Linko, V. Nanometrology and Super-Resolution Imaging with DNA. *MRS Bull.* **2017**, *42*, 951–959.
(10) Maune, H. T.; Han, S.-P.; Barish, R. D.; Bockrath, M.; Goddard, W. A., III; Rothemund, P. W. K.; Winfree, E. Self-Assembly of Carbon Nanotubes into Two-Dimensional Geometries Using DNA Origami Templates. *Nat. Nanotechnol.* **2010**, *5*, 61–66.
(11) Ramakrishnan, S.; Subramaniam, S.; Stewart, A. F.; Grundmeier, G.; Keller, A. Regular Nanoscale Protein Patterns *via* Directed Adsorption through Self-Assembled DNA Origami Masks. *ACS Appl. Mater. Interfaces* **2016**, *8*, 31239–31247.
(12) Yurke, B.; Turberfield, A. J.; Mills, A. P., Jr.; Simmel, F. C.; Neumann, J. L. A DNA-Fuelled Machine Made of DNA. *Nature* **2000**, *406*, 605–608.
(13) Zhang, D. Y.; Seelig, G. Dynamic DNA Nanotechnology Using Strand-Displacement Reactions. *Nat. Chem.* **2011**, *3*, 103–113.
(14) Ijäs, H.; Nummelin, S.; Shen, B.; Kostiainen, M. A.; Linko, V. Dynamic DNA Origami Devices: From Strand-Displacement Reactions to External-Stimuli Responsive Systems. *Int. J. Mol. Sci.* **2018**, *19*, 2114.
(15) Rothemund, P. W. K. Folding DNA to Create Nanoscale Shapes and Patterns. *Nature* **2006**, *440*, 297–302.
(16) Marras, A. E.; Zhou, L.; Su, H.-J.; Castro, C. E. Programmable Motion of DNA Origami Mechanisms. *Proc. Natl. Acad. Sci. U. S. A.* **2015**, *112*, 713–718.
(17) Amir, Y.; Ben-Ishay, E.; Levner, D.; Ittah, S.; Abu-Horowitz, A.; Bachelet, I. Universal Computing by DNA Origami Robots in a Living Animal. *Nat. Nanotechnol.* **2014**, *9*, 353–357.
(18) Thubagere, A. J.; Li, W.; Johnson, R. F.; Chen, Z.; Doroudi, S.; Lee, Y. L.; Izatt, G.; Wittman, S.; Srinivas, N.; Woods, D.; Winfree, E.; Qian, L. A Cargo-Sorting DNA Robot. *Science* **2017**, *357*, No. eaan6558.
(19) Castro, C. E.; Dietz, H.; Högberg, B. DNA Origami Devices for Molecular-Scale Precision Measurements. *MRS Bull.* **2017**, *42*, 925–929.
(20) Kuzyk, A.; Schreiber, R.; Fan, Z.; Pardatscher, G.; Roller, E.-M.; Högele, A.; Simmel, F. C.; Govorov, A. O.; Liedl, T. DNA-Based Self-Assembly of Chiral Plasmonic Nanostructures with Tailored Optical Response. *Nature* **2012**, *483*, 311–314.
(21) Kuzyk, A.; Schreiber, R.; Zhang, H.; Govorov, A. O.; Liedl, T.; Liu, N. Reconfigurable 3D Plasmonic Metamolecules. *Nat. Mater.* **2014**, *13*, 862–866.
(22) Kuzyk, A.; Urban, M. J.; Idili, A.; Ricci, F.; Liu, N. Selective Control of Reconfigurable Chiral Plasmonic Metamolecules. *Sci. Adv.* **2017**, *3*, No. e1602803.

DOI: 10.1021/acsnano.9b01857
ACS Nano 2019, 13, 5959–5967

(23) Song, J.; Li, Z.; Wang, P.; Meyer, T.; Mao, C.; Ke, Y. Reconfiguration of DNA Molecular Arrays Driven by Information Relay. *Science* **2017**, *357*, No. eaan3377.
(24) Douglas, S. M.; Bachelet, I.; Church, G. M. A Logic-Gated Nanorobot for Targeted Transport of Molecular Payloads. *Science* **2012**, *335*, 831−834.
(25) Li, S.; Jiang, Q.; Liu, S.; Zhang, Y.; Tian, Y.; Song, C.; Wang, J.; Zou, Y.; Anderson, G. J.; Han, J. Y.; Chang, Y.; Liu, Y.; Zhang, C.; Chen, L.; Zhou, G.; Nie, G.; Yan, H.; Ding, B.; Zhao, Y. A DNA Nanorobot Functions as a Cancer Therapeutic in Response to a Molecular Trigger *In Vivo*. *Nat. Biotechnol.* **2018**, *36*, 258−264.
(26) Linko, V.; Ora, A.; Kostiainen, M. A. DNA Nanostructures as Smart Drug-Delivery Vehicles and Molecular Devices. *Trends Biotechnol.* **2015**, *33*, 586−594.
(27) Surana, S.; Shenoy, A. R.; Krishnan, Y. Designing DNA Nanodevices for Compatibility with the Immune System of Higher Organisms. *Nat. Nanotechnol.* **2015**, *10*, 741−747.
(28) Banerjee, A.; Bhatia, D.; Saminathan, A.; Chakraborty, S.; Kar, S.; Krishnan, Y. Controlled Release of Encapsulated Cargo from a DNA Icosahedron using a Chemical Trigger. *Angew. Chem.* **2013**, *125*, 6992−6995.
(29) Takenaka, T.; Endo, M.; Suzuki, Y.; Yang, Y.; Emura, T.; Hidaka, K.; Kato, T.; Miyata, T.; Namba, K.; Sugiyama, H. Photoresponsive DNA Nanocapsule Having an Open/Close System for Capture and Release of Nanomaterials. *Chem. - Eur. J.* **2014**, *20*, 14951−14954.
(30) Turek, V. A.; Chikkaraddy, R.; Cormier, S.; Stockham, B.; Ding, T.; Keyser, U. F.; Baumberg, J. J. Thermo-Responsive Actuation of a DNA Origami Flexor. *Adv. Funct. Mater.* **2018**, *28*, 1706410.
(31) Andersen, E. S.; Dong, M.; Nielsen, M. M.; Jahn, K.; Subramani, R.; Mamdouh, W.; Golas, M. M.; Sander, B.; Stark, H.; Oliveira, C. L. P.; Pedersen, J. S.; Birkedal, V.; Besenbacher, F.; Gothelf, K. V.; Kjems, J. Self-Assembly of a Nanoscale DNA Box with a Controllable Lid. *Nature* **2009**, *459*, 73−76.
(32) Tohgasaki, T.; Shitomi, Y.; Feng, Y.; Honna, S.; Emura, T.; Hidaka, K.; Sugiyama, H.; Endo, M. A Photocaged DNA Nanocapsule for Controlled Unlocking and Opening inside the Cell. *Bioconjugate Chem.* **2019**, DOI: 10.1021/acs.bioconjchem.9b00040.
(33) Webb, B. A.; Chimenti, M.; Jacobson, M. P.; Barber, D. L. Dysregulated pH: A Perfect Storm for Cancer Progression. *Nat. Rev. Cancer* **2011**, *11*, 671−677.
(34) White, K. A.; Grillo-Hill, B. K.; Barber, D. L. Cancer Cell Behaviors Mediated by Dysregulated pH Dynamics at a Glance. *J. Cell Sci.* **2017**, *130*, 663−669.
(35) Benabou, S.; Aviño, A.; Eritja, R.; González, C.; Gargallo, R. Fundamental Aspects of the Nucleic Acid I-Motif Structures. *RSC Adv.* **2014**, *4*, 26956−26980.
(36) Hu, Y.; Cecconello, A.; Idili, A.; Ricci, F.; Willner, I. Triplex DNA Nanostructures: From Basic Properties to Applications. *Angew. Chem., Int. Ed.* **2017**, *56*, 15210−15233.
(37) Chandrasekaran, A. R.; Rusling, D. A. Triplex-Forming Oligonucleotides: A Third Strand for DNA Nanotechnology. *Nucleic Acids Res.* **2018**, *46*, 1021−1037.
(38) Kuzuya, A.; Watanabe, R.; Yamanaka, Y.; Tamaki, T.; Kaino, M.; Ohya, Y. Nanomechanical DNA Origami pH Sensors. *Sensors* **2014**, *14*, 19329−19335.
(39) Wu, N.; Willner, I. pH-Stimulated Reconfiguration and Structural Isomerization of Origami Dimer and Trimer Systems. *Nano Lett.* **2016**, *16*, 6650−6655.
(40) Majikes, J. M.; Ferraz, L. C. C.; LaBean, T. H. pH-driven Actuation of DNA Origami *via* Parallel I-Motif Sequences in Solution and on Surfaces. *Bioconjugate Chem.* **2017**, *28*, 1821−1825.
(41) Burns, J. R.; Lamarre, B.; Pyne, A. L. B.; Noble, J. E.; Ryadnov, M. G. DNA Origami Inside-Out Viruses. *ACS Synth. Biol.* **2018**, *7*, 767−773.
(42) Liu, Z.; Li, Y.; Tian, C.; Mao, C. A Smart DNA Tetrahedron That Isothermally Assembles or Dissociates in Response to the Solution pH Value Changes. *Biomacromolecules* **2013**, *14*, 1711−1714.
(43) Kim, S. H.; Kim, K. R.; Ahn, D. R.; Lee, J. E.; Yang, E. G.; Kim, S. Y. Reversible Regulation of Enzyme Activity by pH-Responsive Encapsulation in DNA Nanocages. *ACS Nano* **2017**, *11*, 9352−9359.
(44) Ottaviani, A.; Iacovelli, F.; Idili, A.; Falconi, M.; Ricci, F.; Desideri, A. Engineering a Responsive DNA Triple Helix into an Octahedral DNA Nanostructure for a Reversible Opening/Closing Switching Mechanism: a Computational and Experimental Integrated Study. *Nucleic Acids Res.* **2018**, *46*, 9951−9959.
(45) Idili, A.; Vallée-Bélisle, A.; Ricci, F. Programmable pH-Triggered DNA Nanoswitches. *J. Am. Chem. Soc.* **2014**, *136*, 5836−5839.
(46) Kellum, J. A. Determinants of Blood pH in Health and Disease. *Crit. Care* **2000**, *4*, 6−14.
(47) Marras, A. E.; Shi, Z.; Lindell, M. G.; Patton, R. A.; Huang, C.-M.; Zhou, L.; Su, H.-J.; Arya, G.; Castro, C. E. Cation-Activated Avidity for Rapid Reconfiguration of DNA Nanodevices. *ACS Nano* **2018**, *12*, 9484−9494.
(48) Grossi, G.; Jepsen, M. D. E.; Kjems, J.; Andersen, E. S. Control of Enzyme Reactions by a Reconfigurable DNA Nanovault. *Nat. Commun.* **2017**, *8*, 992.
(49) Bila, M.; Kurisinkal, E. E.; Bastings, M. M. C. Engineering a Stable Future for DNA Origami as a Biomaterial. *Biomater. Sci.* **2019**, *7*, 532−541.
(50) Kielar, C.; Xin, Y.; Shen, B.; Kostiainen, M. A.; Grundmeier, G.; Linko, V.; Keller, A. On the Stability of DNA Origami Nanostructures in Low-Magnesium Buffers. *Angew. Chem., Int. Ed.* **2018**, *57*, 9470−9474.
(51) Heck, C.; Kanehira, Y.; Kneipp, J.; Bald, I. Placement of Single Proteins within the SERS Hot Spots of Self-Assembled Silver Nanolenses. *Angew. Chem., Int. Ed.* **2018**, *57*, 7444−7447.
(52) Stahl, E.; Martin, T. G.; Praetorius, F.; Dietz, H. Facile and Scalable Preparation of Pure and Dense DNA Origami Solutions. *Angew. Chem., Int. Ed.* **2014**, *53*, 12735−12740.
(53) Zhang, Y.; Tsitkov, S.; Hess, H. Proximity Does Not Contribute to Activity Enhancement in the Glucose Oxidase-Horseradish Peroxidase Cascade. *Nat. Commun.* **2016**, *7*, 13982.
(54) Lin, J.-L.; Wheeldon, I. Kinetic Enhancements in DNA−Enzyme Nanostructures Mimic the Sabatier Principle. *ACS Catal.* **2013**, *3*, 560−564.
(55) Zhao, Z.; Fu, J.; Dhakal, S.; Johnson-Buck, A.; Liu, M.; Zhang, T.; Woodbury, N. W.; Liu, Y.; Walter, N. G.; Yan, H. Nanocaged Enzymes with Enhanced Catalytic Activity and Increased Stability Against Protease Digestion. *Nat. Commun.* **2016**, *7*, 10619.
(56) Küchler, A.; Yoshimoto, M.; Luginbühl, S.; Mavelli, F.; Walde, P. Enzymatic Reactions in Confined Environments. *Nat. Nanotechnol.* **2016**, *11*, 409−420.
(57) Ramakrishnan, S.; Ijäs, H.; Linko, V.; Keller, A. Structural Stability of DNA Origami Nanostructures Under Application-Specific Conditions. *Comput. Struct. Biotechnol. J.* **2018**, *16*, 342−349.
(58) Douglas, S. M.; Marblestone, A. H.; Teerapittayanon, S.; Vazquez, A.; Church, G. M.; Shih, W. M. Rapid Prototyping of 3D DNA-Origami Shapes with caDNAno. *Nucleic Acids Res.* **2009**, *37*, 5001−5006.
(59) Castro, C. E.; Kilchherr, F.; Kim, D. N.; Shiao, E. L.; Wauer, T.; Wortmann, P.; Bathe, M.; Dietz, H. A Primer to Scaffolded DNA Origami. *Nat. Methods* **2011**, *8*, 221−229.
(60) Kim, D.-N.; Kilchherr, F.; Dietz, H.; Bathe, M. Quantitative Prediction of 3D Solution Shape and Flexibility of Nucleic Acid Nanostructures. *Nucleic Acids Res.* **2012**, *40*, 2862−2868.
(61) O'Brien, A. M.; Ó'Fágáin, C.; Nielsen, P. F.; Welinder, K. G. Location of Crosslinks in Chemically Stabilized Horseradish Peroxidase: Implications for Design of Crosslinks. *Biotechnol. Bioeng.* **2001**, *76*, 277−284.

DOI: 10.1021/acsnano.9b01857
ACS Nano 2019, 13, 5959−5967

Supporting Information

Reconfigurable DNA Origami Nanocapsule for pH-Controlled Encapsulation and Display of Cargo

Heini Ijäs[†‡], Iiris Hakaste[†], Boxuan Shen[†], Mauri A. Kostiainen[†§], and Veikko Linko[†§]*

[†] Biohybrid Materials, Department of Bioproducts and Biosystems, Aalto University, 00076 Aalto, Finland

[‡] University of Jyväskylä, Nanoscience Center, Department of Biological and Environmental Science, P.O. Box 35, 40014 University of Jyväskylä, Finland

[§] HYBER Center of Excellence, Department of Applied Physics, Aalto University, 00076 Aalto, Finland

Supplementary methods

Agarose gel electrophoresis (AGE). 2% agarose gels were prepared in two different buffer systems: 1× TAE with 11 mM $MgCl_2$ (pH 8.2) or 45 mM MES, 25 mM Tris with 11 mM $MgCl_2$ (pH 6.4). Gels were run for 50 minutes with 90 V on an ice bath. Normal gels were dyed with ethidium bromide and samples loaded with New England Biolabs 6× loading dye, and imaged with BioRad ChemiDoc XRS+. Fluorescent gels were prepared by loading samples with self-made loading dye (1× containing 2.5 w-% Ficoll 400, 3.3 mM Tris-HCl and 0.015 w-% bromophenol blue) and imaged with BioRad ChemiDoc MP imaging system using channels Alexa Fluor 488 (excitation filter 470/30 and emission filter 532/28) and Alexa Fluor 546 (excitation filter 530/28 and emission filter 602/50).

$MgCl_2$ depletion FRET experiments. To study the stability of the closed pHL nanocapsules in low Mg^{2+} (0.6 mM) concentration and subsequent introduction into physiological (150 mM) NaCl concentration, pHL nanocapsules in 1× FOB (pH 6.4) were exchanged to low-Mg^{2+} buffer by spin-filtration. Samples were first diluted with 11 mM Tris buffer at pH 6.4, so that final concentrations of buffer components were 11.2 mM Tris, 0.8 mM acetic acid, 0.04 mM EDTA, 0.6 mM $MgCl_2$, and 0.2 mM NaCl. The diluted sample was then concentrated back to original volume with 100 kDa MWCO Amicon Ultra 100 kDa cutoff centrifugal filters (6000 rcf). For 150 mM NaCl sample, NaCl concentration was adjusted after spin-filtration by adding 5 M NaCl. Emission spectra were collected similarly to previous FRET experiments described in the text

FRET measurements in the presence of blood plasma. In order to test whether closed pHL nanocapsules remain in a closed state after introduction to plasma, emission spectra were measured from pHL nanocapsules in 1× FOB (pH 6.4) after addition of either 1% or 10% plasma from human (Sigma). Emission spectrum of 1% plasma sample was measured 110 min after addition of plasma. 10% plasma sample was first incubated for 72 min in the presence of 1% plasma, after which plasma volume was increased to 10% and spectrum was collected after 40 minutes of incubation. Changes in the FRET signal were first followed with kinetic measurements to ensure that fluorescence signals had stabilized. Emission spectra were then collected similarly to previous FRET experiments described in the text.

Supplementary figures

Supplementary tables S1–S5. List of staple strands.

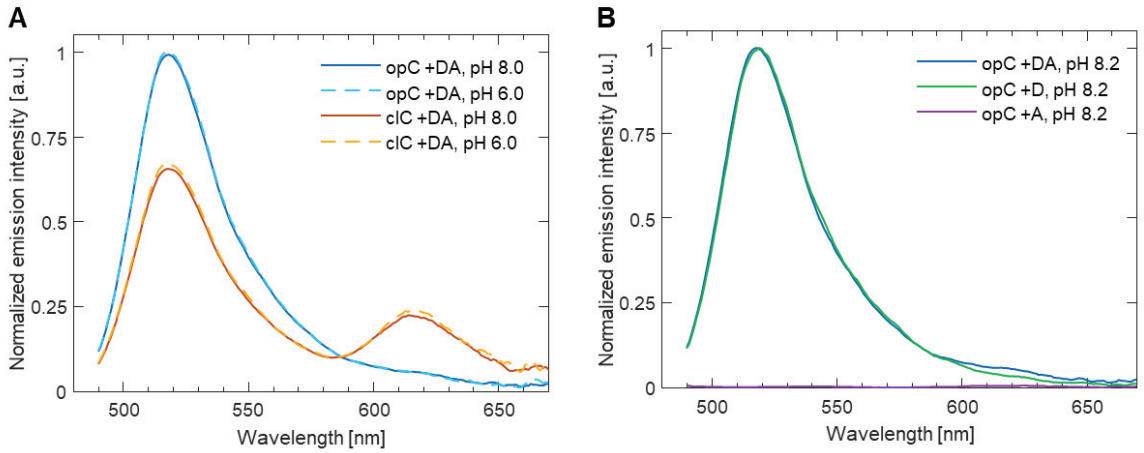

Figure S1. Additional FRET controls. (A) Emission spectra of permanently open (opC) and closed (clC) control samples labeled with both A488 (D) and A594 (A), and measured at pH 6.0 and 8.0 after 460 nm excitation. Emission profiles and FRET efficiencies of the samples are not affected by pH change, indicating that the conformation of opC and clC is not affected by pH and furthermore, that pH change alone does not affect the emission properties of the FRET pair. (B) Comparison of opC sample emission after 460 nm excitation when labeled either with both FRET dyes (opC +DA), or partially labeled with only the donor (opC +D) or acceptor (opC +A). Direct acceptor excitation at the applied donor excitation wavelength is minimal, as seen in the lack of fluorescence in the opC +A sample. Comparison of opC +D to the opC +DA sample shows that even in the open state, presence of the donor leads to a low acceptor emission indicating FRET. All spectra have been normalized to acceptor emission intensity in the sample after excitation at 560 nm. Acceptor intensity after direct excitation at a wavelength where the donor does not absorb can be used as an internal reference for fluorophore concentration.

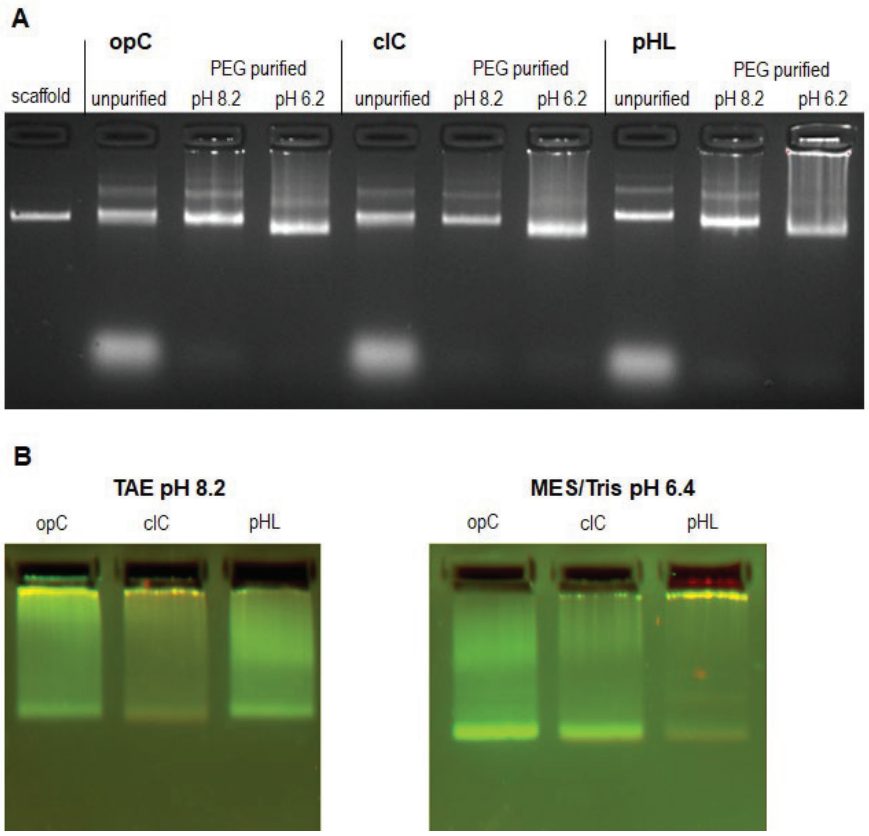

Figure S2. Characterization of the folding quality and electrophoretic mobility of opC, clC, and pHL nanocapsules with agarose gel electrophoresis (AGE). (A) Comparison of the electrophoretic mobility of different sample types before PEG purification of excess staples, and after PEG purification of excess staples and resuspension into 1× FOB (1× TAE, 15 mM $MgCl_2$, 5 mM NaCl) at either pH 8.2 or pH 6.2. Electrophoretic mobility of the nanocapsules is not observably affected by the open/closed state. (B) FRET-labeled capsule samples in 2% agarose gels at either pH 8.2 or pH 6.4. Green channel: donor excitation and detection; red channel: acceptor excitation and detection.

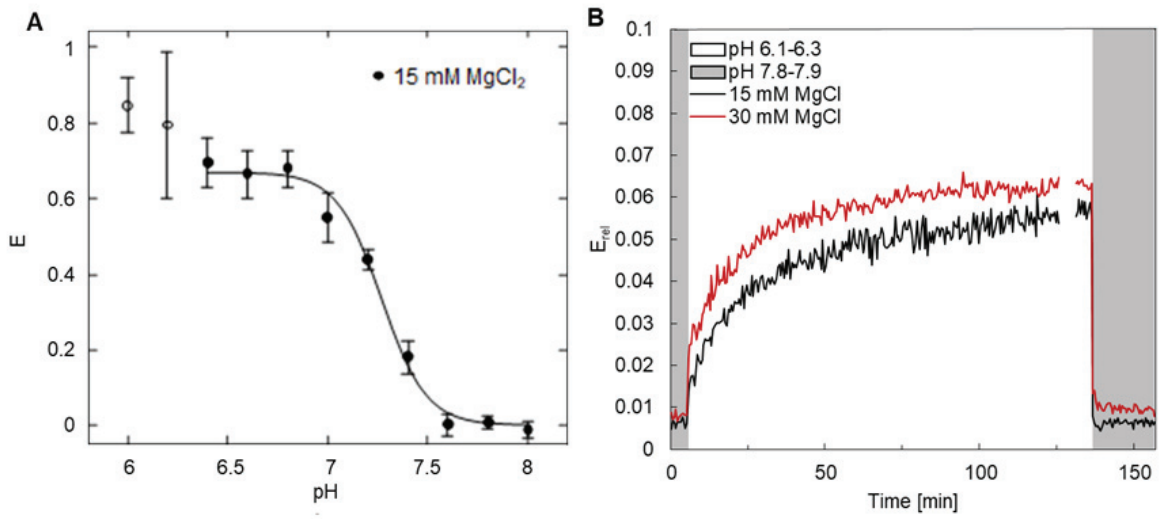

Figure S3. Aggregation of nanocapsules. (A) FRET efficiency of pHL nanocapsules with datapoints measured below pH 6.4. The increase of FRET efficiency at pH < 6.4 (uncolored data points) was accounted for sample aggregation and/or instability at low pH. (B) Kinetic measurement of the closing of pH-latch samples at 15 mM $MgCl_2$ and 30 mM $MgCl_2$. Curves show that the FRET efficiency values or closing kinetics are not significantly different between the 30 mM sample and the 15 mM sample, but the fluorescence intensity recordings of the 30 mM sample (raw data, not shown) show heavy fluctuation of the signal linked to scattering produced by large aggregates.

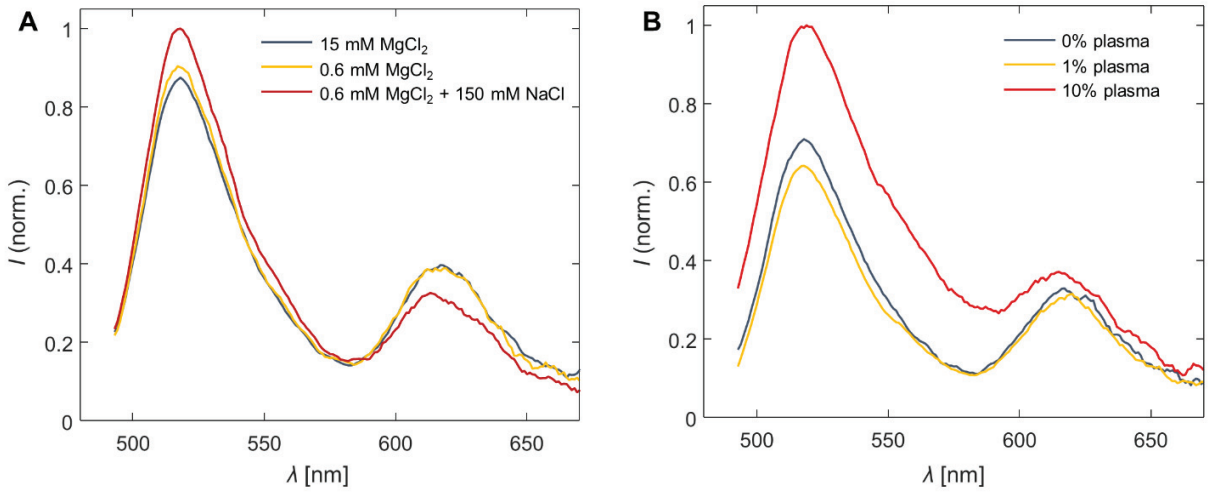

Figure S4. Effect of Mg^{2+} depletion and blood plasma on closed pHL nanocapsules at pH 6.4 studied with FRET. (A) Emission spectra of pHL nanocapsules in 1× FOB pH 6.4 (containing 15 mM $MgCl_2$, 5 mM NaCl), after buffer exchange to low-Mg^{2+} buffer (0.6 mM $MgCl_2$, 0.2 mM NaCl, pH 6.4), and after addition of 150 mM NaCl into theC low-Mg^{2+} sample. FRET efficiency decreases *ca.* 22% upon addition of NaCl. (B) Emission spectra of pHL nanocapsules in 1× FOB (pH 6.4) supplemented with different volumes of plasma. 10% plasma significantly obstructs the fluorescence measurement through increased scattering, preventing a reliable calculation of FRET efficiency from the spectrum. 10% plasma was also observed to increase sample pH (from 6.4 to above 7.0). All spectra in subfigures (A) and (B) have been scaled according to acceptor emission intensity at 616 nm after 560 nm direct excitation.

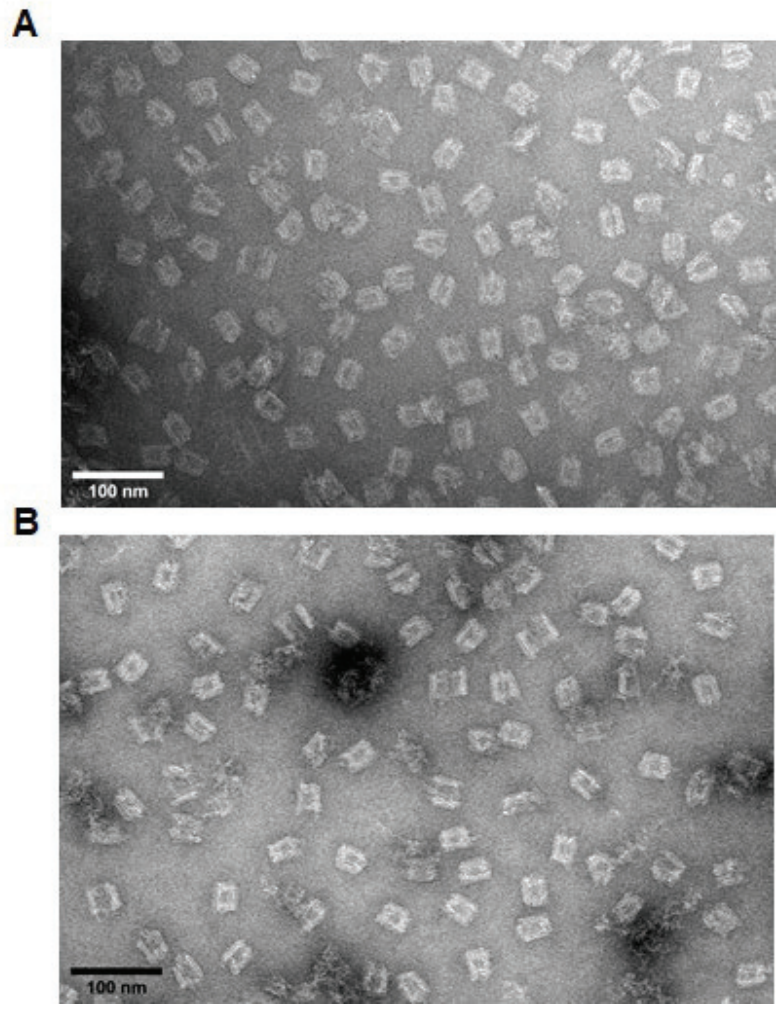

Figure S5. TEM verification of structural damage caused to the clC sample by repeated pH cycling. (A) clC sample at pH 6.3 after the first addition of acetic acid (pH decrease). (B) The same sample at pH 6.3, after changing the pH five times between 7.7 and 6.3 with additions of acetic acid or sodium hydroxide. It has been noted the $MgCl_2$ concentration decreases to ~11.8 mM due to the acid and base additions but is not considered as the main cause for the observed decrease of E_{REL} in the closed control, since the drops occur only with each NaOH addition.

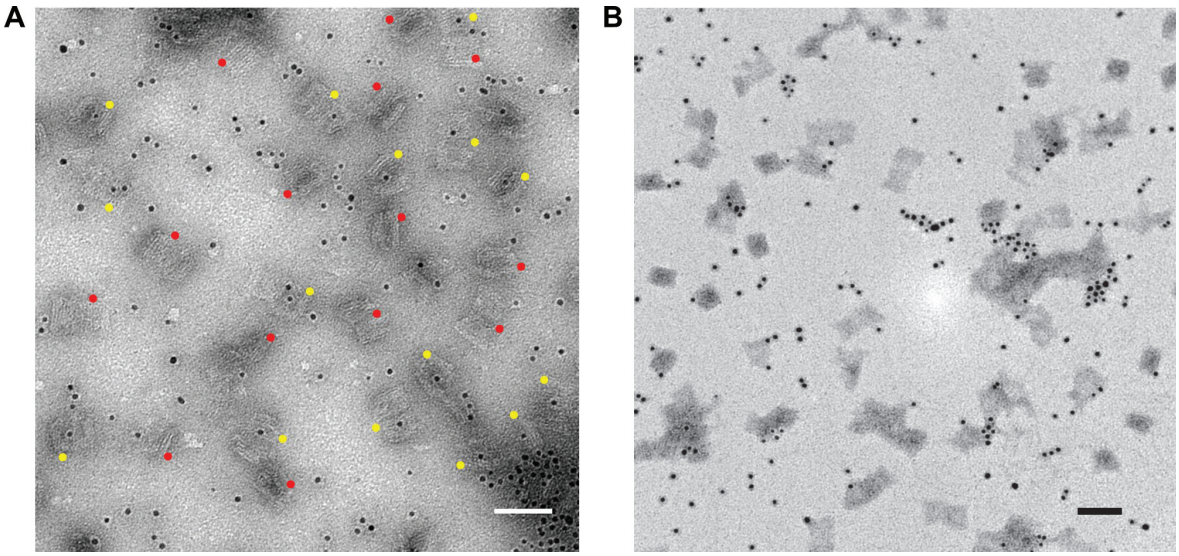

Figure S6. Additional TEM images of AuNP-loaded nanocapsules. (A) A typical sample of AuNP-loaded pHL nanocapsules in the open state used for loading yield estimation. Empty nanocapsules are marked with a red dot, and structures with a yellow dot contain a nanoparticle in the specified cargo-anchoring location. In this case, n = 29 and 52% of the capsules are loaded successfully. (B) When capsules are closed they cannot be loaded with AuNPs. Scale bars are 50 nm.

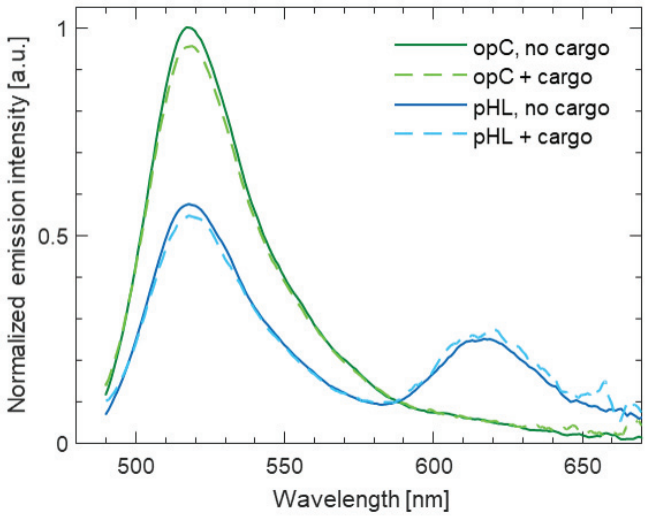

Figure S7. Emission spectra of phL and opC samples at pH 6.4 with and without HRP cargo. HRP loading does not change the emission properties of the nanocapsules labeled with a FRET pair. Most importantly, FRET efficiency in the pHL capsule does not decrease upon cargo loading indicating that cargo loading does not hinder the formation of the closed state. The spectra have been obtained with 460 nm excitation and normalized for concentration differences with the acceptor emission intensity collected after 560 nm excitation.

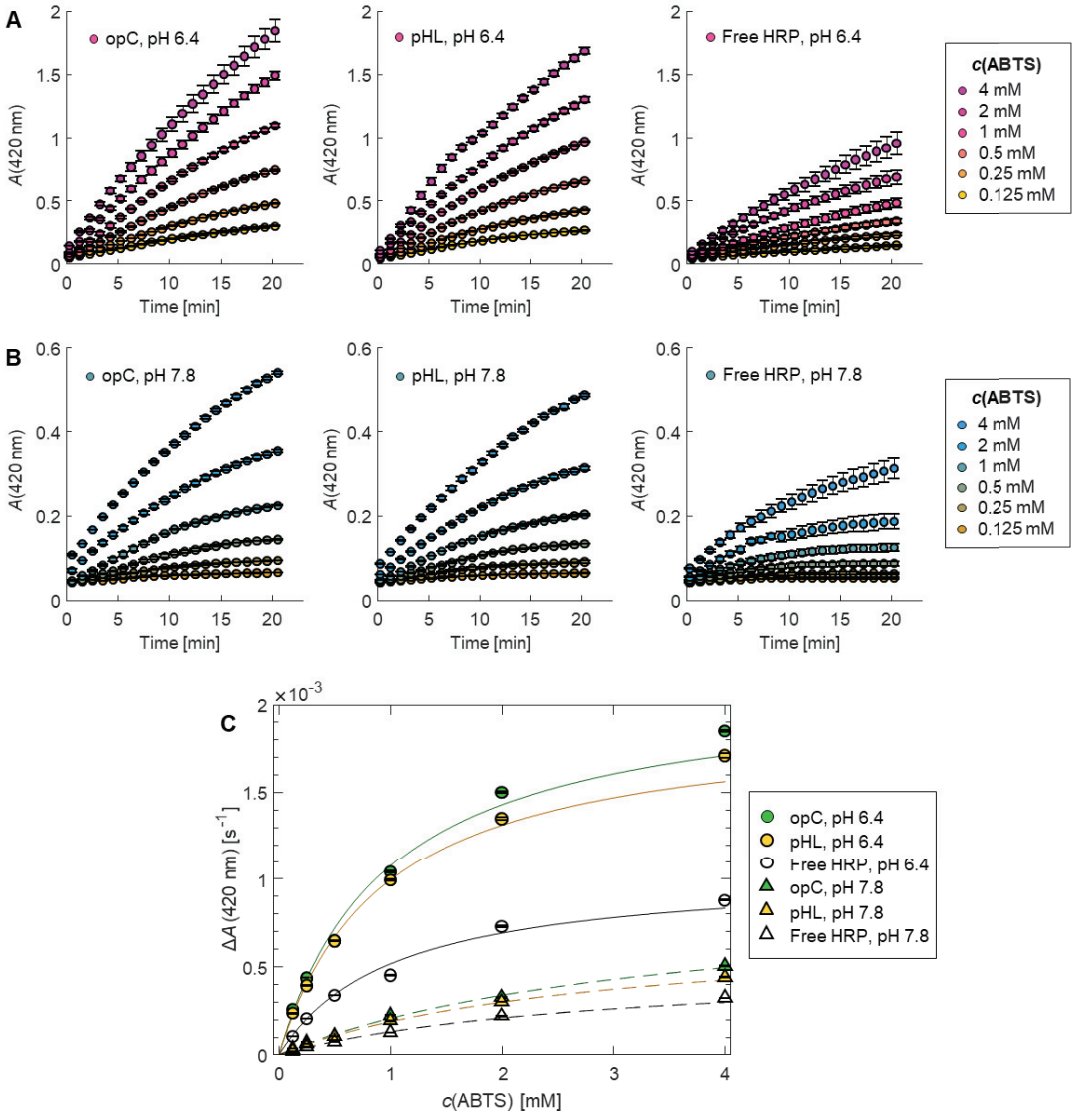

Figure S8. Analysis of the catalytic activity of HRP in HRP-capsule samples and free HRP in solution. (A) Formation of the oxidized product $ABTS^{\cdot+}$ catalyzed by HRP in pH 6.4 samples. The rate of ABTS conversion to $ABTS^{\cdot+}$ was followed according to the increase of absorption at 420 nm, measured in the presence of 0.125−4 mM ABTS and 4 mM H_2O_2. Nanocapsule concentration in opC and pHL samples was 2 nM, and concentration of HRP in the free HRP sample 2 nM. Initial catalytic rates for each ABTS concentration were determined from the slope or a linear equation fitted into the data points in the first 6 minutes. Error bars represent the standard error of the mean of three parallel samples. (B) Product formation in pH 7.8 samples. Apart from the higher pH, experimental conditions were identical to the pH 6.4 measurements. (C) Michaelis-Menten curves for determining V_{max} and K_m in each sample type, representing the relationship between ABTS concentration and the measured initial catalytic rates. The values for V_{max} and K_m are reported in the text.

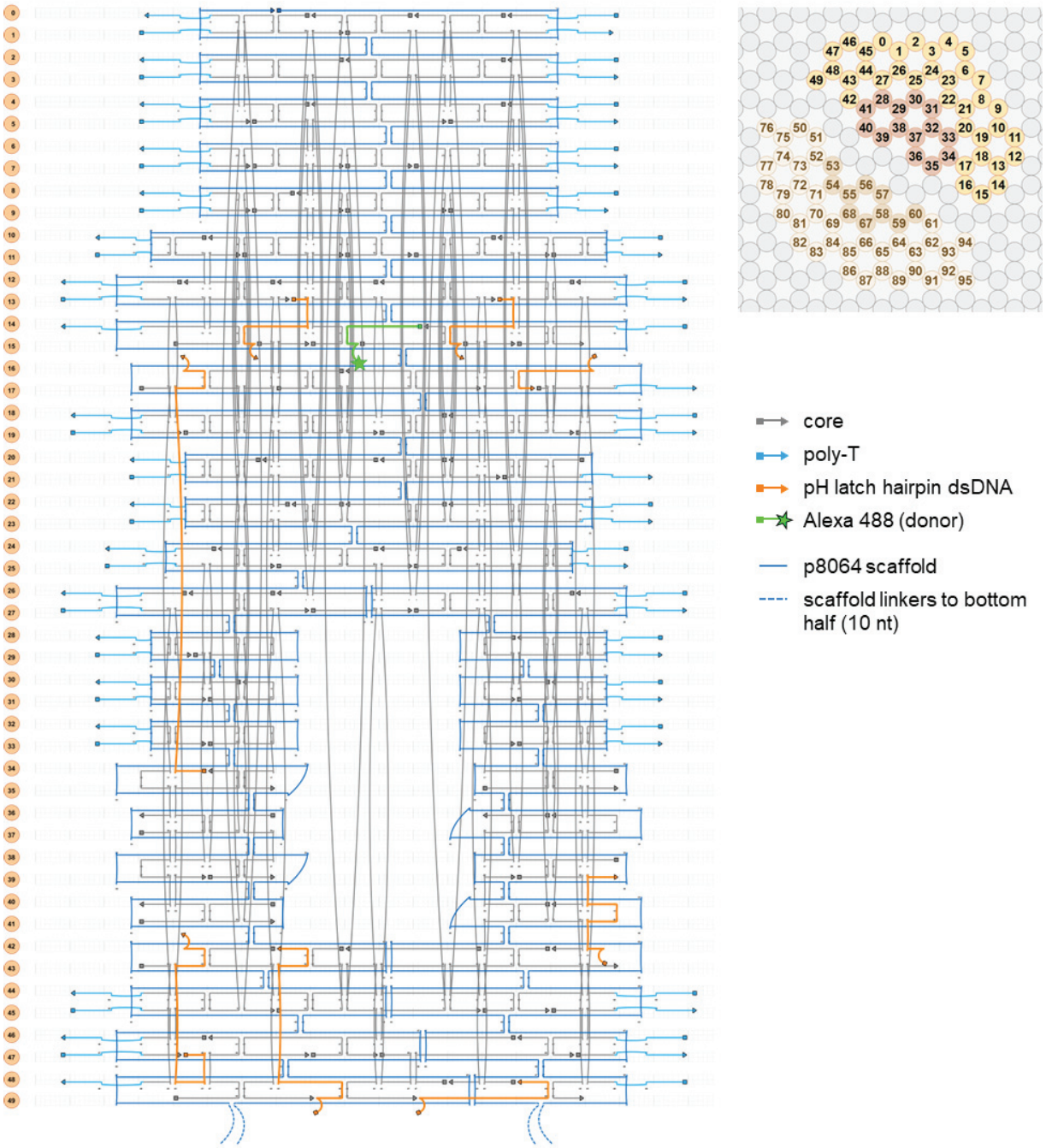

Figure S9. caDNAno blueprint of the nanocapsule top half. The top half of the capsule consists of helices 1-49 according to the helix map shown in the top-right part of the figure. Staple strands have been colored according to the strand type or function in the design. Locations of 3' or 5' extensions in pH latch strands and fluorophore-modified strand has been indicated, as well as location of the unhybridized scaffold regions (4 × 10 nt) linking the capsule halves together.

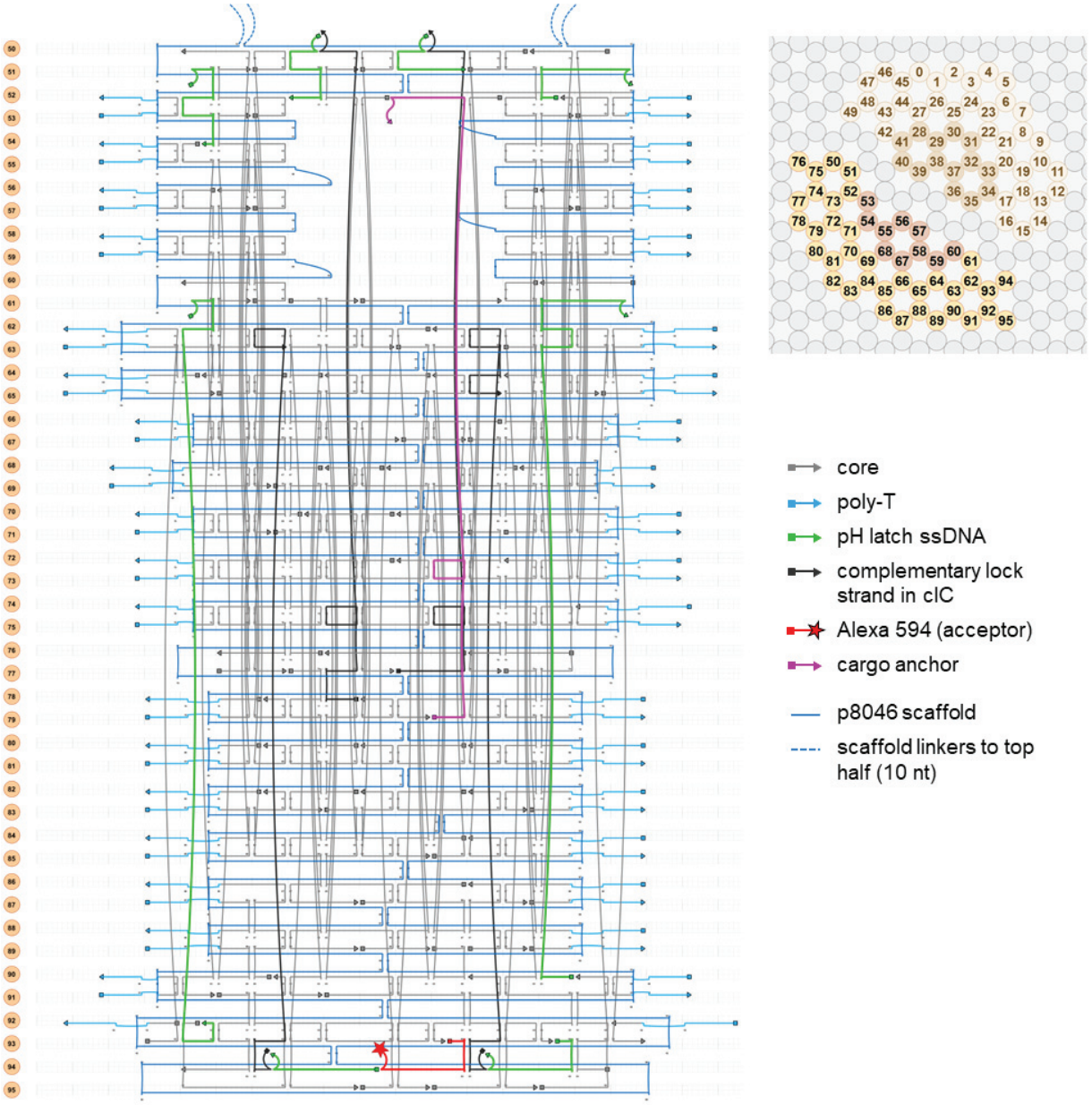

Figure S10. caDNAno blueprint of the nanocapsule bottom half. The bottom half of the capsule consists of helices 50-95 according to the helix map shown in the top-right part of the figure. Staple strands have been colored according to the strand type or function in the design. Locations of 3' or 5' extensions in pH latch strands, fluorophore-modified strand, and cargo anchoring strand has been indicated. To achieve correct strand direction for complementary lock strands in the clC design, the strands colored in black have been used for lock extensions instead of the adjacent pH latch strands.

List of all staple strands

All nanocapsules (pHL, clC, and opC) contain the staple strands listed in Tables S1 and S2. Depending on the nanocapsule type, these strands are combined with one set of staples making up the "lock region"; selected either from Table S3 (pH latch staples for pHL), Table S4 (complementary lock staples for clC), or Table S5 (staples with no lock extensions for opC). Start – end locations correspond to caDNAno design.

Table S1. Staple strands for the core structure and poly-T overhangs. Poly-T regions for passivation of the edges have been written in lowercase letters.

Functionality	Start - end	Sequence
core	0[55] - 26[49]	TCTATCAAATCAAGAAAAGAA
core	0[76] - 25[76]	ACGTCAACCCGAGAATCTACATTTAGTG
core	0[95] - 31[97]	TTAAAGTTCCAGGAGGGTATAAACGAGAACGGTCTAGCAT
core	1[63] - 47[69]	GGGTCAGAGGGCGAGTAACGCATGTGCTTATTACG
core	10[34] - 12[30]	GCCACCGTCTGTCCAACTA
core	10[93] - 18[84]	TAAGTTATCCGCTCGAATTCGTAAACGCGTGAAGGTTT
core	11[105] - 19[109]	ATTCCACAGCCGGACGCGG
core	11[42] - 20[46]	AAATTAATTATAATTCTAAAGTGG
core	11[63] - 19[69]	CTTCTTTCCAGAATACCTCAA
core	11[77] - 20[84]	TCCTGTGTGAAATTAGCCTGGTTTCGCAGCATCAG
core	12[109] - 36[105]	CCCGGCCGTGAGCCCTGCGTGTGTTCTTTCAACAATACTTTGTACCA
core	12[48] - 35[48]	AGTAGAACCATTGCTATTAACAAAACATAGATAGATACCCGG
core	12[69] - 16[63]	AGTAATATCATGGAAAACAGACCGAACGAACCACCCTACCTGAAAGCGT
core	15[28] - 11[41]	CCAGTAATAAAAGGATGGATTCCGCCAGGAACTCAATCACGC
core	15[45] - 10[35]	ATTCCAGACAATATTTTTTAGCCCTACCGCCTTGAAAAACAGTGAG
core	15[56] - 11[62]	CAGAGATTTTGACGAAAACGCACATCACAGCAATA
core	15[66] - 14[79]	ACCCTTCTGGCATCAGACGTCAT
core	15[87] - 17[90]	CCAGGGTGCCGGTGCCCCAGCTCGTCATAAAC
core	15[98] - 11[104]	TCACTGCATGCGGCTTCGCGTGTACCGAGCTCACA
core	16[62] - 9[62]	AAGAATAAAAAATAGGTGAGGTTGCTGACCTGAGATTAGACA
core	17[21] - 36[21]	AATGCGCATTTTCACAGATGAAAACAAT
core	17[49] - 15[55]	CGCCATTCGTGGCATGGCCAA
core	18[83] - 11[76]	CTTTGCACAGGCGCGGTGCCTAATGACGGACTGTT
core	19[70] - 12[70]	ATATCTGGAAGATAAAGTTTCTGCCAGCTCATGGTCATAGTT
core	2[62] - 22[52]	GCCGTAAAGCACTAAGCTTGACTTTGCCACAATTCCAAT
core	2[95] - 21[94]	GGCAAATCCTGTCGGTCCGAACGTGCTGGTCAGTCGG
core	20[111] - 40[105]	GCTTACGGGATAAAACCCTCAATAAAGCGGCAAAGAACATCCCAATTCT
core	20[45] - 39[48]	CAAACTCCGTGAGCTCTCTACCATGCAGCGCCAGAATCG
core	20[69] - 7[62]	CTCAATCAATATCTATCTTTATTTCCTCGCTTTGA
core	20[83] - 9[83]	CGGGGTCCAACGGCTGTCGTGCCAGCATTAGTGAGCTAACTC
core	21[95] - 13[93]	TGGGTGTCCACTCAATCATGGGTACCT
core	22[51] - 13[51]	AGACTAAAATGGTCAGTCATCACCCGGTCAGAAC

core	22[62] - 4[56]	GAGCCGTGACAACTAACCACCCAAGTGTAGCGGTCCGGCGAACGTGGCG
core	22[83] - 7[76]	CGCAAGACATCCTCTGGTTTTTCTTTGCGTTGCAT
core	24[69] - 1[62]	AGCCTTAGGCGGCCAAAATCCCGTAAAATTTTTTG
core	24[86] - 48[84]	TTCGTAAAGTGCTATTTCCTGAGACTTCCTGCCATCAAAGATTCA
core	25[49] - 2[63]	GAACAAGCCGCACATTAAATCCGGGGAAAGCCGCTATGAGGT
core	25[77] - 5[83]	ATGAAGGGTCTCGTCCCAGCACAGCAAGCGGTCCAACTCACCAGTGAGA
core	26[109] - 45[104]	ATTAAATGATATCTGCGAACGAGTGCCTGGAAG
core	27[56] - 49[77]	TCGACATAAAAAGGGTTTTCCCAAGCTTTGGGAAGGGAAACCAGGCAAAG
core	27[77] - 24[70]	GTCATTGTTGAGAGTAGGGTTTATAAATCAAAAGAGGTTTGCCGCTGGC
core	28[97] - 36[91]	GTCAACTAGAGAATAAACGTTTGTAAAATAAGCAA
core	29[32] - 34[35]	TATAAAATCGCTGATTGTCGGGAGATATACAGTAACAGCTGAAAT
core	30[41] - 24[37]	TCAAATTATTATCATATTA
core	35[91] - 15[97]	GTATATGACCCTGTGCCAAAAACAGGAAATCCCTTAGCCAGCCGCAGTG
core	36[104] - 33[97]	AAAACATTTAAGCATATCATATGTACCCTCAGAAA
core	36[48] - 33[34]	CCAGTCCTTTTACACTTTGAAACTATCAAAATTATAACAGAA
core	37[21] - 40[21]	GATTCGCCGCAGAGCATTTCACATCAAG
core	38[118] - 35[118]	CAGGCAACTCAGAGAATCGGTTTGCGGG
core	39[35] - 41[48]	GAGCAAAAAGTTACACCTTAAATTTCTGGCCAGCAATACCTC
core	39[98] - 42[105]	TAGCATTAATTAGCCGGGTAAAGATTCAAAAGGCCTCATTTGGTCAATA
core	4[55] - 8[53]	AGAAAGGGCGCTGGACACCCGTATGGTTGTT
core	4[95] - 10[94]	CTGAGCAGCTGAATTGGGCACGCGCGCCAGTCGTTGCGTTAGTG
core	40[104] - 28[98]	ACTAATATATATTTGGAGACA
core	40[48] - 29[31]	GAAACAAGATGATGTTTAACAGTATCAATATAATCGGAT
core	41[21] - 39[34]	CAAAATTAATTACAAAACAAAATTACCT
core	42[104] - 49[111]	ACCTGTTTCAGATTTAGTTTGTGAATATTGCGGAT
core	42[48] - 49[56]	GGATATTCATTTGACAATATATGTGAAACCTTTTTTCCGGCACCGCTTCT
core	42[62] - 0[56]	GCCGCCACCAGTGCCAGTCACAAGTTGGAAAACCG
core	42[90] - 42[63]	AAATCAGCTCATTTTTTAAAGAGGTGGA
core	45[105] - 47[109]	TTTCATTGCAACTACTGTA
core	45[49] - 27[55]	GAAAATTGACGTTGGTGTACA
core	46[34] - 26[31]	AAGACGCTAATTTTGCTTCTGTGATGGCAATTCTGGAAGGAGCGGA
core	46[97] - 0[77]	GTACAACCCGTCGGATTCTGAAAGGGGGCAATCAACATTAAAGACTCCA
core	47[56] - 47[55]	TCTTCGCGCAAGGCGACATAGCGATAGCCTGAGAGACGGGCC
core	47[70] - 27[76]	CCAGCTGCAACTGTTCCCAATAGGAACGTAGCCAGCTTTCGGCTATCAG
core	48[83] - 46[98]	GGCTGCGGCCCGTGGGAACAAACGGCGGATTGATGAAGTACG
core	48[97] - 39[97]	ATGGGATAAATAATTATTGTTAATTTGCGTTTAAATTTTGAG
core	49[28] - 46[35]	ATGCTGATGCAATTAACCTCCCATAGGTTTAGATT
core	5[44] - 45[48]	CTAGGAAGGGAAGATTTAGAATCGGATCACCCAGGGCGATAATCCTT
core	5[84] - 45[90]	CGGGCAAAGAGTTGGGCGAAAAATCCCTGAGTGTTGAACGTGTGTGAGC
core	50[95] - 68[94]	CGTGCGGTCAGGTAATTCGCAAAAAGAAGCAAAACCATAAGCTC
core	51[42] - 76[35]	TTTAGTTAGATCGCAAGGAAACTCCTTATTACGCA
core	51[63] - 77[69]	ACCTAAAACGACAGTAATAACGGAATAAAATATCTTACCGAATATAAAA
core	51[84] - 76[84]	TCCAACAATCTGCCCTTTGACCAAAAGA
core	52[68] - 72[70]	TGGTTTAATAGCAATAGCATAAGGGTA

core	52[90] - 77[90]	AGCTTCAAAATCCGTATCATCGGGTAAA
core	53[42] - 77[48]	TACTAGAGTGATAAAATAAGAAAGTAAGACATACA
core	56[34] - 64[32]	ATCGCCACGCCAACTAATAAGGTACCGAGCC
core	56[97] - 64[91]	AAACGAGATAAATACAATACTTTTGCCAAACGAAC
core	57[42] - 71[45]	TTAGGCAGGGCTTAAGCCAACGCCTGTTGAGA
core	60[97] - 95[97]	GCAAAAGTCGTTTACAAAAGGAGGTTTACACCCTCGAGGCTG
core	61[42] - 69[45]	TTTATCAACGACGATAAAGTACATTTTCCAATTTTGTTACAAATAA
core	61[49] - 95[62]	ACAATAGCCTAATTGGAGTGTAGAATGGGCCTATTTCGGAAC
core	61[63] - 61[90]	CTGAACAAGAGCAACACTATCATAACCC
core	62[76] - 95[76]	GTAAGAAAGGTGTACAAGCCCTCTGAAA
core	63[70] - 93[79]	GAACATTTAACGATGGAACCCATGTACCGGGATAGTCA
core	63[91] - 93[100]	TCATCAGAGACAGCTGAGTTTCGTCACCGAGCCACGTA
core	64[31] - 91[34]	CAATCATTCCAGACAGGAGGTCAGA
core	64[48] - 82[44]	GGAATCATAAGAACTCAAGATAGCGTCATAGCGACGCACCATATTAG
core	64[55] - 91[55]	CATCGTAACCAAGTACCAGAGATTCACA
core	64[76] - 89[76]	TAAGCAAGCCGTTTCGAACCTCCCGACTACAGTTTAGTTTTG
core	65[35] - 60[28]	GGTATTCTTACCGCCAAAAGGCAATAAACAACATG
core	66[90] - 84[84]	AATCATTAGGAGCCAGGTGAA
core	67[71] - 82[63]	ACGACCACCTTGCGGGAGGTTTCATCGCGATAGCCCGGAAAACCGACT
core	67[84] - 80[84]	GAAACACCAGTGAAAACCGGACTTCATCCTGAGGCCGTCACC
core	68[55] - 89[62]	TTTGCCAATCCTGACCTTAAAGCGAGGCCCTCAGACACCACCCTCAGAG
core	68[67] - 85[76]	TCCAGAACGTCAAAAATCTAAACCATGCAAAGG
core	68[93] - 89[95]	ATTCAGAACGCAACTTTAACTGGCGATTTTGGTTAG
core	69[46] - 80[44]	GAATAACATAAAATTATAGGGA
core	7[44] - 25[48]	CGTACCCGCGCTTTTACAACGAACGTTTTTGCG
core	7[63] - 22[63]	CGAGCACTGCGCGTCGCCGGCCAGAGCAATACTAATAGATTA
core	7[77] - 24[87]	TAATGAATCGGCCAGCCAGGGATAACGGTTTT
core	70[51] - 87[62]	GAAACGATTTTAATCAGGACTGTACCCTTATCCGGAACCAGAGCC
core	70[69] - 80[63]	TAGCAGCTTATCACAGGGCGA
core	71[46] - 78[44]	ATTGATAACCAATTCATGTTTA
core	71[84] - 79[76]	TTTGAAATCATAAGAACGAGGAGACTTTTTCATGAGGAAGAACAAGACA
core	71[91] - 87[95]	GAGGACAGGCTGACTATTCATGCTTTCGTTTAATTTTTTTCAAACTA
core	72[69] - 78[63]	ATTGAGCCCAAAGACGCAAAG
core	76[104] - 72[91]	TAAAACGAAAGAGGCCCCAGCAGATTTGCGACCTGCGGTCAA
core	76[55] - 70[52]	ATTAAGACCGAGGATTAAGAAGCAAGAATCAGAGAAACTGAAGAGA
core	76[83] - 76[56]	ATACACTAAACCCAAAAGAACTGGCATG
core	77[35] - 50[28]	AGAAAATCAGATAGTTACCAGACAAGACAAAGAAC
core	77[49] - 83[55]	TAAAGGTGGAATAAATGGTTTCCGATTGTCATTAATTTGGGATACCATT
core	77[91] - 83[95]	ATACGTAGGACTAAGTAGCAAGCGGGATTTGCAGGAACAACCTACCG
core	8[52] - 12[49]	AGAAAGGGATTAGTGTTTCCGTTGTTTGCCTG
core	80[62] - 51[62]	CATTCAAACCAGCGGCTAATAACAATGAGAAATACTCTTCTG
core	80[83] - 71[83]	CTCAGCAGCGAAAACGTATATTCGGTCGAAGAGTAGACCAAC
core	82[62] - 70[70]	TGAGCCAAGGTGAACTTTACACACCCTGAACAAAGTCAGACTATGAAAA
core	82[83] - 82[84]	ACGCATAACCGATCCGTCACCAATAAACAGCTTGAATCGCCC

core	83[56] - 68[56]	AGCAAGGAGCACCGTTTGTTTAGCCTAA
core	84[83] - 68[68]	TTTCTTGTGACAAGTAAGGCTTGGCGTCTT
core	85[77] - 67[83]	CTCCAAAGTGAATTCTGACGA
core	86[83] - 64[77]	AATCTCCAAAAAATGGAGTGAGAATAGAACTTTCATATGCGAACAACAT
core	87[63] - 67[70]	ACCACGCTTTCGGTCATAGCCGCGCGTTTTTGAAGATCTTACCAACGCTA
core	89[63] - 64[56]	CCGCCAACACGGAACCGCCTCGTTTTAGTTATTTT
core	89[77] - 62[77]	TCGTCTTGTTAGCGACAGGTAAGGCATA
core	89[84] - 86[84]	TCCAGACCTAAACAAAGGAACCGTTGAA
core	9[44] - 30[42]	ATTAATCAGAGCAGGTTATTAATACAAAAAAGACAGCGGA
core	9[63] - 20[70]	GGAACGGAACGTGCGGAGCACTAACAGCATAAACC
core	9[84] - 22[84]	ACATTAAGGAAACCAGCACCGCAGCAAC
core	91[35] - 94[28]	CGATTGGAGTCTCTCTTTTGACGGGGTCAGTGCCT
core	91[56] - 61[62]	AACAAATAAATCTACTACCAGAACCACCACCGCACATCCCATATAAGTC
core	92[31] - 90[46]	TTTATATAAACAGTTAATGCCCCCTAAAGCGCCCTTGATCCG
core	94[111] - 65[109]	GGGGTTTCACCCTCCAGATACTTAGGAAATCTACGACCAG
core	95[63] - 63[69]	CTATTATAACTCATTAAAGCCACATAGCCCGGAATAAATAATTCATCGA
core	95[77] - 90[84]	CATGAAAGTATTAAATTTTCAGTAACACCCTCATA
core	95[98] - 90[105]	AGACTCCTCAAGAGACCCTCAAGTACAACTGTAGC
core + poly-T	0[118] - 0[96]	ttttttttttAGTCCACTA
core + poly-T	1[21] - 2[21]	ttttttttttTGAACCAACCCTAAtttttttttt
core + poly-T	10[127] - 11[127]	ttttttttttATACGACAACtttttttttt
core + poly-T	11[12] - 10[12]	ttttttttttAAGAGAGTAAtttttttttt
core + poly-T	12[132] - 12[110]	ttttttttttTTGAGGATC
core + poly-T	12[29] - 12[5]	TCGGCCTTGttttttttt
core + poly-T	13[5] - 18[7]	ttttttttttCCAGAACTGCCACGttttttttt
core + poly-T	14[132] - 15[111]	ttttttttttGTGCTGCGGCCAGAGCGCCTG
core + poly-T	17[102] - 9[116]	TGGGCTGGTACGCCGGGAGCATAAGCGCTCAttttttt
core + poly-T	18[134] - 13[132]	ttttttttttACTGTTGCCTCCTCttttttttt
core + poly-T	19[110] - 19[134]	TTGCGGTATttttttttt
core + poly-T	19[30] - 14[5]	GCAAAGCAACAGAATATTAATTTACATTGGCAGttttttttt
core + poly-T	19[7] - 19[29]	ttttttttttGAGCCAGCA
core + poly-T	2[118] - 2[96]	ttttttttttTCCGAAATC
core + poly-T	21[19] - 20[19]	ttttttttttAGGAATTGAAttttttttt
core + poly-T	22[125] - 30[105]	ttttttttttGCGTGGTTTTTAAAGAGTAAT
core + poly-T	23[19] - 22[19]	ttttttttttGAAGTATTTAttttttttt
core + poly-T	24[120] - 25[120]	ttttttttttTTCCGTGCCGttttttttt
core + poly-T	24[36] - 24[14]	ATTTTAAAAttttttttt
core + poly-T	25[14] - 31[34]	ttttttttttGAGTAACCTGAATATAGAACC
core + poly-T	26[132] - 26[110]	ttttttttttAGCTGATAA
core + poly-T	26[30] - 26[5]	ATTATCATCAttttttttt
core + poly-T	26[48] - 0[22]	ACCACCAGGCGGTTTAGTGAATAACCTTCCCTTAGGGCCCACttttttttt
core + poly-T	27[5] - 44[7]	ttttttttttTATCAGATAAATCGttttttttt
core + poly-T	28[127] - 29[127]	ttttttttttGTGAGAAAGGttttttttt
core + poly-T	29[12] - 28[12]	ttttttttttTGTTTCTGATttttttttt

core + poly-T	3[21] - 4[21]	ttttttttttAGCCCCCGAAAGCGttttttttt
core + poly-T	30[104] - 3[118]	GTGTAATTGCTGATGCAAACGTTGATGGttttttttt
core + poly-T	30[127] - 31[127]	ttttttttttTGCCTTGCAAttttttttt
core + poly-T	31[12] - 30[12]	ttttttttttAGGGTATGGAttttttttt
core + poly-T	31[35] - 6[21]	TACCAGGTTTGAGGATTAGACTAATGCGttttttttt
core + poly-T	31[98] - 23[125]	GTCAATAGCTGGTCCGGACTTGTAGAACttttttttt
core + poly-T	32[127] - 33[127]	ttttttttttTTAGAAATTTttttttttt
core + poly-T	33[12] - 32[12]	ttttttttttCGTAATTGCAttttttttt
core + poly-T	33[35] - 8[21]	ATAAATTTCAACAGTTGAGGAGGGAGCTttttttttt
core + poly-T	33[98] - 21[125]	AGCCCAAGCTGGAGTGCCATCCCACGCAttttttttt
core + poly-T	34[118] - 17[134]	GCCTTTAAGCAAATttttttttt
core + poly-T	4[118] - 4[96]	ttttttttCGCCTGGCC
core + poly-T	43[21] - 48[5]	AACAGTAGTTGGGTttttttttt
core + poly-T	44[134] - 27[132]	ttttttttttCCCAATTTCAACCGttttttttt
core + poly-T	45[7] - 46[5]	ttttttttttTATTAATTGAGAAGttttttttt
core + poly-T	45[91] - 1[117]	GAGTAGTGTCTGGCGTATCACCATCAATTGCCGGATTTGGAAttttttttt
core + poly-T	46[132] - 45[134]	ttttttttttTAAATATCCATATAttttttttt
core + poly-T	47[110] - 47[132]	GCTCAACATttttttttt
core + poly-T	47[5] - 47[29]	ttttttttGAATTTATC
core + poly-T	48[132] - 43[118]	ttttttttttTAATTGCACCATTA
core + poly-T	5[21] - 5[43]	ttttttttGAGCGGGCG
core + poly-T	50[111] - 75[125]	CTTTTGACCAAGCGttttttttt
core + poly-T	52[127] - 53[127]	ttttttttGACTTCGAAttttttttt
core + poly-T	53[105] - 73[125]	GGAAGCCCAAATATTTACTTAttttttttt
core + poly-T	53[12] - 52[12]	ttttttttTAAACAAGAAttttttttt
core + poly-T	54[127] - 55[127]	ttttttttCCCTGCTTTAttttttttt
core + poly-T	54[31] - 68[14]	TGCGTCTTACCAGCCATAttttttttt
core + poly-T	55[12] - 54[12]	ttttttttCAAATTTATAttttttttt
core + poly-T	56[127] - 57[127]	ttttttttATGCTCTCAAttttttttt
core + poly-T	57[105] - 71[125]	AATCCCCTTAAACAATCAGGTACTATTAGGTGTACttttttttt
core + poly-T	57[12] - 56[12]	ttttttttACAATATTttttttttt
core + poly-T	58[127] - 59[127]	ttttttttGTTTAAAAATttttttttt
core + poly-T	59[12] - 58[12]	ttttttttATAAAAGAATttttttttt
core + poly-T	6[118] - 5[118]	ttttttttttTTGCGTTTGCCCTttttttttt
core + poly-T	60[116] - 67[125]	AAAATAGCGAGATAATAGTGACTGGAAATTGGGttttttttt
core + poly-T	62[132] - 93[118]	ttttttttACTAATGAGAACCG
core + poly-T	63[5] - 64[5]	ttttttttTCCTTATAGCAAGCttttttttt
core + poly-T	64[132] - 63[132]	ttttttttAAGAAAATACCACAttttttttt
core + poly-T	65[110] - 65[132]	TCAGGACGTttttttttt
core + poly-T	65[5] - 65[34]	ttttttttTAGAAGGCTTATCC
core + poly-T	66[125] - 57[104]	ttttttttAGATGGTTTAATTTAGTAGTATAGCGTCTTCATTG
core + poly-T	67[19] - 66[19]	ttttttttTGCACTATTTttttttttt
core + poly-T	68[120] - 69[120]	ttttttttCGTAAATCAAttttttttt
core + poly-T	69[14] - 56[35]	ttttttttTTATCCCAATCCAAAATAAACAGTATAAATTGAGA

core + poly-T	7[21] - 7[43]	ttttttttttTACAGGGCG
core + poly-T	70[125] - 53[104]	ttttttttttCAGGCGCATAGGCTGATGAACTAGTCAGATTAAGA
core + poly-T	71[19] - 70[19]	ttttttttttCGCATGGAAGtttttttttt
core + poly-T	72[125] - 52[102]	ttttttttttGAACGAGGCGCAGACTCCATGCGC
core + poly-T	73[19] - 72[19]	ttttttttttGTTAAATTGAttttttttttt
core + poly-T	74[127] - 74[105]	ttttttttttttACAAAGT
core + poly-T	75[19] - 74[19]	ttttttttttCAAAGCCGAAttttttttt
core + poly-T	78[118] - 50[96]	ttttttttttGCTTTGAATGCCACACAACGGGATTATATATCGTAAC
core + poly-T	78[43] - 78[21]	TTTTGTCACttttttttt
core + poly-T	79[21] - 51[41]	ttttttttttAATAGAACACAAGAGCCCAATATAAGGCAATATAT
core + poly-T	8[118] - 7[118]	ttttttttttCCGCTTTGGGAGAGtttttttttt
core + poly-T	80[118] - 79[118]	ttttttttttCGCTTTTCGGCTACttttttttt
core + poly-T	80[43] - 80[21]	GGGAAGGTAttttttttt
core + poly-T	81[21] - 53[41]	ttttttttttTTGACGGAAAACAGTAGACGGTAGTATCTCATAAT
core + poly-T	82[118] - 81[118]	ttttttttttCAATGACGAGTTAAttttttttt
core + poly-T	82[43] - 82[21]	AGCCAGCAAttttttttt
core + poly-T	83[21] - 84[21]	ttttttttttACCAGTAAGAATCAttttttttt
core + poly-T	83[96] - 83[118]	ATAGTTGCGttttttttt
core + poly-T	84[118] - 56[98]	ttttttttttTCAGCTTTACCCAACAAAGCTATCAAAAGTTCAGA
core + poly-T	85[21] - 57[41]	ttttttttttTGCCTTTTAGTTGCCCAGCTAGAGCCAGATGTAAT
core + poly-T	86[118] - 85[118]	ttttttttttTAATAATGTATCGGttttttttt
core + poly-T	87[21] - 88[21]	ttttttttttCATAATCCCCTCAGttttttttt
core + poly-T	87[96] - 87[118]	AAGGAATTGttttttttt
core + poly-T	88[118] - 60[98]	ttttttttttTGTATGGTCATTATTTAATAAGAGGGGGGGCTTTT
core + poly-T	89[21] - 61[41]	ttttttttttGCCACCCCAGCATTAGAACGGATGTAGAGCGCCTG
core + poly-T	89[96] - 89[118]	TAAATGAATttttttttt
core + poly-T	9[21] - 9[43]	ttttttttttAGGAGGCCG
core + poly-T	90[127] - 91[127]	ttttttttttAACGCACTACttttttttt
core + poly-T	90[45] - 86[21]	CCGCTCAGAGCGCCGCCAAAAATCATAGCGTTTGCCATCtttttttttt
core + poly-T	91[12] - 90[12]	ttttttttttAGGCAGGTTGttttttttt
core + poly-T	92[136] - 92[112]	ttttttttttttAACCGCC
core + poly-T	92[27] - 92[5]	CCGTTCCtttttttttttt
core + poly-T	93[21] - 62[5]	AGCGTCACAATAATttttttttt

Table S2. Staple strands for FRET and cargo anchoring.

Functionality	Start - end	Sequence
Alexa Fluor 488 3', top half FRET	14[78] - 15[65]	ACCGGGGTACCTACATAGAtt/3AlexF488N/
Alexa Fluor 594 3', bottom half FRET	93[80] - 94[67]	CCGTGTGCCGTCGAGAGGGTTtt/3AlexF594N/
Cargo anchoring strand	79[77] - 52[69]	GCATCGGGGAACCGTGTGTCGAAGCGAACCAGATAAtttAAAGAAGAAAGAAAAA

+ 5’ thiol modified strand for cargo molecule - DNA conjugates, complementary to the cargo anchoring strand: /5ThioMC6-D/TTTTTCTTTCTTCTTT

Table S3. Staple strand set for pH latch functionalization of pHL nanocapsules. Hairpin-forming extensions have been colored orange, and ssDNA counterparts green. dsDNA regions and ssDNA sequences with the same set number contain matching polypurine - polypurine sequences for Hoogsten triplex formation. 3×T spacers between the latch and the core structure, as well as 4×T hairpin loops have been marked with lowercase letters.

Functionality	Start - end	Sequence
latch 15/1 - pHL set 1 hairpin	13[52] - 15[44]	AGGACTCAATCGTCTGAAGACtttGAGAGAGAAGAAGAAGAAAGttttCTTTCTTCTTCTTCTCTCTC
latch 15/2 - pHL set 2 hairpin	13[94] - 15[86]	GTTCGGGCCGTTTTCACGGATtttAAAGGAAGAGAGAAGAAAGGttttCCTTTCTTCTCTCTTCCTTT
latch 16/1 - pHL set 3 hairpin	34[34] - 16[30]	TGCGTAGGAACTGAGAATGtttCCTTTCTTTCTTTCTTCCTCttttGAGGAAGAAAGAAAGAAAGG
latch 16/2 - pHL set 4 hairpin	16[114] - 17[101]	AGAGAAGAAAAGAGGAAGGAttttTCCTTCCTCTTTTCTTCTCTtttGATGCCGGGTTACCTGCACAC
latch 50/1 - pHL set 5 hairpin	50[54] - 52[49]	CTTTTCTCTTCTTCCCTTTCttttGAAAGGGAAGAAGAGAAAAGtttTCAGGAAATTTCACGACCGT
latch 50/2 - pHL set 6 hairpin	50[75] - 51[83]	TTTCTTTCCTTTCCCTCTCTttttAGAGAGGGAAAGGAAAGAAAtttGGGACGTTCCGGAAGCAAAC
latch 42/1 - pHL set 7 hairpin	47[30] - 42[30]	AAAATGGCTTAGCATAAATATTACtttCCCCCTTTCTTTTTTCTTCTttttAGAAGAAAAAAGAAAGGGGG
latch 42/2 - pHL set 8 hairpin	42[115] - 39[118]	AAAAGGGAGAAGAAAAGAGGttttCCTCTTTTCTTCTCCCTTTTtttAATGGGGCGCGGTGGCATAATAAAT
latch 94/1 - pHL set 1 ssDNA	94[66] - 94[46]	GATATAAGTTGGTAATAAGTTtttCTCTCTCTTCTTCTTCTTTC
latch 94/2 - pHL set 2 ssDNA	93[101] - 94[88]	CCGCTGCTCAGTACCAGGCGGtttTTTCCTTCTCTCTTCTTTCC
latch 61/1 - pHL set 3 ssDNA	61[30] - 92[32]	CTCCTTCTTTCTTTCTTTCCtttAGAACAACCAATTACATGGGAA
latch 61/2 - pHL set 4 ssDNA	90[104] - 61[114]	ATTCCACTTGAGATATAACGCCCAGACGACGATAAAAAtttTCTCTTCTTTTCTCCTTCCT
latch 49/1 - pHL set 5 ssDNA	49[57] - 42[49]	CTTTCCCTTCTTCTCTTTTCtttGGTGCCGGCGATCGGTGCTAACGACGGCGGGAAC
latch 49/2 - pHL set 6 ssDNA	49[78] - 48[98]	TCTCTCCCTTTCCTTTCTTTttttCGCCATTCGCCGTCACGTTGGTGTATTAACCGTA
latch 51/1 - pHL set 7 ssDNA	50[54] - 52[49]	TCTTCTTTTTTCTTTCCCCCTTtttTCAGTTAAATACCGGAAATA
latch 51/2 - pHL set 8 ssDNA	50[75] - 51[83]	GTTTATTAGAGAGTACCTTTAAtttTTTTCCCTCTTCTTTTCTCC
core	77[70] - 50[76]	GATTTCCATTAAACGCCTGATCACTCATAGTTTGAG
core	78[62] - 50[55]	ACACCACGGCAACAGCCCTTTAACGCAATATCGGCC
core	94[45] - 63[48]	TTAATGATACATACGAGCGTATTAA
core	94[87] - 65[90]	ATAAACTCAGGAATTACGGAAAGATTAACGGATTTTAAG

Table S4. Staple strand set for complementary lock functionalization of clC nanocapsules. Duplex-forming extensions have been colored dark green. Extensions with the same set number contain complementary sequences for duplex formation.

Functionality	Start - end	Sequence
latch 15/1 - clC pair 1 ssDNA	13[52] - 15[44]	AGGACTCAATCGTCTGAAGACtttCTCTCTCTTCAAGAAGAAAG
latch 15/2 - clC pair 2 ssDNA	13[94] - 15[86]	GTTCGGGCCGTTTTCACGGATtttAAAGGAAGAGTCTTCTTTCC
latch 16/1 - clC pair 3 ssDNA	34[34] - 16[30]	TGCGTAGGAACTGAGAATGtttCCTTTCTTTCAAAGAAGGAG
latch 16/2 - clC pair 4 ssDNA	16[114] - 17[101]	TCCTTCCTCTAAAGAAGAGAtttGATGCCGGGTTACCTGCACAC
latch 50/1 - clC pair 5 ssDNA (*)	78[62] - 50[55]	ACACCACGGCAACAGCCCtttAACGCAATATCGGCCTTTGAAAAGAGAAGAAGGGAAAG
latch 50/2 - clC pair 6 ssDNA (*)	77[70] - 50[76]	GATTTCCATTAAACGCCTGATCACTCATAGTTTGAGtttAAAGAAAGGAAAGGGAGAGA
latch 42/1 - clC pair 7 ssDNA	47[30] - 42[30]	AAAATGGCTTAGCATAAATATTACtttCCCCCTTTCTAAAAAGAAGA
latch 42/2 - clC pair 8 ssDNA	42[115] - 39[118]	CCTCTTTTCTAGAGGGAAAAtttAATGGGGCGCGGTGGCATAATAAAT
latch 94/1 - clC pair 1 ssDNA (*)	94[45] - 63[48]	CTTTCTTCTTGAAGAGAGAGtttTTAATGATACATACGAGCGTATTAA
latch 94/2 - clC pair 2 ssDNA (*)	94[87] - 65[90]	GGAAAGAAGACTCTTCCTTTtttATAAACTCAGGAATTACGGAAAGATTAACGGATTTTAAG
latch 61/1 - clC pair 3 ssDNA	61[30] - 92[32]	CTCCTTCTTTGAAAGAAAGGtttAGAACAACCAATTACATGGGAA
latch 61/2 - clC pair 4 ssDNA	90[104] - 61[114]	ATTCCACTTGAGATATAACGCCCAGACGACGATAAAAAtttTCTCTTCTTTAGAGGAAGGA
latch 49/1 - clC pair 5 ssDNA	49[57] - 42[49]	CTTTCCCTTCTTCTCTTTTCtttGGTGCCGGCGATCGGTGCTAACGACGGCGGGAAC
latch 49/2 - clC pair 6 ssDNA	49[78] - 48[98]	TCTCTCCCTTTCCTTTCTTTtttCGCCATTCGCCGTCACGTTGGTGTATTAACCGTA
latch 51/1 - clC pair 7 ssDNA	50[54] - 52[49]	TCTTCTTTTTAGAAAGGGGGTTtttTCAGTTAAATACCGGAAATA
latch 51/2 - clC pair 8 ssDNA	50[75] - 51[83]	GTTTATTAGAGAGTACCTTTAAtttTTTTCCCTCTAGAAAAGAGG
latch 50/1 - clC no extension	50[54] - 52[49]	TCAGGAAATTTCACGACCGT
latch 50/2 - clC no extension	50[75] - 51[83]	GGGACGTTCCGGAAGCAAAC
latch 94/1 - clC no extension	94[66] - 94[46]	GATATAAGTTGGTAATAAGTT
latch 94/2 - clC no extension	93[101] - 94[88]	CCGCTGCTCAGTACCAGGCGG

* the strands marked with an asterisk are core strands adjacent to the corresponding latch strands in the pHL and opC samples. The strands have been exchanged to achieve correct strand directionality for DNA hybridization (see black strands in Figure S10).

Table S5. Staple strand set without strand extensions for opC nanocapsules.

Functionality	Start - end	Sequence
latch 15/1 - opC (no extension)	13[52] - 15[44]	AGGACTCAATCGTCTGAAGAC
latch 15/2 - opC (no extension)	13[94] - 15[86]	GTTCGGGCCGTTTTCACGGAT
latch 16/1 - opC (no extension)	34[34] - 16[30]	TGCGTAGGAACTGAGAATG
latch 16/2 - opC (no extension)	16[114] - 17[101]	GATGCCGGGTTACCTGCACAC
latch 42/1 - opC (no extension)	47[30] - 42[30]	AAAATGGCTTAGCATAAATATTAC
latch 42/2 - opC (no extension)	42[115] - 39[118]	AATGGGGCGCGGTGGCATAATAAAT
latch 49/1 - opC (no extension)	49[57] - 42[49]	GGTGCCGGCGATCGGTGCTAACGACGGCGGGAAC
latch 49/2 - opC (no extension)	49[78] - 48[98]	CGCCATTCGCCGTCACGTTGGTGTATTAACCGTA
latch 50/1 - opC (no extension)	50[54] - 52[49]	TCAGGAAATTTCACGACCGT
latch 50/2 - opC (no extension)	50[75] - 51[83]	GGGACGTTCCGGAAGCAAAC
latch 51/1 - opC (no extension)	51[30] - 54[32]	TTTCAGTTAAATACCGGAAATA
latch 51/2 - opC (no extension)	52[101] - 51[115]	GTTTATTAGAGAGTACCTTTAA
latch 61/1 - opC (no extension)	61[30] - 92[32]	AGAACAACCAATTACATGGGAA
latch 61/2 - opC (no extension)	90[104] - 61[114]	ATTCCACTTGAGATATAACGCCCAGACGACGATAAAAA
latch 94/1 - opC (no extension)	94[66] - 94[46]	GATATAAGTTGGTAATAAGTT
latch 94/2 - opC (no extension)	93[101] - 94[88]	CCGCTGCTCAGTACCAGGCGG
core	77[70] - 50[76]	GATTTCCATTAAACGCCTGATCACTCATAGTTTGAG
core	78[62] - 50[55]	ACACCACGGCAACAGCCCTTTAACGCAATATCGGCC
core	94[45] - 63[48]	TTAATGATACATACGAGCGTATTAA
core	94[87] - 65[90]	ATAAACTCAGGAATTACGGAAAGATTAACGGATTTTAAG

III

PROBING THE CONFORMATIONAL STATES OF A PH-SENSITIVE DNA ORIGAMI ZIPPER VIA LABEL-FREE ELECTROCHEMICAL METHODS

by

Williamson P., Ijäs H., Shen B., Corrigan D.K. & Linko V. 2021

Submitted manuscript.

Request a copy from the author.

IV

UNRAVELING THE INTERACTION BETWEEN DOXORUBICIN AND DNA ORIGAMI NANOSTRUCTURES FOR CUSTOMIZABLE CHEMOTHERAPEUTIC DRUG RELEASE

by

Ijäs H., Shen B., Heuer-Jungemann A., Keller A., Kostiainen M.A., Liedl T., Ihalainen J.A. & Linko V. 2021

Nucleic Acids Research, gkab097

DOI:10.1093/nar/gkab097.

Nucleic Acids Research, 2021 **1**
doi: 10.1093/nar/gkab097

Unraveling the interaction between doxorubicin and DNA origami nanostructures for customizable chemotherapeutic drug release

Heini Ijäs[1,2], Boxuan Shen [1], Amelie Heuer-Jungemann[3,4], Adrian Keller[5], Mauri A. Kostiainen[1,6], Tim Liedl[3], Janne A. Ihalainen[2] and Veikko Linko [1,6,*]

[1]Biohybrid Materials, Department of Bioproducts and Biosystems, Aalto University, P.O. Box 16100, 00076 Aalto, Finland, [2]Nanoscience Center, Department of Biological and Environmental Science, University of Jyväskylä, P.O. Box 35, 40014 Jyväskylä, Finland, [3]Faculty of Physics and Center for NanoScience (CeNS), Ludwig-Maximilians-University, Geschwister-Scholl-Platz 1, 80539 Munich, Germany, [4]Max Planck Institute of Biochemistry, Am Klopferspitz 18, 82152 Martinsried, Germany, [5]Technical and Macromolecular Chemistry, Paderborn University, Warburger Str. 100, 33098 Paderborn, Germany and [6]HYBER Centre, Department of Applied Physics, Aalto University, P.O. Box 15100, 00076 Aalto, Finland

Received September 23, 2020; Revised January 27, 2021; Editorial Decision February 02, 2021; Accepted February 03, 2021

ABSTRACT

Doxorubicin (DOX) is a common drug in cancer chemotherapy, and its high DNA-binding affinity can be harnessed in preparing DOX-loaded DNA nanostructures for targeted delivery and therapeutics. Although DOX has been widely studied, the existing literature of DOX-loaded DNA-carriers remains limited and incoherent. Here, based on an in-depth spectroscopic analysis, we characterize and optimize the DOX loading into different 2D and 3D scaffolded DNA origami nanostructures (DONs). In our experimental conditions, all DONs show similar DOX binding capacities (one DOX molecule per two to three base pairs), and the binding equilibrium is reached within seconds, remarkably faster than previously acknowledged. To characterize drug release profiles, DON degradation and DOX release from the complexes upon DNase I digestion was studied. For the employed DONs, the relative doses (DOX molecules released per unit time) may vary by two orders of magnitude depending on the DON superstructure. In addition, we identify DOX aggregation mechanisms and spectral changes linked to pH, magnesium, and DOX concentration. These features have been largely ignored in experimenting with DNA nanostructures, but are probably the major sources of the incoherence of the experimental results so far. Therefore, we believe this work can act as a guide to tailoring the release profiles and developing better drug delivery systems based on DNA-carriers.

INTRODUCTION

The possibility to employ DNA molecules in engineering artificial nanostructures (1,2) has drawn increasing attention during the past two decades (3–5). The intense development of DNA nanotechnology has yielded new methods to build user-defined nano-objects (6), such as DNA origami (7–11), for a variety of scientific and technological uses (12–16). In particular, these custom DNA nanoshapes show considerable promise in biomedicine and drug delivery (17–21). Rationally designed DNA nanovehicles can encapsulate and display selected cargoes (22–25), act as therapeutics themselves (26), serve as platforms for various targeting ligands and tailored nucleic acid sequences (27,28), or directly host diverse DNA-binding drugs (29,30). In the latter case, the most frequently used drug is anthracycline doxorubicin (DOX), a fluorescent DNA-intercalator, which is applied in the treatments of several cancer types and primarily in solid tumor growth suppression (31). Its main mechanism of action takes place *via* type IIA DNA topoisomerase inhibition, but it also affects multiple other cellular processes through DNA intercalation and generation of reactive oxygen species (ROS) (32). The therapeutic potency of various DOX-loaded DNA origami nanostructures (DONs) has been demonstrated using *in vitro* and *in vivo* models in a number of reports (33–43).

The presumed intercalation and release of DOX are typically characterized using spectroscopic indicators such as spectral changes of visible light absorption or DOX fluorescence quenching upon DNA binding. However, besides intercalation, DOX may be complexed with DNA through (pre-intercalation) minor-groove binding and stacking into aggregates depending on the DNA sequence, prevalent

*To whom correspondence should be addressed. Tel: +358 45 673 9997. Email: veikko.linko@aalto.fi

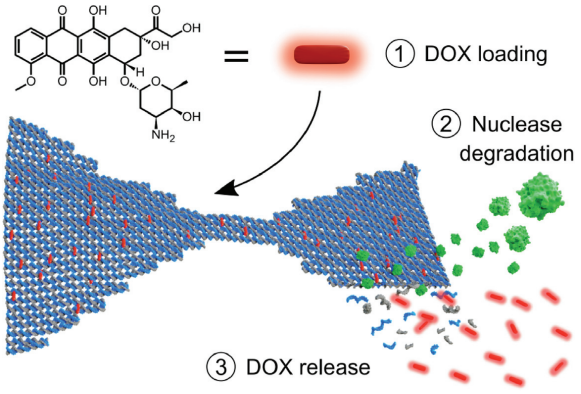

Figure 1. Schematic of the doxorubicin (DOX) loading into a DNA origami nanostructure (DON) and subsequent release upon enzymatic degradation. Here, we 1) study how DOX is loaded into DONs (in seconds), optimize the conditions for the loading by monitoring the spectroscopic features of DOX, and characterize the formed DOX–DON complexes. Through simultaneous real-time detection of the absorbance and fluorescence changes of the DOX-loaded DONs, we then 2) monitor the degradation of DONs into single-stranded DNA fragments by nucleases (DNase I, green) (in minutes to hours under a DNase I concentration of 34 U ml^{-1}) and 3) characterize the subsequent DOX release profiles of different DONs and show that the release profiles of DOX depend on the DNA origami superstructure and the applied DOX content.

DOX concentration and experimental conditions such as pH or the ionic strength of the solution (44–46). Spectroscopic features of bound DOX are likewise dependent on the mode of interaction. In addition, DOX molecules have two distinct protonation states within a physiologically relevant pH range (pH ∼4–9) and they are prone to self-association at high concentrations (47). Therefore, spectroscopic properties of DOX are also subject to change in different media compositions. These effects need to be carefully differentiated from the changes induced by DNA binding to avoid misleading interpretations of DOX loading capacity, release efficiency and the therapeutic effect (20).

In this work, we systematically study the binding of DOX to five structurally distinct two- (2D) and three-dimensional (3D) DONs (one exemplary structure shown in Figure 1). By means of absorption and fluorescence spectroscopy, we optimize the loading process and uncover the contributions of the ionic strength, pH and DOX concentration. The obtained results reveal that the DOX binding capacity of DONs has often been substantially overestimated, in some previously reported cases by more than two orders of magnitude.

Finally, we mimic one plausible and physiologically relevant DOX release pathway by subjecting the DOX-loaded DONs to deoxyribonuclease I (DNase I) digestion (see Figure 1) (48–50). Real-time monitoring of the spectroscopic changes during the digestion show that both the DNA degradation rates and the DOX release profiles depend on the DNA origami superstructure and the amount of loaded DOX. We believe that through identification of these fundamental and some previously undiscovered features of the loading process, the spectroscopic properties of DOX, as well as the superstructure-dependent stability factors of DONs in physiological conditions (51–54), it may become possible to rationally design the delivery capability, control the dose, and thus achieve the optimal therapeutic efficacy in DOX delivery.

MATERIALS AND METHODS

Materials

Doxorubicin hydrochloride (HPLC-purified, Sigma-Aldrich) was dissolved in Milli-Q water for a 10 mM stock solution, divided into aliquots and stored at −20°C. After thawing, the stock solution was stored at +4°C and used within 1–2 days. DNase I was purchased from Sigma-Aldrich. A stock solution was prepared at 2 U/μl concentration in deionized water and stored in aliquots at −20°C, and after thawing stored at room temperature (RT) and used within the same day.

The staple oligonucleotides for DON folding were purchased from Integrated DNA Technologies. For the Rothemund triangle (7), bowtie (55), double-L (55), and the closed capsule (25), the staple strand sequences and folding protocols were adopted from the original publications. The 24-helix bundle (24HB) was designed using caDNAno (56) and its shape was predicted using CanDo software (57,58). The design of the 24HB structure is presented in the Supplementary Figures S16–S18, and its staple strand sequences in the Supplementary Table S5. The self-assembly reaction for the 24HB was carried out in a buffer containing 1× TAE and 17.5 mM $MgCl_2$. The reactions were heated to 65°C, and assembled by first cooling to 59°C with a rate of 1°C/15 min and then to 12°C with a rate of 0.25°C/45 min. The 7249 nt long M13mp18 scaffold was used for folding the triangle, bowtie and double-L. The extended 7560 nt and 8064 nt variants were used for folding the 24HB and capsule, respectively. All DNA scaffold strands were purchased from Tilibit Nanosystems at 100 nM concentration. After thermal annealing, the DONs were purified of excess staple strands using polyethylene glycol (PEG) precipitation (59) in the presence of 7.5% (w/v) PEG 8000 (Sigma-Aldrich). After purification, the DONs were resuspended in 40 mM Tris, 10 mM $MgCl_2$, pH 7.4 and incubated overnight at RT before use. The structural integrity was verified by atomic force microscopy (AFM) and transmission electron microscopy (TEM).

Spectroscopy techniques

Unless otherwise indicated, all UV–Vis absorption and fluorescence measurements were carried out with the Aqualog absorbance-fluorescence system (Horiba Scientific) operated with the Aqualog Software (v4.2) (Horiba Scientific), with the sample in a 10 mm optical path length cuvette. In spectral scans, a 3D excitation–emission matrix and the absorption spectrum of the sample were recorded simultaneously using an excitation light scan at 2 nm increments between 240 and 700 nm with 5 nm slit width. The emission spectrum for each excitation wavelength was collected between 245.16 and 827.17 nm at 1.16 nm increments with the CCD array. All measurements were performed at RT.

A 3 μM DOX concentration was selected for most experiments for avoiding possible DOX aggregation and self-

quenching at high concentration, but also for performing accurate spectroscopic analysis in the low absorbance ($A < 0.1$) region where both A and emission intensity (I) values exhibit linear dependency on the concentration of the studied molecules.

Free DOX characterization: spectroscopic analysis of the effect of pH and $MgCl_2$ concentration

For studying the effect of buffer pH on the spectroscopic properties of DOX, 40 mM Tris–HCl buffers at pH 6.0, 7.0, 7.4, 7.8, 8.0, 8.2, 8.6 or 9.0 were prepared by dissolving the required amount of Tris base in water and adjusting the pH of the solution with 1 M HCl. 3 μM DOX solutions were prepared in each of the buffers from the 10 mM stock solution and the UV–Vis absorption and 3D excitation-emission matrices of all samples were measured separately.

For the measurement of DOX absorption and fluorescence in the presence of different $MgCl_2$ concentrations, 3 μM solutions of DOX were prepared in 40 mM Tris–HCl buffers at pH 7.4 at both 0 mM and 100 mM $MgCl_2$ concentration. The absorption and fluorescence spectra of both samples were first recorded separately. The 3 μM DOX in the 100 mM $MgCl_2$ buffer was then added in small volumes into the 0 mM $MgCl_2$ DOX solution in the cuvette. After each addition, the sample was mixed by vortexing and its absorption and fluorescence spectra were recorded. The $MgCl_2$ concentration at each titration step was calculated according to the added volume of the 100 mM $MgCl_2$ DOX solution.

DOX loading and self-aggregation study

The DOX-DON loading was studied in three different buffers: (i) 40 mM Tris with 10 mM $MgCl_2$, pH 7.4, (ii) 40 mM Tris with 10 mM $MgCl_2$, pH 8.0 and (iii) 1× TAE with 12.5 mM $MgCl_2$ (1× FOB), pH 8.0. DOX-DON samples were prepared in each of the studied buffers by mixing the triangle DON (at 2.5 nM final concentration) with either 2 mM, 200 μM or 20 μM DOX. Corresponding reference samples of DOX without DONs were prepared at 2 mM, 200 μM or 20 μM DOX concentration in each of the buffers.

The UV–Vis absorption spectra of the solutions were measured in the beginning of the experiment using either a Cytation 3 cell imaging multi-mode reader (BioTek) on a Take3 plate with a 0.5 mm optical path length (2 mM and 200 μM samples), or Nanodrop ND-1000 with a 1 mm path length (20 μM samples). After 24, 48 or 96 h incubation in dark at RT, the samples were centrifuged for 10 min at 14 000 g to separate the fraction of insoluble DOX. The effect of the applied centrifugal force (2000–14 000 g) was additionally tested with 200 μM DOX in FOB pH 8.0 after 24 h incubation (Supplementary Methods and Supplementary Figure S3). The concentration of DOX in the supernatant was determined by removing a small volume of the supernatant and measuring the UV–Vis absorption similarly as in the beginning of the incubation. The DOX concentration in the supernatant (c_{free}) relative to the concentration at $t = 0$ was calculated from the A_{480}, and $c_{aggregate}$ was defined as $c_{aggregate} = c_0 - c_{free}$. The experiment was repeated three times and the final values were reported as the mean ± standard error.

DNA origami—DOX titrations

UV–Vis and fluorescence spectroscopy. Association of DOX with DONs was studied by titrating a solution of 3 μM DOX in 40 mM Tris, 10 mM $MgCl_2$, pH 7.4 with a solution containing *ca*. 40 nM DONs (triangle, bowtie, double-L, capsule or 24HB) and 3 μM DOX in the same buffer. 40 nM DON concentration corresponds to 558–605 μM base pair concentration [c(bp)] depending on the DON design (see details in Supplementary Table S1). After each addition of the titrant, the sample was mixed by vortexing and let to equilibrate for 2.5 min before measuring the absorption and fluorescence spectra.

The effect of the equilibrium time was further studied with kinetic measurements for both 2D and 3D structures. The absorption and fluorescence spectra of 3 μM DOX in 40 mM Tris, 10 mM $MgCl_2$, pH 7.4 were first recorded in the absence of DONs. Triangle DONs or 24HB DONs were then added at a molar ratio of bp/DOX ≈ 2 and the absorption and fluorescence spectra of the samples were collected after 0.5, 2.5, 5, 10, 15 and 20 min of incubation.

Data analysis and fitting. The concentration of DNA [total nucleotide concentration c(nt)] at each point of the titration was determined from the DNA absorption at 260 nm (A_{260}). As both DNA and DOX absorb light at 260 nm, the contribution of DOX absorption was removed from the obtained A_{260} values by subtracting the A_{260} of 3 μM DOX solution. c(nt) was then determined according to the Beer-Lambert law. The molar extinction coefficient per nucleotide (ϵ_{260}/nt) was calculated separately for each DON with a formula adapted from Hung *et al*. (60) according to the number of unpaired nucleotides (N_{ss}) and number of hybridized nucleotides (N_{ds}) in the design,

$$\epsilon_{260}/\mathrm{nt} = \frac{6700 \times N_{ds} + 10\,000 \times N_{ss}}{N_{ds} + N_{ss}} \mathrm{M^{-1}cm^{-1}}. \quad (1)$$

The values of N_{ss} and N_{ds} for each DON are presented in Supplementary Table S1. The value of N_{ds} takes into account both the base pairs formed by hybridization of the scaffold and staple strands, and the base pairs formed as secondary structures through hybridization of self-complementary regions of unpaired scaffold loops. The number of base pairs in the secondary structures was simulated with the NUPACK web application (61).

As the intercalation of DOX into DONs depends on the N_{ds}, only the concentration of hybridized nucleotides [base pair concentration $c(\mathrm{bp})_0 = 0.5 \times c(\mathrm{nt}) \times N_{ds}/(N_{ds} + N_{ss})$] was taken into account in the analysis. To justify this, DOX was also titrated with ssDNA (Supplementary Figure S9). ssDNA quenches DOX fluorescence only slightly when compared to the quenching caused by double-stranded DNA (dsDNA). Although all DONs used in this work, except the triangle, contain ssDNA regions at both poly-T_8 extensions at the helix ends and at unpaired scaffold loops, their contribution to DOX quenching is thus negligible. In addition, the fraction of unpaired nucleotides (mostly the inert poly-T sequences) of the total number of

nucleotides [$N_{ss}/(N_{ds} + N_{ss})$] in the structures is small (0.4–12%).

For fitting the fluorescence data, emission intensity values from 450, 460, 470, 480 and 494 nm excitation were obtained from the integrated emission spectra. The values were corrected for the extinction coefficient decrease during titration by dividing with $(1 - T)$ of the excitation wavelength (T denotes the transmittance, obtained from the simultaneous absorption measurement). The corrected values thus represent the decrease of DOX fluorescence quantum yield (Φ) upon DNA binding. The obtained values for $\Delta\Phi_{obs} = \Phi_{obs} - \Phi_0$ for each $c(bp)_0$ were fitted with a 1:2 host–guest binding model with a BindFit online fitting tool at https://supramolecular.org (62). The fit describes the change of the studied physical property (ΔY_{obs}) as

$$\Delta Y_{obs} = \frac{y_{\Delta 11} K_{11} c(bp)_{ub}}{1 + K_{11} c(bp)_{ub} + K_{11} K_{12} c(bp)_{ub}^2} + \frac{y_{\Delta 12} K_{11} K_{12} c(bp)_{ub}^2}{1 + K_{11} c(bp)_{ub} + K_{11} K_{12} c(bp)_{ub}^2}, \quad (2)$$

where in the case of Φ, ΔY_{obs} refers to the measured $\Delta\Phi_{obs}$, while $y_{\Delta 11}$ and $y_{\Delta 12}$ refer to the differences of the quantum yields of the 1:1 and 1:2 DOX:base pair complexes and the quantum yield of free DOX ($\Phi_{\Delta 11}$ and $\Phi_{\Delta 12}$), respectively. The binding constants K_{11} and K_{12}, as well as $\Phi_{\Delta 11}$ and $\Phi_{\Delta 12}$ were obtained from the fit. In Equation (2), $c(bp)_{ub}$ is the concentration of unbound base pairs, *i.e.* the free base pairs not bound to DOX, obtained from

$$Ac(bp)_{ub}^3 + Bc(bp)_{ub}^2 + Cc(bp)_{ub} - c(bp)_0 = 0, \quad (3)$$

$$\text{where } \begin{cases} A = K_{11} K_{12} \\ B = K_{11}[2K_{12} c(DOX)_0 - K_{12} c(bp)_0 + 1]. \\ C = K_{11}[c(DOX)_0 - c(bp)_0] + 1 \end{cases}$$

The fraction of bound DOX molecules f_b at each step of the titration was then calculated as

$$f_b := \frac{c(DOX)_b}{c(DOX)_0} = 1 - \frac{1}{1 + K_{11} c(bp)_{ub} + K_{11} K_{12} c(bp)_{ub}^2}, \quad (4)$$

where $c(DOX)_b$ is the calculated bound DOX concentration at the specific $c(bp)_{ub}$, and $c(DOX)_0$ denotes the total DOX concentration (3 μM).

After K_{11}, K_{12} and $c(bp)_{ub}$ for each $c(bp)_0$ were obtained from the analysis of the fluorescence data, the molar extinction coefficients of the two DOX–DNA complexes, ϵ_{11} and ϵ_{12} at wavelengths 450, 460, 470, 480 and 494 nm, were determined with non-linear least-squares curve fitting with MATLAB R2015b to the Equation (2). For absorbance, $y_{\Delta 11}$ refers to $\epsilon_{\Delta 11}$, and $y_{\Delta 12}$ refers to $\epsilon_{\Delta 12}$ – the differences between the molar extinction coefficients of the two complexes and the molar extinction coefficient of free DOX (listed in the Supplementary Table S2). ΔA_{obs} is the difference between the absorbance of the sample and the absorbance of 3 μM DOX in the absence of DNA.

DNase I digestion of DNA origami

Kinetic UV–Vis and fluorescence measurements. The DNase I digestion and DOX release rates of the studied DONs were determined based on the absorbance and fluorescence spectra of the samples collected during DNase I digestion. The digestion of each DON was studied both in the absence of DOX and after loading the DONs with DOX. The samples without DOX contained 2 nM DONs in 40 mM Tris, 10 mM $MgCl_2$, pH 7.4. The DON-DOX samples contained 2 nM DONs and either 3 or 6 μM DOX. Unbound DOX in the solution was not removed before the digestion, as the removal of free DOX from the system would disturb the binding equilibrium and promote the dissociation of bound DOX from the DONs, complicating the analysis of the release caused solely by DNase I digestion. In addition, the comparison between samples can be performed more accurately when the concentration of each component in the sample (DNA, bound DOX and free DOX) is known precisely and not changed with purification protocols, such as spin-filtration.

The absorbance and fluorescence spectra of the samples were first collected without DNase I. DNase I was then added to final concentration of 34 U ml^{-1}, the sample was gently mixed with a pipette, and the absorbance and fluorescence spectra were collected at regular time intervals until the digestion had been completed. The total duration of the experiment was adjusted for each DON, ranging from <1 h required for a full digestion of the triangle DON with 0 μM DOX, to >40 h for the 24HB with 6 μM DOX.

Samples containing only 3 μM or 6 μM DOX and DNase I were measured similarly for obtaining references for the fluorescence quantum yield of free DOX in the same experimental conditions.

Data analysis of the kinetic measurements. The nuclease digestion of the DONs was quantified from the A_{260} value, which increases during the digestion. The percentage of intact dsDNA residues (% intact) at each time point t was calculated as

$$\%\ \text{intact} = \frac{A_{260}(t) - A_{260}(\text{intact})}{A_{260}(\text{digested}) - A_{260}(\text{intact})} \times 100\% \quad (5)$$

where $A_{260}(t)$ is the A_{260} value detected at a time point t, A_{260}(intact) is the A_{260} of fully intact structures measured before addition of DNase I, and A_{260}(digested) is the A_{260} of fully digested structures, measured after the digestion has been completed (A_{260} value stabilized). The DNase I digestion rates were determined by fitting a linear regression to the obtained % intact values versus time with MATLAB R2015b at the initial period of the digestion where the A_{260} increases linearly. Digestion rates were determined from three repeated experiments and reported as the mean ± standard error.

The analysis of DOX release from the DONs during DNase I digestion was based on the recovery of DOX quantum yield [fluorescence emission intensity from 494 nm excitation divided by (1 – T)]. The mole fraction of bound DOX molecules at each time point [$f_b(t)$] was calculated with Equation (4). In Equation (4), $f_b(t)$ calculation is based on the $c(bp)_{ub}$ at each time point; $c(bp)_{ub}$ was solved from

a modified and rearranged version of Equation (2),

$$(K_{11}K_{12}\Delta\Phi_{obs} - K_{11}K_{12}\Phi_{\Delta 12})c(\mathrm{bp})_{ub}^2 + (K_{11}\Delta\Phi_{obs} - K_{11}\Phi_{\Delta 11})c(\mathrm{bp})_{ub} + \Delta\Phi_{obs} = 0, \quad (6)$$

where $\Delta\Phi_{obs}$ is the measured difference of the quantum yield of the DOX-DON sample and the free DOX reference of the same DOX concentration. $\Phi_{\Delta 11}$ and $\Phi_{\Delta 12}$ are the differences between the quantum yield of free DOX and the quantum yields of the 1:1 and 1:2 DOX-DNA complexes, respectively. K_{11}, K_{12}, $\Phi_{\Delta 11}$ and $\Phi_{\Delta 12}$ are fit parameters averaged from the titration experiments of all the studied DONs (Supplementary Table S2). The percentage of released DOX (Figure 5A) was then defined as

$$\%\ \text{released} = \frac{f_b(\text{intact}) - f_b(t)}{f_b(\text{intact})} \times 100\%, \quad (7)$$

where f_b(intact) is f_b of the sample before addition of DNase I. DOX release rates were acquired by fitting a linear regression to the % released *vs.* time in the initial linear phase of drug release. For calculating the DOX release rate in terms of relative dose (number of released molecules) per unit of time, the rate values were multiplied by the DOX concentration bound to the DONs in the intact state. The DOX release rates were determined from three repeated experiments and reported as the mean ± standard error.

Microscopy imaging

Atomic force microscopy (AFM). To prepare the 2D DON (triangle, bowtie and double-L) samples for AFM imaging, 10 μl of 3 nM DON solution in 1× FOB (with 10 mM $MgCl_2$) was pipetted onto a fresh-cleaved mica sheet and incubated for 5 min. The mica substrate was then washed 3 times with 100 μl ddH_2O by allowing it to flow from one end of the mica to the other and being blotted using a piece of cleanroom sheet. Finally, the sample was rigorously dried by pressurized N_2 gas. The AFM imaging was carried out using either a JPK NanoWizard ULTRA Speed with USCF0.3-k0.3 cantilevers (NanoWorld) in a liquid cell filled with 1× FOB (with 10 mM $MgCl_2$) or using a Bruker Dimension Icon instrument in Scanasyst air mode and Scanasyst-air probes.

Transmission electron microscopy (TEM). The 3D DON samples (capsule and 24HB) were characterized using a Tecnai T12 TEM instrument. Copper TEM grids with both carbon and formvar films (FCF400-Cu from Electron Microscopy Sciences) were cleaned with O_2 plasma for 20 s, followed by pipetting 3 μl of 20 nM DON solution on the grid and incubating for 2 min. Then the excess amount of solution was blotted with a piece of filter paper. To achieve better contrast, the sample was immediately stained with 20 μl of 2% uranyl formate for 40 s followed by blotting the staining solution with the filter paper. The grid was let to dry for at least 30 min before imaging.

RESULTS

Effects of buffer conditions on the spectroscopic features of DOX

To ensure that the obtained spectroscopic changes in later experiments are associated reliably with the DOX–DNA binding events and not caused by the environment, we first identified the effects of the buffer conditions on the spectroscopic properties of DOX. We performed a series of measurements on DOX in the absence of DNA in Tris-based buffers typically applied in DON experiments. In particular, we screened the effect of two buffer parameters; pH and $MgCl_2$ concentration.

Buffer pH. For identifying the effects of buffer pH on the spectroscopic features of DOX, 40 mM Tris–HCl buffers were prepared at pH 6.0–9.0 and the absorption and fluorescence spectra of DOX were collected at each pH. The shape of the DOX absorption spectrum as well as its molar extinction coefficient (ϵ) depends heavily on buffer pH (Figure 2A). Between pH 6.0–8.0, the shape of the spectrum is maintained, but ϵ increases with decreasing pH throughout the whole absorption spectrum. For instance, ϵ_{494} is ∼65% higher at pH 6.0 than at pH 8.0. A higher emission intensity is also observed at lower pH values, as shown in Figure 2A inset with a 494 nm excitation.

Above pH 8.0, the shape of the absorption spectrum changes and a new absorption peak emerges at ∼590 nm. Exciting the molecules at this wavelength does not lead to DOX fluorescence, thus showing that at pH 8.0 and above, an increasing fraction of DOX molecules is non-fluorescent. DOX is known to have a pK_a value for the deprotonation of the amino sugar NH_3^+ group at pH 8.2 (47). The observed emergence of non-fluorescent molecules takes place around the same pH value, being thus likely associated with the deprotonation events. These observations are also in line with previous reports of DOX absorbance in high pH buffers (63), and the spectral changes could thus be expected to become even more pronounced at pH values above 9.0.

Near the pK_a, the sample contains a distribution of charged and neutral molecules, and in the spectroscopic means, a mixture of fluorescent and non-fluorescent DOX molecules. While the sample is thus heterogeneous, the emission spectrum remains homogeneous as the non-fluorescent molecules do not contribute to the signal (Supplementary Figure S1). As the sample heterogeneity would nevertheless complicate the interpretation of experimental results, it is beneficial to conduct experiments at pH well below the pK_a. Based on both the existing literature and the obtained spectra, an optimal pH range for further experiments was determined as 6.0–7.8, where altering the pH does not change the shape of the absorption spectrum.

Buffer $MgCl_2$ concentration at pH 7.4. DOX is known to form complexes with metal ions, such as Fe^{3+}, Cu^{2+}, Mn^{2+}, Ni^{2+}, Co^{2+}, Mg^{2+} and Zn^{2+} (63–65). Metal ion complexation thus presents another source of DOX heterogeneity in buffers supplemented with divalent cations. When the $MgCl_2$ concentration in the buffer increases, both the absorption and fluorescence properties of DOX change indicating complexation of DOX with Mg^{2+} ions (Figure 2B).

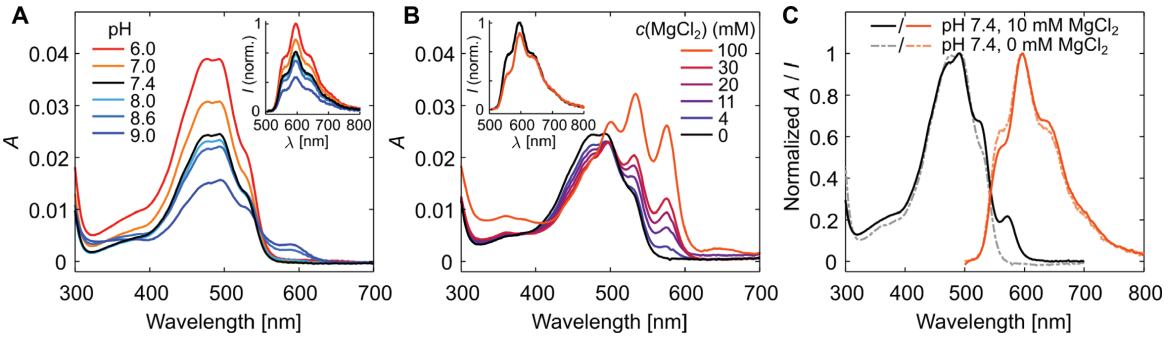

Figure 2. Effects of buffer conditions on the spectral features of DOX in the absence of DNA. (**A**) Absorption and emission (inset) spectra of 3 μM DOX in 40 mM Tris, 0 mM $MgCl_2$ at pH 6.0–9.0. The emission spectra were obtained at an excitation wavelength of 494 nm. (**B**) Spectral features of 3 μM DOX in 40 mM Tris, pH 7.4 buffer at different $MgCl_2$ concentrations. The inset figure shows a comparison of the emission spectra of the 0 mM and 100 mM samples at 494 nm excitation, with the maximum emission intensity of the 0 mM $MgCl_2$ sample normalized to 1. The 0 mM $MgCl_2$ spectrum (black) corresponds to the pH 7.4 spectrum in (A). (**C**) Absorption (black/gray lines) and emission (orange lines) spectra of 3 μM DOX in the chosen experimental conditions: 40 mM Tris, 10 mM $MgCl_2$, pH 7.4. The effect of the 10 mM $MgCl_2$ concentration is shown by comparing the spectra measured at 10 mM $MgCl_2$ (solid lines) with spectra measured at 0 mM $MgCl_2$ (dashed lines).

In the presence of 100 mM $MgCl_2$, three distinct peaks at 500, 534 and 576 nm are observed in the absorption spectrum. The 576 nm peak emerges only in the presence of $MgCl_2$, and excitation at this absorption peak leads to a fluorescence spectral shape that is rather distinct from that of DOX in the absence of $MgCl_2$ (Supplementary Figure S2). While the emission spectrum of DOX at 0 mM $MgCl_2$ is homogeneous over the full absorption spectrum, the addition of $MgCl_2$ induces heterogeneity in the emission measurement reflected as the shape of the emission spectrum changing with the excitation wavelength (Supplementary Figure S2). As a result, the shape of the emission spectrum upon 494 nm excitation depends slightly on the $MgCl_2$ concentration (Figure 2B inset).

A comparison of the absorption and fluorescence spectra of 3 μM DOX in 40 mM Tris, pH 7.4 with either 0 mM or 10 mM $MgCl_2$ is shown in Figure 2C. The spectral differences indicate that at 10 mM $MgCl_2$, the sample and its absorption and fluorescence spectra are a combination of pure DOX and a small concentration of the DOX–Mg^{2+} complex. Despite the slight DOX heterogeneity in these conditions, 40 mM Tris at pH 7.4 supplemented with 10 mM $MgCl_2$ was chosen for all the experiments to maintain structural stability and integrity of the DONs.

DOX loading

DOX self-aggregation during loading. As the buffer pH and $MgCl_2$ concentration have considerable effects on the physical and spectroscopic properties of free DOX, they can be assumed to affect the association of DOX with DONs; i.e. the loading process. To study this, we loaded the triangle DON (Figure 4A) with DOX in three different buffers: in 40 mM Tris, 10 mM $MgCl_2$ at pH 7.4 (Tris/Mg^{2+} pH 7.4); in 40 mM Tris, 10 mM $MgCl_2$ at pH 8.0 (Tris/Mg^{2+} pH 8.0); and in a typical DON folding buffer (FOB) containing 1× TAE [40 mM Tris, 19 mM acetic acid, 1 mM ethylenediaminetetraacetic acid (EDTA)] and 12.5 mM $MgCl_2$ at pH 8.0. The triangle DON was selected, as it has been widely used as a DOX carrier in previous studies.

The protocol for loading (Figure 3A) was adapted from previous studies (33,35–39). In the loading process, DONs (here, triangle DONs at 2.5 nM concentration) are mixed with an excess of DOX, the mixture is incubated at RT, and the DOX-loaded DONs are purified from free DOX by e.g. centrifugation or spin-filtration. In our experiment, the DOX loading concentration (c_0) was varied from 20 μM to 2 mM. Interestingly, DOX loading has often been performed with DOX concentration in the range of 1–2.5 mM in a FOB containing 10–12.5 mM Mg^{2+} at pH 8.0–8.3. At this pH near the pK_a of the NH_3^+ group, part of the DOX molecules are in the deprotonated (uncharged) form and known to be poorly soluble (0.3 mg ml^{-1}; 0.55 mM) (47). In addition, dimerization ($K_a = 1.4\times 10^4$ M^{-1}) (45), oligomerization (47) or Mg^{2+} complexation (63–65) can be expected to lead to DOX aggregation.

During centrifugation, high molecular weight (MW) particles, such as DOX-loaded DONs, are separated from free DOX (low MW) through sedimentation into a dark red precipitate (Figure 3A, middle panel; photographs in the Supplementary Figure S3). In addition to DOX-loaded DONs, the centrifugation can lead to a sedimentation of other high-MW particles, such as DOX aggregates. To distinquish the DOX–DON formation from the possible aggregation and sedimentation of DOX, each DOX–DON sample in the experiment was compared to a reference sample containing only DOX.

The concentration of DOX in the pellet ($c_{aggregate}$) was quantified by determining the concentration of DOX remaining in the supernatant (c_{free}) from DOX absorption at 480 nm (Figure 3A, right panel). As shown in Figure 3B, the $c_{aggregate}$ increases with the incubation time, c_0, pH and the $MgCl_2$ concentration. A comparison of the DOX–DON samples and the DOX-only control samples reveals that nearly identical amounts of DOX are found in the pellets of both DOX–DON samples and DOX-only control samples.

For the DOX-only samples, this supports the hypothesis that DOX self-aggregation takes place during prolonged incubation at RT. Aggregation becomes particularly consid-

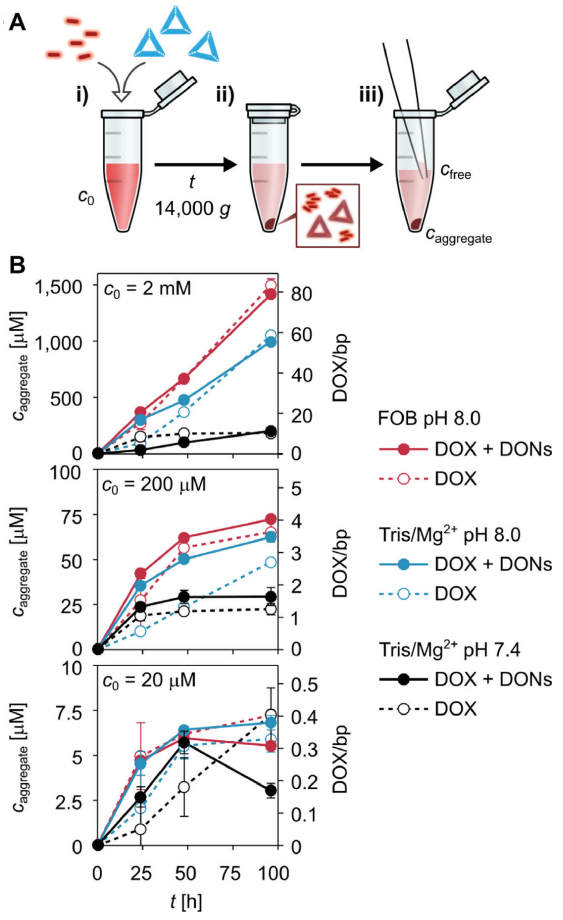

Figure 3. The formation of DOX–DON complexes and DOX aggregates during the loading process. (**A**). In the applied loading protocol, (i) DOX ($c_0 = 2$ mM, 200 μM or 20 μM) is mixed with 2.5 nM triangle DONs and incubated at RT. Control samples are prepared without DONs. (ii) After $t = 24$, 48 or 96 h, centrifugation for 10 min at 14 000 g is used to separate high-MW particles from the solution; either DOX-loaded DONs or DOX aggregates. (iii) The concentration of DOX removed from the solution by precipitation ($c_{aggregate}$) is quantified by removing a small volume of the supernatant and determining the DOX concentration in the supernatant (c_{free}) from DOX absorbance (A_{480}); $c_{aggregate} = c_0 - c_{free}$. (**B**). The concentration of DOX in the pellet ($c_{aggregate}$) versus incubation time in the presence and absence of DONs. The amount of sedimentation was determined for 2 mM, 200 μM and 20 μM DOX loading concentration (c_0) in three different buffers: FOB pH 8.0 (12.5 mM $MgCl_2$), Tris/Mg^{2+} pH 8.0 (10 mM $MgCl_2$) and Tris/Mg^{2+} pH 7.4 (10 mM $MgCl_2$). For the DOX-DON samples, the DOX/bp ratio additionally indicates the number of DOX molecules in the precipitate per DNA base pair ($c_{bp} = 18$ μM for 2.5 nM DONs). The $c_{aggregate}$ values are expressed as the mean ± standard error, $n = 3$.

erable in samples prepared at pH 8.0 at $c_0 = 2$ mM, above the solubility limit of deprotonated DOX, confirming that aggregation takes place due to the low solubility of the deprotonated molecules. In addition, the DOX–Mg^{2+} interaction appears to lead to some degree of aggregation in all tested conditions and for all c_0 values.

As the DOX-DON interaction causes only little or no considerable increase in the $c_{aggregate}$, it is apparent that the main component in the pellets formed in the DOX–DON samples are likewise DOX aggregates. This becomes even more obvious when considering the amount of DOX in the pellet in relation to the amount of DNA base pairs (bp) in the sample; expressed as the DOX/bp molar ratio in Figure 3B. DOX/bp = 1 can be considered an upper limit of DOX intercalated into DONs, where 100% of the intercalation sites in the DONs are occupied by DOX. For both $c_0 = 2$ mM and $c_0 = 200$ μM, the DOX/bp ratio rises above DOX/bp = 1 in less than 24 h. These high DOX/bp ratios observed with triangle DONs indicate a considerable contribution of other aggregation and sedimentation mechanisms, and they are in line with previous reports ranging from DOX/bp = 6.9–56 (12–24 h incubation) (35,37–39) to as high as DOX/bp = 113 (24 h incubation) (33). We note that this is to our knowledge the first time that this type of DOX-only control samples are presented alongside DOX–DON samples to identify the possible role of DOX aggregation to the sample composition. Our results may thus not only describe the DOX aggregation behavior, but also give a simple explanation for some of the surprisingly high DOX contents reported in previous studies.

Absorption and fluorescence properties of the DOX–DON complexes. We then studied in detail the interaction between DOX and DONs in the selected buffer conditions (40 mM Tris, 10 mM $MgCl_2$, pH 7.4). In our experimental setup, a 3 μM solution of DOX is titrated with an increasing concentration of DONs, while maintaining a constant DOX concentration, which causes an increasing fraction of the DOX molecules bind to DNA over the titration. The observed changes in DOX light absorption and fluorescence can be used to extract information about the strength and stoichiometry of the non-covalent binding interaction. To determine whether the DOX loading efficiency into DONs can be tuned with the DON design, we performed the analysis for five structurally distinct DONs (Figure 4A). These include three 2D DONs: the triangle (7), a bowtie (55) and a double-L (55), and two 3D DONs: a capsule (25) and a 24-helix bundle (24HB) (Supplementary Figures S14–S16 and Supplementary Table S5). The correct high-yield folding and structural integrity of the DONs were verified with AFM or TEM (Figure 4A).

Figure 4B shows the spectral changes of DOX upon titration with the triangle DON. Binding to DNA causes a slight red-shift of the absorption spectrum and an overall decrease of ϵ in the visible wavelength region. Additionally, the absorption peak of the DOX–Mg^{2+} complex centered at 576 nm disappears, when the stronger DOX–DNA interaction causes dissociation of the weakly bound DOX–Mg^{2+} complexes. The DOX fluorescence quantum yield (Φ) decreases upon DNA addition, as shown in the inset of Figure 4B for 494 nm excitation. The fluorescence spectra were corrected for the decrease of ϵ_{494}, which also leads to decreasing fluorescence intensity when less light is absorbed in the sample. The dependency of both ϵ_{494} and Φ on the bp/DOX ratio in the sample (titration isotherms) are presented in the left panel of Figure 4C. The results obtained for bowtie, double-L, capsule and 24HB DONs appear highly similar to the triangle DON, and are presented in the Supplementary Figures S4–S5.

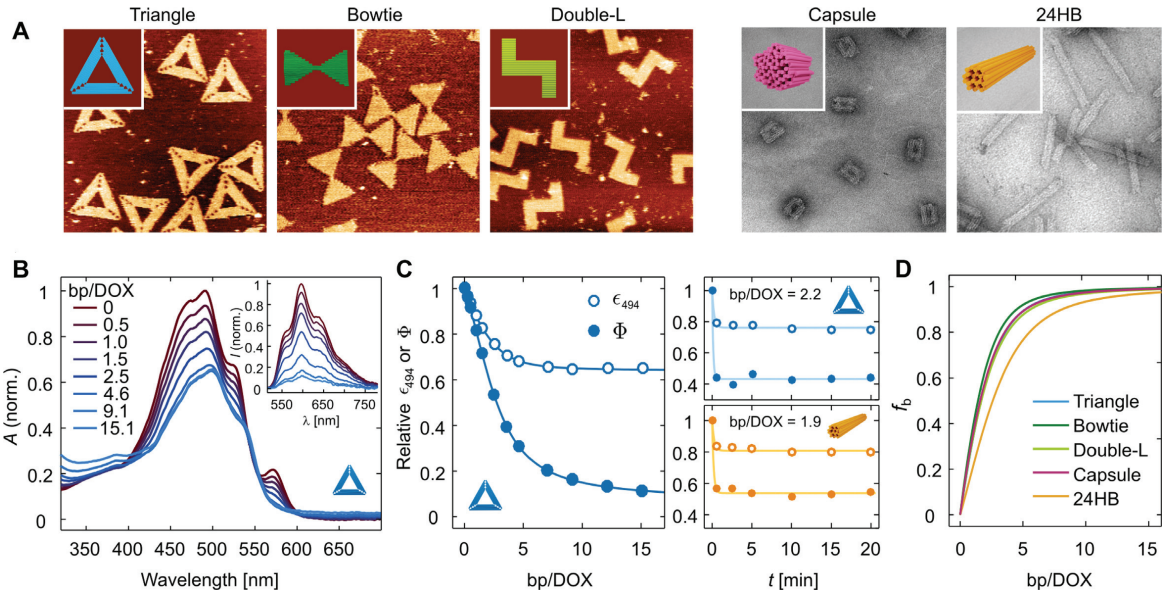

Figure 4. Titration experiments for determining the DOX-loading properties of DONs. (**A**) The models and microscopy images of the studied 2D and 3D DONs. The triangle, bowtie, and double-L 2D DONs are shown on the left accompanied by atomic force microscopy (AFM) images. The 3D DONs—the capsule and the 24-helix bundle (24HB) are shown on the right in TEM images. The AFM images are 500 nm × 500 nm in size, and the TEM images are 300 nm × 300 nm. (**B**) Representative changes in the absorption spectrum and fluorescence emission after 494 nm excitation (inset) of 3 μM DOX when the concentration of DNA base pairs (bp) in the solution is increased. The spectra have been measured for the triangle DON after the system has reached an equilibrium. The DNA concentration at each titration step is expressed as the molar ratio between DNA base pairs and DOX molecules in the sample (bp/DOX), and indicated in the legend. The fluorescence spectra have been corrected for the decrease of the molar extinction coefficient at the excitation wavelength (ϵ_{494}), and represent the quantum yield of the emitting molecules (Φ). (**C**) The dependency of ϵ_{494} and Φ on the bp/DOX ratio (left panel) and the loading kinetics (right panel). In the left panel, the measured values for ϵ_{494} and Φ during a titration with the triangle DON have been fitted with a 2-component binding model (Equation 2). The corresponding spectra and titration isotherms for the other DONs are presented in the Supplementary Figure S4. The kinetics of ϵ_{494} (empty circles) and Φ (filled circles) in the right panel have been measured by monitoring the absorption and fluorescence spectra of the samples after adding DONs (triangle or 24HB) at the indicated bp/DOX ratio at $t = 0$. The data sets have been fitted with a 1-component exponential decay model of the form $ae^{-bx} + c$ to illustrate the observed kinetic trends. (**D**) Increase of the fraction of bound DOX molecules (f_b) when the DNA base pair concentration in the sample increases, obtained by fitting the fluorescence data.

After addition of DNA, the samples were incubated for 2.5 min before the spectra were collected in order to reach an equilibrium where the amount of DOX bound to the DONs has stabilized. The 2.5 min incubation time was found to be sufficient for both 2D and 3D structures, as studied in a separate experiment for both the triangle and the 24HB (Figure 4C, right panel; spectra shown in the Supplementary Figure S8). After addition of DONs, both ϵ_{494} and Φ had stabilized by 30 s of incubation, and no further spectral changes were observed over longer incubation times. This is in accordance with existing literature where the equilibrium is reached within seconds (45), and shows that the DOX–DON loading process is likewise a faster process than has been previously acknowledged.

Increasing the amount of DONs in the sample causes a discernible scattering effect, which is stronger for the 3D structures than for the 2D structures (Supplementary Figure S10). In the absorbance measurement, this is observed as a slight elevation in the spectrum baseline during the titration. Further analysis of the binding was thus based on the fluorescence data, which is less affected by the light scattering. Analysis of the absorption data was then carried out using the parameters obtained from the analysis of the fluorescence data.

Interpretation of the experimental results through a molecular binding model. DOX has been proposed to bind double-stranded DNA (dsDNA) through two prevalent mechanisms: intercalation between G–C base pairs, and minor groove binding at A–T rich areas driven by electrostatic interactions (45). The fluorescence of DOX has been shown to be fully quenched in the strongly bound DOX–GC complex, while the weaker DOX–AT complex remains gently fluorescent (45,66). For describing the observed decrease of Φ and ϵ when increasing the concentration of DONs, we thus applied a 1:2 molecular binding model for including both modes of interaction and the formation of two distinct DOX–DNA complexes with different association constants (K_{11} and K_{12}) and fluorescence quantum yields (Φ_{11} and Φ_{12}). This is also fully supported by our observations: when DOX electrostatically binds to a single-stranded DNA (ssDNA), its fluorescence is not quenched, although its absorption spectrum changes in a similar fashion as in the case of DONs (Supplementary Figure S9). However, it is noteworthy that the staple mixture for folding the triangle DON quenches DOX efficiently, as dsDNA residues are formed through partial hybridization or self-complementarity of the staple strands. Therefore, the purification of the structures from the excess staples after DON folding is required

for reliable quantification of DOX loading efficiency. As DOX can be assumed to bind selectively in the dsDNA regions of the DONs, the ssDNA nucleotides in the DONs (unpaired scaffold regions and the inert poly-T sequences at the end of the helices) were excluded from the binding analysis.

In the left panel of Figure 4C, the dependence of Φ and ϵ_{494} on the base pair concentration (triangle DON) is described according to Equation (2). The model suggests that the two DOX-DNA complexes with an average $K_{11} = (2.0 \pm 0.3) \times 10^5$ M^{-1} and $K_{12} = (2.6 \pm 0.2) \times 10^5$ M^{-1} can be differentiated from each other by the extent of fluorescence quenching ($\Phi_{11}/\Phi_0 = 0.52 \pm 0.07$ and $\Phi_{12}/\Phi_0 = 0.067 \pm 0.009$), but in terms of light absorbance their physical properties are similar ($\epsilon_{11}/\epsilon_0 = 0.58 \pm 0.08$ and $\epsilon_{12}/\epsilon_0 = 0.67 \pm 0.09$ for 494 nm).

While obviously a simplified model of the DOX–DON interaction, the selected binding model can thus be seen to present a reasonable approximation for the behavior of the system and the changes of the physical properties of DOX (Φ and ϵ) upon DNA addition by taking into account the two types of binding modes, and essentially, their distinct fluorescence properties. The determined values of K_{11} and K_{12} are in the same range and order of magnitude as in previous studies (45,66)—nevertheless, we note that generalization of the fitting results and the obtained parameters outside the presented experimental conditions should be carried out with caution due to the simplifications of the model. A comparison of the fitting parameters for all DONs presented in this study can be found in the Supplementary Table S2.

Finally, the fraction of bound DOX molecules at each bp concentration can be obtained from the fit according to Equation (3), which enables a comparison of the DOX loading properties of the studied DONs (Figure 4D). It appears that the DNA origami superstructure has relatively little effect on how much DOX is bound to the structures, as all curves in Figure 4D are rather similar. In the beginning of the titration, the fraction of bound DOX increases sharply when DNA is introduced into the sample, and the maximum number of bound DOX molecules per base pair is reached at 0.36 ± 0.10 (Supplementary Figure S6).

DOX release upon nuclease degradation

After determining that all the studied DONs have a similar DOX loading capacity, we studied their differences towards DNase I digestion both in the absence of DOX and when loaded with DOX. For the experiment, DOX-loaded DONs (2 nM) were prepared at both 3 and 6 μM DOX loading concentrations. The loading concentration can be used to adjust the DOX loading density. Here, increasing the DOX concentration from 3 to 6 μM, while keeping the concentration of DNA base pairs constant, promotes DOX association with the DONs and leads to a higher density of bound DOX molecules. According to the measured quantum yield of DOX and the thermodynamic binding model, the density of bound DOX molecules was 0.17 ± 0.02 DOX/bp for the 3 μM loading concentration and 0.25 ± 0.03 DOX/bp (∼47% higher) for the 6 μM loading concentration. In other words, on average 71% and 63% of DOX molecules in the samples were bound to DONs at 3 μM and 6 μM DOX concentrations, respectively (Supplementary Table S4).

To both confirm the increased loading density at 6 μM DOX concentration and to investigate methods for removing the remaining free DOX from the samples after loading, a supporting experiment was performed: the triangle DON was loaded with DOX at 3–20 μM DOX loading concentration, purified of free DOX with either spin-filtration or with PEG precipitation, and the DOX and DNA contents of the purified samples were measured (Supplementary Figure S12). The determined loading densities were 0.10 ± 0.01 DOX/bp for 3 μM DOX and 0.16 ± 0.02 DOX/bp for 6 μM DOX, with a maximum loading density at 0.45 ± 0.04 DOX/bp. In line with the thermodynamic model, the loading density thus increased by ∼60% when the DOX concentration was doubled. Additionally, both spin-filtration through a 100 kDa MW cut-off membrane and PEG precipitation were termed effective for removing free DOX from DOX–DON samples when the loading was performed at a low (<10 μM) DOX concentration (purification details are presented in the Supplementary Methods, in the Supplementary Note 13, and in the Supplementary Figures S11–S13). However, removing the free DOX disturbs the binding equilibrium, and DOX will be released until a new equilibrium is reached. We importantly observed a fast spontaneous, diffusive release of DOX: freshly spin-filtered, DOX-loaded bowtie DONs had released up to 70% of the initially bound DOX molecules and stabilized into a new binding equilibrium within 10 minutes of the purification (Supplementary Figure S13). The purification of DOX-loaded DNA origami is therefore redundant; while the free DOX concentration is decreased by 80–90%, the DOX loading density of DONs also decreases significantly. The DNase I experiments were thus performed without further purification of the samples.

During DNase I digestion, the nucleases cleave the DONs into short ssDNA fragments. As the ϵ_{260}/nt for ssDNA is higher than the ϵ_{260}/nt for dsDNA (67), the process can be followed from the A_{260} of the sample. When the DONs are digested, their A_{260} increases until reaching a saturation point where the structures are fully digested. The bound DOX is released when the double-helical DNA structure unravels, observed as a recovery of DOX fluorescence. In order to follow both processes in detail during the digestion, we employed a simultaneous kinetic spectroscopic characterization of both the increase of the A_{260} and the recovery of DOX fluorescence quantum yield.

Comparing the digestion profiles of the different DONs reveals that the DONs break down at distinct rates depending both on the DNA origami superstructure and the DOX concentration in the sample (Figure 5A). In the beginning of the digestion, the dependence of A_{260} on the digestion time is roughly linear. Determining the digestion rates from the linear phase allows a detailed comparison of the DNase I resistance of the different samples (Figure 5C). Both of the studied 3D DONs are digested slower than the 2D structures. The fastest digestion was observed for the triangle DON in the absence of DOX, with the structures being completely degraded within 20 min of incubation in the presence of 34 U ml^{-1} DNase I. Loading the DONs with DOX (3 μM) slowed down the digestion considerably, and increas-

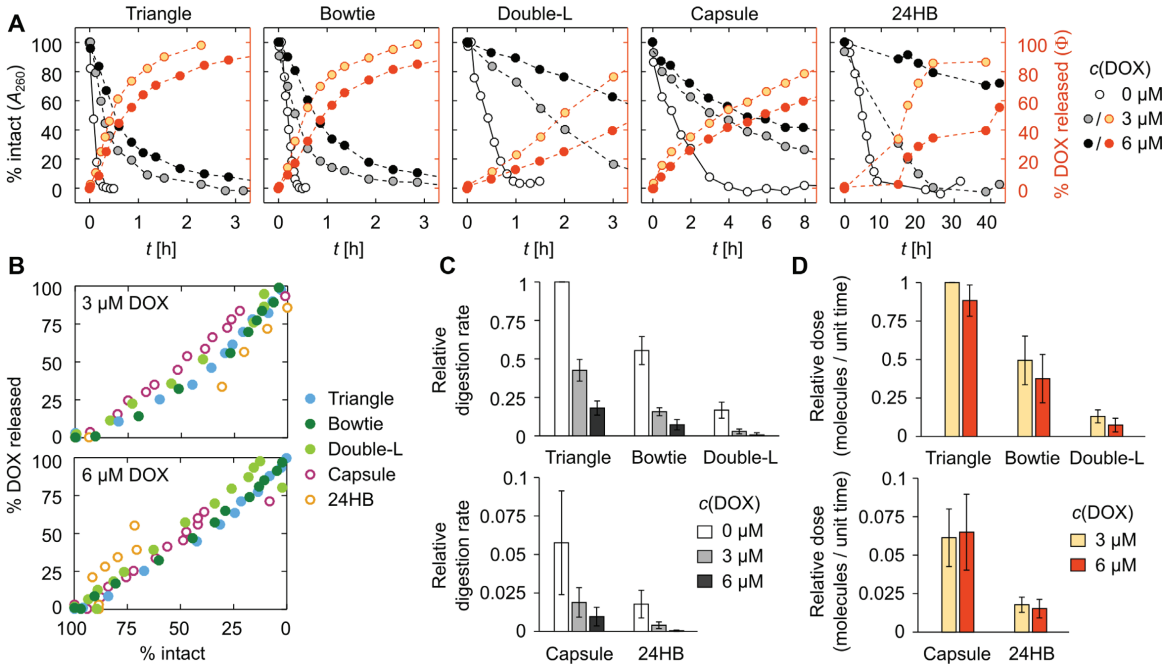

Figure 5. DNase I digestion of the DONs and the subsequent DOX release. (**A**) Representative ($n = 1$) digestion and DOX release profiles of the studied DONs at different DOX loading concentrations, after introducing 34 U ml^{-1} DNase I into the sample at $t = 0$. The structural integrity of the DONs (% intact) has been determined from the increase of the A_{260} signal, and shown with the white, gray, and black markers depending on the DOX concentration (0, 3 or 6 μM). For samples containing 3 or 6 μM DOX, the DOX release (% DOX released) is shown with the light and dark orange markers and represents the percentage of initially bound molecules that have been released due to the digestion. % DOX released has been determined from the recovery of the fluorescence quantum yield of DOX. (**B**) The cross-correlation between % DOX released and % intact for all DONs at 3 and 6 μM DOX loading concentration. (**C**) DNase I digestion rates of the DONs at 0, 3 or 6 μM DOX loading concentration. All digestion rates are shown relative to the triangle DON at 0 μM DOX concentration, and have been averaged from the digestion rates determined from three individual measurements; expressed as the mean ± standard error. (**D**) DOX release rates of the DONs at 3 and 6 μM DOX loading concentration. Relative dose stands for the absolute number of DOX molecules released per unit of time. All values are expressed as the mean ± standard error ($n = 3$).

ing the loading density further by applying a 6 μM DOX concentration led to a further inhibition of the DNase I activity.

Figure 5A shows how the bound DOX molecules are released from the DONs during the digestion, as determined from the recovery of DOX quantum yield. The release profiles of the studied DONs are in line with the superstructure- and DOX loading concentration dependent trends observed for the structural degradation (Figure 5A). A clear correlation between the fraction of released DOX and the intact dsDNA residues in the sample can be seen for both loading concentrations (Figure 5B). This confirms that the release of DOX is caused purely by the DNase I digestion of the dsDNA framework when the sample is in an equilibrium. The 3 μM DOX samples are digested faster than the 6 μM DOX samples, and the bound DOX is likewise released in a shorter period of time.

Although the 6 μM DOX samples are digested slower than the 3 μM samples, they are also more densely loaded with DOX. This leads to a release of more DOX molecules per a digested DNA base pair. In Figure 5D, the DOX release is thus considered in terms of the relative dose, i.e. the number of DOX molecules released per unit of time per unit of DNase I. This decreases the difference between the release properties of 3 μM and 6 μM DOX samples, but does not exceed the effect of the DNase I inhibition. Altogether, the 3 μM samples thus contain less DOX in total and release it faster into the solution, while the loading concentration of 6 μM leads to a slower release of a higher number of loaded DOX molecules.

The spectroscopic results of the DON digestion were also confirmed with an agarose gel electrophoresis (AGE) analysis that was carried out parallel to the spectroscopic experiments (Supplementary Figure S15). The digestion of the structures led to both a lower band intensity and an increased electrophoretic mobility in AGE, correlating well with the % intact values obtained from the spectroscopic measurement. A comparison of the DNase I digestion of unfiltered and spin-filtered bowtie DONs is presented in the Supplementary Figure S14. As the total DOX concentration and the density of bound DOX was drastically reduced through the spin-filtration, the digestion profiles of 3 and 6 μM DOX-loaded bowties started to resemble the digestion of bare origami (0 μM DOX).

DISCUSSION

The choice of conditions for DOX loading

In common experimentation with DONs, the buffer of choice is typically a Tris–HCl or a TAE buffer, either supple-

mented with on average 10–20 mM Mg^{2+}. These conditions have been generally found to be appropriate for stabilizing the DONs: the divalent cations effectively screen the electrostatic repulsion between the negative charges of closely packed phosphate backbones, and the typical pH at 8.0–8.3 is in the optimal buffering range of Tris-based buffers. As it is important to retain the structural integrity of DONs throughout experimental procedures, these conditions are also commonly used together with DOX—particularly during loading the DOX into the DONs. Still, the question of whether these conditions can cause unexpected or undesired behavior of DOX, or change its spectroscopic properties in terms of ϵ or Φ in a way that can lead to a misinterpretation of spectroscopic observables, has been left almost entirely unaddressed.

Our results show that DONs and DOX have very different optimal environments, and typical DON buffers supplemented with $MgCl_2$ at pH 8.0–8.3 are not suited for unequivocal DOX experimentation. In our spectroscopic analysis, we found that when the pH is at or above 8.0 and the $MgCl_2$ concentration is at mM range, the environment will lead to DOX heterogeneity either in terms of charge (deprotonation) or formation of DOX–Mg^{2+} complexes (Figure 2). The effects should be carefully considered when interpreting and comparing spectroscopic results obtained in different buffer conditions. For example, it has been stated that the amount of DOX released from the DNA structures increases with decreasing pH (33), but our results show that the observed elevation in DOX absorbance and fluorescence may also arise from the high absorbance and emission of DOX at low pH instead of from a higher DOX concentration.

In addition to spectral changes, high pH and Mg^{2+} ions can lead to self-aggregation of DOX during prolonged storage times (Figure 3). In line with previous literature (45,47,63,64), the two major aggregation pathways indicated by our results are the low solubility (0.55 mM) of deprotonated DOX molecules—most clearly observed at pH 8.0 for 2 mM DOX—and the Mg^{2+} complexation, which causes slight DOX aggregation and precipitation regardless of the DOX concentration (from μM to mM range). Importantly, the aggregation of DOX can take place also when preparing DOX-loaded DONs over common incubation times of several hours. The effect of aggregation is most dramatic at poorly optimized conditions (2 mM DOX, pH 8.0, and 12.5 mM $MgCl_2$) (Figure 3B) and can significantly complicate the purification of free DOX from DOX-loaded DONs for downstream applications. In particular, we observed that upon centrifugation, DOX aggregates precipitate alongside DOX-loaded DONs and can even form the major component of the precipitate. The centrifugation method has been used for purification of both free DOX (33,35,37,40) and daunorubicin (29) from drug-loaded DONs. Our results indicate that the method may lead to a risk of misidentifying aggregated DOX as DOX-DON complexes, and raise questions on the validity of conclusions made about the therapeutic efficiency of the prepared DOX-loaded DONs.

According to our results in the titration experiment, the binding equilibrium between DOX and DONs is reached in less than one minute regardless of the DNA origami superstructure (Figure 4C). An optimal loading time for producing structurally well-defined DOX-loaded DONs thus appears to be in the order of minutes instead of the commonly used incubation times in the range of 12–24 h, and a short loading time may perhaps be the most efficient approach for preventing DOX aggregation during loading. Moreover, we have shown that DOX-loaded DONs prepared at low (<10 μM) DOX concentrations over short (1 h) loading times can be efficiently purified from free DOX using 100 kDa spin-filtration (34,36,38,39) or PEG precipitation (59) (Supplementary Note 13). However, it is also noteworthy that the sample recovery quickly decreases with an increasing DOX concentration and that the purification leads to rapid dissociation of a fraction of bound DOX in order to reach a new equilibrium state (Supplementary Figures S12 and S13).

Features of DOX-loaded DONs

In our titration experiments, we studied and compared the DOX-loading capacities of five structurally distinct DONs. The different geometries and design choices of the tested 2D structures (triangle, bowtie and double-L) lead to differences in their flexibility and nuclease accessibility (49), which could cause subtle differences in their DOX loading and release properties. The capsule and 24HB DONs contain a more compact 3D-arrangement of DNA helices. The closed capsule DON is a roughly spherical (31 nm $\times$ 28 nm $\times$ 33 nm) structure with a hollow inner cavity (25). Such hollow architectures can be expected to make DNA intercalation sites more accessible to DOX, and therefore they have been previously applied for enhancing the loading efficiency of daunorubicin (29). On the other hand, the DNA helices in the 24HB are arranged into a tight, regular bundle of $\sim$12 nm in diameter and 115 nm in length.

It is thus interesting to note that in our experimental conditions and in the titration experiment presented in Figure 4, roughly identical amounts of DOX were incorporated into all of the tested DONs in terms of density of the drug molecules in the DONs. The maximum DOX loading content was determined to be 0.36 ± 0.10 DOX molecules bound per one DNA base pair. The value is in line with a number of previous studies for calf thymus dsDNA, where the maximum binding efficiency of DOX had been determined to be in the range of $\sim$0.29–0.37 DOX molecules per base pair (45,68). The similarity of the tested DONs is a rather surprising observation, as the steric hindrance from the compact arrangement of DNA helices could be expected to lead to a restricted accessibility of DNA helices and intercalation sites particularly in the 3D DONs. In fact, such kind of restricted loading has recently been observed for the bis-intercalator YOYO-1 (70). The different behavior we observe for DOX might arise from the different binding mechanisms of the two drugs, with bis-intercalation being more affected by the steric hindrance.

Our observations of a low DOX-loading capacity of DONs are additionally contradictory to many previous studies on DON-based DOX delivery, where the reported concentrations of bound drug molecules in DONs are often higher than the concentration of DNA base pairs in the sample—up to 113 DOX molecules per base pair (33).

While it is rather obvious that intercalation cannot be the only DOX binding mechanism behind the previous reported high DOX loading contents, the other possible processes, such as minor-groove binding or even external aggregate formation through stacking interactions (45), are rarely discussed. Our results support the interpretation that all three mechanisms might play a role in the loading process depending on the choice of experimental conditions. An AFM-based characterization of DOX-loaded double-L DONs (Supplementary Figure S7 and Supplementary Table S3) shows that the DOX binding causes a torsional twist in a concentration-dependent manner, indicative of an intercalative binding mode (34,69). Our spectroscopic results also strongly support the presence of a minor-groove binding mode that leads to a lesser extent of DOX fluorescence quenching (45,66). In addition, stacking into aggregates on the DON surface or the observed self-aggregation of DOX could present a plausible explanation for the previous DOX loading contents well above a loading density of DOX/bp > 1, and result from sub-optimal buffer conditions or prolonged incubation times during loading.

In addition to the kinetics of the loading process, a second crucial kinetic parameter of DOX-loaded DONs is the rate of diffusive release of DOX in low-DOX conditions. Interestingly, we observed rapid spontaneous DOX release after the DOX-loaded structures were purified from excess DOX. As seen in the data presented in Supplementary Figure S13, freshly spin-filtered DOX-loaded bowtie DON samples had reached a new equilibrium state through DOX release (recovery of the quantum yield) in less than 10 minutes. No further quantum yield increase was observed between 10 min and 45 h. To our knowledge, such rapid diffusive release has not been previously reported for DOX-loaded DONs, albeit it is in line with the relatively large dissociation rate constant (k_{off}) of DOX. Different sources have reported the k_{off} of DOX as 2.07–8.49 s^{-1} at 25°C (71,72), giving an equilibration half-time of $t_{1/2} = \ln 2/k_{off} = 0.08$–0.33 s. From the pragmatic viewpoint, this indicates that although the amount of free DOX in the solution can be reduced through purification, it simultaneously decreases the amount of bound DOX in DONs, and it seems impossible to eliminate free DOX entirely (decrease of free DOX leads to dissociation of bound DOX). The rate of diffusive release likely depends on the sample composition and the DOX binding mode—intercalation, external binding or aggregation—and the implications for downstream drug delivery applications would in turn present a subject for further studies.

DNase I digestion leads to DOX release at superstructure-dependent rates

As an important prerequisite for biomedical applications, we simulated the possible degradation pathways of the complexes in nuclease-rich environments. DNase I was selected as a degradation agent, as it is the most important and active nuclease in blood serum and mammalian cells. In addition, DON digestion by DNase I has been previously studied (49,51,57,73,74), but not with this kind of an approach that allows detailed simultaneous monitoring of DON cleavage and drug release.

The superstructure-dependent DON degradation rates were resolved by following the increase of DNA absorbance at 260 nm. The stability varies from structure to structure, which has also been observed in the previous studies. In general, the DNase I digestion is notably slower for 3D than 2D structures; in the most extreme case (triangle versus 24HB), by roughly two orders of magnitude (Figure 5A and C). The plain 2D structures contain flexible regions that are likely more susceptible to DNase I digestion (75), and they follow similar digestion profiles as reported earlier (49). The increased stability of the 24HB compared to the capsule may originate from design features such as a more compact, rigid and regular structure and a higher amount of scaffold crossovers, which are all factors known to increase the resiliency of DONs towards nuclease digestion (49–51,57,74).

As the percentage of released DOX correlates well with the degradation level of the DONs (Figure 5B), the different digestion rates enable customized drug release over a rather wide time window. When the structures are loaded with DOX, the digestion slows down with increasing DOX concentration and adds one more controllable parameter to the tunable release profile: 6 μM DOX loading concentration yields lower relative doses (released amount of DOX / unit time) than 3 μM (Figure 5D). As the 6 μM concentration leads to increasing density of DOX molecules loaded into the DONs, the underlying mechanism is most likely DOX-induced DNA protection through interference with the minor-groove binding of DNase I. The inhibitory effect of DOX has been previously observed for dsDNA with variable sequences (76), and shown to be caused specifically by the DNA-bound DOX rather than interactions between free DOX and DNase I (77).

Furthermore, to achieve reasonable time scales for the digestion rate comparison, we have here applied a DNase I concentration (34 U ml^{-1}) that is remarkably higher than for example in blood plasma (0.36 ± 0.20 U ml^{-1} (78)). As the concentration of DNase I is essentially defined through its activity—affected by e.g. the temperature and the salt concentration—the acquired results set an appropriate starting point to estimate the relative susceptibility and the drug release capacity of distinct DNA shapes in DNase I -rich environments. Obviously, DNase I digestion is only one of the factors compromising the stability of DONs in a physiological environment (53,54). A more complete picture of the durability of DONs in DOX delivery, i.e. the combined effects of the physiological cation concentrations, temperature, and interactions with other plasma proteins than DNase I presents an interesting topic for future studies. Here, by studying the DNase I digestion of distinct DONs in isolation from the other destabilizing factors, we have been able to resolve in detail their stability as DOX carriers and their superstructure-dependent differences related to their resistance against nucleases. In a nutshell, the various DON shapes used in this work and the applied DOX-loading levels together provide a broad selection of relative doses for engineered DOX delivery (Figure 5D).

CONCLUSIONS

We have shown that the release of the common therapeutic drug DOX from DONs upon DNase I digestion can be cus-

tomized by rationally designing the DNA superstructures and adjusting the loading concentration of DOX. In our model system, we observed clear correlation between the released DOX and the degradation level of the DONs. Both the superstructure and rigidity of DONs have an impact on their stability against nucleases, which is in agreement with previous studies (49,51,57). The stiffness and resilience of DONs achieved by the close packing of helices may, on the other hand, deteriorate the loading capacity of DNA-binding drugs (70). Nevertheless, here we observed nearly identical DOX loading properties for all tested DONs in terms of the loading time and the loading yield, but drastically different digestion and release profiles. Increasing the amount of loaded DOX slows down the digestion, which is plausibly associated with restricted DNase I cleavage due to the interfering DNA-bound DOX (76,77).

Importantly, our spectroscopic analysis of free DOX, the DOX–DON loading process, and the DOX-loaded DONs under different conditions reveals that a number of studies have inadequately estimated the DOX loading capacity of DONs and overlooked the potential effect of DOX self-aggregation during sample preparation and experimentation. In addition, we present previously unacknowledged fast kinetics of DOX loading and spontaneous release after removal of the free DOX. We propose that suboptimal conditions and procedures in sample preparation and characterization may lead to vaguely defined sample composition and to misleading interpretation of the actual drug efficacy. Therefore, our results may also help in explaining previous, often incoherent reports on DON-mediated DOX delivery. In addition, to resolve the exact amount of DOX that is bound to DONs through the loading procedure is also a matter of the utmost importance when cost-effectiveness of DON-based targeted delivery is assessed (21).

Our observations underline the significant potential of DONs in drug delivery applications and provide guidelines for choosing appropriate protocols for preparing, studying, purifying and storing DOX-loaded DONs. Here, we employed plain DONs without further modifications, but by taking advantage of their unsurpassable addressibility and modularity, multifunctionalities can be further realized. In the bigger picture, we believe our findings will help in building a solid ground for the development of safe and more efficient DNA nanostructure-based therapeutics with promising programmable features.

DATA AVAILABILITY

The authors confirm that the data supporting the findings of this study are available within the article and the Supplementary Information files. Some parts of the raw data are available from the corresponding author, upon reasonable request.

SUPPLEMENTARY DATA

Supplementary Data are available at NAR Online.

ACKNOWLEDGEMENTS

We thank Dr H. Häkkänen for technical assistance and S. Julin for the 24HB DNA origami design. We acknowledge the provision of facilities and technical support by Aalto University Bioeconomy Facilities and OtaNano – Nanomicroscopy Center (Aalto-NMC). The research was carried out under the Academy of Finland Centres of Excellence Programme (2014–2019).

Author contributions: H.I. performed the majority of the experiments, modeled the data and wrote the manuscript. B.S. and A.H.-J. performed additional experiments. A.K. conceived the project. M.A.K., T.L. and J.A.I. supervised the work. V.L. conceived, initialized and supervised the project, and wrote the manuscript. All authors designed the experiments, analyzed and discussed the data, and also commented on and edited the manuscript.

FUNDING

Academy of Finland [308578 to M.A.K.]; Deutsche Forschungsgemeinschaft [Emmy Noether Programme to A.H.-J., SFB1032 (Project A06) to T.L.]; Emil Aaltonen Foundation [to H.I. and V.L.]; Jane and Aatos Erkko Foundation [to J.A.I. and V.L.]; Sigrid Jusélius Foundation [to V.L.]; Vilho, Yrjö and Kalle Väisälä Foundation of the Finnish Academy of Science and Letters [to V.L.]. Funding for open access charge: Emil Aaltonen Foundation.

Conflict of interest statement. None declared.

REFERENCES

1. Seeman,N.C. (1982) Nucleic acid junctions and lattices. *J. Theor. Biol.*, **99**, 237–247.
2. Jones,M.R., Seeman,N.C. and Mirkin,C.A. (2015) Programmable materials and the nature of the DNA bond. *Science*, **347**, 1260901.
3. Hong,F., Zhang,F., Liu,Y. and Yan,H. (2017) DNA origami: scaffolds for creating higher order structures. *Chem. Rev.*, **117**, 12584–12640.
4. Nummelin,S., Kommeri,J., Kostiainen,M.A. and Linko,V. (2018) Evolution of structural DNA nanotechnology. *Adv. Mater.*, **30**, 1703721.
5. Heuer-Jungemann,A. and Liedl,T. (2019) From DNA tiles to functional DNA materials. *Trends Chem.*, **1**, 799–814.
6. Bathe,M. and Rothemund,P.W.K. (2017) DNA nanotechnology: a foundation for programmable nanoscale materials. *MRS Bull.*, **42**, 882–888.
7. Rothemund,P.W.K. (2006) Folding DNA to create nanoscale shapes and patterns. *Nature*, **440**, 297–302.
8. Douglas,S.M., Dietz,H., Liedl,T., Högberg,B., Graf,F. and Shih,W.M. (2009) Self-assembly of DNA into nanoscale three-dimensional shapes. *Nature*, **459**, 414–418.
9. Benson,E., Mohammed,A., Gardell,J., Masich,S., Czeizler,E., Orponen,P. and Högberg,B. (2015) DNA rendering of polyhedral meshes at the nanoscale. *Nature*, **523**, 441–444.
10. Linko,V. and Kostiainen,M.A. (2016) Automated design of DNA origami. *Nat. Biotechnol.*, **34**, 826–827.
11. Veneziano,R., Ratanalert,S., Zhang,K., Zhang,F., Yan,H., Chiu,W. and Bathe,M. (2016) Designer nanoscale DNA assemblies programmed from the top down. *Science*, **352**, 1534.
12. Castro,C.E., Dietz,H. and Högberg,B. (2017) DNA origami devices for molecular-scale precision measurements. *MRS Bull.*, **42**, 925–929.
13. Pilo-Pais,M., Acuna,G.P., Tinnefeld,P. and Liedl,T. (2017) Sculpting light by arranging optical components with DNA nanostructures. *MRS Bull.*, **42**, 936–942.
14. Xu,A., Harb,J.N., Kostiainen,M.A., Hughes,W.L., Woolley,A.T., Liu,H. and Gopinath,A. (2017) DNA origami: the bridge from bottom to top. *MRS Bull.*, **42**, 943–950.
15. Graugnard,E., Hughes,W.L., Jungmann,R., Kostiainen,M.A. and Linko,V. (2017) Nanometrology and super-resolution imaging with DNA. *MRS Bull.*, **42**, 951–959.
16. Nummelin,S., Shen,B., Piskunen,P., Liu,Q., Kostiainen,M.A. and Linko,V. (2020) Robotic DNA nanostructures. *ACS Synth. Biol.*, **9**, 1923–1940.

17. Surana,S., Shenoy,A.R. and Krishnan,Y. (2015) Designing DNA nanodevices for compatibility with the immune system of higher organisms. *Nat. Nanotechnol.*, **10**, 741–747.
18. Bujold,K.E., Lacroix,A. and Sleiman,H.F. (2018) DNA nanostructures at the interface with biology. *Chem*, **4**, 495–521.
19. Hu,Q., Li,H., Wang,L., Gu,H. and Fan,C. (2019) DNA nanotechnology-enabled drug delivery systems. *Chem. Rev.*, **119**, 6459–6506.
20. Keller,A. and Linko,V. (2020) Challenges and perspectives of DNA nanostructures in biomedicine. *Angew. Chem., Int. Ed.*, **59**, 15818–15833.
21. Coleridge,E.L. and Dunn,K.E. (2020) Assessing the cost-effectiveness of DNA origami nanostructures for targeted delivery of anti-cancer drugs to tumours. *Biomed. Phys. Eng. Express*, **6**, 065030.
22. Douglas,S.M., Bachelet,I. and Church,G.M. (2012) A logic-gated nanorobot for targeted transport of molecular payloads. *Science*, **335**, 831–834.
23. Li,S., Jiang,Q., Liu,S., Zhang,Y., Tian,Y., Song,C., Wang,J., Zou,Y., Anderson,G.J., Han,J.Y. *et al.* (2018) A DNA nanorobot functions as a cancer therapeutic in response to a molecular trigger in vivo. *Nat. Biotechnol.*, **36**, 258–264.
24. Grossi,G., Jepsen,M.D.E., Kjems,J. and Andersen,E.S. (2017) Control of enzyme reactions by a reconfigurable DNA nanovault. *Nat. Commun.*, **8**, 992.
25. Ijäs,H., Hakaste,I., Shen,B., Kostiainen,M.A. and Linko,V. (2019) Reconfigurable DNA origami nanocapsule for pH-controlled encapsulation and display of cargo. *ACS Nano*, **13**, 5959–5967.
26. Jiang,D., Ge,Z., Im,H.-J., England,C.G., Ni,D., Hou,J., Zhang,L., Kutyreff,C. J., Yan,Y., Liu,Y. *et al.* (2018) DNA origami nanostructures can exhibit preferential renal uptake and alleviate acute kidney injury. *Nat. Biomed. Eng.*, **2**, 865–877.
27. Lee,H., Lytton-Jean,A.K., Chen,Y., Love,K.T., Park,A.I., Karagiannis,E.D., Sehgal,A., Querbes,W., Zurenko,C.S., Jayaraman,M. *et al.* (2012) Molecularly self-assembled nucleic acid nanoparticles for targeted in vivo siRNA delivery. *Nat. Nanotechnol.*, **7**, 389–393.
28. Schaffert,D.H., Okholm,A.H., SØrensen,R.S., Nielsen,J.S., TØrring,T., Rosen,C.B., Kodal,A.L., Mortensen,M.R., Gothelf,K.V. and Kjems,J. (2016) Intracellular delivery of a planar DNA origami structure by the transferrin-receptor internalization pathway. *Small*, **12**, 2634–2640.
29. Halley,P.D., Lucas,C.R., McWilliams,E.M., Webber,M.J., Patton,R.A., Kural,C., Lucas,D.M., Byrd,J.C. and Castro,C.E. (2016) Daunorubicin-loaded DNA origami nanostructures circumvent drug-resistance mechanisms in a leukemia model. *Small*, **12**, 308–320.
30. Kollmann,F., Ramakrishnan,S., Shen,B., Grundmeier,G., Kostiainen,M.A., Linko,V. and Keller,A. (2018) Superstructure-dependent loading of DNA origami nanostructures with a groove-binding drug. *ACS Omega*, **3**, 9441–9448.
31. Thorn,C.F., Oshiro,C., Marsh,S., Hernandez-Boussard,T., McLeod,H., Klein,T.E. and Altman,R.B. (2011) Doxorubicin pathways: pharmacodynamics and adverse effects. *Pharmacogenet. Genom.*, **21**, 440–446.
32. Pommier,Y., Leo,E., Zhang,H. and Marchand,C. (2010) DNA topoisomerases and their poisoning by anticancer and antibacterial drugs. *Chem. Biol.*, **17**, 421–433.
33. Jiang,Q., Song,C., Nangreave,J., Liu,X., Lin,L., Qiu,D., Wang,Z.G., Zou,G., Liang,X., Yan,H. *et al.* (2012) DNA origami as a carrier for circumvention of drug resistance. *J. Am. Chem. Soc.*, **134**, 13396–13403.
34. Zhao,Y.-X., Shaw,A., Zeng,X., Benson,E., Nyström,A.M. and Högberg,B. (2012) DNA origami delivery system for cancer therapy with tunable release properties. *ACS Nano*, **6**, 8684–8691.
35. Zhang,Q., Jiang,Q., Li,N., Dai,L., Liu,Q., Song,L., Wang,J., Li,Y., Tian,J., Ding,B. *et al.* (2014) DNA origami as an in vivo drug delivery vehicle for cancer therapy. *ACS Nano*, **8**, 6633–6643.
36. Song,L., Jiang,Q., Liu,J., Li,N., Liu,Q., Dai,L., Gao,Y., Liu,W., Liu,D. and Ding,B. (2017) DNA origami/gold nanorod hybrid nanostructures for the circumvention of drug resistance. *Nanoscale*, **9**, 7750–7754.
37. Zeng,Y., Liu,J., Yang,S., Liu,W., Xu,L. and Wang,R. (2018) Time-lapse live cell imaging to monitor doxorubicin release from DNA origami nanostructures. *J. Mater. Chem. B*, **6**, 1605–1612.
38. Liu,J., Song,L., Liu,S., Jiang,Q., Liu,Q., Li,N., Wang,Z.-G. and Ding,B. (2018) A DNA-based nanocarrier for efficient gene delivery and combined cancer therapy. *Nano Lett.*, **18**, 3328–3334.
39. Liu,J., Song,L., Liu,S., Zhao,S., Jiang,Q. and Ding,B. (2018) A tailored DNA nanoplatform for synergistic RNAi-/chemotherapy of multidrug-resistant tumors. *Angew. Chem., Int. Ed.*, **57**, 15486–15490.
40. Pan,Q., Nie,C., Hu,Y., Yi,J., Liu,C., Zhang,J., He,M., He,M., Chen,T. and Chu,X. (2020) Aptamer-functionalized DNA origami for targeted codelivery of antisense oligonucleotides and doxorubicin to enhance therapy in drug-resistant cancer cells. *ACS Appl. Mater. Interfaces*, **12**, 400–409.
41. Wiraja,C., Zhu,Y., Lio,D.C.S., Yeo,D.C., Xie,M., Fang,W., Li,Q., Zheng,M., Van Steensel,M., Wang,L., Fan,C. and Xu,C. (2019) Framework nucleic acids as programmable carrier for transdermal drug delivery. *Nat. Commun.*, **10**, 1147.
42. Ge,Z., Guo,L., Wu,G., Li,J., Sun,Y., Hou,Y., Shi,J., Song,S., Wang,L., Fan,C. *et al.* (2020) DNA origami-enabled engineering of ligand-drug conjugates for targeted drug delivery. *Small*, **16**, 1904857.
43. Wang,S.-T., Gray,M.A., Xuan,S., Lin,Y., Byrnes,J., Nguyen,A.I., Todorova,N., Stevens,M.M., Bertozzi,C.R., Zuckermann,R.N. *et al.* (2020) DNA origami protection and molecular interfacing through engineered sequence-defined peptoids. *Proc. Natl. Acad. Sci. U.S.A.*, **117**, 6339–6348.
44. Lei,H., Wang,X. and Wu,C. (2012) Early stage intercalation of doxorubicin to DNA fragments observed in molecular dynamics binding simulations. *J. Mol. Graph. Model.*, **38**, 279–289.
45. Pérez-Arnaiz,C., Busto,N., Leal,J.M. and García,B. (2014) New insights into the mechanism of the DNA/doxorubicin interaction. *J. Phys. Chem. B*, **118**, 1288–1295.
46. Silva,E.F., Bazoni,R.F., Ramos,E.B. and Rocha,M.S. (2016) DNA-doxorubicin interaction: New insights and peculiarities. *Biopolymers*, **107**, e22998.
47. Fülöp,Z., Gref,R. and Loftsson,T. (2013) A permeation method for detection of self-aggregation of doxorubicin in aqueous environment. *Int. J. Pharm.*, **454**, 559–561.
48. Stopar,A., Coral,L., Di Giacomo,S., Adedeji,A.F. and Castronovo,M. (2018) Binary control of enzymatic cleavage of DNA origami by structural antideterminants. *Nucleic Acids Res.*, **46**, 995–1006.
49. Ramakrishnan,S., Shen,B., Kostiainen,M.A., Grundmeier,G., Keller,A. and Linko,V. (2019) Real-time observation of superstructure-dependent DNA origami digestion by DNase I using high-speed atomic force microscopy. *ChemBioChem*, **20**, 2818–2823.
50. Suma,A., Stopar,A., Nicholson,A.W., Castronovo,M. and Carnevale,V. (2020) Global and local mechanical properties control endonuclease reactivity of a DNA origami nanostructure. *Nucleic Acids Res.*, **48**, 4672–4680.
51. Hahn,J., Wickham,S.F.J., Shih,W.M. and Perrault,S.D. (2014) Addressing the instability of DNA nanostructures in tissue culture. *ACS Nano*, **8**, 8765–8775.
52. Kielar,C., Xin,Y., Shen,B., Kostiainen,M.A., Grundmeier,G., Linko,V. and Keller,A. (2018) On the stability of DNA origami nanostructures in low-magnesium buffers. *Angew. Chem., Int. Ed.*, **57**, 9470–9474.
53. Ramakrishnan,S., Ijäs,H., Linko,V. and Keller,A. (2018) Structural stability of DNA origami nanostructures under application-specific conditions. *Comput. Struct. Biotechnol. J.*, **16**, 342–349.
54. Bila,H., Kurisinkal,E.E. and Bastings,M.M.C. (2019) Engineering a stable future for DNA-origami as a biomaterial. *Biomater. Sci.*, **7**, 532–541.
55. Shen,B., Linko,V., Tapio,K., Pikker,S., Lemma,T., Gopinath,A., Gothelf,K.V., Kostiainen,M.A. and Toppari,J.J. (2018) Plasmonic nanostructures through DNA-assisted lithography. *Sci. Adv.*, **4**, eaap8978.
56. Douglas,S.M., Marblestone,A.H., Teerapittayanon,S., Vazquez,A., Church,G.M. and Shih,W.M. (2009) Rapid prototyping of 3D DNA-origami shapes with caDNAno. *Nucleic Acids Res.*, **37**, 5001–5006.
57. Castro,C.E., Kilchherr,F., Kim,D.-N., Shiao,E.L., Wauer,T., Wortmann,P., Bathe,M. and Dietz,H. (2011) A primer to scaffolded DNA origami. *Nat. Methods*, **8**, 221–229.
58. Kim,D.-N., Kilchherr,F., Dietz,H. and Bathe,M. (2012) Quantitative prediction of 3D solution shape and flexibility of nucleic acid nanostructures. *Nucleic Acids Res.*, **40**, 2862–2868.

59. Stahl,E., Martin,T.G, Praetorius,F. and Dietz,H. (2014) Facile and scalable preparation of pure and dense DNA origami solutions. *Angew. Chem., Int. Ed.*, **53**, 12735–12740.
60. Hung,A.M., Micheel,C.M., Bozano,L.D., Osterbur,L.W., Wallraff,G.M. and Cha,J.N. (2010) Large-area spatially ordered arrays of gold nanoparticles directed by lithographically confined DNA origami. *Nat. Nanotechnol.*, **5**, 121–126.
61. Zadeh,J.N., Steenberg,C.D., Bois,J.S., Wolfe,B.R., Pierce,M.B., Khan,A.R., Dirks,R.M. and Pierce,N.A. (2011) NUPACK: analysis and design of nucleic acid systems. *J. Comput. Chem.*, **32**, 170–173.
62. Thordarson,P. (2011) Determining association constants from titration experiments in supramolecular chemistry. *Chem. Soc. Rev.*, **40**, 1305–1323.
63. Abraham,S.A., Edwards,K., Karlsson,G., MacIntosh,S., Mayer,L.D., McKenzie,C. and Bally,M.B. (2002) Formation of transition metal-doxorubicin complexes inside liposomes. *Biochim. Biophys. Acta - Biomembr.*, **1565**, 41–54.
64. Cheung,B.C.L., Sun,T.H.T., Leenhouts,J.M. and Cullis,P.R. (1998) Loading of doxorubicin into liposomes by forming Mn^{2+}-drug complexes. *Biochim. Biophys. Acta - Biomembr.*, **1414**, 205–216.
65. Jabłońska-Trypuć,A., Świderski,G., Krętowski,R. and Lewandowski,W. (2017) Newly synthesized doxorubicin complexes with selected metals - synthesis, structure and anti-breast cancer activity. *Molecules*, **22**, 1106.
66. Airoldi,M., Barone,G., Gennaro,G., Giuliani,A.M. and Giustini,M. (2014) Interaction of doxorubicin with polynucleotides. A spectroscopic study. *Biochemistry*, **53**, 2197–2207.
67. Tinoco,I. (1960) Hypochromism in polynucleotides. *J. Am. Chem. Soc.*, **82**, 4785–4790.
68. Barcelo,F., Martorell,J., Gavilanes,F. and Gonzalez-Ros,J.M. (1988) Equilibrium binding of daunomycin and adriamycin to calf thymus DNA: Temperature and ionic strength dependence of thermodynamic parameters. *Biochem. Pharmacol.*, **37**, 2133–2138.
69. Chen,K., Zhang,H., Pan,J., Cha,T.-G., Li,S., Andréasson,J. and Choi,J.H. (2016) Dynamic and progressive control of DNA origami conformation by modulating DNA helicity with chemical adducts. *ACS Nano*, **10**, 4989–4996.
70. Miller,H.L., Contrera,S., Wollman,A.J.M., Hirst,A., Dunn,K.E., Schröter,S., O'Connell,D. and Leakel,M. (2020) Biophysical characterisation of DNA origami nanostructures reveals inaccessibility to intercalation binding sites. *Nanotechnology*, **31**, 235605.
71. Gandecha,B.M., Brown,J.R. and Crampton,M.R. (1985) Dissociation kinetics of DNA-anthracycline and DNA-anthraquinone complexes determined by stopped-flow spectrophotometry. *Biochem. Pharmacol.*, **34**, 733–736.
72. Yao,F., Duan,J., Wang,Y., Zhang,Y., Guo,Y., Guo,H. and Kang,X. (2015) Nanopore single-molecule analysis of DNA-doxorubicin interactions. *Anal. Chem.*, **87**, 338–342.
73. Conway,J.W., McLaughlin,C.K., Castor,K.J. and Sleiman,H. (2013) DNA nanostructure serum stability: greater than the sum of its parts. *Chem. Commun.*, **49**, 1172–1174.
74. Chandrasekaran,A.R., Vilcapoma,J., Dey,P., Wong-Deyrup,S.W., Dey,B.K. and Halvorsen,K. (2020) Exceptional nuclease resistance of paranemic crossover (PX) DNA and crossover-dependent biostability of DNA motifs. *J. Am. Chem. Soc.*, **142**, 6814–6821.
75. Suck,D. (1994) DNA recognition by DNase I. *J. Mol. Recognit.*, **7**, 65–70.
76. Jollès,B., Laigle,A., Priebe,W. and Garnier-Suillerot,A. (1996) Comparison of DNA sequence selectivity of anthracycline antibiotics and their 3'-hydroxylated analogs. *Chem. Biol.*, **100**, 165–176.
77. Facchinetti,T., Mantovani,A., Cantoni,L., Cantoni,R. and Salmona,M. (1978) Intercalation with DNA is a prerequisite for Daunomycin, Adriamycin and its congeners in inhibiting DNAase I. *Chem. Biol. Interact.*, **20**, 97–102.
78. Cherepanova,A., Tamkovich,S., Pyshnyi,D., Kharkova,M., Vlassov,V. and Laktionov,P. (2007) Immunochemical assay for deoxyribonuclease activity in body fluids. *J. Immunol. Methods*, **31**, 96–103.

Supplementary Information for Unraveling the interaction between doxorubicin and DNA origami nanostructures for customizable chemotherapeutic drug release

Heini Ijäs[1,2], Boxuan Shen[1], Amelie Heuer-Jungemann[3], Adrian Keller[4], Mauri A. Kostiainen[1,5], Tim Liedl[3], Janne A. Ihalainen[2] & Veikko Linko[1,5,*]

[1]Biohybrid Materials, Department of Bioproducts and Biosystems, Aalto University, P.O. Box 16100, 00076 Aalto, Finland

[2]Nanoscience Center, Department of Biological and Environmental Science, University of Jyväskylä, P.O. Box 35, 40014 Jyväskylä, Finland

[3]Faculty of Physics and Center for NanoScience (CeNS), Ludwig-Maximilians-University, Geschwister-Scholl-Platz 1, 80539 Munich, Germany

[4]Technical and Macromolecular Chemistry, Paderborn University, Warburger Str. 100, 33098 Paderborn, Germany

[5]HYBER Centre, Department of Applied Physics, Aalto University, P.O. Box 15100, 00076 Aalto, Finland

[*]Correspondence and requests for materials should be addressed to veikko.linko@aalto.fi

Contents

Supplementary methods

Materials

All DOX solutions were prepared by diluting 10 mM stock solution of DOX (in deionized (DI) water) with the applied buffer. When preparing solutions with high DOX concentrations ($\geq$ 200 μM), DOX was diluted with DI water and 2× buffer at 1/2 of total sample volume to prevent buffer dilution.

The abbreviations of the buffers applied in the experiments are: Tris/Mg^{2+} pH 7.4 = 40 mM Tris, 10 mM $MgCl_2$, pH 7.4; Tris/Mg^{2+} pH 8.0 = 40 mM Tris, 10 mM $MgCl_2$, pH 8.0; FOB pH 8.0 = 1× DON folding buffer: 1× TAE [40 mM Tris, 19 mM acetic acid, 1 mM ethylenediaminetetraacetic acid (EDTA)] and 12.5 mM $MgCl_2$, pH 8.0.

The spin-filtration for removing free DOX from DOX-DON samples was carried out using Amicon Ultra 0.5 mL centrifugal filter units (Merck Millipore) with 10 kDa, 30 kDa, or 100 kDa molecular weight cutoff.

Additional DOX self-aggregation experiments

The results presented for DOX self-aggregation in Figure 3 in the main article were complemented with supplementary experiments of DOX self-aggregation. To study whether the chosen centrifugation procedure (10 min centrifugation at 14,000 *g*) for separating free DOX from high molecular weight particles can affect the obtained $c_{\mathrm{aggregate}}$ values, the experiment was repeated for 200 μM DOX samples using different centrifugation speeds. In addition, the self-aggregation of 3 μM DOX in the Tris/Mg^{2+} pH 7.4 buffer was studied over 96 h incubation.

The effect of the centrifugal force on the $c_{\mathrm{aggregate}}$. DOX solution at 200 μM concentration was prepared in FOB pH 8.0. To obtain a t = 0 value for A_{480} and the $c_{\mathrm{aggregate}}$, UV-Vis spectrum of the sample between 240–600 nm was collected from a 2 μL droplet on a BioTek Take3 plate with a 0.05 cm optical path using a BioTek Eon microplate spectrophotometer. The DOX solution was then divided into four aliquots, which were incubated for 24 h at RT. After the incubation period, the aliquots were centrifuged for 10 min at either 2,000, 6,000, 10,000, or 14,000 *g*, small volumes of the supernatants were removed, and the UV-Vis absorption spectra were recorded similarly to the t = 0 spectra. The $c_{\mathrm{aggregate}}$ values at the 24 h time point were calculated as $c_{\mathrm{aggregate}}$ = 200 μM × $A_{480}(t = 24\ \mathrm{h})$ / $A_{480}(t = 0)$. The experiment was repeated three times and the $c_{\mathrm{aggregate}}$ values were reported as the mean ± standard deviation of the three experiments.

Self-aggregation of 3 μM DOX. 3 μM DOX solutions were prepared in Tris/Mg^{2+} pH 7.4 and in DI water. The UV-Vis absorbance spectra of the solutions between 240–650 nm were measured directly after preparing the solutions to obtain the t = 0 values for DOX absorbance and concentration in the samples. Spectroscopic measurements were performed with a Varian Cary UV-Vis spectrophotometer for 750 μL of sample in a disposable BRAND micro UV cuvette. Each sample was then aliquoted into three parts and incubated at RT. After 24, 48, or 96 h, one aliquot was centrifuged at 14,000 *g* for 10 minutes and the UV-Vis spectrum of the supernatant was collected identically to the t = 0 measurement. The $c_{\mathrm{aggregate}}$ values at the different time points were calculated as $c_{\mathrm{aggregate}}$ = 3 μM × $A_{480}(t)$ / $A_{480}(t = 0)$. The experiment was repeated three times and the $c_{\mathrm{aggregate}}$ values were reported as the mean ± standard deviation of the three experiments.

Purification of free DOX from DOX-DON samples after loading

Comparison of DOX retention by 10, 30, and 100 kDa molecular weight cutoff filter membranes. Spin-filtration through 10 kDa, 30 kDa, and 100 kDa molecular weight cutoff membranes was used both to study the size of DOX aggregates formed in samples containing 2 mM DOX in FOB pH 8.0, and to evaluate the effectiveness of different filter membranes in the purification of free DOX and DOX aggregates from DON-DOX samples after loading. Prior use, the filters were rinsed with the sample buffer (either FOB pH 8.0 or Tris/Mg^{2+} pH 7.4 depending on the experiment) by adding 500 μL of buffer in the filter unit, centrifuging for 10 min at 14,000 *g*, and removing the buffer remaining in the filter with a pipette.

For the comparison of 10 kDa, 30 kDa, and 100 kDa filter membranes, 2 mM DOX solution was prepared in FOB pH 8.0 and incubated overnight at RT to induce formation of DOX aggregates. 100 μL of the DOX solution was pipetted into pre-rinsed 10, 30, and 100 kDa filters and 10 μL of each solution was removed for UV-Vis measurements. The samples were then centrifuged for 5 min at 14,000 *g*. UV-Vis spectra between 240–600 nm were measured from the unfiltered samples, from the filtrates, and from the concentrates (sample remaining in the filter after centrifugation). c_0, c(filtrate), and c(concentrate) values were determined from the A_{480} values. The experiment was repeated total three times and the relative concentrations of DOX were reported as the mean ± standard deviation.

The extent of DOX binding to the 100 kDa filter membrane was further studied by comparing the c_0 and c(filtrate) values of various DOX-only and DOX-DON samples. DOX-DON samples were prepared by mixing DOX at either 3, 6, 20, or 200 μM concentration with the triangle DON at 2 nM final concentration in Tris/Mg^{2+} pH 7.4, and incubating the samples at RT for 1 h to load the DONs with DOX. DOX-only samples were prepared identically but without DONs. After the incubation, the solutions were pipetted into pre-rinsed 100 kDa cutoff filters and spin-filtered briefly (4 min at 6,000 *g*). UV-Vis absorption spectra were measured both from unfiltered samples and from the collected filtrates. 3 μM and 6 μM samples were analyzed with a Varian Cary UV-Vis spectrophotometer from 750 μL of sample volume in a disposable BRAND micro UV cuvette (l = 1

cm) and UV-Vis spectra were collected between 240–650 nm. Samples containing 20 μM or 200 μM DOX were analyzed with a BioTek Eon microplate spectrophotometer, and the UV-Vis spectra were collected between 240–600 nm from a 2 μL droplet of sample on a BioTek Take3 plate (l = 0.05 cm). Because binding to DONs changes the shape of the absorption spectrum of DOX, the concentration values c_0 and c(filtrate) were calculated from A_{544} values – *i.e.* absorbance at the isosbestic point. The c(filtrate) / c_0 values were reported from a single measurement.

Free DOX removal by spin-filtration. Spin-filtration for removing unbound DOX from DOX-DON samples after loading was carried out with 100 kDa molecular weight cutoff spin-filters. The buffer used in all samples and purification experiments was Tris/Mg^{2+} at pH 7.4. All incubation and spin-filtration steps of the experiment were performed at RT.
For studying the effect of DOX loading concentration on the loading and purification outcome, DOX-loaded DON samples were prepared at 3, 6, and 20 μM DOX concentrations with all samples containing 2 nM triangle DON. The samples were incubated for 1 h for loading the DONs with DOX. UV-Vis spectra of the samples were measured after the incubation with a Varian Cary UV-Vis spectrophotometer. The samples were then purified from unbound DOX with the following spin-filtration protocol:

1. The filter was rinsed by adding 500 μL of buffer in the filter, centrifuging for 10 min at 6,000 g, and discarding the flow-through. The ∼20 μL volume of buffer left in the filter was not removed.

2. 480 μL (of total 800 μL) of DOX-DON sample was added, centrifuged for 10 min at 6,000 g, and the flow-through was discarded.

3. The remaining 320 μL of sample was added to the ∼20 μL of concentrated sample in the filter together with 160 μL of buffer, and centrifuged for 10 min at 6,000 g. The flow-through was discarded.

4. 480 μL of buffer was added and the sample was centrifuged for 10 min at 6,000 g.

5. The concentrated sample was collected into a fresh microcentrifuge tube by inverting the filter unit and centrifuging for 2 min at 1,000 g. The sample was then diluted with 780 μL of buffer to a total volume of 800 μL (original sample volume).

UV-Vis spectra of the purified samples were measured identically as before purification. For comparing the sample composition before and after purification, the concentrations of DOX [c(DOX)] and DNA base pairs [c(bp)] were quantified from the UV-Vis spectra. c(DOX) for each sample was determined from the A_{544} value (isosbestic point) based on a standard curve of A_{544} *vs.* c(DOX) for unpurified samples. The c(bp) values were calculated from A_{260} after subtracting the contribution of DOX absorbance [A_{260}(DOX)] from the measured A_{260}: A_{260}(DNA) = $A_{260} - A_{260}$(DOX). A_{260}(DOX) was estimated as A_{260}(DOX) = $A_{544}\times$ [A_{260}(DOX, free)/A_{544}(DOX, free)], where the ratio of absorbances A_{260}(DOX, free)/A_{544}(DOX, free) was collected and averaged from DOX-only samples at 3, 6, or 20 μM concentration. DOX/bp ratios were calculated from the c(DOX) and c(bp) values of the purified samples. The DNA recovery yield was defined as % DNA recovery = c(bp) / $c(\text{bp})_0 \times 100\%$, where c(bp) refers to DNA base pair concentration in the sample after purification, and $c(\text{bp})_0$ to the base pair concentration in the unpurified sample. The DOX/bp ratios and the DNA recovery yields were reported as an average ± standard deviation after repeating the experiment three times.
The efficiency of spin-filtration in free DOX removal was measured with DOX-only reference samples: 3, 6, and 20 μM solutions of DOX were prepared in the Tris/Mg^{2+} buffer at pH 7.4, incubated for 1 h at RT, and processed with the same spin-filtration procedure as the DOX-DON samples. The remaining concentration of free DOX in the samples (c) was quantified from the A_{544} values. The DOX removal efficiency for each loading concentration was calculated from the difference of c and c_0: % free DOX removed = $(c_0 - c)/c_0 \times 100\%$.

Free DOX removal by PEG precipitation. In addition to spin-filtration, the efficiency of PEG precipitation as a purification method for removing unbound DOX from DOX-loaded DONs was evaluated. The purification was carried out for an identical set of DOX-DON samples (2 nM triangle DON + 3, 6, or 20 μM DOX) and DOX-only references as for the 100 kDa spin-filtration.
The PEG precipitation was carried out by mixing 750 μL of DOX-DON or DOX-only sample with 750 μL of PEG precipitation buffer (1× TAE, 505 mM NaCl, 15% (w/v) PEG8000), centrifuging for 30 min at 14,000 g, removing the supernatants, and resuspending the pellets to 750 μL of buffer (original sample volume). For DOX-DON samples prepared with 3 μM or 6 μM DOX loading concentration, the pellets could be redissolved by first mixing the samples gently with a pipette followed by overnight incubation at RT. The pellets formed in the DOX-DON samples with 20 μM DOX loading concentration required 24 h incubation under shaking (600 rpm) at +30 °C before being completely dissolved.
Free DOX removal efficiency, DNA recovery, and DOX/bp ratios in the purified samples were determined from UV-Vis absorption spectra with an identical protocol to the spin-filtration analysis.

Spin-filtration and DNase I digestion of bowtie DONs. The DNase I digestion of DONs after free DOX removal with spin-filtration, as well as the diffusive release of DOX form DONs after purification was studied with the bowtie DON. The DONs ($\sim$2 nM) were briefly incubated (30–60 min) with 3 or 6 μM DOX to prepare DOX-loaded bowtie DONs. Unbound DOX was then removed with spin-filtration according to the protocol described under the Supplementary Methods subsection "Free DOX removal by spin-filtration", but with the exception that the original sample volume of 921 μL was concentrated to 760 μL in the final buffer addition step to counterbalance for the sample loss in the spin-filtration. The DNase I digestion and DOX release experiment was then carried out as described in the Materials and Methods section of the main text for both the filtered samples and unfiltered DOX-DON samples. The unfiltered samples were diluted before the digestion to a DNA concentration to the concentration of the filtered samples.
The same spin-filtration and DNase I digestion experiment was also carried out for bowtie DONs with 0 μM DOX as a control to ensure that the spin-filtration of plain DONs does not affect the digestion rate. A purification efficiency of $\sim$100% was confirmed by collecting the absorption and fluorescence spectra of 3 μM and 6 μM DOX-only samples before and after a spin-filtration. For studying the diffusion rate of DOX from spin-filtered samples, one set of 3 and 6 μM spin-filtered bowtie DON samples were incubated at RT after the spin-filtration and their absorption and fluorescence spectra were monitored over a 46 hour time period.

Agarose gel electrophoresis (AGE)

2% agarose gels were prepared in a buffer containing 1$\times$ TAE and 11 mM $MgCl_2$ and pre-stained with ethidium bromide (0.47 μg mL^{-1} final concentration in the gel). DON samples were loaded on the gel with loading dye (Sigma-Aldrich). The gel was run for 45 minutes at 90 V on an ice bath, and imaged under UV light with a BioRad ChemiDoc MP imaging system.

Supplementary notes

Note S1: DOX fluorescence in different pH buffers

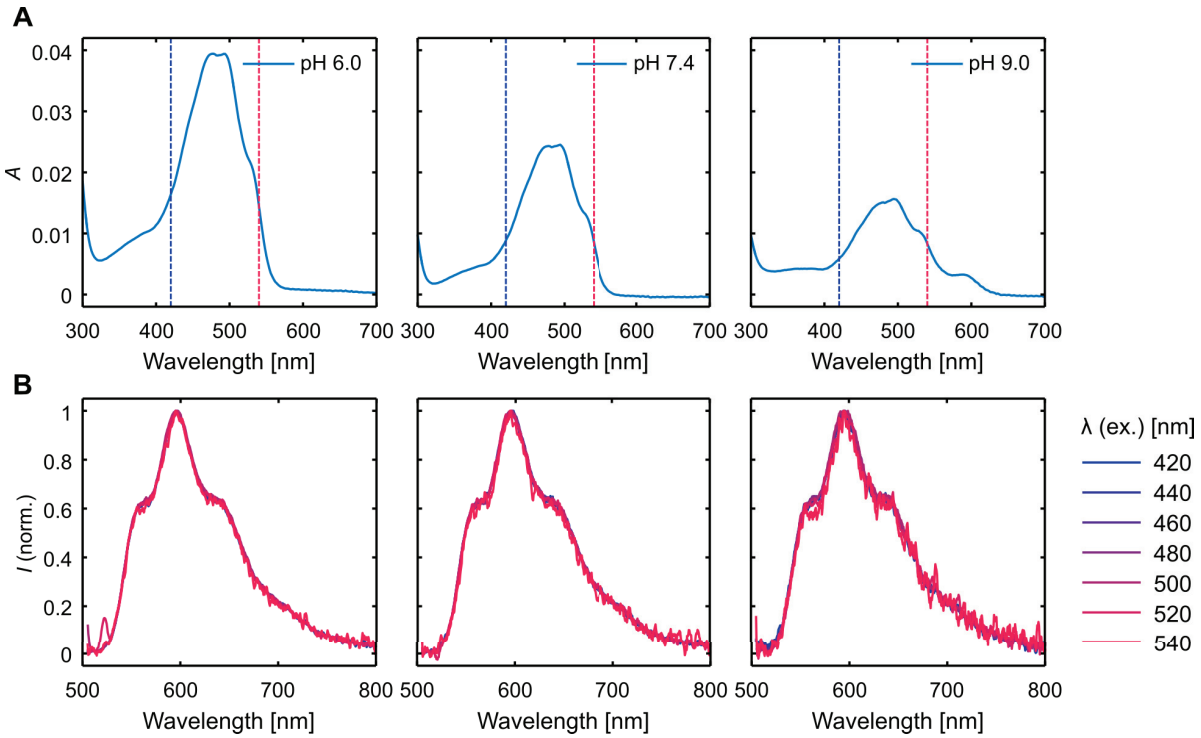

Supplementary Figure 1. Comparison of the shape of the absorption and emission spectra of 3 μM DOX in 40 mM Tris-HCl buffer at pH 6.0, 7.4, and 9.0 prepared without magnesium. (**A**) Absorption spectra at pH 6.0, 7.4, and 9.0. The colored dashed lines indicate the excitation wavelength range applied in Figure B. (**B**) The shape of the emission spectra collected with excitation wavelengths in the range of 420–540 nm. All spectra are normalized to the maximum value. While the emission intensity of DOX depends on the excitation wavelength and the pH of the sample (lower emission intensity at higher pH), the shape of the emission spectrum does not change, indicating that the full emission originates from a homogeneous group of fluorescent molecules.

Note S2: DOX fluorescence spectrum heterogeneity in the presence of different concentrations of $MgCl_2$

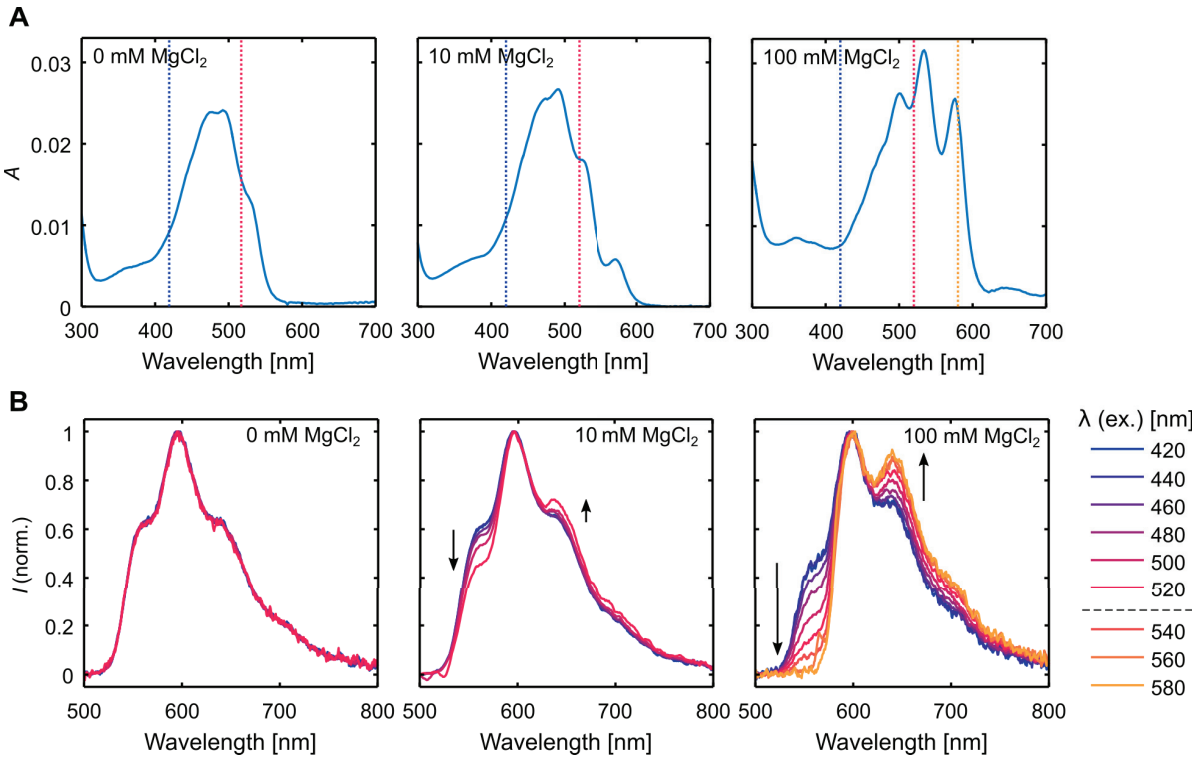

Supplementary Figure 2. Absorption and emission spectra of 3 μM DOX in 40 mM Tris pH 7.4 supplemented with different concentrations of $MgCl_2$. (**A**) Absorption spectra measured at 0, 10, or 100 mM $MgCl_2$ concentration (the concentration indicated in the upper-left corner of each figure). The excitation wavelength range applied for the emission spectra in Figure B (420–520 nm, and 520–580 nm) are indicated with the colored dashed lines. (**B**) Heterogeneity of the emission spectrum of DOX caused by Mg^{2+} complexation. The arrows indicate the changes observed in the shape of the spectrum relative to the spectrum collected with 420 nm excitation when the excitation wavelength changes. For 0 mM and 10 mM $MgCl_2$ samples, the shape of the emission spectrum is compared between 420–520 nm excitation. For the 100 mM $MgCl_2$ sample, additional excitation wavelengths 540–580 are included. The emission spectrum collected with 580 nm excitation originates purely from the DOX-Mg^{2+} complexes, as pure DOX (0 mM $MgCl_2$ sample) does not absorb light at this wavelength. All spectra have been normalized to the intensity at emission maximum.

Note S3: Supplementary DOX self-aggregation data

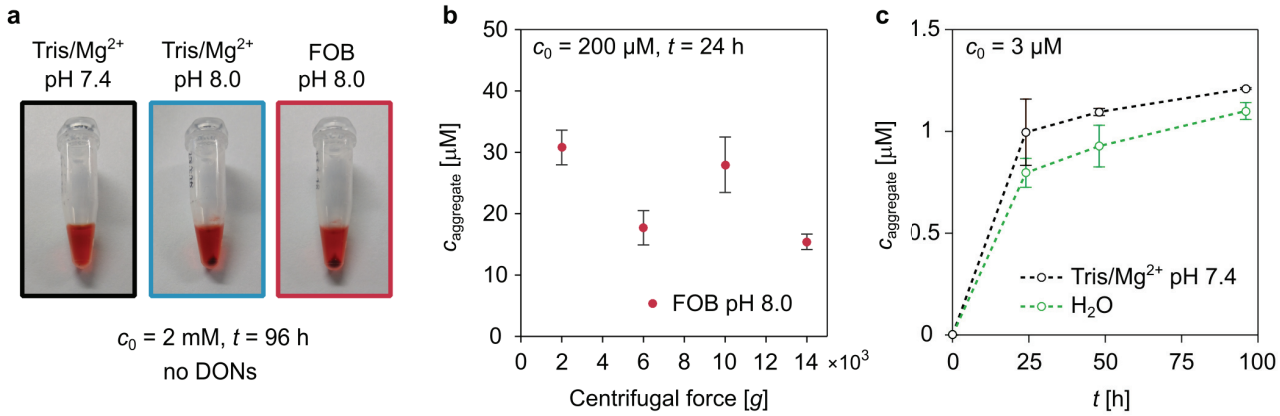

Supplementary Figure 3. Supplementary characterization of DOX self-aggregation. (**a**) Photographs of DOX sedimentation in the DOX-DON loading and aggregation experiment (Figure 3 in the main text). DOX solutions (c_0 = 2 mM) in the absence of DONs were incubated at RT for 96 hours, followed by centrifugation at 14,000 *g* for 10 min to separate DOX aggregates from the solution. DOX self-aggregation was visible to the eye also for 200 µM DOX samples in both Tris/Mg^{2+} pH 8.0 and FOB pH 8.0, but not for smaller (20 and 3 µM) DOX concentrations or any DOX concentrations in Tris/Mg^{2+} pH 7.4 buffer. (**b**) The effect of centrifugal force on the measured $c_{aggregate}$ in the experiment presented in Figure 3 for 200 µM DOX in FOB pH 8.0 after 24 h incubation at RT. (**c**) Self-aggregation of 3 µM DOX in the Tris/Mg^{2+} pH 7.4 buffer and in DI water.

Note S4: Details of the DNA origami designs

Supplementary Table 1. Nucleotide amounts in the studied DNA origami designs (N_{total}) and the fractions of unpaired (N_{ss}) and hybridized (N_{ds}) nucleotides. The N_{ds} includes both the base pairs formed between the staple strands and the scaffold, and the base pairs formed as secondary structures in unpaired scaffold regions (simulated with the NUPACK web application). Molar extinction coefficients per nucleotide at 260 nm (ϵ_{260}/nt) have been calculated for each shape according to Equation (1).

Origami shape	N_{total}	N_{ds}	N_{ss}	$N_{\mathrm{ds}}/N_{\mathrm{total}}$ (%)	ϵ_{260}/nt ($\mathrm{cm^{-1}M^{-1}}$)
Triangle	14,516	14,464	52	99.6	6,700
Bowtie	15,039	13,948	1,091	92.7	6,900
Double-L	15,193	14,324	869	94.3	6,900
24HB	15,504	15,120	384	97.5	6,800
Capsule	16,732	14,704	2,028	87.9	7,000

Note S5: Spectra and titration curves for the bowtie, double-L, 24HB, and capsule origami

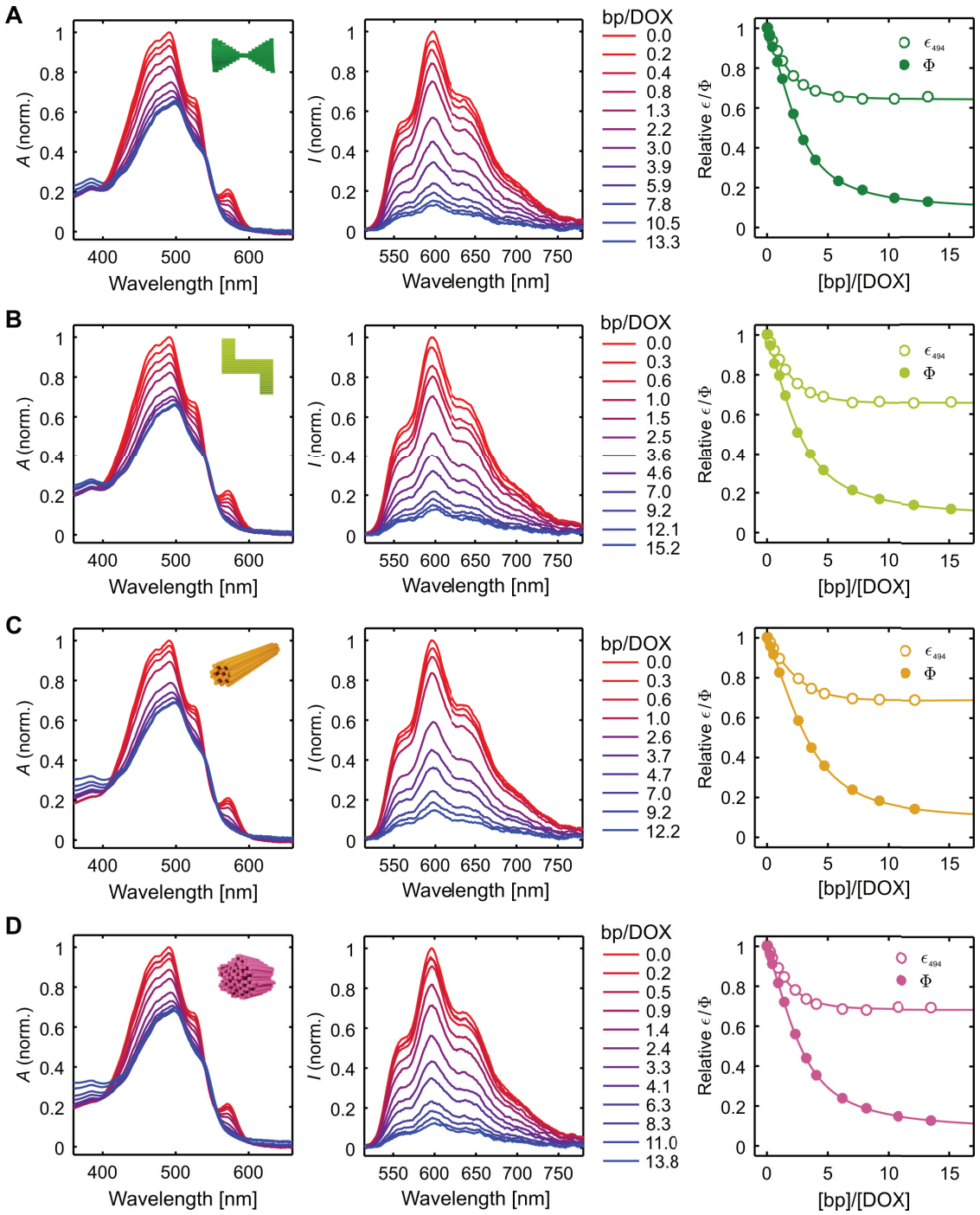

Supplementary Figure 4. DOX absorption spectra (left panel), fluorescence emission spectra (middle panel), and the dependence of DOX extinction coefficient at 494 nm (ϵ_{494}) and fluorescence quantum yield (Φ) on the amount of added DNA (right panel) for all studied DNA origami shapes. For both the absorption and emission spectra, the molar ratio of DNA base pairs and DOX (bp/DOX) is indicated in the legend. The concentration of DOX is 3 μM. The emission spectra have been collected after 494 nm excitation and corrected for the decrease of ϵ_{494}. The titration isotherms on the right panel have been fitted with a 1:2 molecular binding model. The fitting parameters are listed in Supplementary Table 2. (**A**) Bowtie. (**B**) Double-L. (**C**) 24HB. (**D**) Capsule.

Note S6: Comparison of titration isotherms (ϵ and Φ) for all structures

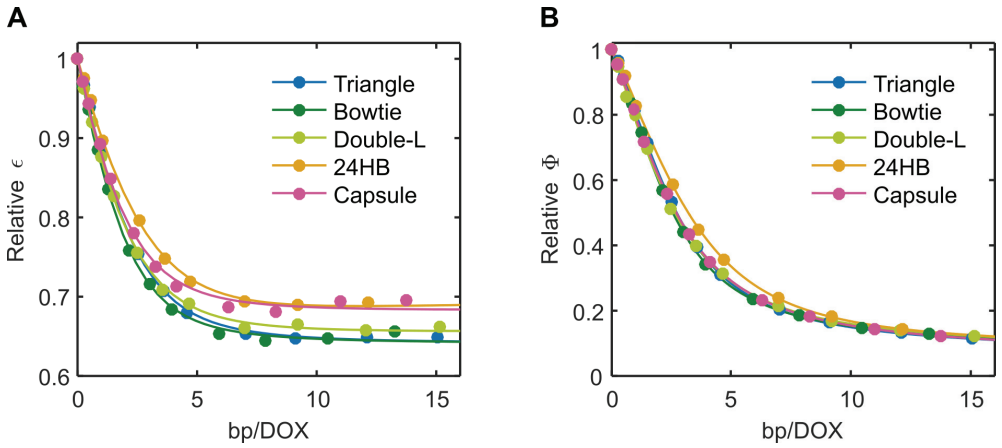

Supplementary Figure 5. Comparison of the effect of titrating DOX with the origami structures in terms of the relative decrease of the molar extinction coefficient at 494 nm (ϵ_{494}) and fluorescence quantum yield (Φ). (**A**) Relative decrease of ϵ_{494} of DOX upon addition of DNA origami. (**B**) Relative decrease of Φ measured with 494 nm excitation.

Note S7: Density of DOX molecules in the DNA origami structures in the titration experiments

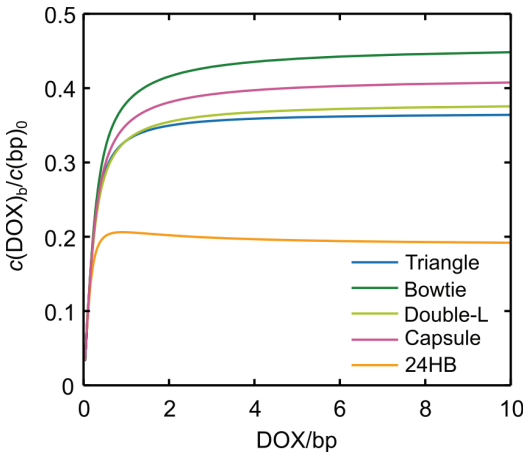

Supplementary Figure 6. Density of DOX molecules in the DNA origami structures in the titration experiments expressed as the number of bound DOX molecules per base pair of DNA (c(DOX)$_b$ / c(bp)$_0$). The molar ratio DOX/bp on the x axis refers to the total concentration of DOX and base pairs in the samples (c(DOX)$_0$ and $(bp)_0$).

Note S8: Fitting parameters K, Φ, and ϵ for all origami shapes obtained from the 1:2 DOX-DNA binding model

Supplementary Table 2. Association constants (K_{11}, K_{12}), fluorescence quantum yields (Φ_{11}, Φ_{12}), and molar extinction coefficients at 494 nm (ϵ_{11}, ϵ_{12}) for the two distinct DOX-DNA complexes. The values have been obtained by fitting the titration data with the 1:2 molecular binding model as described in the Methods section. Φ_{11}, Φ_{12}, ϵ_{11}, and ϵ_{12} are presented relative to the extinction coefficent and quantum yield of free DOX (ϵ_0 and Φ_0.

Origami shape	K_{11} ($\times 10^5 \mathrm{M}^{-1}$)	K_{12} ($\times 10^5 \mathrm{M}^{-1}$)	Φ_{11}/Φ_0 (%)	Φ_{12}/Φ_0 (%)	ϵ_{11}/ϵ_0 (%)	ϵ_{12}/ϵ_0 (%)
Triangle	1.93 ± 0.06	3.07 ± 0.06	62 ± 3	6.2 ± 0.3	62 ± 3	64 ± 3
Bowtie	2.81 ± 0.12	2.95 ± 0.07	64 ± 4	6.9 ± 0.4	64 ± 4	64 ± 4
Double-L	2.0 ± 0.2	2.15 ± 0.14	47 ± 5	7.0 ± 0.7	60 ± 6	66 ± 7
24HB	0.77 ± 0.03	2.59 ± 0.09	27.8 ± 1.2	8.2 ± 0.4	42 ± 2	71 ± 3
Capsule	2.36 ± 0.05	2.26 ± 0.03	57 ± 6	1.3 ± 0.2	64.2 ± 1.5	69 ± 2
Average	$\mathbf{2.0 \pm 0.3}$	$\mathbf{2.6 \pm 0.2}$	$\mathbf{52 \pm 7}$	$\mathbf{6.7 \pm 0.9}$	$\mathbf{58 \pm 8}$	$\mathbf{67 \pm 9}$

Note S9: AFM images of double-L loaded with DOX and DOX-loading estimation

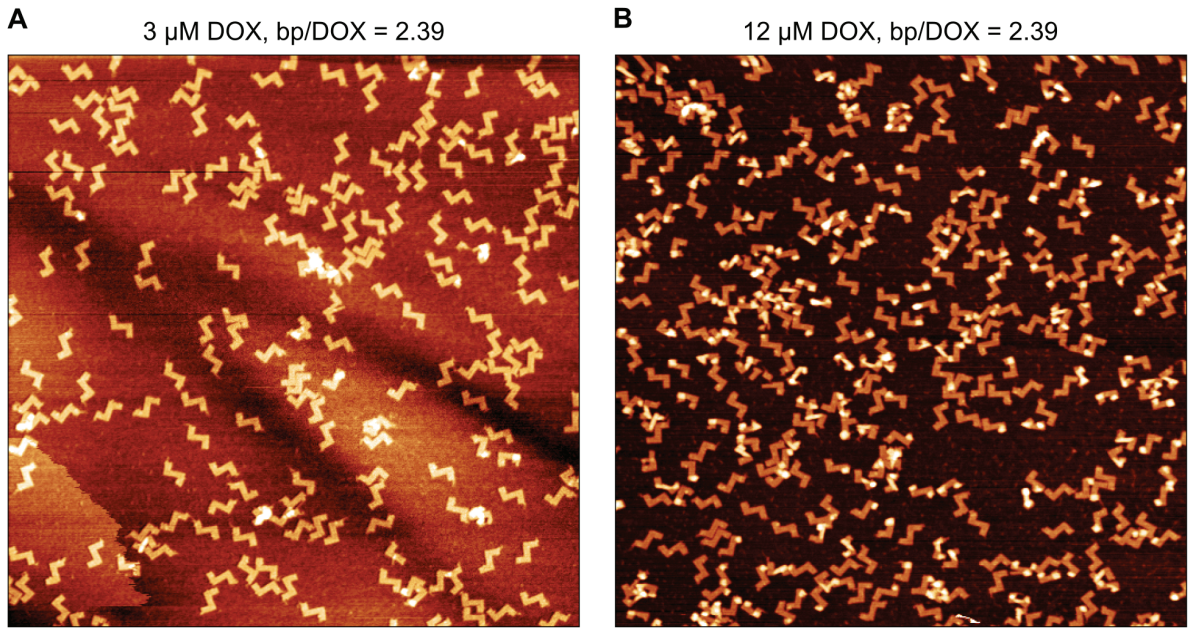

Supplementary Figure 7. AFM images of double-L origami loaded with DOX at two different sample concentrations while keeping the same molar ratio of DNA base pairs (bp) and DOX (bp/DOX). The edge of each figure is 3 μM in length. (**A**) DOX-origami sample prepared with a base pair concentration ($c(\mathrm{bp})_0$) of 7.16 μM and DOX concentration ($c(\mathrm{DOX})_0$) of 3 μM. (**B**) DOX-origami sample prepared at 4 times higher concentration of both DOX and double-L origami than Figure A ($c(\mathrm{bp})_0$ = 28.7 μM, $c(\mathrm{DOX})_0$ = 12 μM). While the bp/DOX ratio is identical in both cases, the higher total concentration of both DNA origami and DOX in Figure B can be seen to lead to an increased fraction of twisted DNA origami shapes, indicating higher DOX binding density through intercalation. The analysis result is in line with the theoretical values predicted by the 1:2 binding model (Supplementary Table 3.

Supplementary Table 3. Theoretical prediction of the density of loaded DOX (number of bound DOX molecules per base pair, $c(\mathrm{DOX})_\mathrm{b}/c(\mathrm{bp})_0$) in the double-L structures shown in Supplementary Figure 7 based on the 1:2 binding model.

	3 μM DOX	**12 μM DOX**
$c(\mathrm{DOX})_0$ (μM)	3.0	12
$c(\mathrm{bp})_0$ (μM)	7.16	28.7
bp/DOX	2.39	2.39
$c(\mathrm{DOX})_\mathrm{b}$ (μM)	1.90	10.6
$c(\mathrm{DOX})_\mathrm{b}/c(\mathrm{bp})_0$	0.27	0.37

Note S10: Kinetics of DOX-DNA association – comparison of different incubation times in the titration experiment

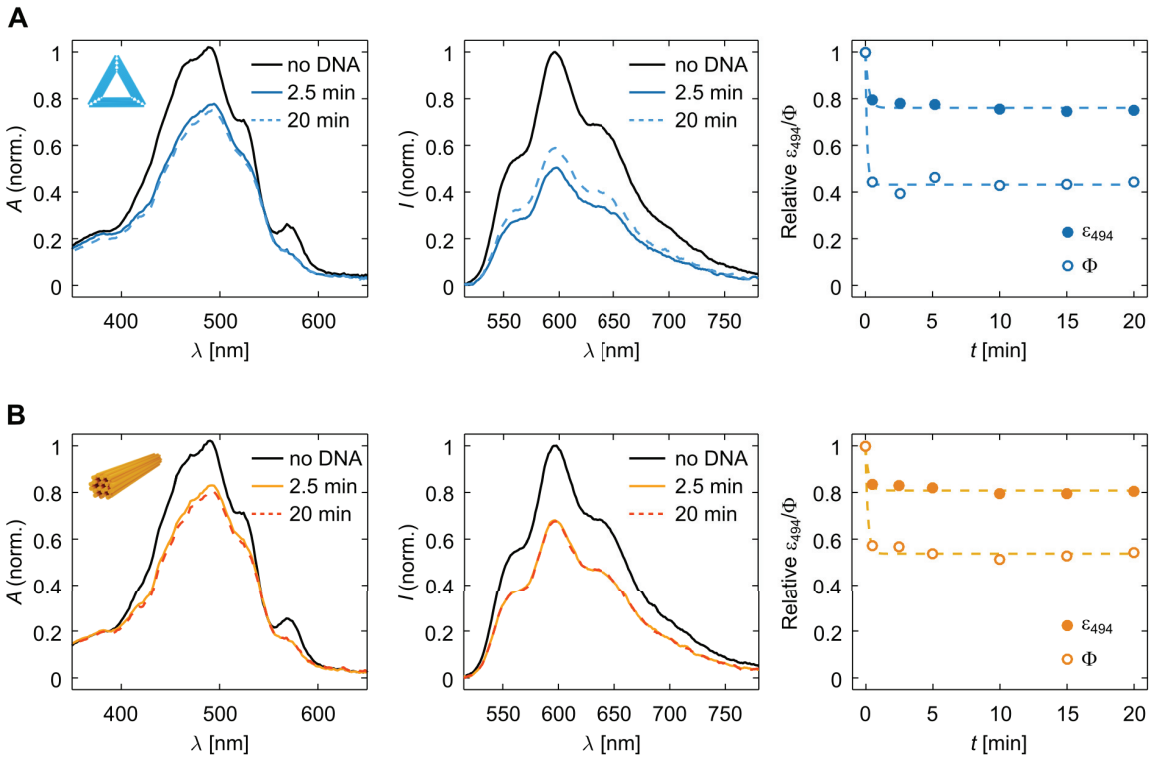

Supplementary Figure 8. The effect of incubation time after DNA addition on the DOX absorption and fluorescence spectra of 3 μM DOX. For confirming that the 2.5 min incubation time in the titration experiment is sufficient for reaching a binding equilibrium for all origami structures, the absorption and fluorescence spectra of 3 μM DOX were collected at different time points after addition of DONs. (**A**) DOX + triangle DON (bp/DOX = 2.16). Left panel: normalized absorption spectra of DOX in the absence of DONs, and 2.5 min and 20 min after an addition of DONs. Middle panel: Normalized fluorescence emission spectra in the absence of DONs, and 2.5 min and 20 min after an addition of DONs. The emission spectra have been collected after 494 nm excitation and corrected for the decrease of ϵ_{494}. Right panel: the relative ϵ_{494} and the fluorescence quantum yield (Φ) of DOX *vs.* the incubation time. (**B**) DOX + 24HB DON (bp/DOX = 1.94). The figures are presented as in Figure A.

Note S11: Titration of DOX with ssDNA

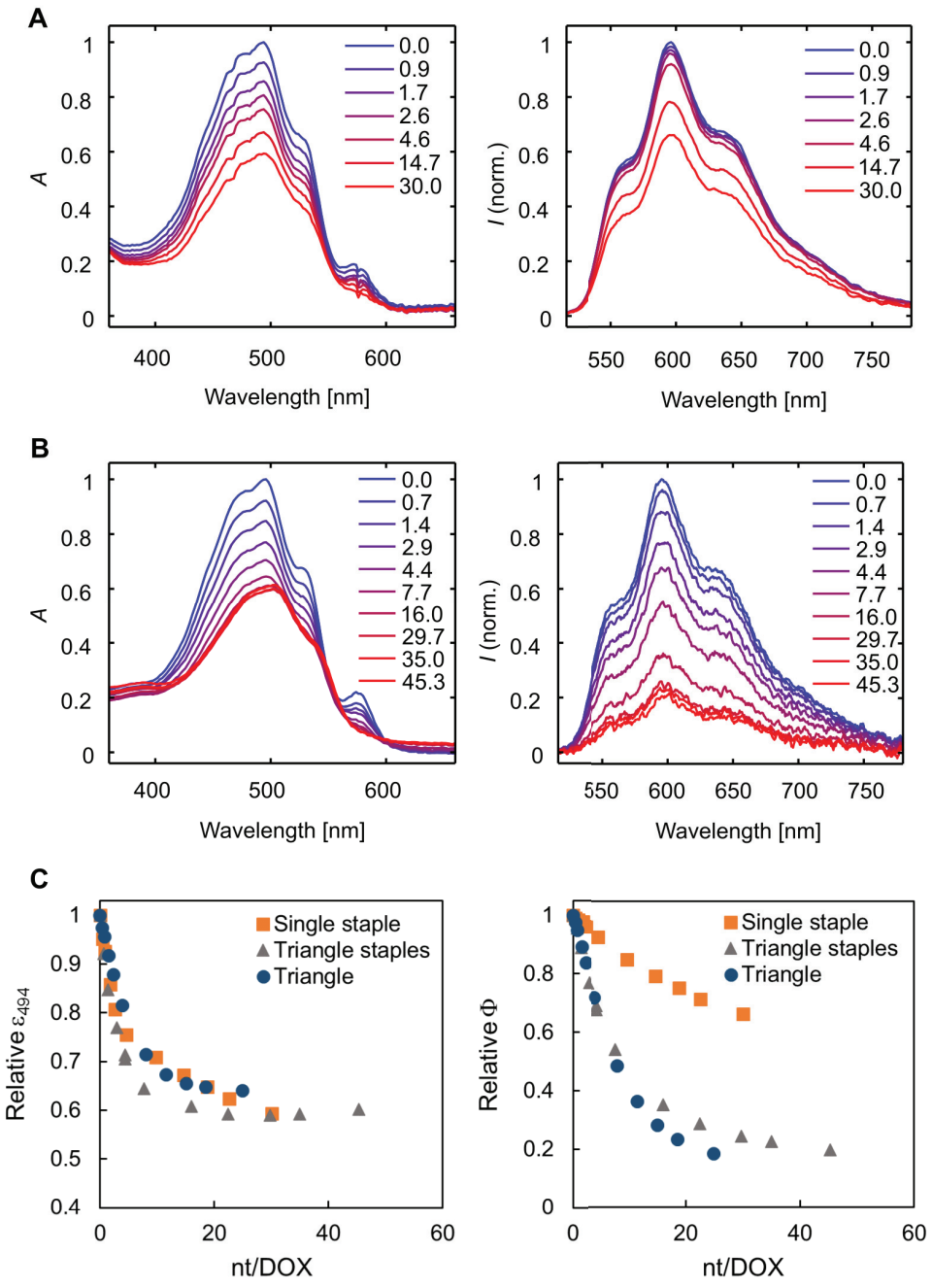

Supplementary Figure 9. Titration of 3 μM DOX with single- and double-stranded DNA. (**A**) Titration with a single oligonucleotide with a low probability of self-hybridization (5'–GAACAACGCTCCAACCATCGC–3'). Absorption spectrum of DOX is shown in the left panel and fluorescence emission in the right panel. The emission intensities have been collected with 494 nm excitation and corrected for the decrease of ϵ_{494} to represent the quantum yield of the DOX molecules (Φ). The legends in both figures denote the molar ratio of nucleotides and DOX (nt/DOX) for each spectrum. The concentration of nucleotides ($c(\text{nt})_0$ has been calculated from the measured A_{260} value and a molar extinction coefficient for 100% single-stranded DNA, ϵ_{260} = 10,000 $\text{M}^{-1}\text{cm}^{-1}$. (**B**) Titration with a mixture of the 232 staple oligonucleotides used for folding the triangle origami, presented as Figure A. While the mixture of staple strands can be expected to contain a high number of hybridized dsDNA regions, the exact fraction of ssDNA and dsDNA nucleotides in the sample is unknown. The nt/DOX ratios presented in the legends have been calculated from the measured A_{260} value and a molar extinction coefficient for 100% single-stranded DNA, ϵ_{260} = 10,000 $\text{M}^{-1}\text{cm}^{-1}$. (**C**) The relative decrease of ϵ_{494} and Φ compared upon titration with a single oligonucleotide (Figure A), the triangle staple oligonucleotide mixture (Figure B), and the folded triangle origami (Figure 3B in the main text).

Note S12: Scattering intensity of the origami

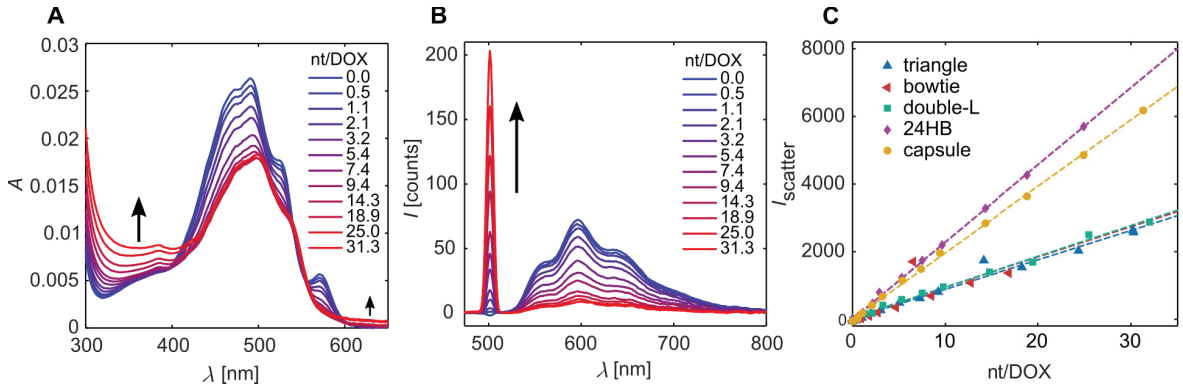

Supplementary Figure 10. Light scattering caused by the DOX-loaded DNA origami. (**A**) Absorption spectrum of a sample containing DOX and an increasing concentration of the capsule origami. Absorption baseline shift upwards during the titration is indicated with the black arrows and shows the increased light scattering in the sample. The amount of DNA origami is described as the total concentration of nucleotides in the sample, and indicated in the legend as the molar ratio of nucleotides vs. DOX (nt/DOX) (c(DOX) = 3 μM). (**B**) Scattered light detected as an increasing intensity of excitation light (494 nm) in the fluorescence emission measurement (90° detection relative to the excitation beam). The spectra are collected for 3 μM DOX upon titration with the capsule origami. (**C**) Intensity of scattered light during titration of DOX with different origami shapes (increasing nt/DOX ratio) shows the stronger light scattering detected with the 3D structures. The scattering intensities have been obtained from the emission spectra by integrating the excitation light peak.

Note S13: Purification of free DOX from DOX-DON samples after loading – comparison of spin-filtration and PEG precipitation

In the experiments presented in the main article, we studied the use of centrifugation as a method for removing free DOX from DOX-loaded DONs after the system has reached an equilibrium and the loading has been completed. As the purification of free DOX from DOX-loaded DONs is an important sample preparation step for downstream applications, we studied it further by performing additional purification experiments. Here, we evaluated the efficiency of other purification methods for free DOX removal: spin-filtration and PEG precipitation.

As an initial experiment for optimizing the spin-filtration process, we studied the suitability of spin-filters with different molecular weight cutoff membranes for DOX removal. The experiment was performed by centrifuging samples of partly aggregated DOX (2 mM DOX solution prepared in FOB pH 8.0 and incubated for 24 h at RT) through 10 kDa, 30 kDa, and 100 kDa spin-filters (Figure S11a). For both 10 kDa and 30 kDa filters, the DOX concentration in the filter increased during centrifugation [c(concentrate) > c_0], which indicates that some of the DOX particles were too large to pass through the membrane (Figure S11b). Only the 100 kDa filters had sufficiently large pore size to allow the DOX molecules and aggregates to freely pass through the membrane during centrifugation, indicated by a similar DOX concentration in the unpurified sample and in the concentrate [$c_0 \approx c$(concentrate)]. In conclusion, this shows both that DOX aggregates formed during long incubation times can be relatively large in size (too large to pass through the 10 kDa and 30 kDa filter membranes), but that they can still be removed with 100 kDa molecular weight cut-off spin-filtration.

However, the DOX concentration in the filtrate [c(filtrate)] decreased relative to c_0 for all tested filters. The filter membranes also turned visibly red during the spin-filtration process. Together these observations show that part of DOX is lost in the spin-filtration process due to binding to the filter membrane. For 2 mM DOX and 100 kDa membrane, ~20% of the DOX molecules were bound to the membrane during centrifugation. The extent of DOX binding to the 100 kDa filter membrane was studied also for smaller DOX concentrations and both DOX-DON and DOX-only samples. As shown in Figure S11c, the percentage of DOX binding to the filter membrane can be considerable especially at low DOX concentrations (> 90% of DOX bound to the membrane at 3 μM and 6 μM DOX concentration) – regardless of the DON concentration in the sample.

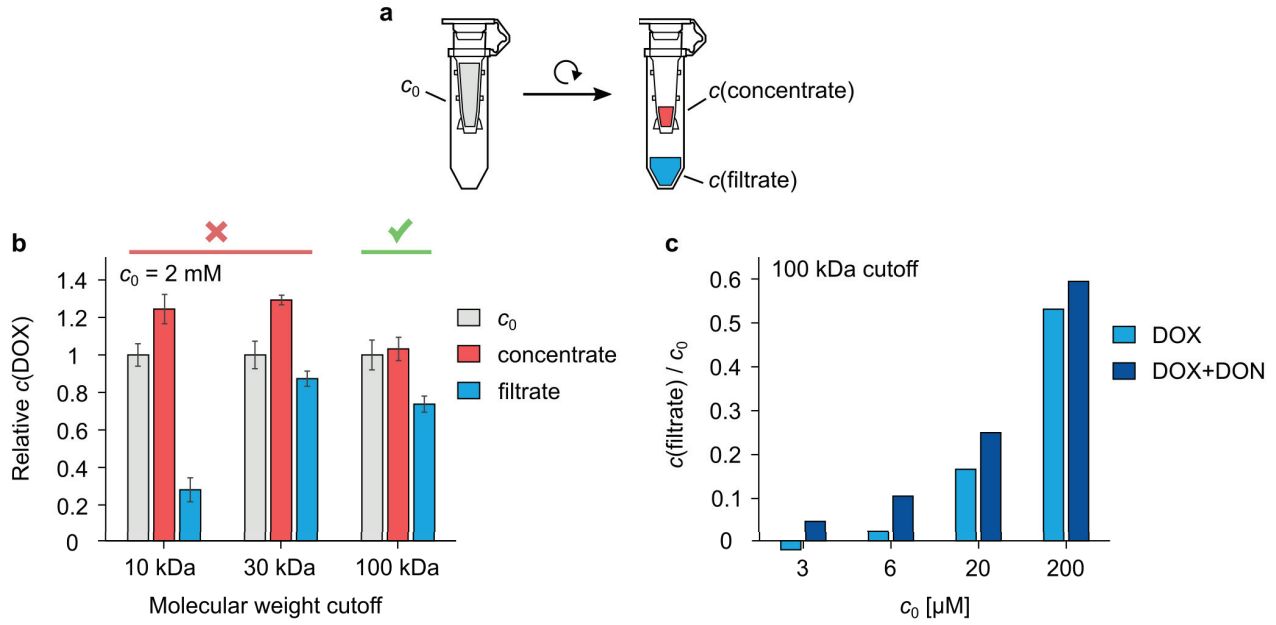

Supplementary Figure 11. Experiments for estimating the DOX aggregate size and the suitability of spin-filtration as a purification method for free DOX. (**a**) Schematic of the spin-filtration experiments. c_0 refers to DOX concentration in the sample before spin-filtration. After centrifugation, the concentration of DOX is measured from the sample remaining in the filter [c(concentrate)] and/or from the flow-through [c(filtrate)]. (**b**) Spin-filtration of 2 mM DOX solution in FOB pH 8.0 through different molecular weight cutoff filters after 24 h incubation at RT to promote aggregate formation. (**c**) c(filtrate) relative to c_0 in DOX and DOX-DON samples after spin-filtration through a 100 kDa membrane, showing the fraction of DOX bound to the filter membrane during the spin-filtration procedure. DOX samples contain the indicated c_0 of DOX in Tris/Mg^{2+} pH 7.4. The DOX-DON samples contain additionally 2 nM of the triangle DON. All samples have been incubated for 1 h at RT before spin-filtration to load the DONs with DOX. The experiment in Figure b was repeated three times and the results are expressed as the mean ± standard deviation. The experiment in Figure c was performed once.

We then prepared DOX-loaded triangle DONs at different DOX loading concentrations (2 nM triangle DON incubated for 1 h with either 3, 6, or 20 μM DOX in Tris/Mg^{2+} pH 7.4) and studied the purification outcome of both 100 kDa spin-filtration and PEG precipitation. The purification protocols have been described in the Supplementary Methods.

Both spin-filtration and PEG precipitation are highly effective for purifying free DOX from the solution (> 99% of free DOX removed with both methods). but spin-filtration leads to notably higher sample loss during purification with all DOX loading concentrations (Figure S12a). Interestingly, increasing the amount of DOX weakens the outcome of both purification methods: for spin-filtration, a clear decrease of sample recovery is observed with increasing DOX concentration. PEG precipitation leads to high sample recovery with all DOX concentrations, but the formed precipitates were observed to become increasingly difficult to resuspend at higher DOX concentrations. While 3 μM and 6 μM pellets were dissolved after overnight incubation at RT, the 20 μM DOX concentration required additional incubation under shaking at +30 °C to dissolve. As this could cause some sample damage, the results for PEG-purification at 20 μM DOX concentration may not be fully comparable to the other loading concentrations, indicated with a different color in the presented figures.

We then studied the composition of the purified samples by determining their DNA and DOX concentrations with UV-Vis analysis. Because free DOX has been removed from the samples, the analysis can be used to determine the DOX loading density (DOX/bp) – number of bound DOX molecules per a DNA base pair – for each DOX loading concentration. This analysis thus also complements the results of DOX loading yield obtained by studying the DOX-DON binding equilibrium with titration experiments as well as the loading yield estimation in the DNase I experiment. As seen in Figure S12b, the DOX/bp ratio increases with the DOX loading concentration, but in a non-linear fashion. This is an expected result based on the DOX-DNA binding equilibrium and in line with the titration experiments, where we estimated the DONs to be saturated with DOX at DOX/bp = 0.36 ± 0.10. The solid line in Figure S12b presents the equation

$$\mathrm{DOX/bp} := \frac{c(\mathrm{DOX})_\mathrm{b}}{c(\mathrm{bp})_0} = \frac{c(\mathrm{DOX})_0}{c(\mathrm{bp})_0} \times s \times f_b \qquad \textbf{(1)}$$

Where f_b for each $c(\mathrm{bp})_0$ is obtained from Equations (3) and (4) in the main article using K_{11} = (2.0 ± 0.3) × 10^5 M^{-1} and K_{12} = (2.6 ± 0.2) × 10^5 M^{-1}. As a feature of the applied binding model, the DOX/bp ratio approaches 1 at high $c(\mathrm{DOX})_0$. A factor s (the DOX/bp saturation value) was thus included in the Equation 1 for correcting the model for a saturation value < 1 by finding a value of s that leads to the best fit to the data with non-linear least-squares fitting. The best fit was obtained with s = $(\mathrm{DOX/bp})_\mathrm{max}$ = 0.45 ± 0.04 DOX/bp.

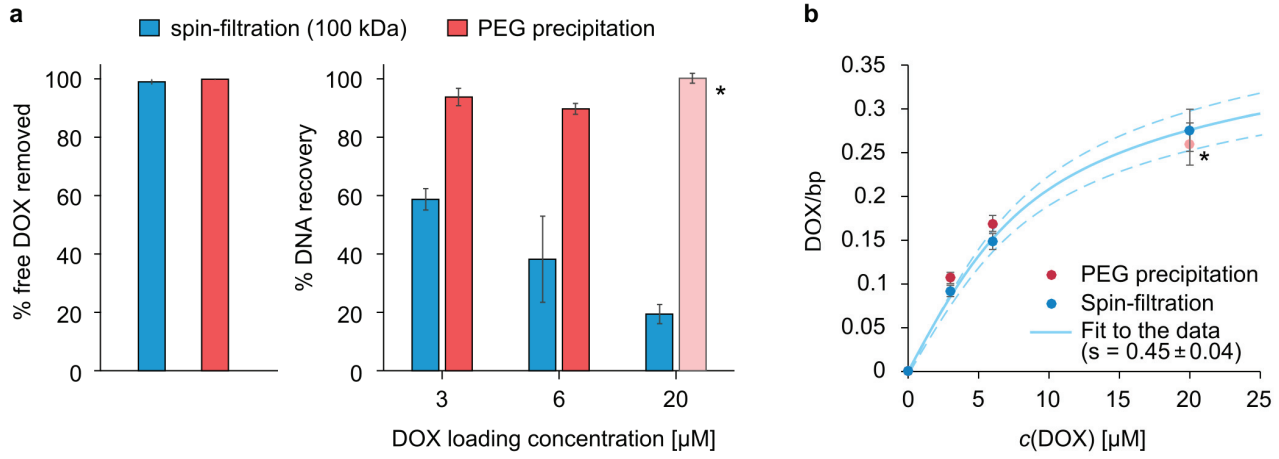

Supplementary Figure 12. Comparison of spin-filtration (100 kDa) and PEG precipitation as purification methods for removing free DOX from DOX-loaded triangle DONs. (**a**) DOX purification (free DOX removal) efficiency and sample loss during the purification. *PEG purification result of the 20 μM sample is shown, although we note that PEG precipitation at this DOX concentration is not recommended as the resulting pellet required heavy processing to dissolve. (**b**) DOX-DON sample composition after purification. The number of bound DOX molecules per DNA base pair (DOX/bp) was determined from purified DOX-DON samples prepared at 3–20 μM DOX loading concentration. The best fit of the thermodynamic binding model to the data is obtained with a saturation at 0.45 ± 0.04 DOX/bp.

Note S14: DOX release from DONs through diffusion after purification

After confirming that spin-filtration efficiently removes free DOX from DOX-loaded DON samples (Supplementary Note S13), we studied the kinetics of the diffusive release of DOX from the DONs. This takes place when the low-DOX environment of the solution favors the dissociation of DOX (Supplementary Figure 13a). Through a series of experiments described below, we conclude that the release of DOX from DONs takes place rapidly after the binding equilibrium is disturbed by removing the unbound DOX molecules. We did not explicitly study the kinetics of the release, but could define that freshly spin-filtered, DOX-loaded bowtie DON samples had already reached a new binding equilibrium in less than 10 minutes after the spin-filtration procedure.

Supplementary Figure 13b shows the change of the base pair concentration [$c(\mathrm{bp})_0$] and DOX concentration [$c(\mathrm{DOX})_0$] when DOX-loaded bowtie samples (2 nM DONs + 3 or 6 μM DOX) were either purified with 100 kDa spin-filtration or diluted to the same $c(\mathrm{bp})_0$ as in the purified sample. The purification of unbound DOX was expected to lead to a considerably reduced observed quantum yield of DOX (Φ_{obs}) when the remaining DOX molecules are bound to DONs. Still, only a slight decrease of Φ_{obs} was observed in the purified sample, indicating a considerable number of free, fluorescent DOX molecules (Supplementary Figure 13c). As the efficiency of the purification of free DOX molecules was confirmed to be $\sim$100% (Supplementary Figure 12a), it can be assumed that the free DOX molecules were released from the DONs after the purification. A dilution of the unpurified samples to the same $c(\mathrm{bp})_0$ as in the purified samples also led to DOX release, observed as a slight increase of the Φ_{obs}.

In a further analysis, the detected values of Φ_{obs} were compared to the expected quantum yields after equilibration (Φ_{eq}) (Supplementary Figure 13c). The Φ_{eq} values were calculated from the Equation 2 for each $c(\mathrm{DOX})_0$ and $c(\mathrm{bp})_0$ according to the applied binding model and the values of K_{11}, K_{12}, Φ_{11}, and Φ_{12} for the bowtie DON (Supplementary Table 2). A close agreement between the measured and calculated values was observed. This indicates that the DOX release from the purified samples had progressed to a thermodynamic equilibrium before the measurement (in less than 10 minutes after spin-filtration). The loading density for the samples in terms of DOX/bp is obtained by dividing the bound DOX concentration $c(\mathrm{DOX})_{\mathrm{b}}$ obtained from the binding model (Equation 4) by the $c(\mathrm{bp})_0$. This shows that the purification and subsequent DOX release decreased the DOX loading density of DONs by 70% for 3 μM and by 66% for the 6 μM loading concentration (Supplementary Figure 13d). No further Φ_{obs} increase was detected when the spin-filtered samples were incubated at RT for 45 hours (Supplementary Figure 13e). This indicates that the equilibrium state had been reached before the first measurement. When the diluted and the purified DOX-bowtie samples were subjected to DNase I digestion, the reduced total DOX concentration in the purified samples led to increased digestion and DOX release rates (Supplementary Figure 14).

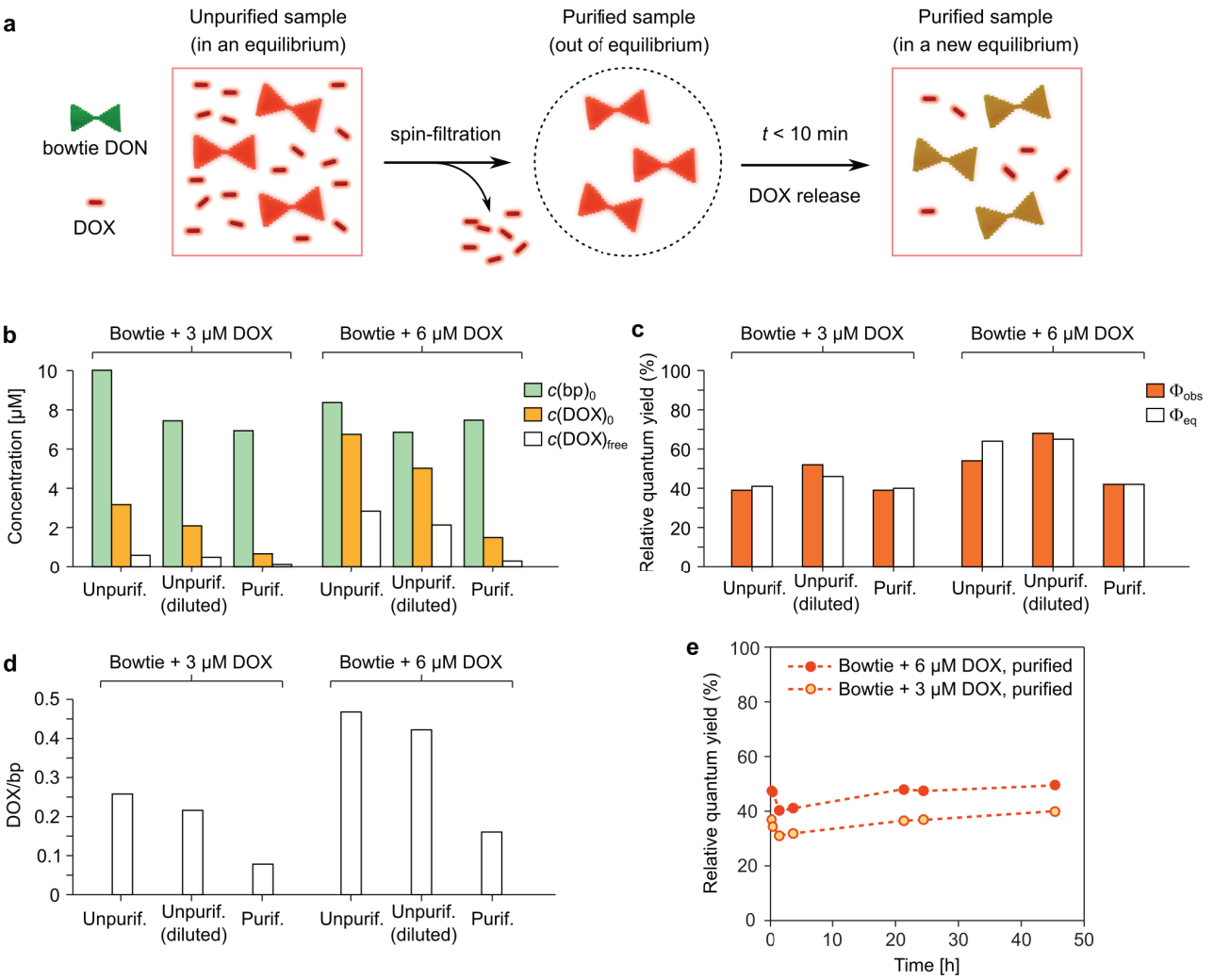

Supplementary Figure 13. Evidence of a fast equilibration and DOX release after free DOX removal from DOX-loaded bowtie DONs. (**a**) Schematic illustration of the sample composition after the spin-filtration and the subsequent equilibration, during which a part of the bound DOX molecules is released from the DONs. (**b**) The measured base pair concentrations [c(bp)$_0$] and total DOX concentrations [c(DOX)$_0$] in the studied DOX-bowtie samples: unpurified samples, unpurified but diluted samples, and spin-filtrated samples. The calculated equilibrium state free DOX concentrations [c(DOX)$_{\mathrm{free}}$] for each sample are also shown. In subfigures b, c, and d, colored bars represent experimentally determined values, while empty bars are values calculated according to the applied binding model (Equations 2–4 in the main text) from the experimental values. (**c**) The measured DOX quantum yield (Φ_{obs}) in freshly spin-filtered DOX-bowtie samples (< 1 h) compared to the calculated equilibrium state quantum yields (Φ_{eq}). The close correspondence between the measured and calculated values suggests that all three sample types have reached an equilibrium before the measurement. (**d**) The calculated DOX loading densities in terms of bound DOX molecules per DNA base pair (DOX/bp). (**e**) The detected Φ_{obs} of spin-filtered samples during 45-hour incubation. Subfigures b, c, and d show representative data obtained for a set of samples in a single experiment. Qualitatively reproducible results were obtained when the experiment was repeated.

Note S15: The DNase I digestion and DOX release profiles of bowtie DON samples before and after spin-filtration

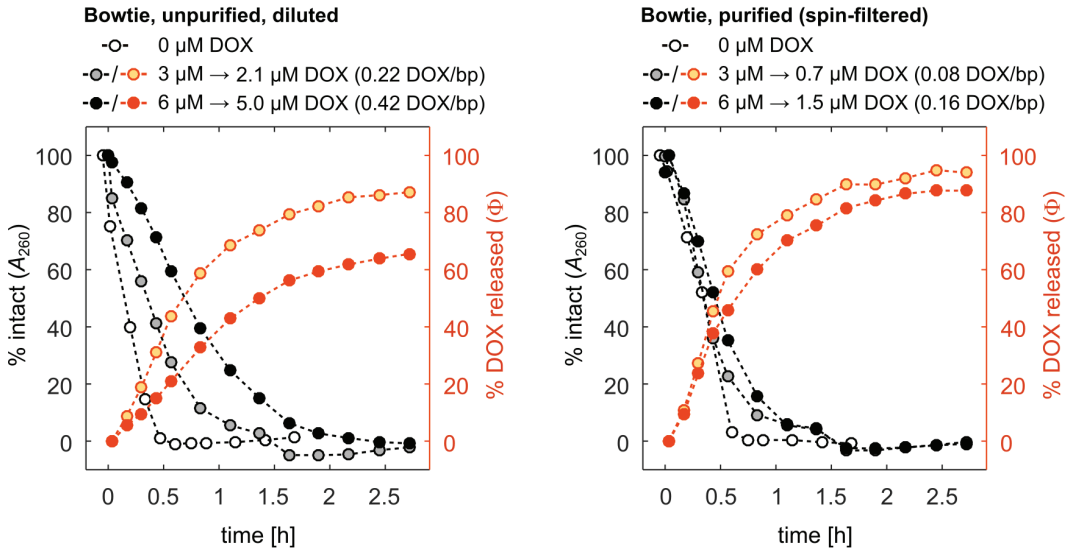

Supplementary Figure 14. The effect of spin-filtration on the the DNase I digestion profiles (white, gray, and black circles) and DOX release (yellow and orange circles) of bowtie DON samples. On the left, DOX-loaded bowtie samples prepared at either 3 or 6 μM DOX loading concentration were diluted before the digestion to a match the base pair concentration of the purified samples. On the right, the samples were purified with spin-filtration to remove the originally unbound DOX before the digestion. As described under Supplementary Note S14, all samples were in a thermodynamic equilibrium before starting the digestion and contain both bound and free DOX molecules as presented in Supplementary Figure 13b. The presented data was obtained for a set of samples in a single experiment. Qualitatively reproducible results were obtained when the experiment was repeated.

Note S16: Details of DOX-DON samples in the DNase I digestion experiments

Supplementary Table 4. Composition of the DNA origami-DOX samples in the DNase I digestion experiments before addition of DNase I. The DOX quantum yields relative to free DOX references (Φ/Φ_{ref}) and the base pair/DOX molar ratios (bp/DOX) are based on the measured DNA absorbance and DOX fluorescence intensities. The concentrations of free DOX ($c(\mathrm{DOX})_{\mathrm{ub}}$), bound DOX ($c(\mathrm{DOX})_{\mathrm{b}}$), and bound DOX molecules bound per base pair of DNA ($c(\mathrm{DOX})_{\mathrm{b}}/c(\mathrm{bp})_0$) have been calculated according to Equation 6 and the parameters in Supplementary Table 2. All values are presented as the mean ± standard error of three individual measurements.

3 μM DOX

	Φ/Φ_{ref}	bp/DOX	$c(\mathrm{DOX})_{\mathrm{ub}}$ (μM)	$c(\mathrm{DOX})_{\mathrm{b}}$ (μM)	$c(\mathrm{DOX})_{\mathrm{b}}/c(\mathrm{bp})_0$
Triangle	0.37 ± 0.06	4.0 ± 0.3	0.68 ± 0.11	2.3 ± 0.2	0.196 ± 0.015
Bowtie	0.44 ± 0.13	3.7 ± 0.2	0.9 ± 0.4	2.1 ± 0.4	0.19 ± 0.04
Double-L	0.43 ± 0.13	3.6 ± 0.2	1.0 ± 0.4	2.0 ± 0.4	0.19 ± 0.04
Capsule	0.48 ± 0.12	4.9 ± 0.5	0.9 ± 0.5	2.1 ± 0.5	0.14 ± 0.02
24HB	0.33 ± 0.05	5.3 ± 0.6	0.9 ± 0.3	2.1 ± 0.3	0.14 ± 0.01

6 μM DOX

	Φ/Φ_{ref}	bp/DOX	$c(\mathrm{DOX})_{\mathrm{ub}}$ (μM)	$c(\mathrm{DOX})_{\mathrm{b}}$ (μM)	$c(\mathrm{DOX})_{\mathrm{b}}/c(\mathrm{bp})_0$
Triangle	0.55 ± 0.05	1.98 ± 0.15	2.4 ± 0.2	3.6 ± 0.2	0.31 ± 0.04
Bowtie	0.62 ± 0.13	1.86 ± 0.10	3.0 ± 0.8	3.0 ± 0.8	0.28 ± 0.09
Double-L	0.60 ± 0.13	1.80 ± 0.10	3.2 ± 0.6	2.8 ± 0.6	0.27 ± 0.07
Capsule	0.63 ± 0.13	2.4 ± 0.3	2.7 ± 1.0	3.3 ± 1.0	0.21 ± 0.05
24HB	0.61 ± 0.12	2.6 ± 0.3	2.7 ± 0.9	3.3 ± 0.9	0.20 ± 0.04

Note S17: Comparison of the spectroscopic results and an agarose gel electrophoresis (AGE) analysis of the DNase I digestion

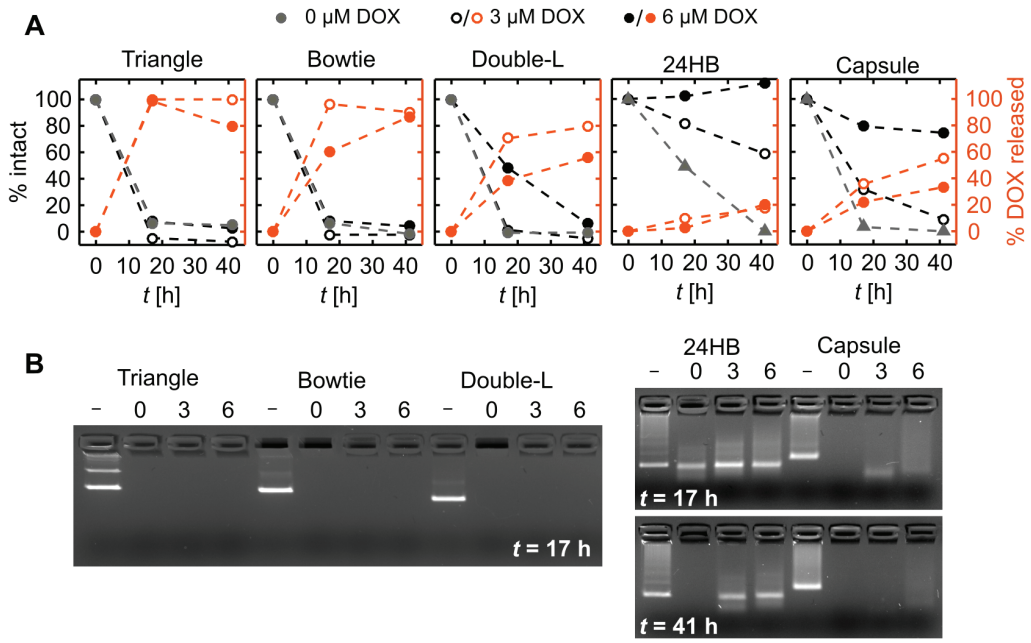

Supplementary Figure 15. Parallel analysis of the DNase I digestion of DONs with both spectroscopic means and with an agarose gel electrophoresis (AGE). 28.2 U/mL DNase I has been added in all samples at $t = 0$. (**A**) Digestion and DOX release profiles based on the A_{260} readings (% intact) and the recovery of DOX quantum yield (% DOX released). The structural integrity of the DONs is shown with the gray markers for the samples without DOX, and with the empty and filled black markers for the samples containing DOX at either 3 or 6 μM concentration. For the samples with 3 and 6 μM DOX, the empty and filled orange markers depict the fraction of released DOX molecules relative to the initial concentration of bound DOX molecules. (**B**) AGE result of the 2D DONs after 17 h digestion and 3D DONs after 17 h and 41 h digestion. The first lane for each sample (–) contains intact DONs in the absence of DNase I at 0 μM DOX concentration; the lanes marked with 0, 3, and 6 contain the digested DONs with the indicated concentration of DOX (in μM).

Note S18: 24HB design and staple sequences

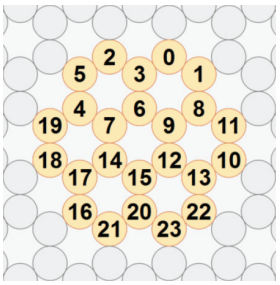

Supplementary Figure 16. Cross-section of the 24 helix bundle (24HB) design and the helix numbers.

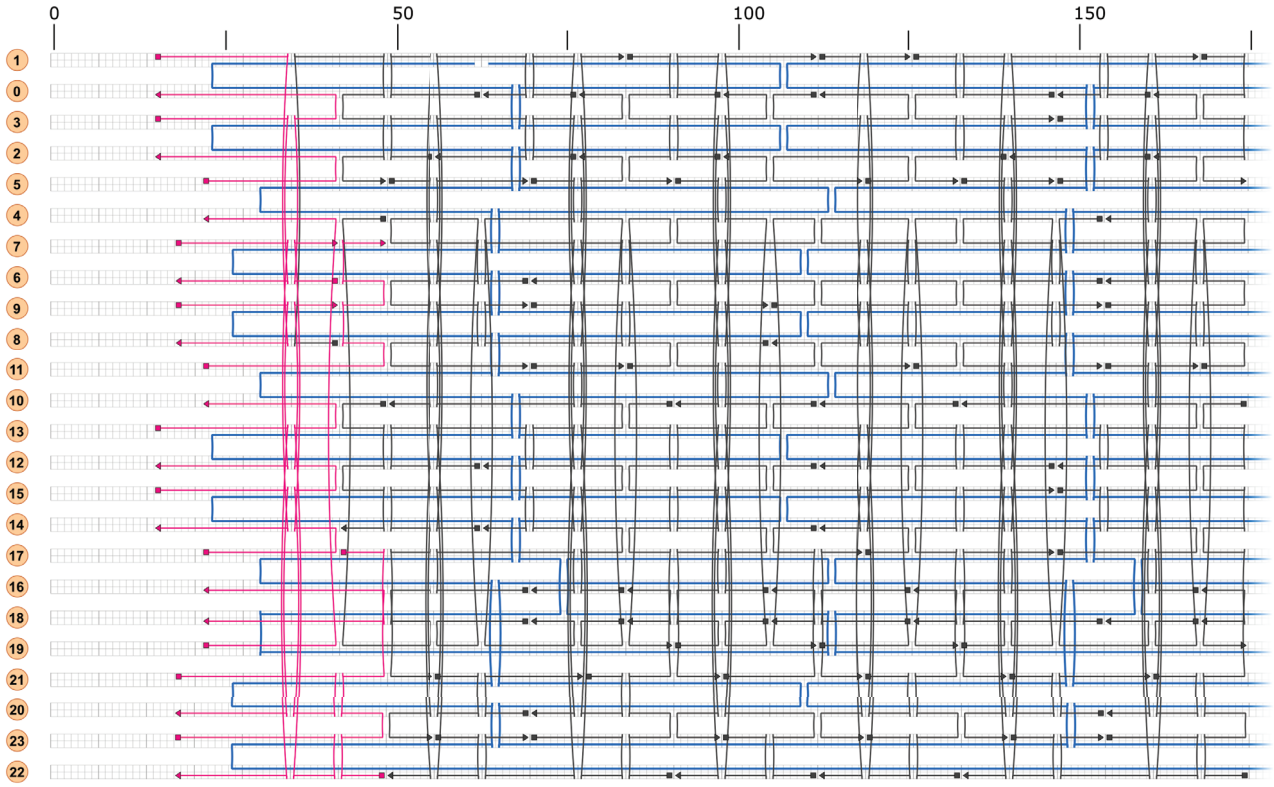

Supplementary Figure 17. Part 1 (grid positions 15–174) of the 24HB CaDNAno blueprint. The helix numbers are shown on the left side of the figure, and the numbers on top indicate the grid position. The 7,560-nt scaffold is shown in blue, fully complementary scaffold strands in dark gray, and scaffold strands containing 8× poly-T overhang sequences in pink.

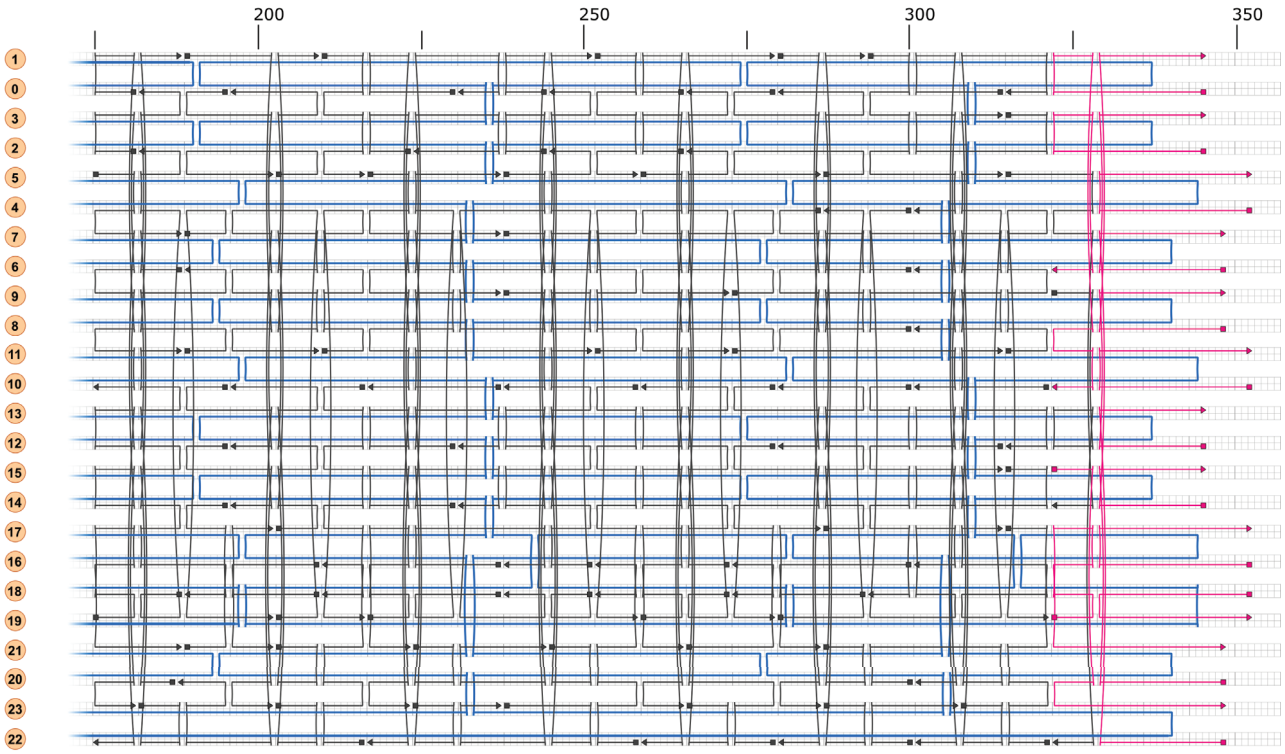

Supplementary Figure 18. Part 2 (grid positions 175–352) of the 24HB CaDNAno blueprint.

Supplementary Table 5. Staple strand sequences for the 24HB design. Nucleotide bases complementary to the scaffold strand are written in capital letters. The 8× poly-T overhang sequences in staples #174–202 have been indicated by lowercase letters. Start pos. and end pos. indicate the positions of the staple strand termini in the caDNAno design (helix number[grid position]).

#	Start pos.	End pos.	Sequence
1	3[147]	2[140]	TTGAAATTCAAATCCAATCGC
2	6[153]	20[154]	CTCATTTATCTAATTTACGAGAGAGAGAATTTATCAAAGACA
3	22[279]	9[272]	GACAGTAGTTGGGAGAGGCTTGAGATGGGCAAAAGGGAAGTTAGCTTGA
4	21[78]	1[83]	GAAGGTAGATAATCAGTCACGGATTATATCCTGAGCAAATTTACGTGA
5	1[210]	5[216]	GTACCGCTAAGTATTTTTGCTTTAAGAGGCCCCCT
6	5[238]	18[238]	TTTTGTCGAGAATAGAAAGTACCGGAACGAGGCGCATGAAAC
7	10[48]	14[42]	TATCCGCTCGAATTGTGCTTGGACCTCCTTGAATC
8	22[258]	16[252]	ATCGCACGCTCATTTCAACTTGAAACACACGTAAC
9	5[70]	18[70]	GGCGCTAGCGTACTATGGTCAAATACCGAACGAACGCACGTG
10	10[195]	20[188]	GAAGCCTTTCCAGAGCCACCAGCCATTCGCCATTCGGTTTACAAATACAT
11	5[287]	5[286]	CGGAAGCTTAATTGCTCCTTTTGATAATTCTGTATGGCAGAC
12	7[238]	21[244]	ACTAAAGCGATTATACGAAGGTGTGAATTACCTAGGAATAAGGCTTGCC
13	20[153]	21[160]	CCACGACGCTTAAGACTCCTT
14	17[287]	0[280]	CCAAAAGATAACCCAAGACTTTCAAAAATGCGGATTAGCTCAACATGTT
15	21[140]	15[146]	GATGATGATTATCATACCTTT
16	19[217]	21[223]	TCCATGTATTTGTAGTCACCAAGCAAAACTTGAGC
17	21[189]	7[188]	AATACAGACCGAGGAAACGCACAAAGTTCGTCAAATCGGCTG
18	0[195]	12[196]	GTATCAGAGAGGATTAGGATTCGTCATACAAACAAAAATCAC
19	2[265]	22[259]	ACAGCCCCTACAACAGGCTCCCTTAAACTCCATTACTAAAGACAGGAAG
20	0[181]	10[175]	TTGAGAAGCCAACGCAAGCAAAACCTCCAGATTAG
21	2[181]	22[175]	AGTACCGTCGAGCCAAGAACGTCATCGTAATTTGCGCTAACGGCAACTG
22	16[83]	0[77]	AGTTGGCCAAATGATTCTGACCACGTATAAGGGATCCCGATTCTAAATC
23	18[167]	2[161]	CCCTTTTAAGAATTAGAAAAAACAATAAGTAAAGT
24	1[126]	5[132]	AAAGCCTTAAGGCGTTCTGACAGAACGCATATAAC
25	4[300]	16[301]	TTCGAGCTTGATAATCAGAAATAATCGTGAGGCATTCCCACA
26	21[98]	16[105]	TTAGGAGCACTAGCATATCAA
27	1[252]	5[258]	TCAGAGCATAGGAAGTACAAATCATAGTCAGACGT
28	20[69]	21[77]	AGGATGCTCGAAAGGAATTGAG
29	15[147]	3[146]	TACATTTATAATTATTTGCACTATCAAACCCTTAGTAATGGT
30	9[70]	23[69]	CGCCAGATTACATTATTGCAACCCAGTCACGACGTATTTAGA
31	5[315]	14[322]	AAAGGTGGCATCAAAAATCATAATAAAGGAGAGTC
32	10[111]	22[112]	ACTATCGATTTACAAAATCGCGATGTGC
33	20[300]	15[314]	GGAACAAGATTTAGGAATAGCGTCTGGCCGGATTCGCTTTTG
34	6[300]	20[301]	GATTGCACAAATATCGCGTATAGAGCAAGGCTTTTTCCTAAC
35	17[203]	0[196]	GCAAGGCAGAATCAATGATACCAGTAAGAGCGGGGAGCCCGGAATAGGT
36	10[300]	18[294]	TTCATTGCAATACTTTTGCCAAGCGAGACACTATCGAATTACAAAACTA
37	10[279]	22[280]	TCGTCACATGTTTAGACTGGAGGACGAC
38	16[104]	19[111]	ACCCTCACACCTTGTGGCCAAGTTAGAATCAGATACCACACCGCGGTCA
39	19[91]	21[97]	AAAACAGACAGTGCAAAGCATATCAATAAATATCT
40	0[230]	10[217]	CGAGAGGGTTGATACACCCTCGAGGCAGCCGCCGCTCAGAGC
41	21[266]	16[273]	AGTAGTAAATTGAAGGATATT
42	23[140]	12[147]	GTTTGAGTCGCTATCAATTACCTGAGATTACGGGA
43	11[168]	19[174]	TTTAGCGATCAGATTTTATTTGGTATTAAAACCAACTGAACAGAGTTAA
44	6[69]	20[70]	AGGAATGTTTGCTTTGACGAGCTGAAAGGATTCACACATTTG
45	0[314]	8[301]	ATTAGGCTGAATATAGTTTCATTAGAAT
46	11[84]	19[90]	ATAACATCCATCACGAAGTGTCCGATTAAACGTGCCGCCGCTAGAAGAT
47	19[175]	21[188]	GCCCAATCTATCTTAGCCGAAATAATAATAGCAAACGTAGAA
48	21[224]	14[231]	CATTTGGGGAGGGATCGGTCATAGCCCTACATAGC
49	9[273]	0[266]	TACCGTTAGTCTCCAAAAAAAGCCTGTAGGATAGC
50	23[308]	12[315]	TGGGAACTCGTAACCGTCAATATGATATGAGGGTA

51	11[126]	19[132]	AACAATTACATAAATAAATCGGAAAACAGTCAATATACCTTTGGTAATT
52	4[48]	21[55]	AACAGCTCCCTAAAACATCGCTTTGAATCTGTAAGTCGCCCTAACCCCG
53	22[111]	9[104]	TGCAAGGTTAAATCGAACAACTAATAGAAAGGGACTGACGCTATCAGTG
54	12[195]	23[202]	CGGAACCTTGCGTCAGACTGTATTCATTCAGCGCC
55	14[111]	18[105]	ATTTTTCCTGAACCTAACACC
56	0[265]	10[259]	AAGCCCACACCACCACAATGAGGAGTTAAGCGAAA
57	22[132]	16[126]	GCTGGCGTATTAATGAACAAAATTCCTGCCTGATT
58	12[314]	0[315]	GCTATAATAATACTCATATATTTCCATATAACAGTTTTGACC
59	17[119]	0[112]	GAATAATAAGAAATGAGAAGATAGCGATTTTCATCTTAAATAAGAATAA
60	18[188]	2[182]	GCAATAGAATAAGAACAATAGTAATGCAAATATAA
61	9[154]	23[153]	ACAAGCAACAGCCATTTATCCCGGTGCGGGCCTCTTAGAATA
62	1[280]	10[301]	AACTAAAAATCAGGGGATGCTTTAAACAGTTCAGAAAACGTAATAAATA
63	0[111]	12[112]	ACACCTGGGTATTTTAGTTAAAGCTTAGTAACCTTTTGAATA
64	8[300]	22[301]	GACCATATAGTCAGAAGCATGAAGAAGTGCGGAATCGTGCAT
65	20[187]	6[189]	AAAGGTTTTTTGTAGAGCCTAGGAATCATTACCACACCTTA
66	10[258]	18[252]	GACAGCATTGAGGAAACGGGTCTAAAACTCTTTGAGACCTTCTACAGAC
67	11[315]	19[321]	TGCCTGAGAACCCTTTTGCGGAAAAACAATTAAGCACAGGCAAAAACAG
68	15[315]	3[314]	AGAGATCTGGAGCAAACAATATAGCAAATTATGACTTATACA
69	17[147]	17[146]	ATCAAAACATAAAGGAACTGGCATGAAATTCATCACTACCAT
70	5[259]	23[265]	TAGTAAATTTCAACAATTTTTACACTCAGAAAGAGTTTAATTATACCAG
71	22[174]	16[168]	TTGGGAACAATCAATATAAAAAGTATGTCGGAATA
72	2[223]	22[217]	GAAAGTACAGTACCTGAATTTAAGCCAGTTTGCCACTCAGAGGTGCCGG
73	21[119]	1[125]	TCATCATGAAACCACAGATGAGATTGCTGCTTCTGTCAATATACTAGAA
74	0[97]	10[91]	GGTGCCGCCCAAATAGTCTGTCACTTGCTGGTAAT
75	10[216]	18[210]	CACCACCCGCCTCCTCTTTTCTTTCATCTAGCGACCGGAAACTCATCGC
76	2[139]	22[133]	AAGACAACTAAATTAATCCTTTCGCTATTAACGGATTCATTTTACGCCA
77	14[195]	18[189]	CTTTAAAACCAGAATGAAATA
78	16[272]	19[279]	CATTACCGTAATCTCACTAAATCACGTTGAAAAGATTTTGCTGACCAAC
79	0[160]	9[153]	AACGCCAACAAATTGCTTATCCGGTATTTTCGAGA
80	2[55]	22[49]	AGCAGGCAAAGAATCATTAATGTCGGGACTACGTGCGTAATCCGACGGC
81	2[244]	7[237]	ACGATCTGAGTTTCATTGTATCGGTTCGTTGAACA
82	21[203]	1[209]	ATCACCGGGAAATTAGCGCGTATAATCAATAAATCGATTGGCAGGTTTA
83	23[182]	11[188]	TTCATATAGGCTGCAGCGTCTTAAATCACGACTTG
84	23[98]	8[105]	ACTCGTACGATTAATACCTACGCCTTGCCTGAGTAGAAGAACTGACCGA
85	22[216]	16[210]	AAACCAGAAAGGGCTATTGACTCACCGATCACCAG
86	9[322]	22[322]	GAGAAGCTGCCGGATCAACCGTGTAGAT
87	11[210]	19[216]	ACCAGAGGTCAGACCTCATTAACCGTTCAGGAGTGTTGAGTAGACCTGC
88	1[112]	11[125]	CATAATTATGTGAGTCTTAATTACATTT
89	9[238]	23[237]	GCTTGCTGTAATGCCGGCTACAGCTTTCCGGCACCTGTATGC
90	11[70]	11[69]	TTCTTTGTACCGCCAGGTTTCCTGTGTGTGTAAAGCCAATAC
91	22[300]	23[307]	CTGCCAGTAATAAAACGAACG
92	0[244]	9[237]	ACCGTAACAGAACCCACGCATAACCGCAAGTATCA
93	21[161]	1[167]	ATTACGCGAAACGCCCAATCCAAAATAAAGCCGTTATAGAAGCTTACCA
94	7[189]	19[202]	TCTTTTGTTTATCAGCAAGAAACGTCGA
95	6[188]	0[182]	TCATTCCAGTAATAGGCTTAA
96	23[154]	11[167]	AGTTTATTTTGTCAGGGCGATTGAATCTTTTGCACGAGGCGT
97	23[70]	11[83]	AGTATTAGACTTTAGGGTTTTCAGGAAAACAATATATTAGTA
98	0[76]	9[69]	GGAACCCGGCCCACAACCGTTGTAGCTGCGCGGTA
99	5[133]	23[139]	TATATGTGAGAGACGTGAATTGTAAAACGTAACAGTTTTGCGTTTAAAA
100	1[84]	5[90]	ACCATCATAAAGCATAGAGCTGGAAGGGGGCAAGT

101	23[203]	10[196]	AAAGACAGCAAAGCCCGGAACCTCAGAGCCGCCTT
102	22[90]	16[84]	AACGCCACAAACAACGTCAATTATCTAATCTGGTC
103	12[62]	0[63]	GCTTAAGAACCTGTGGGTGCCTCTATCAGGGCGATTAGGTTG
104	5[203]	5[202]	AGTTAATGCTGAGACTCCTCAAGAGAAGGAACGCGCCTAAAC
105	19[112]	14[112]	GTACAAAGTCAGAGTTAACCTCCGGCCAAGACGCTTGCGTAG
106	21[56]	14[63]	CTTCTAAGCACGACTGTAATGAGTAACACGGGGCA
107	2[160]	6[154]	AATTCTGGTAATTTTACCGCA
108	18[125]	17[118]	TGAACACCCTGAATTCCTTCT
109	3[315]	6[301]	TTTCGCATTTGGGGCGCGAGGATTAGAGAGCTTAACCAAGCG
110	4[286]	18[273]	CGAACGAAGCCCGATCGTTTACCAGATATGACAAGAAAGAGG
111	23[266]	11[272]	TCAGGACTCGGCCTCTTTTTCCCTCAGCAAGGCCG
112	11[189]	1[188]	CGGGAGGTTCGCGCCCAATAGCTCAACA
113	5[49]	23[55]	TTGCAGCGACGGGCGGGTGGTAGGGGCCTGGTTGGTTAAGTGGTGGTTG
114	1[168]	5[174]	GTATAAATCGCCATGGCATTTACAAAAGACAACAT
115	16[237]	16[238]	AGTGAATTAGAGCCATGAAACCATCGCAAGCGCAGCTCATTC
116	5[175]	23[181]	GTTCAGCATAAGTCTCAATAAAATGAAAAAACGATGGCAACATAGAAAA
117	18[209]	17[202]	CTGATAAATTGTAAGGCATTA
118	5[217]	23[223]	GCCTATTCAGTGCCTACTGGTTAATCAGGGCATTTAGGTAAAGACATTC
119	23[224]	12[231]	AACCGATGCTTCTGCCGCCACCCTCAAACACCCTT
120	12[111]	23[118]	CCAAGTTATCAGGTTTAACGTCCAGAAGCTTTGCC
121	17[315]	5[314]	TCATTCGTTAAAGATGAACGGAGCCCCAAGGCAAACAGCTGA
122	9[105]	0[98]	AGGCCAAATGCGGGAGCTAAAGAAAGCCGGGTCGA
123	16[69]	16[70]	CAGTTTATTTACGCCAACTCGTCGGTTAAGAATAGAAATCAA
124	23[287]	10[280]	TCTACGTTTTGAGGTAGCGTCAATCCCCCTCAAGA
125	14[230]	2[224]	AGCACCGAATAAGTCAGTCTCAGGCGGATAAGTCTAAATTCTGAAACAT
126	18[293]	17[286]	GCATGTCAATCATGAATAACG
127	18[104]	2[98]	GCCTGCAAGGTGAGCGCCGCGTCACGCTAACGTGG
128	21[245]	1[251]	CTGACGATAATCATCACCAACAAAATACTTCGAGGCATCGCCGCCACCC
129	1[189]	11[209]	GTACCGTACTCAGGCTTGATATTACCAGAACCACC
130	16[251]	0[245]	AAAGCTGGCTGGCTCCCCCAGGAATTGCGCCTTTAGTCACCACCCATGT
131	10[237]	10[238]	GCGAACCGCCACCCCAGCATTGAATATATTCGGTCGAGGGTA
132	10[132]	18[126]	AAACATCCGAATTATTCGCCTATATACAAGAAATAGGAAGGGAATTAAC
133	16[300]	21[286]	TTCAACTAATGCAGATACACCGATTCAT
134	18[251]	2[245]	CAGGCGCAGACGGTGCGGAGTGTCTTTCTAGCGTA
135	10[174]	18[168]	TTGCTATTACCAACCAGTTACAAATAAGATAGCAGAGCAGATACCGAAG
136	12[146]	0[147]	GAAACAATAATTAATTAATGGATCATATGCGTTATACATACC
137	10[90]	18[84]	ATCCAGAAACGCTCCTGAAATACGACCAAGAACCCAAAATCTCACGCTG
138	19[203]	14[196]	AATCCGCACAGTGCCCGTATGGCTTTTGAGTTTGC
139	18[237]	5[237]	AAAGTACAACGGAGTACTTAGACGGGGTTCGGAACCTATTAG
140	8[104]	1[111]	GTAAAAGCAAGTTTTTGGAAT
141	11[154]	11[153]	AGAACGCCCAGCTACACAAAAGAAGATGAATTACCTTTTCTA
142	16[167]	0[161]	CCCAAAAAAAAAGTACCTTTACCATGTAGAACCAAGAGGCAGAATTTAAC
143	19[280]	4[287]	TTTATGTACCCCGGTTCAAAG
144	11[273]	1[279]	CTTTTGCTCATAGTTGCGCCGCTCATTTTCTATGC
145	12[279]	23[286]	AAAATGAAACGACGATAAAAAACAGGTAAGAAAAA
146	0[279]	12[280]	TTAAAAGGCAGAGGTCATTTTGATTAAGTACCCTGTAATAGT
147	18[83]	2[77]	AGAGCCACACCAGCACAGGGCGGGCGCTAAGAAAG
148	14[62]	2[56]	CGAATATTTTTCTTCCAGCTGAGCCCGAGATAGAAAGCTGGTTTGCCCC
149	10[321]	11[314]	GTCAAATCACCATCAATGCAA
150	11[252]	19[258]	CTTGCAGCAACAACTGAATTTAAAAGGAGAATAATAGTTTCACAATCAT

151	1[294]	4[301]	GTCTGGAAATGCTGGGCTTAGAGTACCTAAACTCCAACAGGTGATTTAA
152	21[287]	1[293]	CAGTTGACATTATTCCAAAATGAGGGGGACTATTAAATCAAAGTACGGT
153	23[56]	12[63]	TGAATTCTGTAAAAATGGTCATAGCTCCGGACAGG
154	23[238]	11[251]	GATTTTAAGAACTGTCCAGCCAGAGGCTTCGGAACGCTGAGG
155	12[230]	0[231]	ATTAGCGAATGGAAGGAGGTTAGAACCGCCACCCTCAGCCGT
156	16[209]	21[202]	TAGCACCATTACAAGTGAATT
157	18[272]	2[266]	ACAGATGCCGAACTAAACAACTGAATTTTCCACAG
158	5[147]	4[154]	GATGCCAGACGACGTAATATC
159	2[97]	22[91]	CGAGAAATGACGGGCAGGAGGTTTTATACAATCGTATGGAAAGTTGGGT
160	16[125]	21[118]	GTTTGGATTATAAAGGAATTA
161	5[91]	23[97]	GTAGCGGCTTAATGTTTCCTCCAGAGATGTAATAATTAGAGCTTCGACA
162	23[119]	10[112]	CGAACGTAAAGGGGGCAGAGGAAGAAAACAAAAAA
163	4[153]	18[154]	CCATCCAGAGAGATAACCCACTAAAACA
164	0[146]	10[133]	GACCGTGTGATAAAGTTTAGTAAACAGTTCATTTGATGAAAC
165	22[321]	17[314]	GGGCGCAAAACGGCAACCCGTCTTCCTGCCATCAAAAATAATAGGAGAA
166	19[133]	21[139]	GAGCGCTACGGGAGTTAGAACATATAATATTATCA
167	2[76]	6[70]	CGAAAGGGGGAGCCTTTAGAC
168	18[69]	5[69]	GCACAGACAATATTCATTAAACCAGTGAAAGCGGTCCACGCG
169	8[41]	5[48]	ACTCACAACGTCAAAGGGCGATTGGAACTAAATCAGAAAATCGAGAGAG
170	19[259]	21[265]	AAGGGAAAACGGTGATCAAGACAAATCACAGAACG
171	5[119]	5[118]	TTGGGTTGAGAAAACTTTTTCAAATACGGCGCGTAACTTAGG
172	0[62]	10[49]	AGTGTTGTTCCAGTAAAACCGTAATGAGCATAAAGAAATTGT
173	18[153]	5[146]	GGGAAGCGCATTAGAATATCATAGGTCTAAATGCT
174	8[348]	1[345]	tttttttGCAAGGATAAAACAATTCTGCttttttt
175	5[22]	2[15]	tttttttCCGCCTGGCCCTCTGTTTGATGGTGGTTCCGttttttt
176	9[18]	12[15]	tttttttTTGCGCTCAGATAAAGACGGAttttttt
177	14[345]	7[348]	tttttttTCATTGCCTCCTCAGAGCATAttttttt
178	1[15]	8[18]	tttttttACGTGGACTCCATTAATTGCGttttttt
179	6[41]	0[15]	CCAACGCTCCCTTAAAGAGTCCACTATTAAAGAttttttt
180	20[348]	15[345]	tttttttTTAAATGTGAGCGCTATCAGGttttttt
181	3[15]	6[18]	tttttttAAATCGGCAAAAGCGGGGAGAttttttt
182	6[348]	3[345]	tttttttAAGCTAAATCGGAATAACCTGttttttt
183	12[345]	9[348]	tttttttATAAATTAACTTTATTTCAACttttttt
184	13[15]	22[18]	tttttttGGATCCCCGGGTCTCAGGAGAttttttt
185	21[18]	9[41]	tttttttTTATGACAATGTCCCGTGCTGAAGAACTCTTTACCTCCTGCCCG
186	15[322]	23[348]	TACAAAGGAGTAACGGATTGACCGTAATGGGATttttttt
187	23[18]	10[22]	tttttttAGCCAGGGTGGATGTTAAGCTTTACCGAGCTCACAATTCCACttttttt
188	11[22]	7[48]	tttttttACAACATACGAGCCGGAAGTGAGCTACTTTCCAGAATCGGGGCGCCA
189	0[345]	10[322]	tttttttGAACGAGTAGATTTAGTGATTCCATTTTTAGTAATGTGGAGACA
190	22[348]	13[345]	tttttttAGGTCACGTTGGTTCTAGCTGttttttt
191	22[48]	16[22]	CAGTGCCCTTCTAATCCTTAGCCAAAATGGAGTGACTCTATGATACCttttttt
192	19[22]	4[22]	tttttttGCGAACTGATAGGATTGCCCTTCAttttttt
193	17[42]	18[22]	CTGCCATGGCTATTAGTCTTTAATGCttttttt
194	7[18]	14[15]	tttttttGGCGGTTTGGCATTTCACATAttttttt
195	19[322]	21[348]	GAAGATTTATTTTGCATTAAAAGGAACGTAGCCAGCTTTCATCAACAttttttt
196	15[15]	20[18]	tttttttAATCATTTCTCCTTGTCAACCttttttt
197	17[22]	7[41]	tttttttGACAGTGCGGCCGGCTGACCGTATTG
198	2[345]	6[322]	tttttttTTTAGCTATATTTTCAAATGGTCTTGTACC
199	18[352]	19[352]	tttttttAAATTGTAAACGTTAAGTATAAGCAAATATTTttttttt
200	10[352]	11[352]	tttttttAAGGGTGAGAAAGGCCGTAGGTAAAGATTCAAttttttt
201	16[352]	17[352]	tttttttTCATTTTTTAACCAATTTTTTGTTAAATCAGCttttttt
202	4[352]	5[352]	tttttttAGCATTAACATCCAATTTCTACTAATAGTAGTttttttt